

UC San Diego

Research Theses and Dissertations

Title

Theory and Simulation of Diffusion Processes in Porous Media

Permalink

<https://escholarship.org/uc/item/8mw7h8hz>

Author

LaBolle, Eric M.

Publication Date

1999-06-01

Peer reviewed

INFORMATION TO USERS

This manuscript has been reproduced from the microfilm master. UMI films the text directly from the original or copy submitted. Thus, some thesis and dissertation copies are in typewriter face, while others may be from any type of computer printer.

The quality of this reproduction is dependent upon the quality of the copy submitted. Broken or indistinct print, colored or poor quality illustrations and photographs, print bleedthrough, substandard margins, and improper alignment can adversely affect reproduction.

In the unlikely event that the author did not send UMI a complete manuscript and there are missing pages, these will be noted. Also, if unauthorized copyright material had to be removed, a note will indicate the deletion.

Oversize materials (e.g., maps, drawings, charts) are reproduced by sectioning the original, beginning at the upper left-hand corner and continuing from left to right in equal sections with small overlaps. Each original is also photographed in one exposure and is included in reduced form at the back of the book.

Photographs included in the original manuscript have been reproduced xerographically in this copy. Higher quality 6" x 9" black and white photographic prints are available for any photographs or illustrations appearing in this copy for an additional charge. Contact UMI directly to order.

UMI[®]

Bell & Howell Information and Learning
300 North Zeeb Road, Ann Arbor, MI 48106-1346 USA
800-521-0600

.

Theory and Simulation of Diffusion Processes in Porous Media

BY

ERIC MATTHEW LABOLLE

B.S. (Environmental Resources Engineering, Humboldt State University) 1987

M.S. (Civil Engineering, University of California, Davis) 1993

DISSERTATION

Submitted in partial satisfaction of the requirements for the degree of

DOCTOR OF PHILOSOPHY

in

Hydrologic Sciences

in the

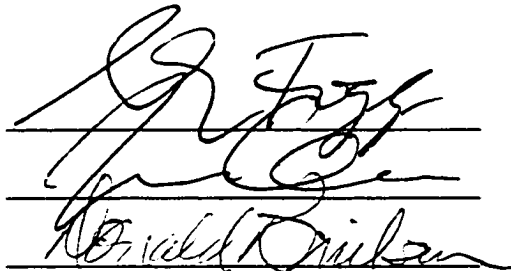
OFFICE OF GRADUATE STUDIES

of the

UNIVERSITY OF CALIFORNIA

Davis

Approved:



Committee in Charge

1999

i

UMI Number: 9940107

UMI Microform 9940107
Copyright 1999, by UMI Company. All rights reserved.

**This microform edition is protected against unauthorized
copying under Title 17, United States Code.**

UMI
300 North Zeeb Road
Ann Arbor, MI 48103

Abstract

The subsurface is spatially heterogeneous in geologic material composition leading to non-uniform groundwater flow fields. Preferential flow in highly conductive materials and diffusion into less conductive materials such as silts and clays, commonly present in alluvial aquifer systems in substantial volume fractions as high as 20 to 80 percent, enhance the dispersion, sequestration, and dilution of contaminants. This dissertation elucidates processes affecting groundwater solute migration in highly heterogeneous porous media, concentrating on (1) the role of diffusion in the dilution and sequestration of contaminants in the subsurface, (2) the modeling methods needed to address this phenomenon, and (3) the implications for natural attenuation of contaminant plumes.

Simulations of contaminant migration and remediation in the alluvial-fan system of Lawrence Livermore National Laboratory confirm the importance of molecular diffusion in sequestering contaminants due to its role in promoting mass transfer in local- and field-scale low-permeability zones. Overall transport behavior and efficacy of pump-and-treat remediation show acute sensitivity to magnitude of effective diffusion coefficient, particularly within the range of uncertainty as inferred through laboratory studies of solute diffusion in clays. Simulations reveal an increase in the holdback of mass near source locations and a decrease in pump-and-treat efficiency with increase in effective diffusion coefficient. Results help to explain observations of scale-dependent-dispersion phenomena and confirm the well-founded limitations of pump and treat. Further, they emphasize the importance of characterizing the geologic structure of low-permeability lithologic

units in assessing the viability of remedial technologies. In light of the need for scientific justification of natural attenuation phenomena recently endorsed as remedial technologies by the EPA, this research is particularly relevant to groundwater remediation problems confronting hydrologists and engineers.

Transport simulations are facilitated by new theory and numerical methods to simulate diffusion processes by random walks in composite porous media, i.e., porous media in which effective subsurface transport parameters may be discontinuous (step functions). Discontinuities in effective subsurface transport properties commonly arise (1) at abrupt contacts between geologic materials (i.e., composite porous media) and (2) in discrete velocity fields of numerical groundwater-flow solutions. However, standard random-walk methods for simulating transport and the theory on which they are based only apply when effective transport properties are sufficiently smooth. Limitations of standard theory have precluded development of random-walk methods that obey advection dispersion equations in composite porous media. This problem is solved by generalizing stochastic differential equations (SDEs) to the case of discontinuous coefficients and developing random-walk methods to numerically integrate these equations. The new random-walk methods obey advection-dispersion equations, even in composite media. The techniques retain many of the computational advantages of standard random-walk methods, including the ability to efficiently simulate solute-mass distributions and arrival times while suppressing errors, such as numerical dispersion. The results apply to problems found in many scientific disciplines and offer a unique contribution to diffusion theory and the theory of SDEs.

Acknowledgements

This work is dedicated to my wife, Juana B. Eweis, for her kindness, love and support. I thank my father, Victor LaBolle, and mother, June L. LaBolle, for encouraging my education with their generosity and love. I am grateful to my brothers, Dave L. LaBolle and Michael S. LaBolle, who influenced me to question the status quo and fostered my quest for knowledge.

I extend my deepest appreciation, gratitude and respect to my Major Professor, Dr. Graham E. Fogg, for his generous support, guidance and friendship throughout my degree work. I would also like to thank Drs. Jeremy Quastel, Andrew F.B. Tompson and Janko Gravner whose contributions to this work made it possible. I am also grateful to Professor Donald R. Nielsen for his advice, encouragement and insightful review.

Table of Contents

Title Page.....	i
Abstract	ii
Acknowledgements.....	iv
Table of Contents	v
List of Tables.....	viii
List of Figures	ix
Chapter 1: Executive Summary	1
1.1 Background.....	1
1.2 Research Scope.....	4
1.3 References	6
Chapter 2: Random-Walk Simulation of Transport in Heterogeneous Porous Media: Local Mass-Conservation Problem and Implementation Methods	8
2.1 Abstract.....	8
2.2 Introduction	9
2.3 The Random Walk Particle Method (RWPM)	11
2.3.1 Gradient Terms and Discontinuities in D	13
2.4 Reflection and Interpolation Techniques.....	16
2.4.1 Reflection Principle	16
2.4.2 Interpolation Technique.....	18
2.4.3 Comparison with Theory	20
2.4.4 Limitation of the Reflection Method	22
2.5 Interpolation Methods for Implementing the RWPM	23
2.5.1 Linear Interpolation (LI).....	24
2.5.2 Bilinear Interpolation (BLI).....	26
2.5.3 Block-Discrete Interpolation (BDI).....	26
2.5.4 Hybrid Schemes.....	27
2.6 Test Cases.....	27
2.6.1 Solute Transport in a Stratified System	28
2.6.1.1 Results and Discussion	31
2.6.2 Transport in Heterogeneous Porous Media	33
2.6.2.1 Results and Discussion	35
2.7 Conclusions	36
2.8 References	40
Chapter 3: Diffusion Theory for Transport in Porous Media: Transition-Probability Densities of Diffusion Processes Corresponding to Advection-Dispersion Equations	43
3.1 Abstract.....	43
3.2 Introduction	44
3.3 Background and Problem Description.....	45
3.3.1 Governing Equations	46
3.3.2 Diffusion Processes and Kolmogorov's Equations	48
3.4. Diffusion Processes and Advection-Dispersion Equations	50

3.4.1. Transition-Probability Densities of Diffusion Processes Corresponding to ADEs	51
3.4.2. Detailed Balance	54
3.5. Examples: Random-Walk Simulation Methods	56
3.5.1. Methods	57
3.5.2. Comparison with Theory	58
3.5.2.1 Invariant distribution	59
3.5.2.2 Correspondence with an analytical solution	59
3.5.2.3 Symmetric transition-probability density	61
3.5.3. Discussion	61
3.6. Summary and Conclusions	63
3.7. References	64
Chapter 4: Diffusion processes in composite porous media and their numerical integration by random walks: Generalized stochastic differential equations with discontinuous coefficients.....	68
4.1 Abstract.....	68
4.2 Introduction	69
4.3 Standard Methods for Simulating Diffusion Processes	72
4.4 Diffusion Processes in Composite Media.....	75
4.4.1 Isotropic Diffusions	76
4.4.1.1 Numerical Integration	78
4.4.1.2 Diffusion in One-Dimensional Composite Media.	79
4.4.1.3 Effective Diffusivity of Composite Media.	82
4.4.1.4 Discussion	84
4.4.2 Anisotropic Diffusions.....	85
4.4.2.1 Anisotropic Diffusion in Composite Media.....	87
4.4.2.2 Advective-Dispersive Transport in Composite Media	91
4.5 Discussion and Conclusions	93
4.6 References	96
Appendix 4A: Necessary Conditions for Weak Convergence	99
Appendix 4B: Stochastic Calculus with Generalized Functions	102
Appendix 4C: Taylor Series Expansion of Equation (15a)	103
Chapter 5: On the Role of Molecular Diffusion in Contaminant Migration and Remediation in an Alluvial Aquifer System	105
5.1 Introduction	105
5.2 Background.....	106
5.3 Study Area	110
5.4 Simulation Procedure	111
5.4.1 Geostatistical Simulations	112
5.4.2 Flow Simulations	119
5.4.3 Transport Simulations.....	124
5.4.3.1 Transport Parameters	124
5.4.3.2 Numerical Simulation	128
5.4.3.4 Analysis of Particle Mass Distributions.....	129

5.5 Transport Experiments	131
5.5.1 Results and Discussion	132
5.5.1.1 Ambient Hydraulic Conditions, Scenarios 1 – 4	132
5.5.1.1.1 Concentration and mass distributions	133
5.5.1.1.2 Macrodispersive behavior	136
5.5.1.1.3 Partitioning of mass among hydrofacies	144
5.5.1.2 Pump and Treat, Scenarios 1 – 4	149
5.5.1.2.1 Mass recovery.	149
5.5.1.2.2 Partitioning of mass among hydrofacies	150
5.5.1.2.3 Contaminated volume.	150
5.5.1.2.4 Concentration and mass distributions	157
5.5.1.2.4 Technical impracticability.....	161
5.5.1.3 Ambient Transport, Scenarios 5 and 6.....	161
5.6 Summary and Conclusions.....	164
5.6.1 Sequestration of Contamination near Source Locations.....	164
5.6.2 On the Role of Diffusion in Contaminant Migration and Remediation	165
5.6.3 Geologic Characterization	166
5.6.4 Technical Impracticability and Natural Attenuation as a Remediation Technology.....	167
5.7 References	168
Appendix 5A: Boundary Conditions of the Groundwater-Flow Simulations	171
5A.1: GHB Conductances	171
5A.2: Recharge	172
Appendix 5B: Grid Refinement Experiments.....	173
5B.1 Simulation Procedure.....	173
5B.2 Results and Discussion	174
Appendix 5C: Sensitivity of Contaminant Migration to Local-Scale Dispersivities	183
5C.1 Simulation Procedure.....	183
5C.2 Results and Discussion	183

List of Tables

Table 2.1: Velocity Interpolation Schemes	25
Table 4.1: Parameters corresponding to simulation results presented in Figures 4.7a-4.7d and 4.8a-4.8d.	88
Table 4.2: Parameters Corresponding to Simulation Results Presented in Figures 4.9a-4.9c	93
Table 5.1: Mean lengths (m) of hydrofacies in the strike, dip and vertical directions in Markov-chain model.	113
Table 5.2: Hydraulic Properties of Hydrofacies	124
Table 5.3: Controlling Transport Process in Hydrofacies	127
Table 5.4: Transport Parameters.....	129
Table 5C: Longitudinal and Transverse Dispersivities of Scenarios 5C.1 - 5C.5.....	183

List of Figures

Figure 2.1: Analytical steady-state solution to (2.13), compared with two, approximately steady state and coarse, particle solutions at $t = 0.1$ obtained with and without gradient term.....	15
Figure 2.2: A two-layer system with a discontinuous diffusion coefficient across an interface.	17
Figure 2.3: Component parts (bold lines) of analytical solution given in (a) equations (2.19a) - (2.19d) for point source in Ω_1 and (b) equivalent form of equations (2.19a) - (2.19d) for point source in Ω_2 are summed to form final solution (bold dashed line) about an interface.	19
Figure 2.4: Comparison in ratios of particle numbers (N_1/N_2) on either side of discontinuity in D for different alternative techniques of reflecting to conserve mass.	21
Figure 2.5: Comparison of concentrations from simulations using the different alternative techniques and the analytical solution given in equations (2.19a) - (2.19d) at $t = 6.0$ for $x_0 = -5.0$, $D_1 = 5.0$, and $D_2 = 0.25$. The method of Uffink [1985] produces results virtually identical to the analytical solution. The linear-interpolation method yields a close approximation.....	21
Figure 2.6: Velocity interpolation from a block-centered finite-difference flow scheme.	24
Figure 2.7: A stratified system with a thin high-permeability layer bounded by a low-permeability porous matrix.....	29
Figure 2.8: Comparison of analytical solution with solute breakthrough curve predicted using LI with and without a reflection principle ($\Delta y = 0.03$ m). There is no solute breakthrough for LI without a reflection principle. Simulations using $\Delta y = 0.01$ m and 0.006 m produce identical results for this test case.	32
Figure 2.9: Comparison of analytical solution with solute breakthrough curves predicted using BDI.....	32
Figure 2.10: Comparison of analytical solution with solute breakthrough curves predicted using BLI/LI and BLI/BDI schemes. The BLI/LI and BLI/BDI schemes produce identical results for this test case.	34
Figure 2.11: Gaussian conditional simulation of hydraulic-conductivity field with log-K mean and standard deviation of 1.69×10^{-3} and 2.75×10^{-3} , respectively, and vertical and horizontal variogram ranges of 10 and 400, respectively (modified from Fogg et al., 1991).	35
Figure 2.12: Comparison of solute breakthrough curves predicted using BDI, BLI/BDI, BLI/LI, and BLI.	37
Figure 2.13: Comparison of first moments predicted using BDI, BLI/BDI, BLI/LI, and BLI.....	37
Figure 2.14: Comparison of longitudinal second moments predicted using BDI, BLI/BDI, BLI/LI, and BLI.	38

Figure 3.1: Porous media system composed of subdomains Ω_1 and Ω_2 with contrasting material properties that give rise to discontinuous characteristic transport coefficients at the interface Γ .	47
Figure 3.2: Ratios N_1/N_2 simulated by alternative Markov-chain approximations for various values of D_1/D_2 .	60
Figure 3.3: Comparison of concentrations from simulations by the alternative Markov-chain approximations with the analytical solution to equations (3.25a) - (3.25g) at $t = 6.0$ for $x_0 = -5.5$, $D_1 = 5.0$, and $D_2 = 0.25$. Methods of <i>Semra et al.</i> [1993] and <i>Uffink</i> [1985] produce results virtually identical to the analytical solution.	60
Figure 3.4: Transition-probability density illustrated by evolving Markov chains for 40,000 particles initially uniformly distributed over the interval from $[-1/2, 1/2]$ over a single time step using the approximations of (a) <i>Uffink</i> [1985] (b) <i>Ackerer</i> [1985] (c) <i>Cordes et al.</i> [1991], and (d) <i>Semra et al.</i> [1993]. Asymmetry in the method of <i>Ackerer</i> results in a contrast between particle densities in the second and fourth quadrants.	62
Figure 4.1: The two step process of random-walk simulation of advection and isotropic dispersion in composite porous media for the algorithm given in equations (4.11a) and (4.11b).	80
Figures 4.2a and 4.2b: Simulation results for (a) and (b) are compared with analytical values for $\Delta t = 10.0, 1.0, 0.1$, and 0.01 .	81
Figure 4.3: Simulation results for concentration are compared with analytical solutions for $D_1 = 5.0$ and $D_2 = 2.5$ (diamonds), 0.5 (squares), and 0.05 (circles).	82
Figure 4.4: Square array of cylinders with known diffusivity, D_2 , embedded in a matrix with contrasting diffusivity, D_1 .	83
Figure 4.5: Simulated effective diffusivities are compared with values reported by Perrins et al. [1979] for cylinder volume fractions of 0.1, 0.2, 0.3, 0.4, 0.5, 0.6, 0.7, and 0.75, matrix diffusivity $D_1 = 1$, and cylinder diffusivities, $D_2 = 2$ (solid circles), 5 (triangles), 10 (diamonds), 20 (squares), and 50 (open circles).	85
Figure 4.6: Composite media with anisotropic diffusion tensors.	88
Figures 4.7a – 4.7b: Simulated first moments in the x - and y -directions as a function of time for the system illustrated in Figure 4.6 with periodic boundaries in the x -direction and reflective, no-flux boundaries at $y = 0$ and $y = 2$, initially uniform number density, and parameters given in Table 4.1.	89
Figures 4.7c – 4.7d: Simulated first moments in the x - and y -directions as a function of time for the system illustrated in Figure 4.6 with periodic boundaries in the x -direction and reflective, no-flux boundaries at $y = 0$ and $y = 2$, initially uniform number density, and parameters given in Table 4.1.	90
Figures 4.8a - 4.8d: Contours of $c(x,t)/c_0$ from simulations of anisotropic diffusion in the composite media shown in Figure 4.6 with absorbing (zero concentration) boundaries on $x = 0$, $x = 2$, $y = 0$, and $y = 2$, initial distribution $c(x,0) = c_0$ in the region $0.99 < x < 1.00$ and $0.99 < y < 1.00$ and $c(x,0) = 0$ outside this region, and parameters given Table 4.1.	92
Figures 4.9a - 4.9c: Contours of $c(x,t)/c_0$ from simulations of advective-dispersive transport in the composite media shown in Figure 4.6 with absorbing (zero	

concentration) boundaries on $x = 0$, $x = 2$, $y = 0$, and $y = 2$, initial distribution $c(x,0) = c_0$ as shown and $c(x,0) = 0$ outside this region, and parameters given Table 4.2. 94

Figure 5.1: Location Lawrence Livermore National Laboratory. 106

Figure 5.2: Detailed study area (after Carle [1996]). 112

Figure 5.3: Cross section in strike-vertical (x - z) plane of interpolated Markov chain model (after Carle [1996]). 114

Figure 5.4: Cross section in strike-dip (x - y) plane of interpolated Markov chain model (after Carle [1996]). 115

Figure 5.5: Cross section in dip-vertical (y - z) plane of interpolated Markov chain model (after Carle [1996]). 116

Figure 5.6: Conditional simulation of hydrostratigraphic architecture (realization 4). The pumping well is located in the channel hydrofacies units at the center of the system. 118

Figure 5.7: Conditional simulation of hydrostratigraphic architecture (realization 7). The pumping well is located in the channel hydrofacies units at the center of the system. 119

Figure 5.8: Schematic of flow system. The mean direction of flow is in the dip direction. 120

Figure 5.9: Hydraulic conductivity distribution categorized by hydrofacies. 121

Figure 5.10: Hydraulic head of realization 4 with (a) ambient and (b) stressed hydraulic conditions - pumping well located at the center of the system. 122

Figure 5.11: Hydraulic head of realization 7 with (a) ambient and (b) stressed hydraulic conditions - pumping well located at the center of the system. 123

Figure 5.12. Normalized x - z average concentration at year 40 for scenarios 1 – 4, realizations 1 – 5. A plume generated for a homogeneous system with average $K = 0.93$ m/day is shown for reference. 134

Figure 5.13. Normalized x - z average concentration at year 40 for scenarios 1 – 4, realizations 6 – 10. A plume generated for a homogeneous system with average $K = 0.93$ m/day is shown for reference. 135

Figure 5.14: Normalized z -average concentrations at year 40 for scenarios 2 ($D^* = 5.2 \times 10^{-5}$ m²/day) and 3 ($D^* = 10^{-6}$ m²/day), realization 4. 137

Figure 5.15: Normalized z -average concentrations at year 40 for scenarios 2 ($D^* = 5.2 \times 10^{-5}$ m²/day) and 3 ($D^* = 10^{-6}$ m²/day), realization 7. 137

138

Figure 5.16. First spatial moments for scenarios 1 – 4, realizations 1 – 5. 138

Figure 5.17. First spatial moments for scenarios 1 – 4, realizations 6 – 10. 139

Figure 5.18. Second spatial moments for scenarios 1 – 4, realizations 1 – 5. 140

Figure 5.19. Second spatial moments for scenarios 1 – 4, realizations 6 – 10. 141

Figure 5.20. Macrodispersion coefficient A_1 a function of time for scenarios 1 – 4, realizations 1 – 5. 142

Figure 5.21. Macrodispersion coefficient A_1 a function of time for scenarios 1 – 4, realizations 6 – 10. 143

Figure 5.22. Fraction of total mass contained in each of the 4 hydrofacies as a function of time for scenarios 1 – 4, realizations 1 – 5. 145

Figure 5.23. Fraction of total mass contained in each of the 4 hydrofacies as a function of time for scenarios 1 – 4, realizations 6 – 10.....	146
Figure 5.24: Fraction of total mass contained in each of the 4 hydrofacies as a function of distance in the dip direction for scenarios 1 – 4, realizations 1 – 5.	147
Figure 5.25: Fraction of total mass contained in each of the 4 hydrofacies as a function of distance in the dip direction for scenarios 1 – 4, realizations 6 – 10.	148
Figure 5.26. Mass remaining $M(t)/M_0$ as a function of time from year 40, the start of pump-and-treat, for scenarios 1 – 4, realizations 1 – 5.	151
Figure 5.27. Mass remaining $M(t)/M_0$ as a function of time from year 40, the start of PAT, for scenarios 1 – 4, realizations 6 – 10.....	152
Figure 5.28. Fraction of total mass contained in each of the 4 hydrofacies as a function of time for scenarios 1 – 4, realizations 1 – 5.....	153
Figure 5.29. Fraction of total mass contained in each of the 4 hydrofacies as a function of time for scenarios 1 – 4, realizations 6 – 10.....	154
Figure 5.30. Volume of porous media in which concentration is greater than MCL ($c/c_0 > 10^{-3}$) as a function of time from the start of PAT for scenarios 1 – 4, realizations 1 – 5.....	155
Figure 5.31. Volume of porous media in which concentration is greater than MCL ($c/c_0 > 10^{-3}$) as a function of time from the start of PAT for scenarios 1 – 4, realizations 6 – 10.....	156
Figure 5.32. Normalized x-z average concentrations at the start of pumping and after 30 years of PAT for scenarios 1 - 4, realizations 1 – 5.	158
Figure 5.33. Normalized x-z average concentrations at the start of pumping and after 30 years of PAT for scenarios 1 - 4, realizations 6 – 10.	159
Figure 5.34: Normalized z-average concentrations at year 40 and year 70, 30 years after the start of PAT, for scenarios 2 and 3, realization 4.....	160
Figure 5.35: Normalized z-average concentrations at year 40 and year 70, 30 years after the start of PAT, for scenarios 2 and 3, realization 4 and 7.	160
Figure 5.36. Maximum concentration in the system compared with concentration at the pumping well during PAT for scenarios 1 - 4, realizations 4 and 7.	162
Figure 5.37: Normalized x-z-average concentrations at year 40 and at year 70. 30 years after the start of pump and treat, for scenarios 2 (ADE), 5 (advection diffusion equation) and 6 (ADE, no diffusion), realization 4 and 7.....	163
Figure 5B.1: Two-dimensional Illustration of the 3 grid resolutions used. Contrast in shades represents different hydrostratigraphic units. Typically one hydrostratigraphic unit contacts at least several grid blocks in any given direction.	174
Figure 5B.2: Simulated hydraulic head for realization 2 at 1x (top), 3x (middle) and 5x (bottom) resolutions.....	175
Figure 5B.3: Normalized x-z-average plumes, realizations 1 – 5, at years 10 and 20 are compared for 1x, 3x and 5x resolutions.	176
Figure 5B.4: Normalized x-z-average plumes, realizations 6 – 10, at years 10 and 20 are compared for 1x, 3x and 5x resolutions.	177

Figure 5B.5: Longitudinal first spatial moments for realizations 1 – 5 are compared for 1x, 3x and 5x resolutions.....	179
Figure 5B.6: Longitudinal first spatial moments for realizations 6 – 10 are compared for 1x, 3x and 5x resolutions.....	180
Figure 5B.7: Longitudinal second moments for realizations 1 – 5 are compared for 1x, 3x and 5x resolutions.....	181
Figure 5B.8: Longitudinal second spatial moments for realizations 6 – 10 are compared for 1x, 3x and 5x resolutions.	182
Figure 5C.1: Normalized x-z-average plumes, realizations 1 – 5, at year 20 are compared for scenarios 5C.1 – 5C.5.	184
Figure 5C.2: Normalized x-z-average plumes, realizations 6 – 10, at year 20 are compared for scenarios 5C.1 – 5C.5.	186
Figure 5C.3: First spatial moments for realizations 1 – 5 are compared for scenarios 5C.1 – 5C.5.....	187
Figure 5C.4: First spatial moments for realizations 6 – 10 are compared for scenarios 5C.1 – 5C.5.....	188
Figure 5C.5: Longitudinal second spatial moments for realizations 1 – 5 are compared for scenarios 5C.1 – 5C.5.	189
Figure 5C.6: Longitudinal second spatial moments for realizations 6 – 10 are compared for scenarios 5C.1 – 5C.5.	190
Figure 5C.7: Concentration at the pumping well for realizations 1 – 5 are compared for scenarios 5C.1 – 5C.5.....	191
Figure 5C.8: Concentration at the pumping well for realizations 6 – 10 are compared for scenarios 5C.1 – 5C.5.	192
Figure 5D.1a: Three dimensional particle distribution for scenario 2 ($D^* = 5.2 \times 10^{-5}$ m ² /day), realization 1, year 40.....	193
Figure 5D.1b: Three dimensional particle distribution for scenario 3 ($D^* = 10^{-6}$ m ² /day), realization 1, year 40.	193
Figure 5D.2a: Three dimensional particle distribution for scenario 2 ($D^* = 5.2 \times 10^{-5}$ m ² /day), realization 2, year 40.....	194
Figure 5D.2b: Three dimensional particle distribution for scenario 3 ($D^* = 10^{-6}$ m ² /day), realization 2, year 40.	194
Figure 5D.3a: Three dimensional particle distribution for scenario 2 ($D^* = 5.2 \times 10^{-5}$ m ² /day), realization 3, year 40.....	195
Figure 5D.3b: Three dimensional particle distribution for scenario 3 ($D^* = 10^{-6}$ m ² /day), realization 3, year 40.	195
Figure 5D.4a: Three dimensional particle distribution for scenario 2 ($D^* = 5.2 \times 10^{-5}$ m ² /day), realization 4, year 40.....	196
Figure 5D.4b: Three dimensional particle distribution for scenario 3 ($D^* = 10^{-6}$ m ² /day), realization 4, year 40.	196
Figure 5D.5a: Three dimensional particle distribution for scenario 2 ($D^* = 5.2 \times 10^{-5}$ m ² /day), realization 5, year 40.....	197
Figure 5D.5b: Three dimensional particle distribution for scenario 3 ($D^* = 10^{-6}$ m ² /day), realization 5, year 40.	197

Figure 5D.6a: Three dimensional particle distribution for scenario 2 ($D^* = 5.2 \times 10^{-5}$ m ² /day), realization 6, year 40.....	198
Figure 5D.6b: Three dimensional particle distribution for scenario 3 ($D^* = 10^{-6}$ m ² /day), realization 6, year 40.	198
Figure 5D.7a: Three dimensional particle distribution for scenario 2 ($D^* = 5.2 \times 10^{-5}$ m ² /day), realization 7, year 40.....	199
Figure 5D.7b: Three dimensional particle distribution for scenario 3 ($D^* = 10^{-6}$ m ² /day), realization 7, year 40.	199
Figure 5D.8a: Three dimensional particle distribution for scenario 2 ($D^* = 5.2 \times 10^{-5}$ m ² /day), realization 8, year 40.....	200
Figure 5D.8b: Three dimensional particle distribution for scenario 3 ($D^* = 10^{-6}$ m ² /day), realization 8, year 40.	200
Figure 5D.9a: Three dimensional particle distribution for scenario 2 ($D^* = 5.2 \times 10^{-5}$ m ² /day), realization 9, year 40.....	201
Figure 5D.9b: Three dimensional particle distribution for scenario 3 ($D^* = 10^{-6}$ m ² /day), realization 9, year 40.	201
Figure 5D.10a: Three dimensional particle distribution for scenario 2 ($D^* = 5.2 \times 10^{-5}$ m ² /day), realization 10, year 40.....	202
Figure 5D.10b: Three dimensional particle distribution for scenario 3 ($D^* = 10^{-6}$ m ² /day), realization 10, year 40.....	202

Chapter 1

Executive Summary

This research was motivated by the need to elucidate processes affecting groundwater solute migration in highly heterogeneous porous media. In particular, the work focuses on the role of diffusion in the dilution and sequestration of contaminants in the subsurface, the modeling methods needed to address this phenomena in typical alluvial heterogeneity, and the implications for natural attenuation of contaminant plumes.

1.1 Background

The subsurface is spatially heterogeneous in geologic material composition leading to non-uniform groundwater flow fields. Preferential flow in highly conductive materials and diffusion into less conductive materials such as silts and clays, commonly present in alluvial aquifer systems in substantial volume fractions as high as 20 to 80 percent, enhance the dispersion, sequestration, and dilution of contaminants.

While the diffusion of contaminants into low-conductivity (K) materials can hinder active remediation technologies, it may also be an important process in passive remediation by natural attenuation. The EPA recently endorsed natural attenuation, including dilution and dispersion, as a means of achieving remediation objectives stating that “natu-

ral attenuation processes may reduce contaminant mass or concentration at sufficiently rapid rates to be integrated into a site's soil or groundwater remedy" [Office of Solid Waste and Emergency Response (OSWER) Directive 9200.4-17, 1997].

Previous studies (e.g., *Gillham et al.*, 1984; *Feenstra et al.*, 1984; *Wilson, et al.*, 1993) have demonstrated how diffusion into low- K media natural attenuates the migration of contaminants. These studies relied on simple models of heterogeneity as surrogates of real geologic systems. Hydrologists generally agree, however, that realistic predictions of solute migration must account for the spatial distribution of geologic materials in detail. Indeed, the OSWER *Directive 9200.4-17* [1997] concluded that "decisions to employ monitored natural attenuation as a remedy or remedy component should be thoroughly and adequately supported with site-specific characterization and data analysis," stressing the need for realistic forecasts to scientifically justify natural attenuation phenomena as remedial technologies.

The prospects for realistic site-specific simulations of subsurface transport hinge on our ability to (1) characterize the subsurface in sufficient detail and (2) accurately solve equations governing flow and transport on the ensuing immense computational grids. New geologic characterization methods can now incorporate information from quantitative and interpretive descriptions of stratigraphic sequences in geostatistical simulations of facies architecture that honor lithologic data (e.g., *Carle* [1996] and *Carle et al.*, [1998]). These new methods have been used successfully to simulate detailed hydrostratigraphic sequences that reproduce field observations from well interference tests [*Carle, et al.*, 1996] and isotopic studies of mean groundwater age [*Tompson et al.*, 1998].

Accurate modeling of advection and dispersion in such systems is challenging: Heterogeneity is highly resolved in three dimensions, often entailing 10^5 to 10^8 nodes or more, and grid Peclet numbers may be as high as 1000 [LaBolle *et al.*, 1996]. Common numerical techniques for solving advection-dispersion equations (ADEs) include finite elements, finite differences, and Eulerian-Lagrangian methods, such as method of characteristics. All of these techniques suffer from numerical inaccuracies at high grid Peclet numbers and/or computational inefficiencies that limit their practical application to large detailed simulations. In contrast, random-walk particle methods (RWPMs) promise computationally efficient and accurate solutions to ADEs [Ahlstrom, *et al.*, 1977; Prickett, *et al.*, 1981; Uffink, 1988; Tompson *et al.*, 1987; Tompson, 1993; LaBolle, 1996; Tompson, 1998]. In RWPMs, equations governing the movement of particles do not depend directly on the resolution of the computational grid and do not suffer from numerical inaccuracies at high grid Peclet numbers. These methods therefore appear ideally suited for solving ADEs on the immense computational grids of detailed geologic characterizations [Tompson *et al.*, 1987; LaBolle *et al.*, 1996].

Nevertheless, the distinct computational advantages of standard RWPMs over other numerical solutions to ADEs have been frequently overstated. RWPMs are based on the direct numerical simulation of diffusion processes, equations that predict trajectories (in space) of “solute-particles” whose density obeys ADEs. These equations are described in diffusion theory, the fundamentals of which were first introduced by *Einstein* [1905] in his classic paper on molecular diffusion in liquids and later formalized in probability theory [Kolmogorov, 1931] and the theory of stochastic differential equations [Itô, 1961]. Standard diffusion theory relies on the assumption that coefficients are sufficiently

smooth functions of space. Discontinuities in effective transport properties, however, arise (1) naturally in the subsurface at abrupt transitions between geologic materials (i.e., composite porous media) and (2) artificially on computational domains, discretized for numerical solution of groundwater flow equations. Previously, the limitations of standard diffusion theory precluded development of diffusion processes, and therefore RWPMs, that obey ADEs in composite media.

The use of numerical models to elucidate processes affecting groundwater solute migration in highly heterogeneous porous media demands highly-accurate and efficient modeling methods. The apparent lack of such methods for solving ADEs has hindered accurate simulation of transport in detailed geologic characterizations, key to realistic forecasts of subsurface contaminant migration and to scientific justification of dilution and dispersion phenomena in support of remediation by natural attenuation.

1.2 Research Scope

The specific goal of this research was to explore the role of diffusion in the natural attenuation of contaminants in the alluvial aquifer underlying Lawrence Livermore National Laboratory (LLNL). Chapters 2 (published in *Water Resources Research* [LaBolle *et al.*, 1996]), 3 (published in *Water Resources Research* [LaBolle *et al.*, 1998]) and 4 (accepted for publication in *Water Resources Research* [LaBolle *et al.*, 1998]) were devoted to developing RWPMs that obey ADEs in composite porous media, i.e., tools necessary to conduct the research. Chapter 5 comprises the first study using detailed (on the order of meters) site-specific characterizations to explore the role of diffusion in the migration of contaminants and pump-and-treat remediation system performance.

Chapter 2 [*LaBolle et al.*, 1996] discusses numerical inaccuracies in previous attempts to apply RWPMs to simulate transport on numerical flow solutions. We proposed an accurate RWPM, based on interpolation of velocities from numerical flow solutions, that has since found numerous applications in the simulation of transport. Improving accuracy with this method, however, requires simultaneously resolving both the interpolation procedure and time step. The paper stressed the need for new theory and methods that are independent of the resolution of the interpolation scheme. These methods are presented Chapters 3 and 4. In Chapter 3 [*LaBolle et al.*, 1998] we developed new diffusion theory that gives necessary conditions for the convergence of diffusion processes to ADEs in composite media. This new theory was used to test the validity of several RWPMs proposed in the literature. In Chapter 4 we generalized stochastic differential equations to the case of discontinuous coefficients to yield RWPMs that satisfy the necessary conditions for convergence to ADEs in composite porous media. These methods do not depend on resolving an interpolation scheme to improve accuracy. Examples relevant to the simulation of subsurface transport demonstrate the new theory and methods. The results apply to problems found in many scientific disciplines and offer a unique contribution to diffusion theory and the theory of SDEs.

The new methods facilitate the simulations of contaminant migration and remediation presented in Chapter 5. Here I explore the role of diffusion in the migration of contaminants and pump-and-treat remediation system performance in detailed (on the order of meters) site-specific characterizations of the LLNL alluvial-fan aquifer system. This work lays the foundation for scientifically justifying natural attenuation phenomena in support of negotiated waste site closure at LLNL and elsewhere.

1.3 References

- Ahlstrom, S.W., H.P. Foote, R.C. Arnett, C.R. Cole and R.J. Serne, Multi-component mass transport model: theory and numerical implementation. Rep. BNWL-2127, Battelle Pacific Northwest Lab., Richland, Washington, 1977.
- Carle, S.F., A transition probability-based approach to geostatistical characterization of hydrostratigraphic architecture, Ph.D. Dissertation, University of California, Davis, 1996.
- Carle, S.F., E.M. LaBolle, G.S. Weissmann, D. VanBrocklin, and G.E. Fogg, Geostatistical simulation of hydrofacies architecture: A transition probability/Markov approach, in SEPM Concepts in Hydrogeology and Environmental Geology No. 1, Hydrogeologic Models of Sedimentary Aquifers, G.S. Fraser and J.M. Davis (eds), SEPM (Society for Sedimentary Geology), Tulsa Oklahoma, 1998.
- Einstein, A., Über die von der molekularkinetischen theorie der wärme geforderte bewegung von in ruhenden flüssigkeiten suspendierten teilchen, *Ann. Phys.*, 17, 549-560, 1905.
- Feenstra, S., J.A. Cherry, E.A. Sudicky, and Z. Haq, Matrix diffusion effects on contaminant migration from an injection well in fractured sandstone, *Ground Water*, 22(3), 307-316, 1984.
- Gillham, R.W., E.A. Sudicky, J.A. Cherry and E.O. Frind, An advection diffusion concept for solute transport in heterogeneous unconsolidated geologic deposits, *Water Resources Research*, 20(3), 369-378, 1984.
- Itô, K. and H.P. McKean, *Diffusion Processes and their Sample Paths*, Springer-Verlag, New York, 1961.
- Kolmogorov, A.N., Über die analytischen methoden in der wahrscheinlichkeitsrechnung, *Math. Anal.*, 104, 415-458, 1931.
- LaBolle, E.M., G.E. Fogg, and A.F.B. Tompson, Random-walk simulation of transport in heterogeneous porous media: Local mass-conservation problem and implementation methods, *Water Resources Research*, 32(3), 583-593, 1996.
- LaBolle, E.M., J. Quastel, and G.E. Fogg, Diffusion theory for transport in porous media: Transition-probability densities of diffusion processes corresponding to advection-dispersion equations, *Water Resources Research*, 34(7), 1685-1693, 1998.
- LaBolle, E.M., J. Quastel, G.E. Fogg, and J. Gravner, Diffusion processes in composite porous media and their numerical integration by random walks: Generalized stochastic differential equations with discontinuous coefficients, submitted to *Water Resources Research*, 1999.
- OSWER Directive 9200.4-17, Use of Monitored Natural Attenuation at Superfund, RCRA Corrective Action, and Underground Storage Tank Sites, U.S. EPA Office of Solid Waste and Emergency Response Directive 9200.4-17, 29 pp, November, 1997.
- Prickett, Th.A., Th.G. Naymik and C.G. Longquist, A random walk solute transport model for selected groundwater quality evaluations, Rep. Illinois State Water Survey, Urbana Illinois, 1981.
- Tompson, A.F.B., E.G. Vomoris, and L.W. Gelhar, Numerical simulation of solute transport in randomly heterogeneous porous media: motivation, model development,

- and application, Report UCID-21281, Lawrence Livermore National Laboratory, 1987.
- Tompson, A.F.B., Numerical simulation of chemical migration in physically in chemically heterogeneous porous media, *Water Resources Research*, 29(11), 3709-3726, 1993.
- Tompson, A.F.B., R.D. Falgout, S.G. Smith, W. J. Bosl, and S.F. Ashby, Analysis of subsurface contaminant migration and remediation using high performance computing, *Advances in Water Resources*, 22(3), pp 203-221, 1998.
- Uffink, G.J.M., Modeling of solute transport with the random walk method, in *Groundwater Flow and Quality Modelling*, ed. Custidio, E., A. Gurgui, and J.P. Lobo Ferreria, NATO ASI Series C: Math and Phys. Sci. 224: 247-265, Reidel Publishing Company. 1988.
- Wilson, D.J., R.D. Mutch, and J.I. Scott, Matrix diffusion in the cleanup of heterogeneous aquifers, *Environmental Monitoring and Assessment*, 26, 49-64, 1993.

Chapter 2

Random-Walk Simulation of Transport in Heterogeneous Porous Media: Local Mass-Conservation Problem and Implementation Methods*

2.1 Abstract

The random walk method for simulating solute transport in porous media is typically based on the assumption that the velocity, and velocity-dependent dispersion tensor, vary smoothly in space. However, in cases where sharp interfaces separate materials with contrasting hydraulic properties, these quantities may be discontinuous. Normally, velocities are interpolated to arbitrary particle locations when finite difference or finite element methods are used to solve the flow equation. The use of interpolation schemes that preserve discontinuities in velocity at material contacts can result in a random walk model that does not locally conserve mass unless a correction is applied at these contacts. Test simulations of random-walk particle tracking with and without special treatment of material contacts demonstrate the problem. Techniques for resolving the problem, including interpolation schemes and a reflection principle, are reviewed and tested. Results

* published in Water Resources Research [*LaBolle et al.*, 1996].

from simulations of transport in porous media with discontinuities in the dispersion tensor show which methods satisfy continuity. Simulations of transport in two-dimensional heterogeneous porous media demonstrate the potentially significant effect of using a non-conservative model to compute spatial moments and breakthrough of a solute plume.

2.2 Introduction

The random-walk particle method (RWPM) has been used successfully for years to simulate conservative and reactive transport in porous media [Ahlstrom, *et al.*, 1977; Prickett, *et al.*, 1981; Uffink, 1985; Tompson *et al.*, 1987; Tompson, 1993]. This method is computationally appealing because it is grid independent and therefore, given the proper conditions, will require little computer storage relative to finite element, finite difference and method of characteristic models. In addition, this method does not suffer from numerical dispersion in problems dominated by advection. Traditional finite element and finite difference models generally perform poorly under such conditions unless the computational grid is highly resolved. As a result, a random walk is often the method of choice for simulating transport in large, highly-resolved heterogeneous flow systems [Tompson and Gelhar, 1990; Tompson, 1993; Tompson *et al.*, 1994].

Global mass conservation is compulsory with the RWPM because particles cannot disappear. This distinct advantage of the RWPM, however, is often overstated; accurate solutions require local as well as global mass conservation.

In practice, the flow problem is often solved numerically and velocities are interpolated to arbitrary particle locations. Advective particle tracking models can be made mass conservative by using a divergence-free velocity interpolation scheme [Schafer-Perini and Wilson, 1991]. However, additional criteria are necessary to formulate a mass

conservative random walk model. For example, discontinuities in the velocity or effective porosity may yield a dispersion tensor that is discontinuous in space. Local mass conservation conditions for the RWPM require that the dispersion tensor be continuous in space unless a reflection principle [Feller, 1957] or similar method is applied. Therefore, neglecting discontinuities in the dispersion tensor will result in local mass conservation errors. As these problems only occur when parameters are functions of the spatial coordinates, model errors will not necessarily be detected during routine verification checks.

In some applications of the RWPM to transport in heterogeneous porous media (e.g., *Tompson et al.* [1987] and *Tompson and Gelhar* [1990]), accuracy in local mass conservation has been traded for computational efficiency by specifying coefficients in the RWPM as block discrete (constant with a finite-difference grid block). Though we do not believe this tradeoff led to significant errors in the simulation results of *Tompson et al.* [1987] and *Tompson and Gelhar* [1990], results from random-walk simulations presented herein demonstrate that this approach violates local mass conservation and under certain circumstances can significantly affect solute-transport predictions. This paper reviews the conditions required for local mass conservation for the RWPM and demonstrates consequences of violating these conditions when the dispersion tensor is discontinuous due to a discontinuous velocity field. We discuss and demonstrate techniques for applying the RWPM in the presence of the discontinuities. Random walk simulations of solute transport in two-dimensional heterogeneous porous media are presented that illustrate the potential effect of local mass conservation errors on simulation of a developing plume.

2.3 The Random Walk Particle Method (RWPM)

The RWPM is commonly used in the field of statistical physics to model and analyze processes involving diffusion. In the hydrologic community, the approach has been widely applied to simulate advective and diffusive mass transport problems in subsurface systems (e.g., *Ahlstrom, et al., 1977; Prickett, et al., 1981; Uffink, 1985; Tompson et al., 1987*). Mass concentration of an aqueous solute is represented by a finite system of N_p particles of constant mass m_p via

$$\Theta(\mathbf{x})c^p(\mathbf{x}, t) = \sum_{p \in N_p} m_p \delta(\mathbf{x} - \mathbf{X}_p(t)) \quad (2.1)$$

where Θ is the effective porosity, δ is a Dirac function and $\mathbf{X}_p(t)$ is the location of particle p at time t . Because (2.1) is discontinuous, a modified expression of the form

$$\Theta(\mathbf{x})c^s(\mathbf{x}, t) = \sum_{p \in N_p} m_p \zeta(\mathbf{x} - \mathbf{X}_p(t)) \quad (2.2)$$

is typically used to "smooth" the spatial distribution of concentration, where ζ is an interpolation, or projection function [*Bagtzoglou et al., 1992*] normalized such that $\int_{\Omega} \zeta dV = 1$, where Ω is the domain of porous medium. The degree of smoothness obtained is controlled by the shape of ζ and the particle resolution, N_r , the number of particles used to represent an arbitrary unit of mass. Mass in Ω is $M = \int_{\Omega} \Theta c dV = \sum_{p \in N_p} m_p$.

Simulation of advective and diffusive mass transport may proceed by changing particle positions with time via an *Euler* integration scheme given as [*Gardiner, 1990*]

$$\mathbf{X}_p(t + \Delta t) - \mathbf{X}_p(t) = \mathbf{A}(\mathbf{X}_p, t)\Delta t + \mathbf{B}(\mathbf{X}_p, t) \bullet \Delta \mathbf{W}(\Delta t) \quad (2.3)$$

where \mathbf{A} is a "drift" vector [LT^{-1}], \mathbf{B} is a tensor [$LT^{-1/2}$] defining the strength of diffusion, and \mathbf{W} , a Wiener process [$T^{1/2}$], is a vector of independent normally-distributed random variables with zero mean and covariance

$$\langle \Delta \mathbf{W} \Delta \mathbf{W} \rangle = \mathbf{I} \Delta t \quad (2.4)$$

The particle number density $f \equiv (\Theta c^p / m_p)$ obtained through repeated use of (2.1) on all particles satisfies the *Itô Fokker-Planck* Equation [*Risken*, 1989]

$$\frac{\partial f}{\partial t} + \nabla \cdot (\mathbf{A}f) - \frac{1}{2} \nabla \nabla \cdot (\mathbf{B} \cdot \mathbf{B}^T f) = 0 \quad (2.5)$$

in the limit as $N_r \rightarrow \infty$ and $\Delta t \rightarrow 0$, where

$$\mathbf{A} = \lim_{\Delta t \rightarrow 0} \frac{1}{\Delta t} \langle \mathbf{X}_p(t + \Delta t) - \mathbf{X}_p(t) \rangle \quad (2.6)$$

$$\mathbf{B} \cdot \mathbf{B}^T = \lim_{\Delta t \rightarrow 0} \frac{1}{\Delta t} \langle [\mathbf{X}_p(t + \Delta t) - \mathbf{X}_p(t)]^2 \rangle \quad (2.7)$$

To simulate conservative transport, we specify \mathbf{A} and \mathbf{B} in (2.5) such that the mass density satisfies the familiar advection-dispersion equation

$$\frac{\partial(\Theta c)}{\partial t} + \nabla \cdot (\mathbf{v} \Theta c) - \nabla \cdot (\Theta \mathbf{D} \nabla c) = 0 \quad (2.8)$$

In (2.8) c is the aqueous concentration [ML^{-3}], \mathbf{v} is the average groundwater velocity vector in the porous medium [LT^{-1}], and \mathbf{D} is the local hydrodynamic dispersion tensor [L^2T^{-1}], [*Bear*, 1972]

$$\mathbf{D} = (\alpha_T |\mathbf{v}| + D^*) \mathbf{I} + \frac{\alpha_L - \alpha_T}{|\mathbf{v}|} \mathbf{v} \mathbf{v} \quad (2.9)$$

where α_L [L] and α_T [L] are the longitudinal and transverse dispersivities, respectively, and D^* is the molecular diffusivity of the porous medium [L^2T^{-1}]. By choosing \mathbf{A} and \mathbf{B} as [Kinzelbach, 1988; Uffink, 1988; Tompson *et al.*, 1987]

$$\mathbf{A} = \mathbf{v} + \frac{1}{\Theta} \nabla \bullet (\Theta \mathbf{D}) \quad (2.10)$$

$$2\mathbf{D} = \mathbf{B} \bullet \mathbf{B}^T, \quad (2.11)$$

and noting that $m_p f = \Theta c^p$, equations (2.5) and (2.8) become equivalent. Substituting (2.10) and (2.11) into (2.3) yields the equation for a particle displacement

$$\begin{aligned} & \mathbf{X}_p(t + \Delta t) - \mathbf{X}_p(t) \\ &= \left(\mathbf{v}(\mathbf{X}_p, t) + \Theta(\mathbf{X}_p)^{-1} \nabla \bullet (\Theta(\mathbf{X}_p) \mathbf{D}(\mathbf{X}_p, t)) \right) \Delta t + \mathbf{B}(\mathbf{X}_p, t) \bullet \Delta \mathbf{W}(\Delta t) \end{aligned} \quad (2.12)$$

where coefficients in the right-hand-side of (2.12) are evaluated at $\mathbf{X}_p(t)$. Because \mathbf{D} is real and symmetric, elements of the tensor \mathbf{B} can be calculated by diagonalizing \mathbf{D} , taking the positive root of the eigenvalues, transforming back and multiplying by an arbitrary orthogonal matrix, \mathbf{R} [Risken, 1989] (for details refer to Tompson *et al.* [1987]). In the case $|\mathbf{v}| = 0$ (stagnation point with a scalar diffusion function), we use $B_{ij} = (2D_m)^{1/2}$ for ($i=j$) and $B_{ij} = 0$ for ($i \neq j$). This development can be extended to treat reactive transport for constituents that undergo binary reversible equilibrium sorption [Tompson, 1993] and kinetic decay [Tompson and Dougherty, 1992].

2.3.1 Gradient Terms and Discontinuities in \mathbf{D}

In some previous applications of the RWPM, the gradient terms in (2.12) have been ignored or overlooked (e.g., Ahlstrom, *et al.*, 1977; Prickett, *et al.*, 1981) leaving simply $\mathbf{A} = \mathbf{v}$. When \mathbf{D} or Θ vary spatially, however, these gradients can be quite significant, as il-

illustrated by applying the RWPM to find a steady state solution to the purely-diffusive system with $\Theta = 1$,

$$\frac{\partial c}{\partial t} - \frac{\partial}{\partial x} \left(D(x) \frac{\partial c}{\partial x} \right) = 0 \quad (2.13)$$

for $0 < x < 1$, where $D(x) = 1 + 99x$, $c(0,t) = 1$, and $c(1,t) = 0$. Figure 2.1 shows the steady-state analytical solution of this system [Crank, 1975] along with two coarse (i.e., noisy) particle solutions obtained from equation (2.12) with and without the gradient correction quantity in the drift term. Both particle solutions were evolved over time to an approximate steady state at $t = 0.1$, based upon a zero initial condition, and properly maintained boundary conditions [Tompson and Dougherty, 1992]. Importance of the correction in the drift term (A) is clearly evident.

Because of their dependence on gradients of velocity, porosity, and dispersivity, the importance of the correction terms in hydrologic applications will be most significant near sharp wetting fronts, stagnation zones, material contacts, and abrupt changes in the flow field [Uffink, 1988; Tompson, et al., 1987]. General incorporation of gradient terms may require careful interpolation of velocities, porosities, dispersivities, and diffusivities. A problem arises, however, at contacts between materials with contrasting hydraulic properties. Here, effective porosities, dispersivities, diffusivities, and flow velocities, and therefore the velocity dependent dispersion tensor, may be discontinuous in space.

In the case of discontinuities in the dispersion tensor or effective porosity, the gradient terms in (2.12) are undefined. Ignoring the effect of discontinuities in the dispersion tensor will result in local mass conservation errors even in the limit as the time step approaches zero. In this paper we consider particle methods that address discontinuities

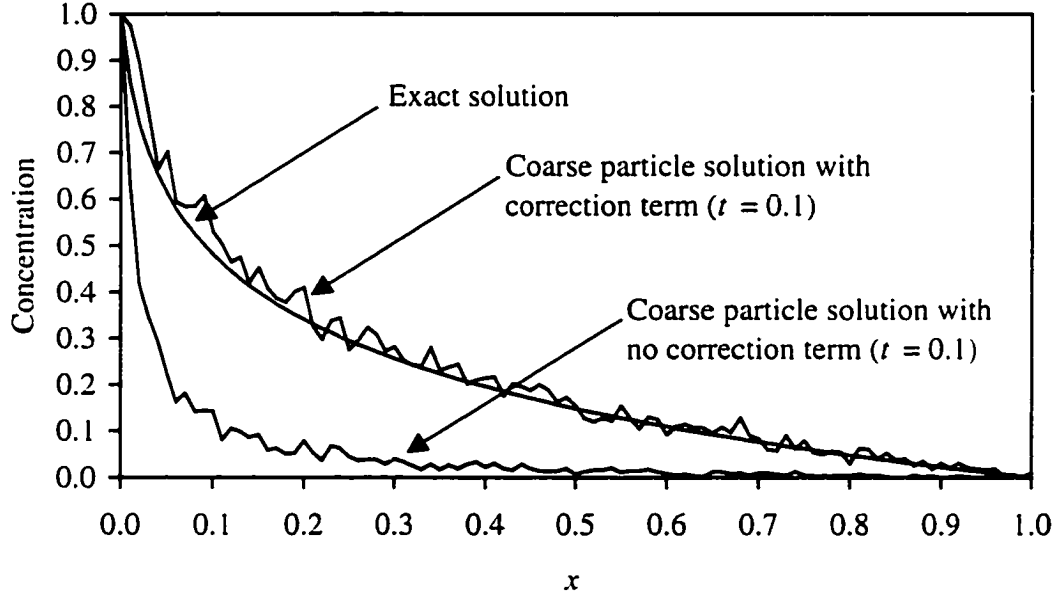


Figure 2.1: Analytical steady-state solution to (2.13), compared with two, approximately steady state and coarse, particle solutions at $t = 0.1$ obtained with and without gradient term.

in dispersion tensor caused by discontinuities in the velocity field only, and will consider dispersivities and porosity to be constant. Nevertheless, methods similar to those presented here can be applied to locally conserve mass where dispersivity and porosity have discontinuities.

In general, the statement expressing local mass conservation at an interface, denoted here by the surface s , is [Gardiner, 1990]

$$\lim_{x \rightarrow s^-} \mathbf{J}^- \cdot \mathbf{n} = \lim_{x \rightarrow s^+} \mathbf{J}^+ \cdot \mathbf{n} \quad (2.14)$$

$$\lim_{x \rightarrow s^-} c^- = \lim_{x \rightarrow s^+} c^+ \quad (2.15)$$

where \mathbf{J} is mass flux, given as

$$\mathbf{J} = \Theta \mathbf{A} c - \Theta \mathbf{D} \cdot \nabla c \quad (2.16)$$

and \mathbf{n} is the outward normal to \mathbf{s} , and the superscripts + and - refer to quantities on opposite sides of \mathbf{s} . When \mathbf{D} is discontinuous at $\mathbf{s} \in \Omega$, within the simulation domain, equation (2.14) may not be satisfied by the RWPM. Below, we review a reflection technique that has been developed to address this problem and introduce another approach based on interpolation of \mathbf{D} .

2.4 Reflection and Interpolation Techniques

Uffink [1985] treated the problem of a discontinuous dispersion tensor through application of a reflection principle based on the method of images [*Feller*, 1957]. He applied this method to transport in stratified porous media with flow parallel to the bedding plane where the tangential velocity and velocity-dependent dispersion tensor are discontinuous at interfaces between strata (Figure 2.2). Here we present and test the method of *Uffink* [1985] and an alternative interpolation technique .

2.4.1 Reflection Principle

A reflection principle can be developed for one-dimensional diffusion across an interface with constant (yet different) diffusion coefficients on both sides of this interface and $\Theta = 1$ (Figure 2.2). Here we have

$$\frac{\partial c_1}{\partial t} - \frac{\partial}{\partial x} \left(D_1 \frac{\partial c_1}{\partial x} \right) = 0 \quad \text{for } x < 0$$

$$\frac{\partial c_2}{\partial t} - \frac{\partial}{\partial x} \left(D_2 \frac{\partial c_2}{\partial x} \right) = 0 \quad \text{for } x > 0$$

where D_1 and D_2 are the diffusion coefficients, and the subscripts 1 and 2 refer to quantities in Ω_1 and Ω_2 , respectively. Conservation of mass requires that

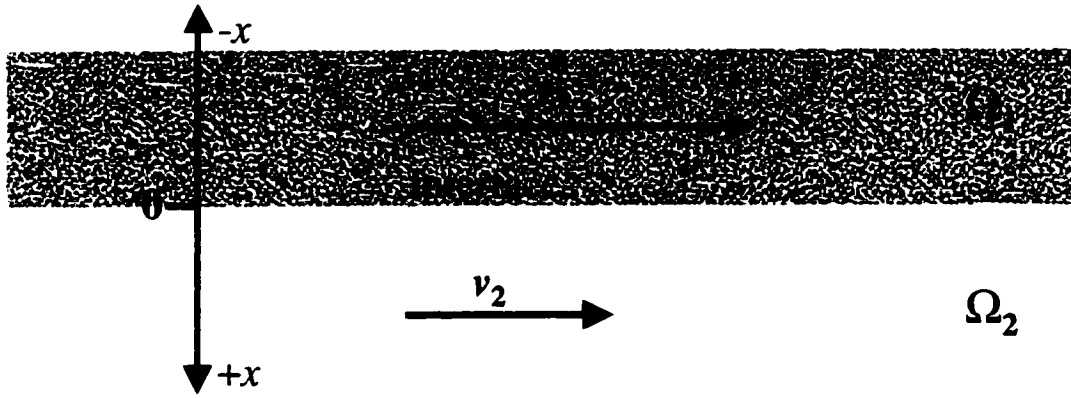


Figure 2.2: A two-layer system with a discontinuous diffusion coefficient across an interface.

$$\lim_{x \rightarrow 0^-} D_1 \frac{\partial c_1}{\partial x} = \lim_{x \rightarrow 0^+} D_2 \frac{\partial c_2}{\partial x}$$

$$\lim_{x \rightarrow 0^-} c_1 = \lim_{x \rightarrow 0^+} c_2$$

For the case of a partially-reflecting interface, $D_1 > D_2 > 0$, an instantaneous point source in Ω_1 , $c(x_0, 0) = 1$, $x_0 < 0$, and a system of infinite spatial extent, applying the method of images yields a solution to (2.17a) and (2.17b) in terms of source and reflected components (superscripts S and R, respectively) [Carslaw and Jaeger, 1959]:

$$c_1(x, t) = c_1^S(x, t) + c_1^R(x, t) \quad \text{for } x < 0$$

$$c_1^S(x, t) = \frac{1}{\sqrt{4\pi D_1 t}} \exp\left(\frac{-(x - x_0)^2}{4D_1 t}\right)$$

$$c_1^R(x, t) = \frac{R_1}{\sqrt{4\pi D_1 t}} \exp\left(\frac{-(x + x_0)^2}{4D_1 t}\right)$$

$$c_2(x, t) = \frac{1 - R_1}{\sqrt{4\pi D_2 t}} \exp\left(\frac{-(x - x_0 \beta_1)^2}{4D_2 t}\right) \quad \text{for } x > 0$$

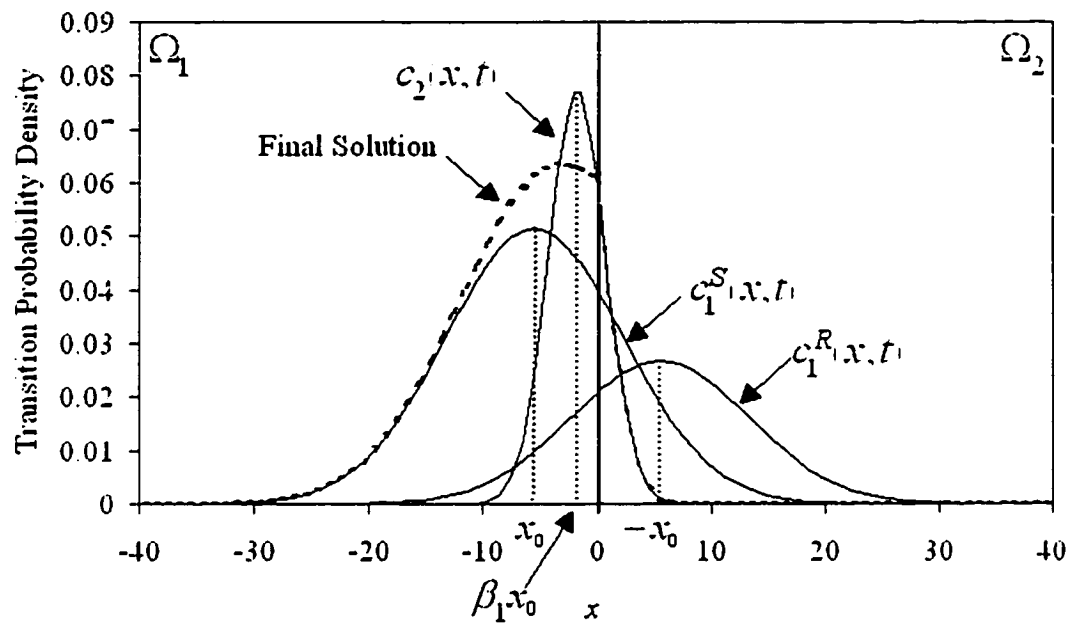
where R_1 is a reflection coefficient and the factor $\beta_1 = (D_2/D_1)^{1/2}$ accounts for the difference in mean-square displacements between the two strata by effectively adjusting the origin of the source in Ω_1 ($x < 0$) for solution in Ω_2 ($x > 0$). In order to satisfy equations (2.22a) and (2.22b), $R_1 = (D_1^{1/2} - D_2^{1/2}) / (D_1^{1/2} + D_2^{1/2})$. For a source located in Ω_2 ($x_0 > 0$) replace R_1 with $R_2 = -R_1$ and β_1 with $\beta_2 = D_1^{1/2} / D_2^{1/2}$. This solution is illustrated in Figures 3a and 3b.

Development of a reflection principle based on the method of images for application to the RWPM in one dimension is easily accomplished by modifying the transition probability density (TPD), that is, $\mathbf{B} \cdot \Delta \mathbf{w}$ in (2.12), for a particle that may cross the interface in the following time step [Uffink, 1985]. The modification consists of summing the component parts of the modified density function given by equations (2.19a) - (2.19d). In this context, Figures 3a and 3b can be interpreted as TPDs for particles located at x_0 in Ω_1 and Ω_2 , respectively. Alternatively, when approximating $\Delta \mathbf{w}$ by a uniform TPD with mean zero and unit variance in the RWPM (see *Tompson et al.*, 1987), the uniform TPDs for particles located in Ω_1 and Ω_2 may be modified similarly, as was done by Uffink [1985]. For the more general one-dimensional problem with multiple interfaces, use of a uniform TPD together with small Δt can limit necessary image densities to those arising from a single interface.

2.4.2 Interpolation Technique

Discontinuities in the dispersion tensor can also be addressed through interpolation. This method, also discussed in the context of random-walk particle tracking on a block-centered finite-difference solution later in this paper, smoothes the dispersion tensor in

(2.3a)



(2.3b)

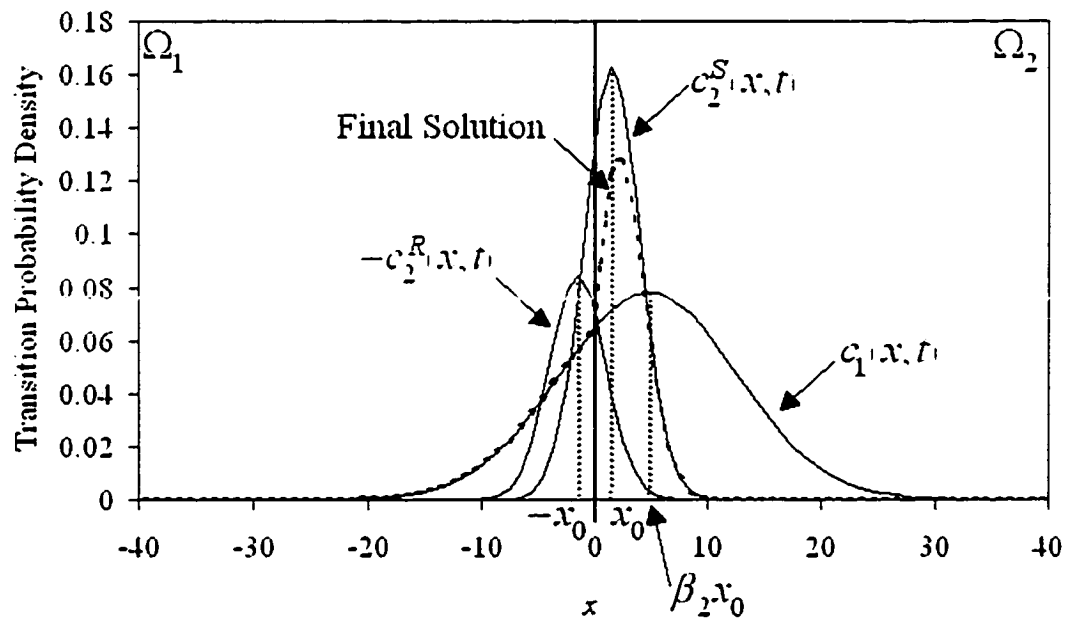


Figure 2.3: Component parts (bold lines) of analytical solution given in (a) equations (2.19a) - (2.19d) for point source in Ω_1 and (b) equivalent form of equations (2.19a) - (2.19d) for point source in Ω_2 are summed to form final solution (bold dashed line) about an interface.

the vicinity of the interface to eliminate discontinuities and define the gradient term in the drift vector. For convergence to the true solution, this method requires convergence in time step as well as the spatial discretization associated the interpolation scheme. Below we evaluate interpolation and the reflection technique.

2.4.3 Comparison with Theory

We test the interpolation and reflection techniques in a closed one-dimensional constant-concentration system with reflecting boundaries on both ends and a partially reflecting interface located in the center such that the two equal-volume portions of the domain, Ω_1 and Ω_2 , are delineated by a discrete contrast in dispersion coefficients (see *Semra et al.*, 1993). When there is no drift in Ω_1 and Ω_2 ($\mathbf{A} = \mathbf{0}$) a correct technique will maintain a uniform particle number density on either side of the partially reflecting interface, i.e., $N_1/N_2 = 1$. Figure 2.4 shows results of a test of the alternative methods presented above using the RWPM for a one-dimensional system with reflecting boundaries at $x = -49$ and $x = 49$, $\Delta t = 0.005$, 588 particles, $D_1 = 5.0$ ($x < 0$), and D_2 ($x > 0$) prescribed such that the ratio, D_1/D_2 , ranges from 2.5 to 20.0. For this problem the alternative interpolation technique is applied by linearly interpolating D through a unit length across the interface at $x = 0$. The results for N_1/N_2 at an approximate steady state show that using no correction fails to maintain uniform number density. Interpolation and the method of *Uffink* [1985] correctly maintain a uniform number density, identical to the analytical solution. The linear-interpolation method yields a close approximation.

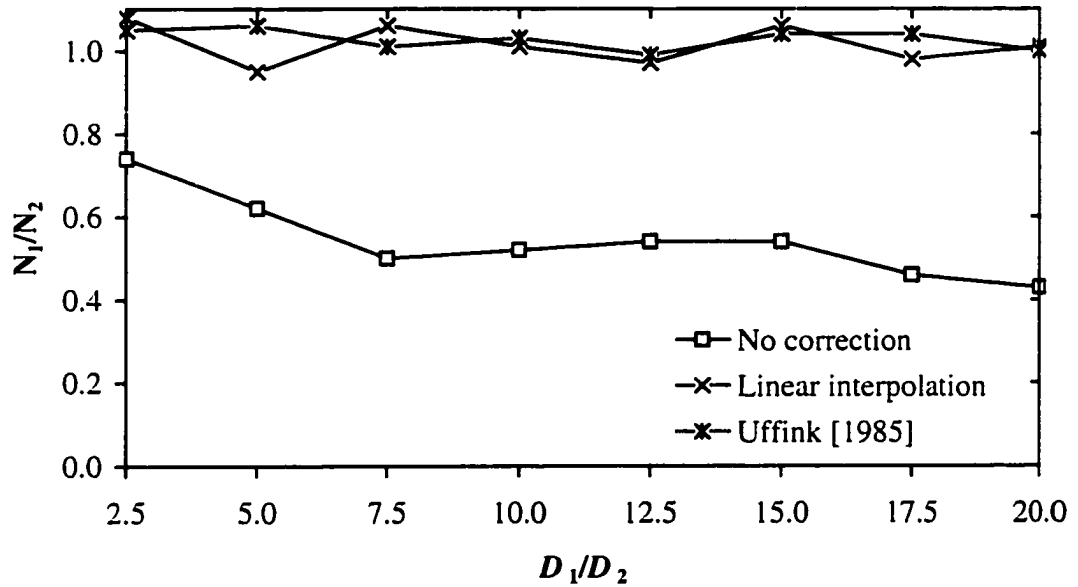


Figure 2.4: Comparison in ratios of particle numbers (N_1/N_2) on either side of discontinuity in D for different alternative techniques of reflecting to conserve mass.

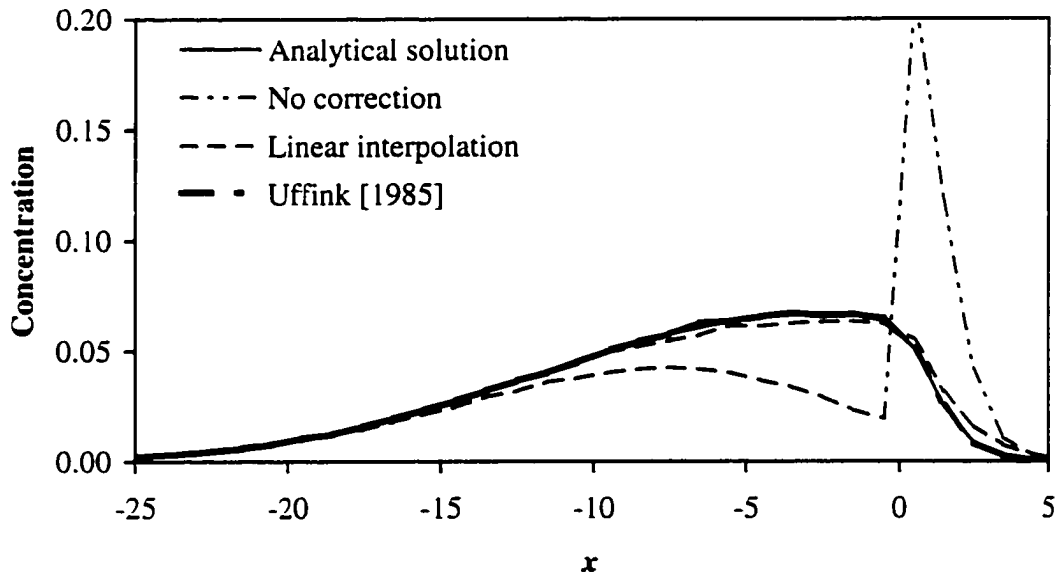


Figure 2.5: Comparison of concentrations from simulations using the different alternative techniques and the analytical solution given in equations (2.19a) - (2.19d) at $t = 6.0$ for $x_0 = -5.0$, $D_1 = 5.0$, and $D_2 = 0.25$. The method of *Uffink* [1985] produces results virtually

To further test these methods we compare results for a point source initial condition with the analytical solution given by equations (2.19a) - (2.19d) and illustrated in Figure 2.3a. A total of 100,000 particles were used in each simulation, wherein $x_0 = -5.0$, $D_1 = 5.0$, $D_2 = 0.25$, and $\Delta t = 0.005$. Figure 2.5 compares concentrations approximated at discrete spatial locations by the normalized number of particles contained in a unit length along the x -axis with the analytical solution at time $t = 6.0$. The result labeled "no correction" clearly shows the error imposed by neglecting to reflect particles or interpolate. Interpolation and the method of *Uffink* [1985] compare well with the analytical solution.

Note the distinct differences between the two successful techniques. *Uffink's* technique reconstructs the exact TPD. Thus we consider this approach to converge strongly, when the TPD is simulated using Wiener processes (strong convergence refers to the approach of a simulated particle path to the exact path $\mathbf{X}_p(t)$ [*Kloeden and Platen*, 1989]). Interpolation does not simulate the exact TPD but still balances mass.

2.4.4 Limitation of the Reflection Method

For many problems *Uffink's* [1985] reflection method may become computationally infeasible because of the need for multiple images (or reflections) around two- or three-dimensional discontinuities in the \mathbf{D} field. A comparable situation arises with solutions to the flow problem through image well theory (e.g., no-flow boundaries intersecting at a right angle [*Ferris et al.*, 1962]). Although, the number of images required for reasonably accurate solutions is finite (due to the normally small time steps used with the RWPM,) this problem quickly becomes intractable for heterogeneous multi-dimensional systems. Interpolation, easily implemented in three dimensions, appears to provide a reasonable

alternative to the method of images. Convergence, however, requires convergence in the spatial discretization associated with the interpolation as well as a simultaneous convergence with decreasing time-step size. In the following section, we address the application of velocity interpolation and a reflection principle to random walks on a block-centered finite-difference flow solution and introduce a new algorithm based on a modified hybrid velocity interpolation scheme.

2.5 Interpolation Methods for Implementing the RWPM

Application of the RWPM requires knowledge of the groundwater velocity and velocity gradient at particle locations, which are typically determined by numerical solution of the relevant flow problem. As an example, consider the solution of a two-dimensional flow problem with no sources or sinks, as defined by

$$\frac{\partial}{\partial x} \left(K_x \frac{\partial h}{\partial x} \right) + \frac{\partial}{\partial y} \left(K_y \frac{\partial h}{\partial y} \right) = 0$$

where h is hydraulic head [L], and K_x and K_y are the principal components of hydraulic conductivity in the x - and y -directions [LT^{-1}]. In terms of the RWPM, application of a block-centered finite difference scheme for the solution of (2.20) is particularly attractive because particles are easily located with respect to volumetric blocks in an orthogonal grid. Here, hydraulic conductivities are specified on a regular grid of nodes with coordinates $(i\Delta x, j\Delta y)$, and nodal values of the hydraulic head are determined from a finite difference approximation of (2.20):

$$\begin{aligned} & \frac{1}{\Delta x} \left[\left(K_{x(i+1/2, j)} \frac{h_{(i+1, j)} - h_{(i, j)}}{\Delta x} \right) - \left(K_{x(i-1/2, j)} \frac{h_{(i, j)} - h_{(i-1, j)}}{\Delta x} \right) \right] \\ & + \frac{1}{\Delta y} \left[\left(K_{y(i, j+1/2)} \frac{h_{(i, j+1)} - h_{(i, j)}}{\Delta y} \right) - \left(K_{y(i, j-1/2)} \frac{h_{(i, j)} - h_{(i, j-1)}}{\Delta y} \right) \right] = 0 \end{aligned} \quad (2.21)$$

where Δx and Δy are the constant nodal spacings [L] (Figure 2.6). Intermediate (mid-node) values of the conductivity are usually based on a harmonic average of the adjacent nodal values along a segment between two nodes.

Given a nodal solution for the heads, the most obvious way to estimate velocity components is to first compute mid-node components along segments between two nodes, i.e.,

$$v_{x(i+1/2,j)} = -\frac{1}{\Theta} K_{x(i+1/2,j)} \frac{h_{(i+1,j)} - h_{(i,j)}}{\Delta x} \quad (2.22)$$

As shown in Figure 2.6, this will yield normal components of velocity on the volumetric “block” surrounding node (i,j) . However, information on all velocity components at one location is not provided in this way, nor is the velocity at any other point in the domain. Velocities at particle locations must be interpolated from these basic mid-node values. Several approaches can be used to do this, as reviewed below.

2.5.1 Linear Interpolation (LI)

In this approach, one approximates velocity components linearly and independently within each block based on the available mid-node values (Table 2.1). As such, there is no variation of v_x in the y -direction, nor any variation of v_y in the x -direction. Although derivatives of specific velocity components, as required to evaluate the divergence of the dispersion tensor, may not be fully defined, the interpolated velocity field within each

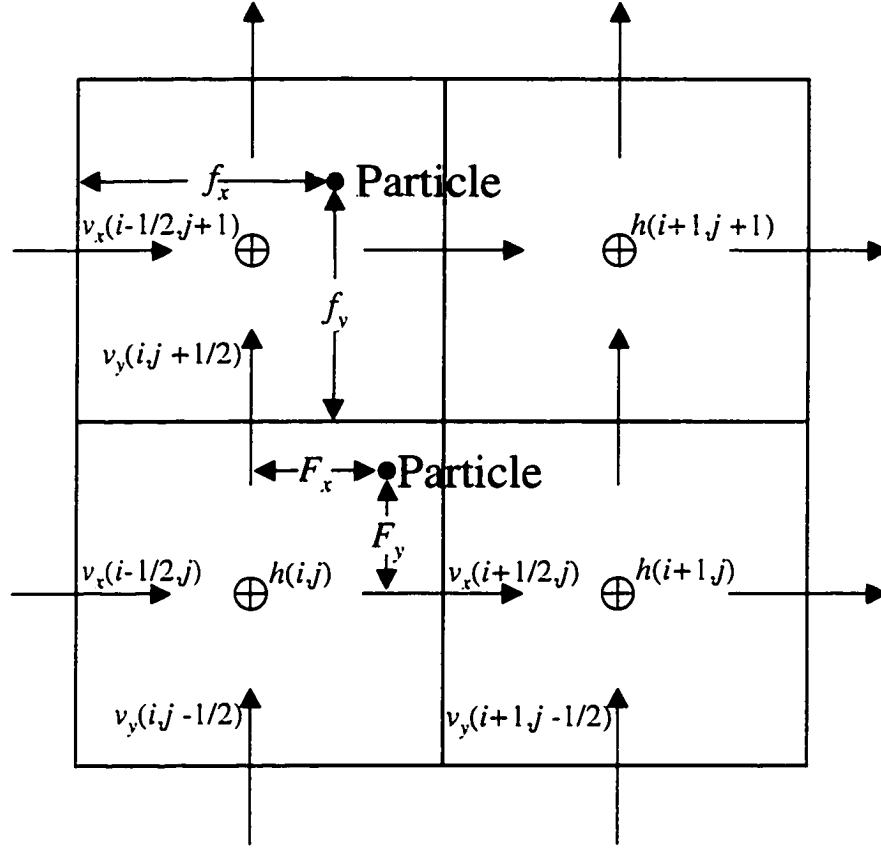


Figure 2.6: Velocity interpolation from a block-centered finite-difference flow scheme.

Table 2.1: Velocity Interpolation Schemes

Interpolation	v_x	v_y
Linear (LI) ¹	$(1-f_x)v_{x(i-1/2,j)}+f_xv_{x(i+1/2,j)}$	$(1-f_y)v_{y(i,j-1/2)}+f_yv_{y(i,j+1/2)}$
Bilinear (BLI) ²	$(1-F_x)[(1-F_x)v_{x(i,j)}+F_xv_{x(i+1/2,j)}]$ $+F_y[(1-F_x)v_{x(i,j+1/2)}+F_xv_{x(i+1/2,j+1/2)}]$	$(1-F_x)[(1-F_y)v_{y(i,j)}+F_yv_{y(i,j+1/2)}]$ $+F_x[(1-F_y)v_{y(i+1/2,j)}+F_yv_{y(i+1/2,j+1/2)}]$
Block Discrete (BDI)	$(v_{x(i+1/2,j)}+v_{x(i-1/2,j)})/2$	$(v_{y(i,j+1/2)}+v_{y(i,j-1/2)})/2$

¹ $f_x = (x - x_{i-1/2})/\Delta x$ and $f_y = (y - y_{j-1/2})/\Delta y$.

² values apply over a block of dimension $\Delta x/2$ by $\Delta y/2$ centered on $(i+1/4, j+1/4)$; $F_x = 2(x - x_{i,j})/\Delta x$ and $F_y = 2(y - y_{i,j})/\Delta y$; and x -velocity terms are defined as $v_{x(i,j)} = (v_{x(i+1/2,j)} + v_{x(i-1/2,j)})/2$, $v_{x(i+1/2,j+1/2)} = (v_{x(i+1/2,j+1)} + v_{x(i+1/2,j)})/2$, and $v_{x(i,j+1/2)} = (v_{x(i+1/2,j+1)} + v_{x(i+1/2,j)} + v_{x(i-1/2,j+1)} + v_{x(i-1/2,j)})/4$.

block, $\mathbf{v}_{LI}(\mathbf{x})$, satisfies the fluid mass balance $\nabla \cdot \mathbf{v} = 0$ exactly. The LI scheme may yield discontinuities in tangential velocities, and therefore the velocity-dependent dispersion tensor, at block interfaces. Mass conservation therefore requires a reflection principle or alternative technique be applied at these interfaces. The LI scheme has been used in the context of advective particle-tracking by *Pollock* [1988], *Goode* [1990], *Schafer-Perini and Wilson* [1991] and *Cordes and Kinzelbach* [1992].

2.5.2 Bilinear Interpolation (BLI)

In this approach, mid-node velocity components surrounding a node are first averaged to provide estimates of velocity at the node (Table 2.1). In this way, both components are available at each location. The interpolated velocity may then be estimated in a bilinear fashion within cell volumes, or quarter segments of these volumes, as shown in Table 2.1 and Figure 2.6. Here, the interpolated velocity field, $\mathbf{v}_{BLI}(\mathbf{x})$, does not satisfy fluid mass balance, however, it allows all first-order derivatives of velocity components to be estimated. An important advantage of BLI is that the dispersion tensor is continuous in this case; a reflection principle is therefore not required. *Konikow and Bredehoeft* [1978] applied BLI in a method of characteristics model and *Goode* [1990] used it for advective particle tracking.

2.5.3 Block-Discrete Interpolation (BDI)

In this approach, mid-node velocity components are averaged to obtain values considered constant within specific finite-difference blocks. *Tompson et al.* [1987] and *Tompson and Gelhar* [1990] focus on the cell volumes created by neighboring nodes to (1) average the mid-node fluxes on each cell edge and obtain constant cell velocities, \mathbf{v}_{BDI} , and (2) to

form central-difference approximations for estimating velocity gradients; these are also uniform within each grid block. This approach supports easy implementation of the RWPM because direct interpolation onto each particle is not required, but is otherwise very approximate. Nevertheless, if spatial variation of velocity is small with respect to the grid resolution, errors might still be acceptably small.

2.5.4 Hybrid Schemes

For purely advective particle tracking, the LI scheme is mass conservative and clearly an appropriate choice. However, for the dispersive component of the random walk, the LI scheme may be impractical because of the need for reflection corrections. This raises the possibility of applying LI for the advective component and BLI for velocities in the dispersive component. Below, we compare hybrid schemes that use bilinear interpolation to estimate velocities in the dispersion tensor, and either linear or block-discrete methods to approximate advective terms; we will refer to these hybrid schemes as BLI/LI and BLI/BDI, respectively. These hybrid schemes yield a continuous dispersion tensor, so a reflection principle is not required to satisfy mass balance at block interfaces.

2.6 Test Cases

Two problems are considered, (1) transport in highly permeable stratum bounded by low-permeability material in which transport occurs only by diffusion and (2) transport in two-dimensional heterogeneous porous media. The first problem assesses the relative accuracy, with respect to balancing mass at material contacts, of the three-interpolation schemes and a reflection principle presented above by comparing results from numerical experiments with a known analytical solution. This problem serves as a surrogate for the general case where, due to the nature of the block-centered finite-difference scheme, tan-

gential velocities, and therefore the velocity-dependent dispersion tensor, are often discontinuous at block interfaces. Furthermore, this problem represents the “worst case scenario” of a discontinuous dispersion tensor that might be encountered in more general two- and three-dimensional simulations. The second problem demonstrates the potentially significant effects of neglecting discontinuities in the dispersion tensor in random-walk simulations of transport in complex heterogeneous porous media. In this case, results from hybrid interpolation schemes, BLI/LI and BLI/BDI, which locally balance mass by bilinearly interpolating velocities in the dispersion tensor, are compared with the BDI scheme of *Tompson et al.* [1987] and *Tompson and Gelhar* [1990], which tries to correct for these discontinuities by including approximations for gradient terms.

2.6.1 Solute Transport in a Stratified System

The stratified saturated system shown in Figure 2.7 shows a thin horizontal high-permeability layer of thickness $2b$ and length 1.0 m. This layer is bounded by low-permeability porous layers considered to be of infinite thickness in the vertical. A conservative constituent is introduced at constant concentration, c_0 , at the upstream end of the high-permeability layer during a time period t_p . As the constituent progresses along the high-permeability layer, diffusive transport between this layer and the adjacent low-permeability layers accentuates the overall dispersion of solutes in the system. Obtaining an accurate solution to this problem is highly dependent on a correct simulation of mass transfer across the interfaces between high- and low-permeability layers.

Initial and boundary conditions for the problem are specified as

$$c(x,y,0)=0 \tag{2.23a}$$

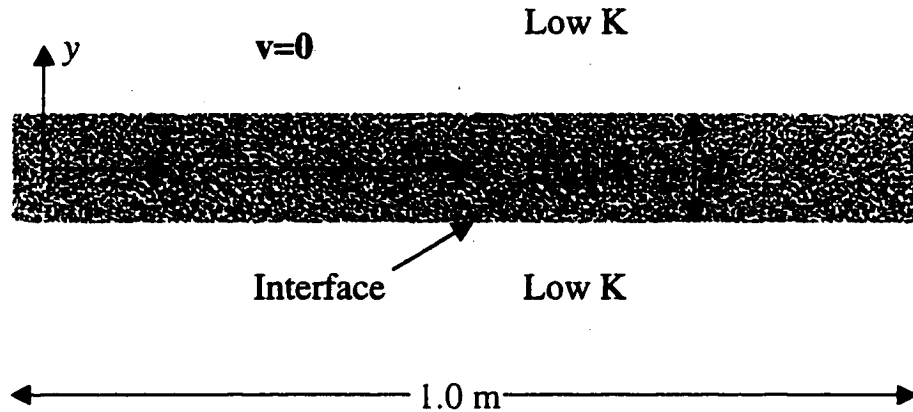


Figure 2.7: A stratified system with a thin high-permeability layer bounded by a low-permeability porous matrix.

$$c(0, y, t) = \begin{cases} c_0 & 0 < t < t_p, -b \leq y \leq +b \\ 0 & \text{otherwise} \end{cases} \quad (2.23b)$$

$$c(\infty, y, t) = 0 \quad (2.23c)$$

$$c(y, \pm\infty, t) = 0 \quad (2.23d)$$

For $t_p = 7$ days, these conditions represent a seven day input of a conservative constituent at the upstream end of the high-permeability layer as was addressed in the laboratory study of *Sudicky et al.* [1985]. For this problem, the pore-scale longitudinal dispersivity has been shown to contribute little to the development of the solute plume and neglecting it will introduce little error in predictions. For simplicity, the porosity was specified as a constant of 1.0 throughout the system. Superposition in time of the analytical solution presented by *Gillham et al.* [1984], which assumes solute in the high-permeability layer is well mixed, is used to obtain an analytical solution to (2.23a) - (2.23d).

For the numerical experiments, the various interpolation schemes were incorporated into the SLIM1 random-walk code [*Tompson et al.*, 1987]. In all numerical simu-

lations, the domain was discretized in a manner consistent with a velocity field computed by a block-centered finite-difference flow model.

The average concentration, \bar{c}_H^s , across the entire high-permeability layer at a point x may be discretely estimated from the particle mass contained within a narrow area centered at x of length Δx and width $2b$, divided by the area, $\Delta a = 2b\Delta x$. In terms of equation (2.2), with $\Theta = 1$, \bar{c}_H^s can be expressed by

$$\bar{c}_H^s(x) = \left(\frac{1}{\Delta a} \right) \sum_p m_p, \quad \forall \mathbf{X}_p \in \Delta a|_x. \quad (2.24)$$

Transport in this stratified system may be modeled with the particle approach by releasing particles along the upstream edge of the high-permeability layer and allowing them to advect downstream and disperse into the adjacent low permeability zones. To simulate the Dirichlet boundary condition at the upstream end of the system, the concentration, \hat{c}_H^s , in the leftmost column cells is maintained at a value of 1.0 for 7 days using a total of 5000 particles and properly maintained boundary conditions [Tompson and Dougherty, 1992] after which it is turned off.

Simulations were performed for three levels of discretization, $\Delta y = 0.03$ m, $\Delta y = 0.01$, and $\Delta y = 0.006$ corresponding to 1, 3, and 5 grid blocks, respectively, for the entire width of the high permeability layer. Discretization in the x -direction, used to calculate concentration, is specified as 0.001 m. The following parameter values were used in all simulations: $b = 0.015$ m, $D^* = 1.0454 \times 10^{-4}$ m²/day, $\alpha_T = 0.01$ m, $\nu_J = 0.5$ m/day, and $\Delta t = 0.001$ days

2.6.1.1 Results and Discussion

Simulations were performed for the LI scheme with and without a reflection principle.

The results for \bar{c}_μ^s at $x = 1.0$ m are compared with the analytical solution in Figure 2.8.

Predictions using LI with a reflection principle agree well with the analytical solution.

Predictions using LI alone yield little or no solute breakthrough; mass in the high-permeability layer is lost to the low-permeability matrix. The discretization in the y -direction does not affect results from either LI with a reflection principle or LI alone, hence, the cases $\Delta y = 0.01$ m and $\Delta y = 0.006$ m are not shown.

The LI scheme without a reflection principle preserves discontinuities in velocity at material contacts and fails to address them. This is similar to the “no correction” case considered in the tests of the various reflection principles. Without special treatment of random walks at these contacts, mass flux from high- to low-dispersion layers is over estimated and mass flux from low- to high-dispersion layers is underestimated.

Predictions using BDI are compared with predictions from the analytical solution in Figure 2.9. As expected, results from BDI compare poorly to the analytical solution because discontinuities in the velocity-dependent dispersion tensor are not addressed. The gradient terms in BDI seek to offset mass-conservation errors due to discontinuities. However, the magnitudes of these terms and the areas over which they apply change with discretization in the y -direction whereas the impulse in drift due to the discontinuity in the transverse dispersion is independent of this discretization.

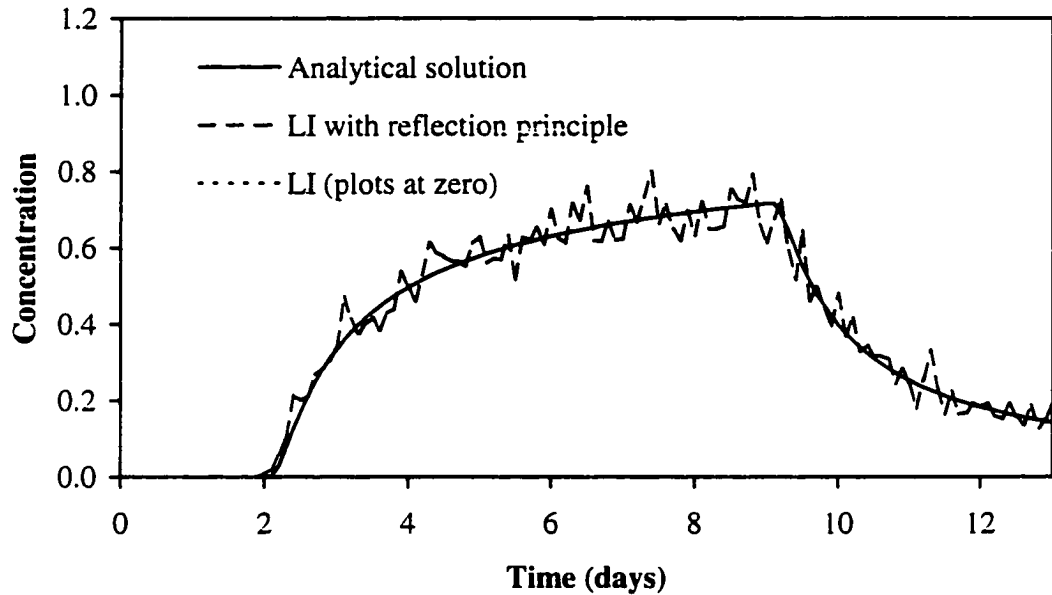


Figure 2.8: Comparison of analytical solution with solute breakthrough curve predicted using LI with and without a reflection principle ($\Delta y = 0.03$ m). There is no solute breakthrough for LI without a reflection principle. Simulations using $\Delta y = 0.01$ m and 0.006 m produce identical results for this test case.

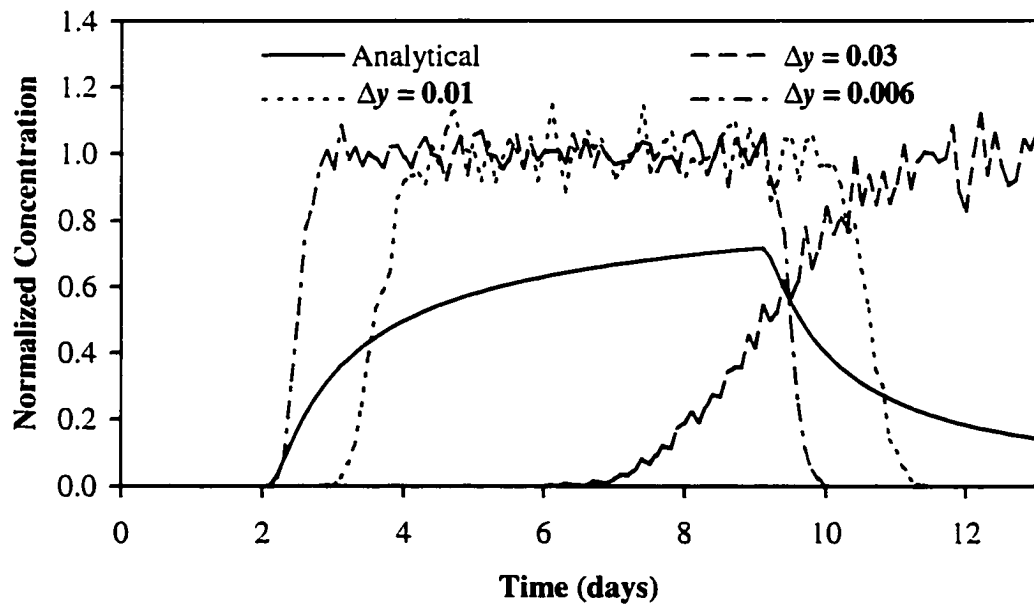


Figure 2.9: Comparison of analytical solution with solute breakthrough curves predicted using BDI.

Results from the BLI/LI and BLI/BDI hybrid schemes are compared with the analytical solution in Figure 2.10. Note that simulations using the BLI/LI and BLI/BDI hybrid schemes yield the same results for this test case. As expected, results indicate convergence of these schemes to the analytical solution as the grid is refined. As the grid becomes more coarse, breakthrough is shifted to later times, however, the main features of the breakthrough curves, in particular peak concentrations, are maintained. The extent to which this BLI/LI and BLI/BDI can approximate discontinuous tangential velocities will depend on the resolution of the grid.

Ideally, one would also hope to test the BLI/LI hybrid scheme in cases with more complex heterogeneity in two- and three-dimensions, however, we know of no analytical solutions to represent a “ground truth” for such conditions. Furthermore, comparing with other numerical solutions would be circular. Nevertheless, we believe the above two-dimensional test is sufficient to conclude that the BLI/LI hybrid scheme is capable of producing reliable results provided the discretization is adequately refined.

2.6.2 Transport in Heterogeneous Porous Media

The transport of a conservative constituent in a heterogeneous system is considered here. This problem is of interest because the RWPM has been proposed [Tompson *et al.*, 1987] to verify stochastic transport theories [e.g., Matheron and de Marsily, 1980; Gelhar and Axness, 1983] and to investigate the effects of porous-media heterogeneity on solute transport [Tompson *et al.*, 1994]. In these cases, random-walk model solutions are considered true representations of transport. Accuracy in these random walk simulations is therefore critical.

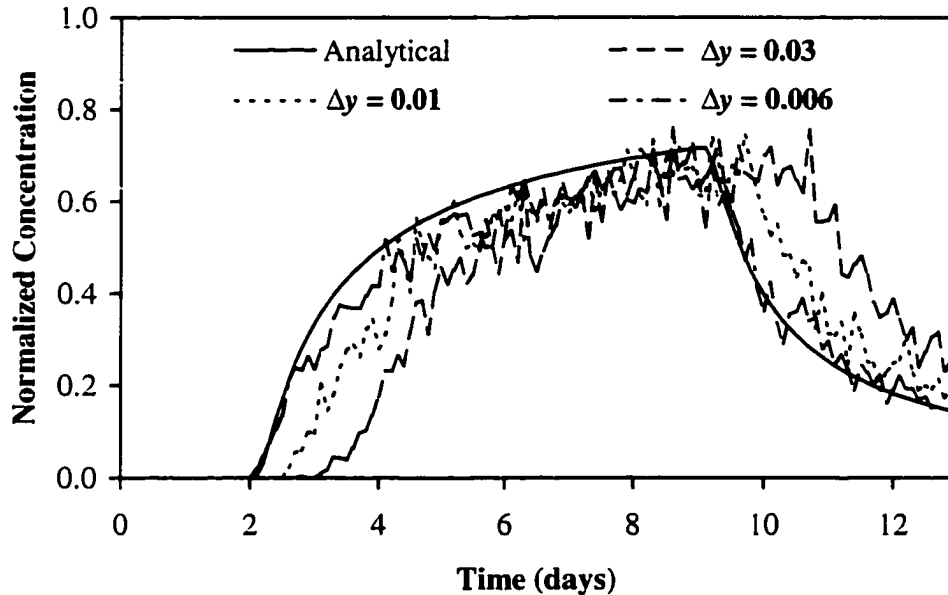


Figure 2.10: Comparison of analytical solution with solute breakthrough curves predicted using BLI/LI and BLI/BDI schemes. The BLI/LI and BLI/BDI schemes produce identical results for this test case.

The two-dimensional conductivity field illustrated in Figure 2.11 was generated on a grid with dimensions 85 ($\Delta z = 1$) in the vertical and 1400 ($\Delta x = 100$) in the horizontal using a Gaussian conditional simulation technique [Fogg *et al.*, 1991] with a spherical variogram model having vertical and horizontal variogram ranges of 10 and 400, respectively. For flow simulations, the numerical grid is refined in the x -direction, so that $\Delta x = 10$, while still preserving the geometry of the simulated conductivity field. A steady-state hydraulic-head distribution was simulated using the MODFLOW block-centered finite-difference flow program [McDonald and Harbaugh, 1988]. No flux boundary conditions are specified at $z=0$ ft and $z=85$. Constant head boundary conditions at $x=5$ and $x=1395$, are specified as $h=37$ and $h=0$, respectively, for all z .

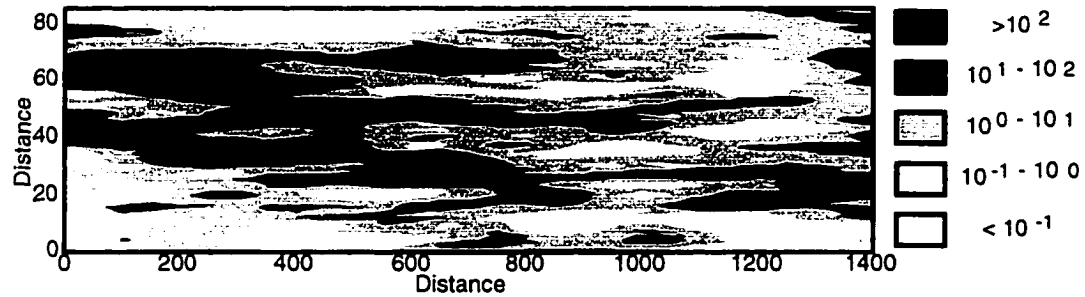


Figure 2.11: Gaussian conditional simulation of hydraulic-conductivity field with $\log\text{-}K$ mean and standard deviation of 1.69×10^{-3} and 2.75×10^{-3} , respectively, and vertical and horizontal variogram ranges of 10 and 400, respectively (modified from *Fogg et al.*, 1991).

Transport is simulated for an instantaneous injection of a contaminant in a fully penetrating line source at location $x = 10$. Boundary conditions for transport simulations are specified as reflecting no-flux conditions at $z = 0$ and $z = 85$ and open boundaries at $x = 10$ and $x = 1390$. Initially, 50,000 particles are distributed uniformly over the vertical in the column of grid blocks from $x=0$ to $x=10$. These particles are allowed to advect and disperse into the domain over a single time step. After this time step, particles at locations $x < 10$ are eliminated in order to approximate an instantaneous injection of mass. The following parameter values are used in all simulations: $\Theta = 0.33$, $D^* = 1.1 \times 10^{-3}$, and $\alpha_L = \alpha_T = 0.03$.

2.6.2.1 Results and Discussion

In this example, we use BDI, BLI and the two hybrid schemes, BLI/LI and BLI/BDI and compare results for mass-breakthrough curves and first and second spatial moments of the mass distribution [*Tompson et al.*, 1987]. Results for mass breakthrough at $x=1390$ versus time from simulations using the various interpolation schemes are compared in Figure 2.12. Results for the first and longitudinal second moments are presented in Fig-

ures 13 and 14, respectively. For this problem, results from the three schemes that bilinearly-interpolate velocities in the dispersion tensor are virtually identical, indicating little effect of change in advective-component interpolation method on predicted average transport behavior. In contrast, BDI model predictions differ considerably from the three BLI schemes, showing that average transport behavior predicted by the RWPM is sensitive to the way in which \mathbf{D} is treated for this case.

Considerable effort has been devoted to accurate interpolation of velocities for the case of pure solute advection ($\mathbf{A} = \mathbf{v}$, $\mathbf{B} = \mathbf{0}$) [Reddell and Sunada, 1970; Konikow and Bredehoeft, 1978; Pollock, 1988; Goode, 1990; Schafer-Perini and Wilson, 1991; Cordes and Kinzelbach, 1992]. It is well known that by maintaining aquifer geometry at a given scale and refining the computational grid, in the limit, interpolation errors in advective components will vanish [Goode, 1990]; however, as demonstrated in the transport experiment in stratified media (Figures 2.8, 2.9, and 2.10), discontinuities in the dispersion tensor and the consequent mass-conservation errors will remain unless an interpolation or reflection method is applied. Agreement between schemes that bilinearly interpolate velocities in the dispersion tensor and disagreement between these schemes and BDI (Figures 2.12, 2.13, and 2.14) suggests that when transport is dispersive ($\mathbf{D} \neq \mathbf{0}$), the choice of interpolation scheme for advective components has relatively little effect on overall transport compared to the choice of how one handles discontinuities in dispersion tensor.

2.7 Conclusions

In this paper we have reviewed conditions required for local mass conservation by the RWPM and discussed consequences of violating these conditions. A problem occurs in cases where interfaces separate materials with contrasting hydraulic properties;

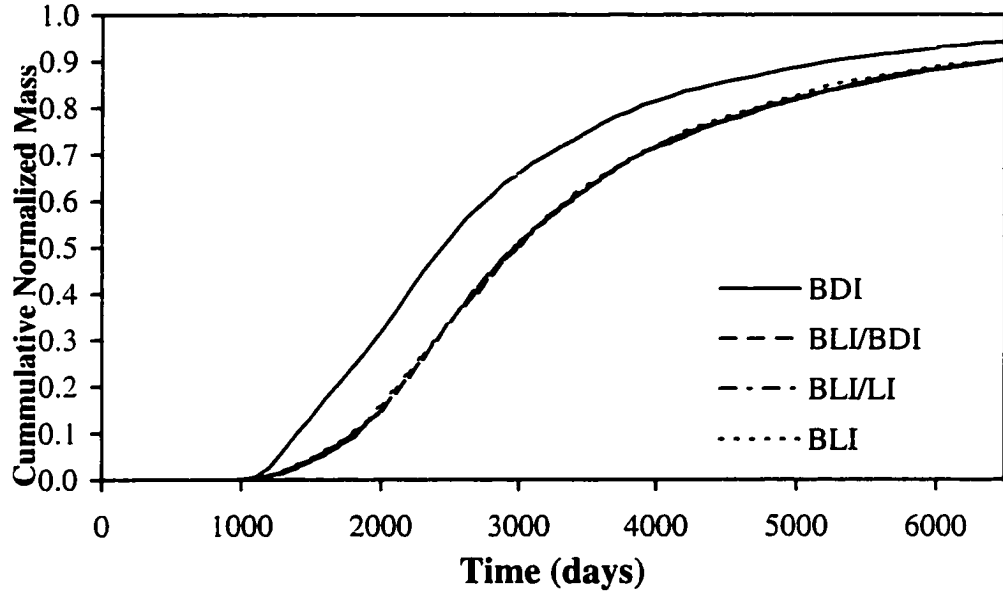


Figure 2.12: Comparison of solute breakthrough curves predicted using BDI, BLI/BDI, BLI/LI, and BLI.

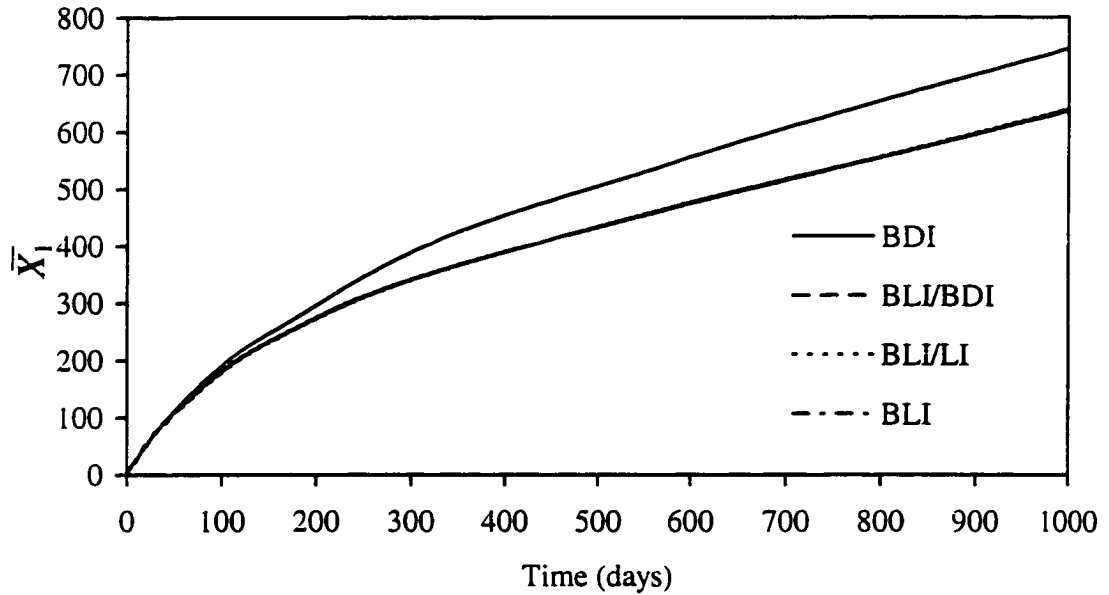


Figure 2.13: Comparison of first moments predicted using BDI, BLI/BDI, BLI/LI, and BLI.

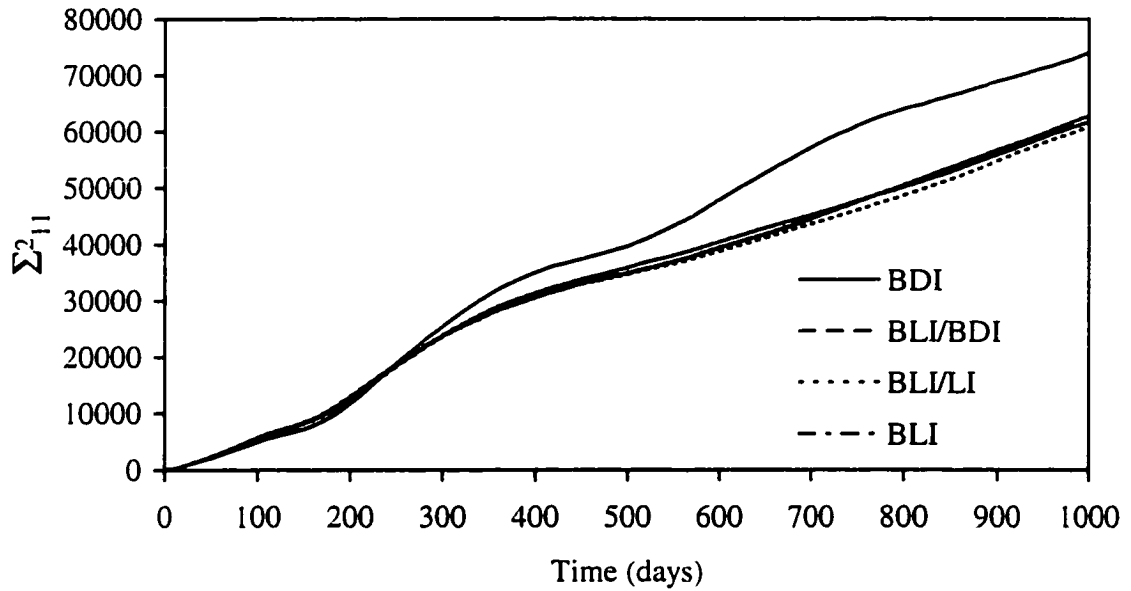


Figure 2.14: Comparison of longitudinal second moments predicted using BDI, BLI/BDI, BLI/LI, and BLI.

dispersivities, effective porosities, and velocities, and therefore the velocity-dependent dispersion tensor, may be discontinuous. We find that when the dispersion tensor is discontinuous, due to a discontinuous velocity field, mass flux can be conserved in the RWPM through the use of a carefully chosen interpolation scheme or a reflection principle. Similar methods may be applied when dispersivities or effective porosities are discontinuous.

A reflection principle based on the method of images yields a mass-conservative random walk near interfaces representing discontinuities in the dispersion tensor. However, application of this method to general three-dimensional problems in which multiple interfaces intersect appears problematic; numerous images (reflections) must be superimposed to obtain the transition probability density. Velocity interpolation provides a mass-conservative approximation that does not require superposition of multiple images. Ve-

locity interpolation is easily implemented and simulation results indicate convergence as the spatial and temporal discretizations are refined.

When a block-centered finite-difference scheme is used to solve the flow equation, linear interpolation in the direction of the velocity component, although consistent with the governing flow equations, may yield discontinuities in tangential velocities, even when the effective porosity is continuous in space. These discontinuities are not a problem in advective particle-tracking models. However, with the RWPM, velocities tangent to an interface also contribute to the dispersive flux across that interface. Discontinuities in this flux violate local mass conservation. Bilinear (or trilinear) interpolation of velocities in the dispersion tensor or a reflection principle provide methods for conserving mass in these cases. The results presented herein show that, unless one of these methods (or a similar method) is applied, discontinuities in tangential velocities may lead to severe local mass-conservation errors in the random walk which can significantly affect transport predictions. Simulation results suggest local-mass conservation errors, due to incorrectly handling discontinuities in dispersive components of the random walk, outweigh mass-conservation errors due to inaccurate interpolation of advective components.

Lastly, we find that additional development of the theory behind the RWPM for the advection-dispersion equation with discontinuous coefficients is needed. While the interpolation approach has been applied with some success here, it appears that a more accurate, efficient method without the need for grid refinement might arise from such an effort.

2.8 References

- Ahlstrom, S.W., H.P. Foote, R.C. Arnett, C.R. Cole and R.J. Serne, Multi-component mass transport model: theory and numerical implementation. Rep. BNWL-2127, Battelle Pacific Northwest Lab., Richland, Washington, 1977.
- Bagtzoglou, A.C., A.F.B. Tompson and D.E. Dougherty, Projection functions for particle grid methods, *Numerical Methods for Partial Differential Equations*, 8, 325-340, 1992.
- Bear, J., *Dynamics of Fluids in Porous Media*, Elsevier, New York, 1972.
- Carslaw, H.S. and J.C. Jaeger, *Conduction of heat in solids*, Clarendon Press, Oxford, 363-365, 1959.
- Cordes, C. and W. Kinzelbach, Continuous groundwater velocity fields and path lines in linear, bilinear, and trilinear elements, *Water Resources Research*, 28(11), 2903-2911, 1992.
- Crank, J., *The Mathematics of Diffusion*, 2nd Ed., Clarendon Press, Oxford, p162-164, 1975.
- Feller, W., *An Introduction to Probability Theory and its Applications*, John Wiley and Sons, Inc., New York, 1957.
- Ferris, J.G., D.B. Knowles, R.H. Brown, and R.W. Stallman, Theory of Aquifer Tests, U.S. Geological Survey, Water Supply Paper 1536-E, 1962.
- Fogg, G.E., F.J. Lucia, and R.K. Senger, Stochastic simulation of interwell-scale heterogeneity for improved prediction of sweep efficiency in carbonate reservoirs, in *Reservoir Characterization II*, Lake, L.W., H.B. Carroll, Jr., and T.C. Wesson (eds), Academic Press, Inc., San Diego, 355-381, 1991.
- Gardiner, C.W., *Handbook of Stochastic Methods for Physics Chemistry and the Natural Sciences*, Springer-Verlag, Berlin, 1990.
- Gelhar, L.W. and C.W. Axness, Three dimensional analysis of macrodispersion in aquifers, *Water Resources Research*, 19(1), 161-180, 1983.
- Gillham, R.W., E.A. Sudicky, J.A. Cherry and E.O. Frind, An advection diffusion concept for solute transport in heterogeneous unconsolidated geologic deposits, *Water Resources Research*, 20(3), 369-378, 1984.
- Goode, D.J., Particle velocity interpolation in block-centered finite difference groundwater flow models, *Water Resources Research*, 26(5), 925-940, 1990.
- LaBolle, E.M., G.E. Fogg, and A.F.B. Tompson, Random-walk simulation of transport in heterogeneous porous media: Local mass-conservation problem and implementation methods, *Water Resources Research*, 32(3), 583-593, 1996.
- Kinzelbach, W., The random walk method in pollutant transport simulation, in *Groundwater Flow and Quality Modelling*, ed. Custidio, E., A. Gurgui, and J.P. Lobo Ferreria, NATO ASI Series C: Math and Phys. Sci. 224: 227-246, Reidel Publishing Company, 1988.
- Kloeden, P. E. and F. Platen, A survey of numerical methods for stochastic differential equations, *Stochastic Hydrology and Hydraulics*, 3, 155-178, 1989.
- Konikow, L.F. and J.D. Bredehoeft, Computer model of two-dimensional solute transport and dispersion in ground water, U.S. Geol. Surv. Tech. Water Resour. Invest. Book 7, Chap. C2, 1978.

- Matheron, G., and G. de Marsily, Is transport in porous media always diffusive? A counterexample, *Water Resources Research*, 16(5), 901-917, 1980.
- McDonald, M.G., A. Harbaugh, A modular three-dimensional finite difference groundwater flow model, *Techniques of Water-Resources Investigations of the United States Geological Survey*, United States Government Printing Office, WA., 1988.
- Pollock, D.W., Semianalytical computation of path lines for finite-difference models, *Groundwater*, 26(6), 743-750, 1988.
- Prickett, Th.A., Th.G. Naymik and C.G. Longquist, A random walk solute transport model for selected groundwater quality evaluations, Rep. Illinois State Water Survey, Urbana Illinois, 1981.
- Reddel, D.L. and D.K. Sunada, Numerical simulation of dispersion in groundwater aquifers, Colo. State Univ. Hydrol. Pap., 41, 1970.
- Risken, H., *The Fokker-Planck Equation*, Springer Verlag, Berlin, 1989.
- Schafer-Perini, A.L. and J.L. Wilson, Efficient and accurate front tracking for 2-dimensional groundwater flow models, *Water Resources Research*, 27(7), 1471-1485, 1991.
- Semra, K., Ph. Ackerer, and R. Mosé, Three-dimensional groundwater quality modelling in heterogeneous media, in *Water Pollution II, Modelling, Measuring and Prediction*, Wrobel, L.C. and C.A. Brebbia (eds), Computational Mechanics Publications, Southampton Boston, 3-11, 1993.
- Sudicky, E.A., R.W. Gilham and E.O. Frind, Experimental investigation of solute transport in stratified porous media 1. The nonreactive case, *Water Resources Research*, 21(7), 1035-1041, 1985.
- Tompson, A.F.B., S.F. Ashby, R.D. Falgout, S.G. Smith, T.W. Fogwell, and G.A. Loosmore, Use of High performance Computing to Examine the Effectiveness of Aquifer Remediation, Report UCRL-JC-115374, Lawrence Livermore National Laboratory, 1994.
- Tompson, A.F.B. and D.E. Dougherty, Particle-grid methods for reacting flows in porous media with application to Fisher's equation, *Applied Mathematical Modelling*, 16, 374-383, 1992.
- Tompson, A.F.B., Numerical simulation of chemical migration in physically in chemically heterogeneous porous media, *Water Resources Research*, 29(11), 3709-3726, 1993.
- Tompson, A.F.B. and L.W. Gelhar, Numerical simulation of solute transport in three-dimensional randomly heterogeneous porous media, *Water Resources Research*, 26(10), 2541-2562, 1990.
- Tompson, A.F.B., E.G. Vomoris, and L.W. Gelhar, Numerical simulation of solute transport in randomly heterogeneous porous media: motivation, model development, and application, Report UCID-21281, Lawrence Livermore National Laboratory, 1987.
- Uffink, G.J.M., A random walk method for the simulation of macrodispersion in a stratified aquifer, in *Relation of Groundwater Quality and Quantity*, IAHS Pub No. 146, 103-114, 1985.
- Uffink, G.J.M., Modeling of solute transport with the random walk method, in *Groundwater Flow and Quality Modelling*, ed. Custidio, E., A. Gurgui, and J.P. Lobo

Ferreria, NATO ASI Series C: Math and Phys. Sci. 224: 247-265, Reidel Publishing Company. 1988.

Chapter 3

Diffusion Theory for Transport in Porous Media: Transition-Probability Densities of Diffusion Processes Corresponding to Advection-Dispersion Equations*

3.1 Abstract

Local-scale spatial averaging of pore-scale advection-diffusion equations in porous media leads to advection-dispersion equations (ADEs). While often used to describe subsurface transport, ADEs may pose special problems in the context of diffusion theory. Standard diffusion theory only applies when characteristic coefficients, velocity, porosity and dispersion tensor, are smooth functions of space. Subsurface porous-material properties, however, naturally exhibit spatial variability. Transitions between material types are often abrupt rather than smooth, such as sand in contact with clay. In such composite porous media, characteristic coefficients in spatially-averaged transport equations may be discontinuous. Although commonly called on to model transport in these cases, standard diffusion theory does not apply. Herein we develop diffusion theory for ADEs of transport in porous media. Derivation of ADEs from probabilistic assumptions yields (1) necessary

* published in *Water Resources Research* [*LaBolle et al.*, 1998].

conditions for convergence of diffusion processes to ADEs, even when coefficients are discontinuous, and (2) general probabilistic definitions of physical quantities, velocity and dispersion tensor. As examples of how the new theory can be applied to theoretical and numerical problems of transport in porous media, we evaluate several random-walk methods that have appeared in the water resources literature.

3.2 Introduction

The need to forecast long-term transport phenomena such as groundwater remediation at complex field sites is placing more stringent demands on models of transport in porous media. Detailed site characterizations based on geostatistical simulations that are conditional to subsurface core and geophysical data are producing ever more realistic models of heterogeneity, perhaps including most of the intricacies that strongly govern scale-dependent dispersion (e.g., *Carle et al.* in press; *Copty and Rubin* [1995], *McKenna and Poeter* [1995], and *Sheibe and Freyburg* [1995]). These models commonly include large contrasts in hydraulic conductivity (K) characterized by both gradational and abrupt contacts between geologic materials (e.g., clean sand resting on a clay bed) and with $\ln K$ variances as high as 24. Furthermore, the volume fraction of low- K media composed of silts and clays, where diffusion tends to dominate over advection, is often substantial at 20 to 80 percent. Accurate modeling of advection and dispersion in such composite media is challenging because (1) the heterogeneity must be highly resolved in three dimensions, often entailing 10^5 to 10^6 nodes or more, and (2) even small errors in the numerical solution can result in significant, erroneous distribution of contaminant mass among the high- and low- K materials (see Chapter 2 and *LaBolle et al.* [1996a] and [1996b]).

The random walk particle method (RWPM) is attractive for simulating transport in highly resolved heterogeneous media because of its computational efficiency and lack of numerical dispersion [Prickett *et al.*, 1981; Uffink, 1985; Ahlstrom *et al.*, 1985; Kinzelbach, 1988; Tompson *et al.*, 1987; LaBolle *et al.*, 1996a]. Standard diffusion theory underlying the RWPM, however, relies on the assumption that material properties vary smoothly in space. This paper is motivated by the desire to eventually develop and apply a RWPM to simulate local-scale transport in composite media. To accomplish this in a mathematically rigorous way, one must first develop diffusion theory for local-scale, spatially-averaged subsurface diffusion processes in composite media.

Herein we develop new diffusion theory for problems of subsurface transport in composite media described by local-scale, spatially-averaged advection-dispersion equations (ADEs) and demonstrate relevance of the theory to analyses published previously in the water-resources literature. In the spirit of *Kolmogorov* [1931], this paper derives ADEs from principles of probability to yield (1) necessary conditions for convergence of diffusion processes in composite porous media to ADEs with discontinuous coefficients and (2) probabilistic definitions of velocity and dispersion tensor that are consistent with the mass balance principles referred to in the physics literature as detailed balance. We finish with an evaluation of several RWPM's that have appeared in the water-resources literature.

3.3 Background and Problem Description

Rigorous treatment of transport in porous media must begin with diffusion theory applied at the pore scale. In flowing pore water, diffusion theory predicts transport according to advection-diffusion equations. Fundamentals of this theory were first introduced by *Ein-*

stein [1905] in his classic paper on molecular diffusion in liquids. Therein, *Einstein* mathematically defined a diffusion process through probabilistic assumptions regarding the apparent stochastic motion of Brownian particles and showed that the densities of such processes obey diffusion equations for the time evolution of concentration. While this work laid the foundations of diffusion theory, the mathematics of diffusion processes have since been improved and formalized in probability theory, the theory of stochastic differential equations and the theory of stochastic processes. Diffusion theory has seen diverse hydrogeological applications and has played a key role in developing theories of water flow [*Scheidegger*, 1974; *Bhattacharya et al.*, 1976], theories for effective-medium properties and macroscopic transport in heterogeneous media [*Matheron and de Marsily*, 1980; *Dagan*, 1984; *Van Den Broeck*, 1990; *Brenner*, 1991; *Bhattacharya and Gupta*, 1990] and RWPM's for numerical simulation [*Prickett et al.*, 1981; *Uffink*, 1985; *Ahlstrom et al.*, 1985; *Kinzelbach*, 1988; *Tompson et al.*, 1987; *LaBolle et al.*, 1996].

3.3.1 Governing Equations

The process of local-scale, spatial averaging of pore-scale advection-diffusion equations commonly gives rise to ADEs of the form [*Scheidegger*, 1974; *Bear*, 1972; *Koch and Brady*, 1985; *Plumb and Whitaker*, 1990; *Quintard and Whitaker*, 1993]

$$\frac{\partial}{\partial t} [\Theta(\mathbf{x})c(\mathbf{x}, t)] + \frac{\partial}{\partial x_i} [\Theta(\mathbf{x})v_i(\mathbf{x}, t)c(\mathbf{x}, t)] - \frac{\partial}{\partial x_i} \left[\Theta(\mathbf{x})D_{ij}(\mathbf{x}, t) \frac{\partial c(\mathbf{x}, t)}{\partial x_j} \right] = 0 \quad (3.1)$$

where $c(\mathbf{x}, t)$ is aqueous concentration [ML^{-3}], $\Theta(\mathbf{x})$ is effective porosity, $\mathbf{v}(\mathbf{x}, t)$ is average groundwater-velocity vector [LT^{-1}], and $\mathbf{D}(\mathbf{x}, t)$ is a hydrodynamic dispersion tensor [L^2T^{-1}]. When there is free flow of mass across material interfaces in composite media (Figure 3.1), continuity requires

$$\frac{\partial}{\partial t}(\Theta c_1) = -\frac{\partial}{\partial x_i}(\Theta v_{1,i} c_1) + \frac{\partial}{\partial x_i} \left(\Theta D_{1,i} \frac{\partial c_1}{\partial x_j} \right) \quad \text{in } \Omega_1 \quad (3.2a)$$



Figure 3.1: Porous media system composed of subdomains Ω_1 and Ω_2 with contrasting material properties that give rise to discontinuous characteristic transport coefficients at the interface Γ .

$$\frac{\partial}{\partial t}(\Theta c_2) = -\frac{\partial}{\partial x_i}(\Theta v_{2,i} c_2) + \frac{\partial}{\partial x_i} \left(\Theta D_{2,i} \frac{\partial c_2}{\partial x_j} \right) \quad \text{in } \Omega_2 \quad (3.2b)$$

$$c_1 = c_2 \quad \text{on } \Gamma \quad (3.2c)$$

$$\Theta_1 n_{1,i} \left(v_{1,i} c_1 - \Theta D_{1,i} \frac{\partial c_1}{\partial x_j} \right) \Big|_1 = \Theta_2 n_{2,i} \left(v_{2,i} c_2 - \Theta D_{2,i} \frac{\partial c_2}{\partial x_j} \right) \Big|_2 \quad (3.2d)$$

where subscripts 1 and 2 represent smoothly-varying quantities or fields in Ω_1 and Ω_2 , respectively, \mathbf{n}_i is a unit outward normal in Ω_i to the interface denoted by Γ , and $|_i$ means the approach to Γ in Ω_i . Similar equations arise in the description of thin films optics, the electrical and thermal properties of composite materials, and numerous other applications. Such problems have received considerable attention in the literature, particularly diffusive transport between flowing and stagnant water in rock [*Neretnieks*, 1980; *Bibby*, 1981; *Grisak and Pickens*, 1981; *Neretnieks et al.*, 1982; *Mutch et al.*, 1993], soil particles [*van Genuchten and Wierenga*, 1976; *Koch and Brady*, 1985; *Quintard and Whi-*

taker, 1993] and low-permeability granular materials [Gillham et al., 1984; Sudicky et al., 1985; Wilson et al., 1993; Berglund and Cvetkovic, 1995].

3.3.2 Diffusion Processes and Kolmogorov's Equations

As with advection and diffusion at the pore scale, one can also develop diffusion processes that correspond to local-scale, spatially-averaged transport equations in the form of (3.1). Diffusion processes are Markov processes with continuous sample paths. In the context of subsurface transport, it is conceptually appealing to consider a realization of a diffusion process $\mathbf{X}(t)$ as a continuous function of time describing the “average” trajectory of a solute molecule (or particle) in three-dimensional Euclidean space. Standard diffusion theory relates the dynamics of a diffusion process to *Kolmogorov's* equations [Kolmogorov, 1931], diffusion equations which describe its probabilistic evolution in time.

The Markov property, can be expressed in terms of conditional probabilities as [Jazwinski, 1970]

$$p(\mathbf{x}_n, t_n | \mathbf{x}_{n-1}, t_{n-1}, \dots, \mathbf{x}_0, t_0) = p(\mathbf{x}_n, t_n | \mathbf{x}_{n-1}, t_{n-1}) \quad (3.3a)$$

$$\int_{\mathbf{x}_n \in \Omega} p(\xi, t_n | \mathbf{x}_{n-1}, t_{n-1}) d\xi = \mathbb{P}[\mathbf{X}(t_n) \in \Omega | \mathbf{X}(t_{n-1}) = \mathbf{x}_{n-1}] \quad (3.3b)$$

where \mathbf{x}_n , \mathbf{x}_{n-1} and \mathbf{x}_0 are values of \mathbf{X} at discrete times $t_n \geq t_{n-1} \geq t_0$ and the conditional (or transition) probability density function, $p(\mathbf{x}_n, t_n | \mathbf{x}_{n-1}, t_{n-1})$ is positive with integral one. The Markov process \mathbf{X} is a diffusion process if its transition-probability density satisfies [Arnold, 1974]

$$\lim_{\Delta t \rightarrow 0} \frac{1}{\Delta t} \int (z_i - x_i) p(\mathbf{z}, t + \Delta t | \mathbf{x}, t) d\mathbf{z} = A_i(\mathbf{x}, t) \quad (3.4a)$$

$$\lim_{\Delta t \rightarrow 0} \frac{1}{2\Delta t} \int (z_i - x_i)(z_j - x_j) p(\mathbf{z}, t + \Delta t | \mathbf{x}, t) d\mathbf{z} = D_{ij}(\mathbf{x}, t) \quad (3.4b)$$

$$\lim_{\Delta t \rightarrow 0} \frac{1}{\Delta t} \int_{|\mathbf{z} - \mathbf{x}| \geq \varepsilon} p(\mathbf{z}, t + \Delta t | \mathbf{x}, t) d\mathbf{z} = 0, \forall \varepsilon > 0 \quad (3.4c)$$

where \mathbf{z} and \mathbf{x} are values of \mathbf{X} , \mathbf{A} [LT^{-1}] is a drift vector and \mathbf{D} [L^2T^{-1}] is a diffusion or dispersion tensor. Condition (3.4c) ensures that the process \mathbf{X} has continuous sample paths.

Evolution of the probability density $p(\mathbf{x}, t)$ of a diffusion processes satisfying (3.4a) - (3.4c) is given by a diffusion equation referred to as Kolmogorov's forward (or the Fokker-Planck) equation (for a derivation, see p 126 - 129 of *Jazwinski* [1970])

$$\frac{\partial p(\mathbf{x}, t)}{\partial t} + \frac{\partial}{\partial x_i} [A_i(\mathbf{x}, t) p(\mathbf{x}, t)] - \frac{\partial^2}{\partial x_i \partial x_j} [D_{ij}(\mathbf{x}, t) p(\mathbf{x}, t)] = 0 \quad (3.5)$$

with initial condition $p(\mathbf{x}, t_0)$, $t \geq t_0$. In applications of diffusion theory to subsurface transport, equation (3.1) has normally been treated as a special case of Kolmogorov's forward equation (3.5) with $p(\mathbf{x}, t) = \Theta(\mathbf{x})c(\mathbf{x}, t)$ [*Tompson et al.*, 1987; *Bhattacharya and Gupta*, 1990]. Using this relationship in equation (3.5), one finds that equivalence between (3.5) and (3.1) is obtained by specifying the drift as [*Tompson et al.*, 1987]

$$A_i(\mathbf{x}, t) = v_i(\mathbf{x}, t) + \Theta^{-1}(\mathbf{x}) \frac{\partial}{\partial x_j} [\Theta(\mathbf{x}) D_{ij}(\mathbf{x}, t)] \quad (3.6)$$

As the need for gradient terms in equation (3.6) suggests, standard theory [*Einstein*, 1956; *Kolmogorov*, 1950; *Feller*, 1968; *Feller*, 1971; *Itô*, 1961] only applies to ADEs when coefficients, porosity Θ and dispersion tensor \mathbf{D} , are smooth functions of space. This theory cannot generally address diffusion processes in composite porous media in which abrupt transitions between materials with contrasting hydraulic and transport properties lead to discontinuous characteristic coefficients. In some cases, limitations of

standard theory have been discounted or have gone unnoticed. This has led to published results and the proliferation of numerical models with unintended, unphysical meaning (see *LaBolle et al.*, 1996a). Clearly, development of a rigorous theory that applies to local-scale, spatially-averaged equations of transport in composite porous media is important to forecasting long-term transport phenomena. In the following section, we develop (1) more general results for subsurface transport described by ADEs and (2) conditions necessary to ensure conservation of mass and convergence of diffusion processes to these equations in the presence of material interfaces (discontinuous coefficients).

3.4. Diffusion Processes and Advection-Dispersion Equations

Here we derive ADEs from principles of probability. Similar derivations for concentration described by Kolmogorov's forward equation are given in *Einstein* [1905; 1956] (for constant coefficients) and in various texts on stochastic processes (e.g., p. 48-50 of *Gardiner* [1990] and p. 126-129 of *Jazwinski* [1970]) for spatially varying coefficients. However, these results do not generally apply to subsurface transport described by ADEs. To generalize theory for transport in composite porous media, we use the mathematical abstraction of a "weak" form of ADEs. This new form of the governing equations can be found by forming the integral of (3.1) against a smooth test function $f(\mathbf{x},t)$:

$$\int_0^t \int f \left[\frac{\partial(\Theta c)}{\partial s} - \frac{\partial}{\partial x_i} \left(\Theta D_{ij} \frac{\partial c}{\partial x_j} \right) + \frac{\partial}{\partial x_i} (\Theta v_i c) \right] d\mathbf{x} ds = 0 \quad (3.7)$$

and integrating by parts to yield

$$\int f c d\mu(\mathbf{x}) \Big|_0^t - \int_0^t \int \frac{\partial f}{\partial s} c d\mu(\mathbf{x}) ds + \int_0^t \int \frac{\partial f}{\partial x_i} \left(D_{ij} \frac{\partial c}{\partial x_j} - v_i c \right) d\mu(\mathbf{x}) ds = 0 \quad (3.8)$$

where the quantity $d\mu(\mathbf{x})$ is referred to as a measure and $d\mu(\mathbf{x}) = \Theta d\mathbf{x}$. This measure arises naturally in the formulation of a probabilistic description of transport in a phase

that occupies a fraction Θ of the entire domain. Distributions c satisfying (3.8) for smooth and bounded f are said to converge weakly to (3.1). Derivation of (3.8) will relate the physical quantities \mathbf{v} , \mathbf{D} and Θ to concepts from probability, i.e., transition-probability densities of diffusion processes that correspond to this new governing equation.

3.4.1. Transition-Probability Densities of Diffusion Processes Corresponding to ADEs

For derivation of (3.8), we begin with the time derivative of the probability density $p_\epsilon(\mathbf{x}, t) d\mu(\mathbf{x})$ integrated in space and time against the test function $f(\mathbf{x}, t)$:

$$\begin{aligned} & \epsilon^2 \int_0^t \int \frac{\partial p_\epsilon(\mathbf{x}, s)}{\partial s} f(\mathbf{x}, s) d\mu(\mathbf{x}) ds + o(\epsilon^2) \\ &= \int_0^t \int [p_\epsilon(\mathbf{x}, s + \epsilon^2) - p_\epsilon(\mathbf{x}, s)] f(\mathbf{x}, s) d\mu(\mathbf{x}) ds \end{aligned} \quad (3.9)$$

where $\epsilon^2 = \Delta t$. Integrating the left-hand side by parts yields

$$\begin{aligned} & \epsilon^2 \int_0^t \int \frac{\partial p_\epsilon(\mathbf{x}, s)}{\partial s} f(\mathbf{x}, s) d\mu(\mathbf{x}) ds + o(\epsilon^2) \\ &= \epsilon^2 \int f(\mathbf{x}, s) p_\epsilon(\mathbf{x}, s) d\mu(\mathbf{x}) \Big|_0^t - \epsilon^2 \int_0^t \int \frac{\partial f(\mathbf{x}, s)}{\partial s} p_\epsilon(\mathbf{x}, s) d\mu(\mathbf{x}) ds \end{aligned} \quad (3.10)$$

Substituting this result into (3.9) gives

$$\begin{aligned} & \epsilon^2 \int f(\mathbf{x}, s) p_\epsilon(\mathbf{x}, s) d\mu(\mathbf{x}) \Big|_0^t - \epsilon^2 \int_0^t \int \frac{\partial f(\mathbf{x}, s)}{\partial s} p_\epsilon(\mathbf{x}, s) d\mu(\mathbf{x}) ds \\ & - \int_0^t \int [p_\epsilon(\mathbf{x}, s + \epsilon^2) - p_\epsilon(\mathbf{x}, s)] f(\mathbf{x}, s) d\mu(\mathbf{x}) ds + o(\epsilon^2) = 0 \end{aligned} \quad (3.11)$$

Substituting the relationship

$$p_\epsilon(\mathbf{x}, s + \epsilon^2) = \int p_\epsilon(\mathbf{x}, s + \epsilon^2 | \mathbf{z}, s) p_\epsilon(\mathbf{z}, s) d\mu(\mathbf{z}) \quad (3.12)$$

into the last term in (3.11) yields

$$\begin{aligned}
& \int \left[p_\epsilon(\mathbf{x}, s + \epsilon^2) - p_\epsilon(\mathbf{x}, s) \right] f(\mathbf{x}, s) d\mu(\mathbf{x}) \\
&= \int \left[\int p_\epsilon(\mathbf{x}, s + \epsilon^2 | \mathbf{z}, s) p_\epsilon(\mathbf{z}, s) d\mu(\mathbf{z}) - p_\epsilon(\mathbf{x}, s) \right] f(\mathbf{x}, s) d\mu(\mathbf{x}) \\
&= \int \int p_\epsilon(\mathbf{x}, s + \epsilon^2 | \mathbf{z}, s) p_\epsilon(\mathbf{z}, s) f(\mathbf{x}, s) d\mu(\mathbf{z}) d\mu(\mathbf{x}) - \int p_\epsilon(\mathbf{x}, s) f(\mathbf{x}, s) d\mu(\mathbf{x}) \\
&= \int \int p_\epsilon(\mathbf{z}, s + \epsilon^2 | \mathbf{x}, s) p_\epsilon(\mathbf{x}, s) f(\mathbf{z}, s) d\mu(\mathbf{z}) d\mu(\mathbf{x}) - \int p_\epsilon(\mathbf{x}, s) f(\mathbf{x}, s) d\mu(\mathbf{x})
\end{aligned} \tag{3.13}$$

Inserting the relationship

$$\int p_\epsilon(\mathbf{z}, s + \epsilon^2 | \mathbf{x}, s) d\mu(\mathbf{z}) = 1 \tag{3.14}$$

into the last integral in the right-hand-side of (3.13) gives

$$\begin{aligned}
& \int \left[p_\epsilon(\mathbf{x}, s + \epsilon^2) - p_\epsilon(\mathbf{x}, s) \right] f(\mathbf{x}, s) d\mu(\mathbf{x}) \\
&= \int \int p_\epsilon(\mathbf{z}, s + \epsilon^2 | \mathbf{x}, s) p_\epsilon(\mathbf{x}, s) f(\mathbf{z}, s) d\mu(\mathbf{z}) d\mu(\mathbf{x}) \\
&\quad - \int \left[\int p_\epsilon(\mathbf{z}, s + \epsilon^2 | \mathbf{x}, s) d\mu(\mathbf{z}) \right] p_\epsilon(\mathbf{x}, s) f(\mathbf{x}, s) d\mu(\mathbf{x}) \\
&= \int \int p_\epsilon(\mathbf{z}, s + \epsilon^2 | \mathbf{x}, s) p_\epsilon(\mathbf{x}, s) f(\mathbf{z}, s) d\mu(\mathbf{z}) d\mu(\mathbf{x}) \\
&\quad - \int \int p_\epsilon(\mathbf{z}, s + \epsilon^2 | \mathbf{x}, s) p_\epsilon(\mathbf{x}, s) f(\mathbf{x}, s) d\mu(\mathbf{z}) d\mu(\mathbf{x}) \\
&= \int \int p_\epsilon(\mathbf{z}, s + \epsilon^2 | \mathbf{x}, s) p_\epsilon(\mathbf{x}, s) [f(\mathbf{z}, s) - f(\mathbf{x}, s)] d\mu(\mathbf{z}) d\mu(\mathbf{x})
\end{aligned} \tag{3.15}$$

Substituting (3.15) into (3.12) yields

$$\begin{aligned}
& \epsilon^2 \int f(\mathbf{x}, s) p_\epsilon(\mathbf{x}, s) d\mu(\mathbf{x}) \Big|_0^t - \epsilon^2 \int_0^t \int \frac{\partial f(\mathbf{x}, s)}{\partial s} p_\epsilon(\mathbf{x}, s) d\mu(\mathbf{x}) ds \\
&\quad - \int_0^t \int \int [f(\mathbf{z}, s) - f(\mathbf{x}, s)] p_\epsilon(\mathbf{z}, s + \epsilon^2 | \mathbf{x}, s) d\mu(\mathbf{z}) p_\epsilon(\mathbf{x}, s) d\mu(\mathbf{x}) ds + o(\epsilon^2) = 0
\end{aligned} \tag{3.16}$$

For the last integral in (3.16) we have

$$\begin{aligned}
& \int \int [f(\mathbf{z}, s) - f(\mathbf{x}, s)] p_\epsilon(\mathbf{z}, s + \epsilon^2 | \mathbf{x}, s) p_\epsilon(\mathbf{x}, s) d\mu(\mathbf{z}) d\mu(\mathbf{x}) \\
&= \int \int [f(\mathbf{x}, s) - f(\mathbf{z}, s)] p_\epsilon(\mathbf{x}, s + \epsilon^2 | \mathbf{z}, s) p_\epsilon(\mathbf{z}, s) d\mu(\mathbf{z}) d\mu(\mathbf{x}) \\
&= - \int \int [f(\mathbf{z}, s) - f(\mathbf{x}, s)] p_\epsilon(\mathbf{x}, s + \epsilon^2 | \mathbf{z}, s) p_\epsilon(\mathbf{z}, s) d\mu(\mathbf{z}) d\mu(\mathbf{x}) \\
&= \frac{1}{2} \int \int [f(\mathbf{z}, s) - f(\mathbf{x}, s)] \left[p_\epsilon(\mathbf{x}, s) p(\mathbf{z}, s + \epsilon^2 | \mathbf{x}, s) - p_\epsilon(\mathbf{z}, s) p_\epsilon(\mathbf{x}, s + \epsilon^2 | \mathbf{z}, s) \right] d\mu(\mathbf{z}) d\mu(\mathbf{x}) \\
&= \frac{1}{2} \int \int \left[p_\epsilon(\mathbf{z}, s + \epsilon^2 | \mathbf{x}, s) - p_\epsilon(\mathbf{x}, s + \epsilon^2 | \mathbf{z}, s) \right] p_\epsilon(\mathbf{z}, s) [f(\mathbf{z}, s) - f(\mathbf{x}, s)] d\mu(\mathbf{z}) d\mu(\mathbf{x}) \\
&\quad - \frac{1}{2} \int \int p_\epsilon(\mathbf{z}, s + \epsilon^2 | \mathbf{x}, s) [f(\mathbf{z}, s) - f(\mathbf{x}, s)] \left[p_\epsilon(\mathbf{z}, s) - p_\epsilon(\mathbf{x}, s) \right] d\mu(\mathbf{z}) d\mu(\mathbf{x}) \\
&= \frac{1}{2} \int \int \left[p_\epsilon(\mathbf{z}, s + \epsilon^2 | \mathbf{x}, s) - p_\epsilon(\mathbf{x}, s + \epsilon^2 | \mathbf{z}, s) \right] p_\epsilon(\mathbf{x}, s) [f(\mathbf{z}, s) - f(\mathbf{x}, s)] d\mu(\mathbf{z}) d\mu(\mathbf{x}) \\
&\quad - \frac{1}{2} \int \int p_\epsilon(\mathbf{z}, s + \epsilon^2 | \mathbf{x}, s) [f(\mathbf{z}, s) - f(\mathbf{x}, s)] \left[p_\epsilon(\mathbf{z}, s) - p_\epsilon(\mathbf{x}, s) \right] d\mu(\mathbf{z}) d\mu(\mathbf{x})
\end{aligned} \tag{3.17}$$

Formally expanding $f(\mathbf{z}, t)$ and $p(\mathbf{z}, t)$ in Taylor series yields

$$f(\mathbf{z}, t) = f(\mathbf{x}, t) + (z_i - x_i) \frac{\partial f(\mathbf{x}, t)}{\partial x_i} + \dots \tag{3.18a}$$

$$p_\epsilon(\mathbf{z}, t) = p_\epsilon(\mathbf{x}, t) + (z_i - x_i) \frac{\partial p_\epsilon(\mathbf{x}, t)}{\partial x_i} + \dots \tag{3.18b}$$

Note that the Taylor series expansion in (3.18b) is usually unjustified when p is not smooth. However, in this case, one does expect p to have one generalized derivative, i.e., p should have one derivative that is continuous with discontinuities at subdomain boundaries. For such functions, one expects (3.18b) to be correct. Substituting (3.18a) and (3.18b) into (3.17) and retaining terms to order $(z_i - x_i)(z_j - x_j)$ gives

$$\begin{aligned}
& \frac{1}{2} \int \int \left[p_\epsilon(\mathbf{z}, s + \epsilon^2 | \mathbf{x}, s) - p_\epsilon(\mathbf{x}, s + \epsilon^2 | \mathbf{z}, s) \right] p_\epsilon(\mathbf{x}, s) (z_i - x_i) \frac{\partial f(\mathbf{x}, s)}{\partial x_i} d\mu(\mathbf{z}) d\mu(\mathbf{x}) \\
&\quad - \frac{1}{2} \int \int p_\epsilon(\mathbf{z}, s + \epsilon^2 | \mathbf{x}, s) (z_i - x_i) \frac{\partial f(\mathbf{x}, s)}{\partial x_i} (z_j - x_j) \frac{\partial p_\epsilon(\mathbf{x}, s)}{\partial x_j} d\mu(\mathbf{z}) d\mu(\mathbf{x}) \\
&= \frac{1}{2} \int \int \left[p_\epsilon(\mathbf{z}, s + \epsilon^2 | \mathbf{x}, s) - p_\epsilon(\mathbf{x}, s + \epsilon^2 | \mathbf{z}, s) \right] p_\epsilon(\mathbf{x}, s) (z_i - x_i) \frac{\partial f(\mathbf{x}, s)}{\partial x_i} d\mu(\mathbf{z}) d\mu(\mathbf{x}) \\
&\quad - \frac{1}{2} \int \int p_\epsilon(\mathbf{z}, s + \epsilon^2 | \mathbf{x}, s) (z_i - x_i) \frac{\partial f(\mathbf{x}, s)}{\partial x_i} (z_j - x_j) \frac{\partial p_\epsilon(\mathbf{x}, s)}{\partial x_j} d\mu(\mathbf{z}) d\mu(\mathbf{x})
\end{aligned} \tag{3.19}$$

Substituting (3.19) into (3.16) yields

$$\begin{aligned}
& \varepsilon^2 \int f(\mathbf{x}, s) p_\varepsilon(\mathbf{x}, s) d\mu(\mathbf{x}) \Big|_0^t - \varepsilon^2 \int_0^t \int \frac{\partial f(\mathbf{x}, s)}{\partial s} p_\varepsilon(\mathbf{x}, s) d\mu(\mathbf{x}) ds \\
& + \frac{1}{2} \int_0^t \int \int (z_i - x_i)(z_j - x_j) p_\varepsilon(\mathbf{z}, s + \varepsilon^2 | \mathbf{x}, s) \frac{\partial f(\mathbf{x}, s)}{\partial x_i} \frac{\partial p_\varepsilon(\mathbf{x}, s)}{\partial x_j} d\mu(\mathbf{z}) d\mu(\mathbf{x}) ds \\
& - \frac{1}{2} \int_0^t \int \int (z_i - x_i) \left[p_\varepsilon(\mathbf{z}, s + \varepsilon^2 | \mathbf{x}, s) - p_\varepsilon(\mathbf{x}, s + \varepsilon^2 | \mathbf{z}, s) \right] p_\varepsilon(\mathbf{x}, s) \frac{\partial f(\mathbf{x}, s)}{\partial x_i} d\mu(\mathbf{z}) d\mu(\mathbf{x}) ds \\
& + o(\varepsilon^2) = 0
\end{aligned} \tag{3.20}$$

Finally, in the limit, equation (3.20) converges to (3.8) provided $p_\varepsilon(\mathbf{x}, t)$ converges to $c(\mathbf{x}, t)$ and \mathbf{v} and \mathbf{D} are chosen as

$$\lim_{\varepsilon \rightarrow 0} \frac{1}{2\varepsilon^2} \int (z_i - x_i) \left[p_\varepsilon(\mathbf{z}, t + \varepsilon^2 | \mathbf{x}, t) - p_\varepsilon(\mathbf{x}, t + \varepsilon^2 | \mathbf{z}, t) \right] d\mu(\mathbf{z}) = v_i(\mathbf{x}, t) \tag{3.21a}$$

$$\lim_{\varepsilon \rightarrow 0} \frac{1}{2\varepsilon^2} \int (z_i - x_i)(z_j - x_j) p_\varepsilon(\mathbf{z}, t + \varepsilon^2 | \mathbf{x}, t) d\mu(\mathbf{z}) = D_{ij}(\mathbf{x}, t) \tag{3.21b}$$

Equations (3.21a) and (3.21b) are the main theoretical results of this paper. They give general probabilistic definitions of physical quantities, velocity and dispersion tensor, in terms of the transition-probability density function of a diffusion process that simulates ADEs. These conditions must be satisfied by the transition-probability density of a diffusion process corresponding to ADEs. As derivation of (3.8) was not restricted to smooth \mathbf{v} , \mathbf{D} or Θ , the new theory does not preclude representing (3.2) by a diffusion process satisfying (3.21a) and (3.21b). For ADEs, these definitions of the physical quantities, velocity and dispersion tensor, are more general than, and can replace, the usual definitions for drift and dispersion given in (3.4a) and (3.4b). Next we consider a probabilistic analogy to mass balance that is referred to in the physics literature as “detailed balance.” We will show that the principle of detailed balance arises naturally from the definition of velocity given in (3.21a).

3.4.2. Detailed Balance

The principle of detailed balance is a probabilistic analogy to mass balance for steady-state solutions to equation (3.1), with time-independent transport coefficients and $\mathbf{v} = \mathbf{0}$, in which the mass (or probability) flux vanishes (for a discussion of detailed balance as it relates to Kolmogorov's equations, see p. 148-155 of *Gardiner* [1990]). For the mass flux to vanish, transitions of mass from one location to another must balance, on the average, with reverse transitions at any instant in time. A statement of detailed balance in terms of conditional probabilities may be written as

$$p(\mathbf{z}, t + \Delta t | \mathbf{x}, t) p_s(\mathbf{x}) = p(\mathbf{x}, t + \Delta t | \mathbf{z}, t) p_s(\mathbf{z}) \quad (3.22)$$

where $p_s(\mathbf{x}) = c(\mathbf{x})$ is a steady-state solution to an ADE with time-independent transport coefficients and $\mathbf{v} = \mathbf{0}$. A process satisfying (3.22) will maintain detailed balance regardless of whether or not coefficients are smooth.

The form of (3.22) closely resembles that of (3.21a). In particular, consider diffusion in a closed system with domain Ω . Here the steady-state solution (invariant distribution) is a uniform concentration distribution (probability density) such that $p_s(\mathbf{x}) = p_s(\mathbf{z})$, for any \mathbf{x} and \mathbf{z} in Ω (this is not necessarily true for Kolmogorov's equations with zero drift). This result in combination with (3.22) leads to the following detailed-balance condition:

$$p(\mathbf{z}, t + \Delta t | \mathbf{x}, t) = p(\mathbf{x}, t + \Delta t | \mathbf{z}, t) \quad (3.23)$$

Subtracting $p(\mathbf{x}, t + \Delta t | \mathbf{z}, t)$ from both sides of (3.23), multiplying by $(2\Delta t)^{-1}(\mathbf{z} - \mathbf{x}) \Theta$, integrating over all \mathbf{z} , and taking the limit as $\Delta t \rightarrow 0$ yields

$$\lim_{\Delta t \rightarrow 0} \frac{1}{2\Delta t} \int (\mathbf{z}_i - \mathbf{x}_i) [p(\mathbf{z}, t + \Delta t | \mathbf{x}, t) - p(\mathbf{x}, t + \Delta t | \mathbf{z}, t)] d\mu(\mathbf{z}) = 0 \quad (3.24)$$

which is (3.21a) for the case of $\mathbf{v} = \mathbf{0}$. For this case, equation (3.21a) is a statement that detailed balance holds microscopically, in the limit of small Δt (as opposed to the definition of drift in (3.4a) which displays no obvious connection with the physics and is less general for ADEs). Equation (3.21a) also shows how lack of detailed balance relates to the advective flux. It is no surprise that the probabilistic definition of velocity embraces the principle of mass balance.

Equation (3.24) is a necessary condition to simulate the dynamic dispersion process described by (3.2) with $\mathbf{v} = \mathbf{0}$. A diffusion process can satisfy (3.24) by satisfying (3.23), i.e., by maintaining a symmetric transition-probability density. However, symmetry is not a necessary condition; standard RWPM's based on numerical integration of stochastic differential equations (e.g., as discussed in *Tompson et al.* [1987] and *Kinzelbach* [1988]) will satisfy (3.24) when coefficients are smooth, but do not necessarily maintain a symmetric transition-probability density. The concept of detailed balance is used in the following examples in which we evaluate several RWPM's presented in the water resources literature.

3.5. Examples: Random-Walk Simulation Methods

Here we apply the results above to evaluate RWPM's for ADEs with discontinuous coefficients [*Uffink*, 1985; *Ackerer*, 1985; *Cordes et al.*, 1991; *Semra et al.*, 1993] about which the literature reports conflicting claims of success. The approximations considered here address the simple problem of random walk simulation of one-dimensional dispersive transport in an infinite domain with instantaneous point source at x_0 , constant Θ , constant coefficients within subdomains Ω_1 ($x < 0$) and Ω_2 ($x > 0$), and discontinuous dis-

persion coefficient at $x = 0$. In this case, the coupled boundary-value problem in (3.2) reduces to:

$$\frac{\partial c_1}{\partial t} = \frac{\partial}{\partial x} \left(D_1 \frac{\partial c_1}{\partial x} \right) \quad \text{in } \Omega_1 \quad (3.25a)$$

$$\frac{\partial c_2}{\partial t} = \frac{\partial}{\partial x} \left(D_2 \frac{\partial c_2}{\partial x} \right) \quad \text{in } \Omega_2 \quad (3.25b)$$

$$c_1 = c_2 \quad \text{on } x = 0 \quad (3.25c)$$

$$\lim_{x \rightarrow 0^-} D_1 \frac{\partial c_1}{\partial x} = \lim_{x \rightarrow 0^+} D_2 \frac{\partial c_2}{\partial x} \quad (3.25d)$$

$$c_1(-\infty, t) = c_2(+\infty, t) = 0 \quad (3.25e)$$

$$c_1(x, 0) = \delta(x - x_0) \quad \text{for } x_0 \in \Omega_1 \quad (3.25f)$$

$$c_2(x, 0) = \delta(x - x_0) \quad \text{for } x_0 \in \Omega_2 \quad (3.25g)$$

In applications of the RWPM's to be presented, Markov-chains will be constructed within subdomains by discrete-time Euler approximations to stochastic differential equations as

$$\Delta X(t) = B(x) \Delta W(t) \quad (3.26)$$

where $B^2 = 2D$ and $W [T^{1/2}]$ is a Wiener process (Brownian motion). Furthermore, the Wiener process will be "discretized" and simulated by a uniformly distributed random variable U with mean zero and variance Δt . Individual approximation methods discussed below differ by their construction of Markov chains at the boundary between subdomains.

3.5.1. Methods

The method of *Uffink* [1985] constructs transition-probability densities by superposition of uniform densities according to an analytical solution to (3.25) (see *LaBolle et al.*, 1996a). Particles that may cross the interface in the following time step use this modified transition-probability density.

The method of *Ackerer* [1985] splits the time step of a random walker into two smaller time steps for all particles that would cross the interface over a span Δt . The first step occurs over a time interval Δt_1 that moves the particle to the interface. The second step occurs over a time interval $\Delta t_2 = \Delta t - \Delta t_1$, starts from the interface, and is performed such that there is a 50% probability of entering either Ω_1 or Ω_2 with uniform transition-probability density on the intervals $(-\sqrt{6D_1\Delta t_2}, 0)$ and $(0, \sqrt{6D_2\Delta t_2})$, respectively.

Cordes et al. [1991] conclude that the methods of *Uffink* [1985] and *Ackerer* [1985] both fail, and present another alternative. They reason that for a constant concentration in the vicinity of the interface, the same number of particles must cross the interface from either side in a given amount of time. They propose, based on the difference in mean-square displacements in Ω_1 and Ω_2 , fully reflecting a fraction of particles $(\sqrt{D_1} - \sqrt{D_2})/\sqrt{D_1}$ crossing from the region of high to low dispersion. For each particle that crosses the interface from the region of high to low dispersion, this operation can be performed by drawing a random number from a uniform distribution over the interval from 0 to 1; when this number is less than $(\sqrt{D_1} - \sqrt{D_2})/\sqrt{D_1}$, the particle is reflected about the interface with no loss of momentum.

More recently, *Semra et al.* [1993] conclude that the methods of *Uffink* [1985], *Ackerer* [1985], and *Cordes et al.* [1991] all fail to conserve mass; they present a third

alternative. As with *Ackerer's* method, they split the time step. Once at the interface, however, the transition-probability density is specified by a uniform distribution on the interval $(-\sqrt{6D_1\Delta t_2}, \sqrt{6D_2\Delta t_2})$.

3.5.2. Comparison with Theory

To test the four RWPM's discussed above, we (1) examine their ability to maintain the invariant distribution (i.e., uniform number density) in a closed system with discontinuous dispersion coefficient, (2) compare simulation results with an analytical solution to equations (3.25a) - (3.25g), and (3) qualitatively evaluate the transition-probability densities for symmetry. The theory presented above suggests that those approximations that maintain a symmetric transition-probability density should be successful and correctly pass tests (1) and (2).

3.5.2.1 Invariant distribution

Consider a closed one-dimensional constant-concentration system with reflecting boundaries on both ends and a material interface located in the center such that the two equal-volume portions of the domain, Ω_1 and Ω_2 , are delineated by a discontinuity in dispersion coefficients (see *Semra et al.* [1993] and *LaBolle et al.* [1996a]). When transport is purely dispersive, a correct approximation will maintain steady-state uniform particle number density, i.e., $N_1/N_2 \approx 1$, where N_1 and N_2 are the numbers of particles at locations $x < 0$ and $x > 0$, respectively. Figure 3.2 shows results from tests of the four methods for a one-dimensional system with reflecting boundaries at $x = -49$ and $x = 49$, $\Delta t = 0.005$, 588 particles, $D_1 = 5.0$ ($x < 0$,) and D_2 ($x > 0$) prescribed such that the ratio, D_1/D_2 , ranges from 2.5 to 20.0. The methods of *Ackerer* [1985] and *Cordes et al.* [1991]

do not maintain uniform number density. The methods of *Uffink* [1985] and *Semra et al.* [1993] correctly maintain uniform number density.

3.5.2.2 Correspondence with an analytical solution

Figure 3.3 compares results for 100,000 realizations from a point source initial condition $x_0 = -5.5$ with an analytical solution to (3.25a) – (3.25g) at time $t = 6.0$ [see *LaBolle et al.*, 1996a] for parameter values $D_1 = 5.0$, $D_2 = 0.25$, and $\Delta t = 0.005$. Concentrations are approximated at discrete spatial locations by the normalized number of particles contained in a unit length along the x -axis. Results from the methods of *Ackerer* [1985] and *Cordes et al.* [1991] do not match the analytical solution. The methods of *Uffink* [1985] and *Semra et al.* [1993] correctly simulate the problem.

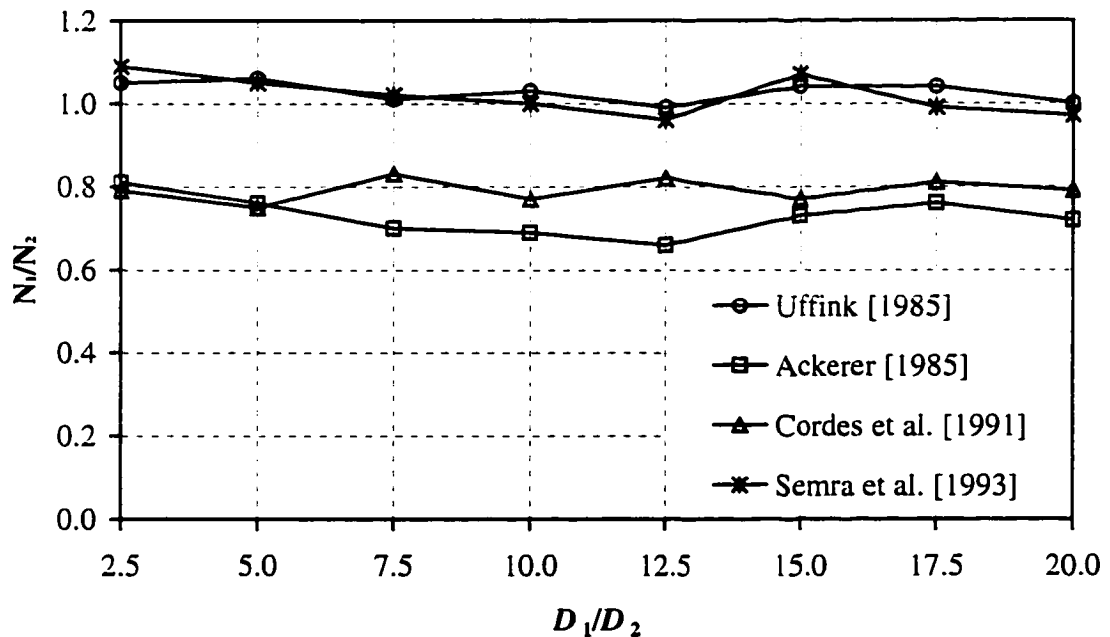


Figure 3.2: Ratios N_1/N_2 simulated by alternative Markov-chain approximations for various values of D_1/D_2 .

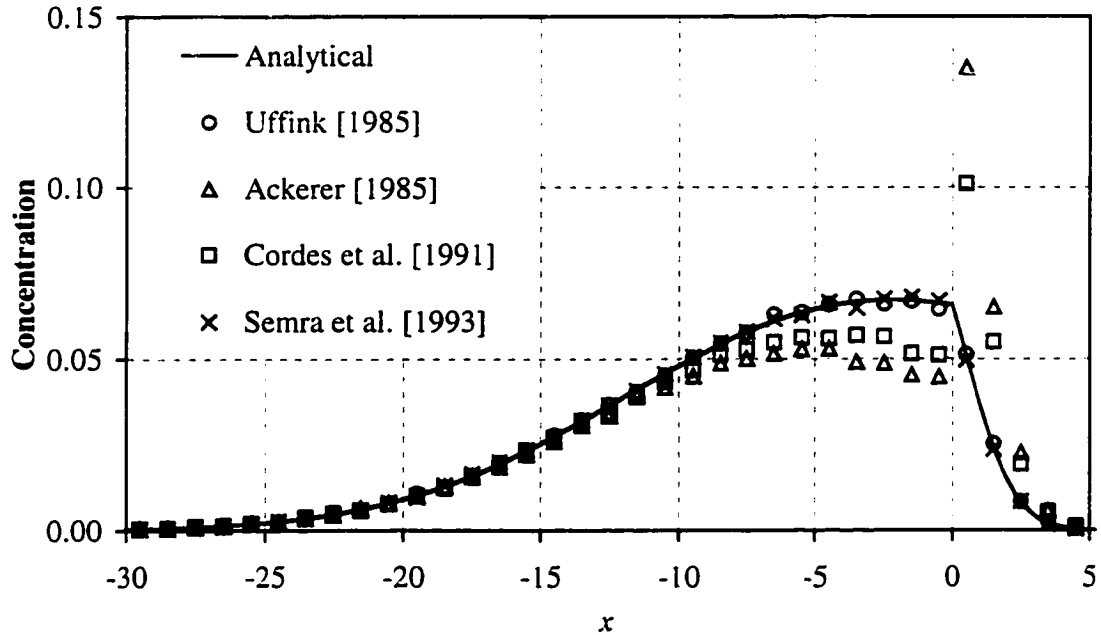


Figure 3.3: Comparison of concentrations from simulations by the alternative Markov-chain approximations with the analytical solution to equations (3.25a) - (3.25g) at $t = 6.0$ for $x_0 = -5.5$, $D_1 = 5.0$, and $D_2 = 0.25$. Methods of *Semra et al.* [1993] and *Uffink* [1985] produce results virtually identical to the analytical solution.

3.5.2.3 Symmetric transition-probability density

For an infinite system with an interface located at $x = 0$, $D_1 = 5.0$, $D_2 = 1.0$, and $\Delta t = 0.005$, the graphs in Figure 3.4 each plot 40,000 particle locations after a single time step versus initial location uniformly distributed over the interval from $[-1/2, 1/2]$. Particle number density illustrates the transition-probability density in the region near the interface at $x = 0$. The methods of *Uffink* [1985] and *Semra et al.* [1993] show symmetric transition-probability densities; those of *Ackerer* [1985] and *Cordes et al.* [1991] do not.

3.5.3. Discussion

The RWPM's for ADEs given by *Uffink* [1985] and *Semra et al.* [1993] are successful and correspond with theory by maintaining symmetric transition-probability density.

However, since one can conceive of a process that satisfies (3.24), in the limit, without symmetric transition-probability density, these results fail to explain how the methods of *Ackerer* [1985] and *Cordes et al.* [1991] violate theory. Although a detailed analysis of these methods is beyond the scope of this paper, consider that the method of *Ackerer* specifies a constant probability of reflection, independent of the contrast in dispersion coefficients between subdomains. Taking the limit as $D_2 \rightarrow 0$, the interface should approach a fully reflecting boundary, yet the method of *Ackerer* [1985] incorrectly does nothing to impede diffusion of particles across the interface from Ω_1 to Ω_2 .

The method of *Cordes et al.* [1991] falls short for more subtle reasons. Brownian motion is a rapidly fluctuating process. A particle undergoing Brownian motion at an interface will, in theory, attempt to cross that interface an infinite number of times in any finite time interval. Therefore, provided the probability of reflection is less than one and the time step approaches zero, i.e., the simulated process approaches a theoretical

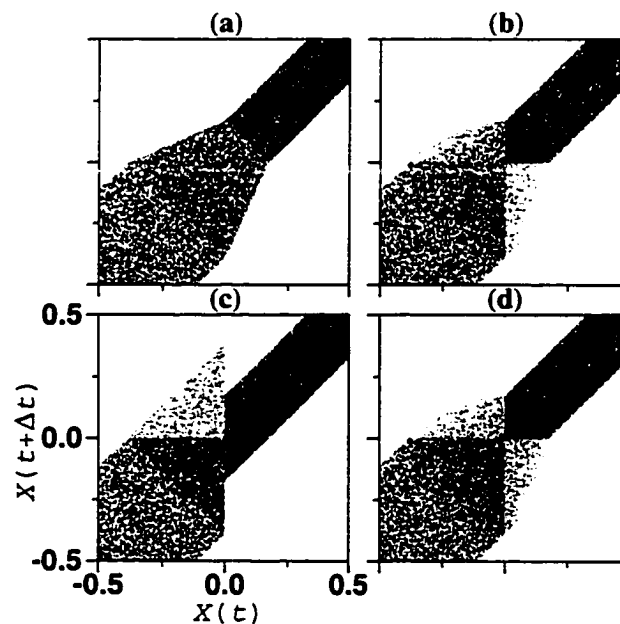


Figure 3.4: Transition-probability density illustrated by evolving Markov chains for 40,000 particles initially uniformly distributed over the interval from $[-1/2, 1/2]$ over a

single time step using the approximations of (a) *Uffink* [1985] (b) *Ackerer* [1985] (c) *Cordes et al.* [1991], and (d) *Semra et al.* [1993]. Asymmetry in the method of *Ackerer* results in a contrast between particle densities in the second and fourth quadrants.

Brownian motion, application of the method developed by *Cordes et al.* [1991] will have no effect. This suggests that a successful one-sided “reflection technique,” such as that proposed by *Cordes et al.* [1991], would specify a probability of reflection that depends not only on the contrast in dispersion coefficients, but also on time-step size.

Success with the method of *Uffink* [1985] confirms the obvious: transition-probability densities of Markov-chain approximations to ADEs may be constructed from an analytical solution to the governing initial boundary-value problem. However, in contrast to the simple one-dimensional problem considered above, analytical solutions are normally not at hand for more complex multidimensional problems. Success with the method of *Semra et al.* [1993] demonstrates that conditions (3.21a) and (3.21b) may be satisfied by other, more simple, techniques; knowledge of an analytical solution is not generally needed to construct successful approximation methods.

The RWPM’s presented above apply to one-dimensional diffusion problems with constant coefficients in subdomains and discontinuous coefficients at material interfaces. Alternative methods must be developed for more general multidimensional problems that may include advection, smoothly varying coefficients in subdomains and discontinuous coefficients at material interfaces. Nevertheless, the transition-probability density of a successful Markov-chain approximation must satisfy conditions (3.21a) and (3.21b).

3.6. Summary and Conclusions

Diffusion theory has played an important role in developing theory for subsurface transport. Standard diffusion theory only applies to subsurface transport described by ADEs

when coefficients, velocity, porosity, and dispersion tensor, are smooth functions of space. Subsurface porous-material properties, however, commonly exhibit abrupt transitions between material types, such as where sand is in contact with clay. Abrupt transitions between materials with contrasting hydraulic and transport properties may lead to discontinuous coefficients in macroscopic equations of transport. Although commonly called on to model transport in such cases, standard diffusion theory does not apply.

In this paper we have developed new diffusion theory for transport in porous media. Development of the theory relied on a weak form of ADEs, a mathematical abstraction that facilitates development of diffusion processes that apply when coefficients, velocity, porosity, and dispersion tensor, are discontinuous. Derivation of this equation from principles of probability related these coefficients to the transition-probability density of a diffusion process that simulates ADEs. A diffusion process that simulates subsurface transport described by ADEs must satisfy these relationships.

The new theory adds to our knowledge of diffusion processes corresponding to local-scale, spatially-averaged equations of transport in porous media and is important to forecasting long-term transport phenomena. Conditions that arise from diffusion theory for ADEs are consistent with probabilistic mass balance principles, referred to in the physics literature as detailed balance. Theory and examples demonstrated that a diffusion process with symmetric transition-probability density satisfies the necessary conditions to simulate ADEs with discontinuous coefficients. Evaluation of several random-walk methods for transport in one-dimensional composite porous media showed which methods are successful and correspond with theory. In a subsequent paper, we will show how one can generalize stochastic differential equations to the case of discontinuous coeffi-

cients to yield simple Markov-chain approximations for subsurface transport that satisfy the necessary conditions presented here.

3.7. References

- Ackerer, Ph., Propagation d'un fluide en aquifère poreux saturé en eau. Prise en compte et localisation des hétérogénéités par outils théoriques et expérimentaux, Ph.D. thesis, Université Louis Pasteur de Strasbourg, France, 1985.
- Ahlstrom, S.W., H.P. Foote, R.C. Arnett, C.R. Cole and R.J. Serne, Multi-component mass transport model: theory and numerical implementation. Rep. BNWL-2127, Battelle Pacific Northwest Lab., Richland, Washington, 1977.
- Arnold, L., *Stochastic Differential Equations*, Krieger Publishing Company, Florida, 1974.
- Bear, J., *Dynamics of Fluids in Porous Media*, Elsevier, New York, 1972.
- Berglund, S. and V. Cvetkovic, Pump-and-Treat Remediation of Heterogeneous Aquifers: Effects of Rate-Limited Mass Transfer, *Groundwater*, 33(4), 1995.
- Bhattacharya, R. and V.K. Gupta, Application of central limit theorems to solute dispersion in saturated porous media: From Kinetic to Field Scales, in *Dynamics of Fluids in Hierarchical Porous Media*, ed. Cushman, J.H., Academic Press, Inc., California, 61-96, 1990.
- Bhattacharya, R. and V.K. Gupta, and G. Sposito, On the stochastic foundations of the theory of water flow through unsaturated soil, *Water Resources Research*, 12(3), 503-512, 1976.
- Bibby, R., Mass transport of solutes in dual porosity media, *Water Resources Research*, 17(4), 1075-1081, 1981.
- Brenner, H, Macrotransport processes: Brownian tracers as stochastic averagers in effective-medium theories of heterogeneous media, *Journal of Statistical Physics*, 62, 5/6, 1095 - 1119, 1991.
- Carle S.F. and G.E. Fogg, Transition probability-based indicator geostatistics, *Mathematical Geology*, V28, N4, 453-476, 1996.
- Carle, S.F., E.M. LaBolle, G.S. Weissmann, D. VanBrocklin, and G.E. Fogg, Geostatistical simulation of hydrofacies architecture: A transition probability/Markov approach, in *SEPM Concepts in Hydrogeology and Environmental Geology No. 1, Hydrogeologic Models of Sedimentary Aquifers*, G.S. Fraser and J.M. Davis (eds), Tulsa Oklahoma, 1998.
- Coats, K. H. and B.D. Smith, Dead-end pores volume and dispersion in porous media, *J. Soc. Pet. Eng.*, 4, 73-84, 1964.
- Cordes, C., H. Daniels, and G. Rouvé, A new very efficient algorithm for particle tracking in layered aquifers, in *Computer Methods in Water Resources II, Vol. 1: Groundwater Modelling and Pressure Flow*, Sari, D.B., C.A. Brebbia, and D. Ouazar (eds), Springer-Verlag, 41-55, 1991.
- Copt, N. and Y. Rubin, A stochastic approach to the characterization of lithofacies from surface seismic and well data, *Water Resources Research*, 31(7), 1673-1686, 1995.

- Dagan, G., Solute transport in heterogeneous porous formations, *Journal of Fluid Mechanics*, 145, 151-177, 1984.
- Einstein, A., Über die von der molekularkinetischen theorie der wärme geforderte bewegung von in ruhenden flüssigkeiten suspendierten teilchen, *Ann. Phys.*, 17, 549-560, 1905.
- Feller, W., *An Introduction to Probability Theory and its Applications*, Vol. 1, John Wiley and Sons, 1968.
- Feller, W., *An Introduction to Probability Theory and its Applications*, Vol. 2, John Wiley and Sons, New York, 1971.
- Gardiner, C.W., *Handbook of Stochastic Methods for Physics Chemistry and the Natural Sciences*, Springer-Verlag, Berlin, 1990.
- Gillham, R.W., E.A. Sudicky, J.A. Cherry and E.O. Frind, An advection diffusion concept for solute transport in heterogeneous unconsolidated geologic deposits, *Water Resources Research*, 20(3), 369-378, 1984.
- Grisak, G.E. and J.F. Pickens, Solute transport through fractured media 1. Effect of matrix diffusion, *Water Resources Research*, 16(4), 719-730, 1980.
- Itô, K. and H.P. McKean, *Diffusion Processes and their Sample Paths*, Springer-Verlag, New York, 1961.
- Jazwinski, A.J., *Stochastic Processes and Filtering Theory*, Academic Press, Inc., New York, 1970.
- Kinzelbach, W., The random walk method in pollutant transport simulation, in *Groundwater Flow and Quality Modelling*, ed. Custidio, E., A. Gurgui, and J.P. Lobo Ferreria, NATO ASI Series C: Math and Phys. Sci. 224: 227-246, Reidel Publishing Company, 1988.
- Koch, D.L. and J.F. Brady, Dispersion in fixed beds, *Journal of Fluid Mechanics*, 154, 399-427, 1985.
- Kolmogorov, A.N., Über die analytischen methoden in der wahrscheinlichkeitsrechnung, *Math. Anal.*, 104, 415-458, 1931.
- Kolmogorov, A.N., *Foundations of the Theory of Probability*, Chelsea Press, New York, 1950.
- LaBolle, E.M., G.E. Fogg, and A.F.B. Tompson, Random-walk simulation of transport in heterogeneous porous media: Local mass-conservation problem and implementation methods, *Water Resources Research*, 32(3), 583-593, 1996a.
- LaBolle, E.M., S.F. Carle, and G.E. Fogg, Effects of Physical Heterogeneity and Diffusion on Aquifer Restoration by Pump-and-Treat, EOS, Transactions, American Geophysical Union, 1996 Fall Meeting, Abstract H21C-11, 77(48), 1996b.
- LaBolle, E.M., J. Quastel, and G.E. Fogg, Diffusion theory for transport in porous media: Transition-probability densities of diffusion processes corresponding to advection-dispersion equations, *Water Resources Research*, 34(7), 1685-1693, 1998.
- Matheron, G., and G. de Marsily, Is transport in porous media always diffusive? A counterexample, *Water Resources Research*, 16(5), 901-917, 1980.
- McKenna S.A. and E.P. Poeter, Field example of data fusion in site characterization, *Water Resources Research*, 31(12), 3229-3240, 1995.
- Mutch, Jr., R.D., J.I. Scott, and D.J. Wilson, Cleanup of fractured rock aquifers: Implications of matrix diffusion, *Environmental Monitoring and Assessment*, 24, 45-70, 1993.

- Neretniek, I., Diffusion in the rock matrix: An important factor in radionuclide retardation, *Journal of Geophysical Research*, 85, B8, 4379-4397, August 10, 1980.
- Neretniek, I., T. Eriksen, and P. Tähtinen, Tracer movement in a single fissure in granitic rock: Some experimental results and their implications, *Water Resources Research*, 18(4), 849-858, 1982.
- Plumb, O.A. and S. Whitaker, Diffusion, adsorption and dispersion in porous media: Small-scale averaging and local-volume averaging, in *Dynamics of Fluids in Hierarchical Porous Media*, ed. Cushman, J.H., Academic Press, Inc., California, 97-176, 1990.
- Prickett, Th.A., Th.G. Naymik and C.G. Longquist, A random walk solute transport model for selected groundwater quality evaluations, Rep. Illinois State Water Survey, Urbana Illinois, 1981.
- Quintard, M. and S. Whitaker, Transport in ordered and disordered porous media: Volume-averaged equations, closure problems, and comparison with experiment, *Chemical Engineering Science*, 48, 14, 2537-2564, 1993.
- Semra, K., Ph. Ackerer, and R. Mosé, Three-dimensional groundwater quality modelling in heterogeneous media, in *Water Pollution II, Modelling, Measuring and Prediction*, Wrobel, L.C. and C.A. Brebbia (eds), Computational Mechanics Publications, Southampton Boston, 3-11, 1993.
- Scheidegger, A. E., *The Physics of Flow through Porous Media*, 3rd ed., University of Toronto Press, New York, 1974.
- Sheibe, T.D. and D.L. Freyberg, Use of sedimentological information for geometric simulation of natural porous media structure, *Water Resources Research*, 31(12), 3259-3270, 1995.
- Sudicky, E.A., R.W. Gilham and E.O. Frind, Experimental investigation of solute transport in stratified porous media 1. The nonreactive case, *Water Resources Research*, 21(7), 1035-1041, 1985.
- Tompson, A.F.B., E.G. Vomoris, and L.W. Gelhar, Numerical simulation of solute transport in randomly heterogeneous porous media: motivation, model development, and application, Report UCID-21281, Lawrence Livermore National Laboratory, 1987.
- Uffink, G.J.M., A random walk method for the simulation of macrodispersion in a stratified aquifer, in *Relation of Groundwater Quality and Quantity*, IAHS Pub No. 146, 103-114, 1985.
- Van Den Broeck, C., Taylor dispersion revisited, *Physica A*, 168, 677-696, 1990.
- Van Kampen, N.G., *Stochastic Processes in Chemistry and Physics*, Elsevier Science Publishers, Amsterdam, The Netherlands, 1992.
- van Genuchten, M. Th. and P.J. Wierenga, Numerical solution for convective dispersion with intra-aggregate diffusion and non-linear adsorption, in *Simulation in Water Resources*, ed. G.C. Vansteenkiste, North-Holland, Amsterdam, 1976.
- Wilson, D.J., R.D. Mutch, Jr., and J.I. Scott, Matrix diffusion in the cleanup of heterogeneous aquifers, *Environmental Monitoring and Assessment*, 26, 49-64, 1993.

Chapter 4

Diffusion Processes in Composite Porous Media and their Numerical Integration by Random Walks: Generalized Stochastic Differential Equations with Discontinuous Coefficients*

4.1 Abstract

Discontinuities in effective subsurface transport properties commonly arise (1) at abrupt contacts between geologic materials (i.e., composite porous media) and (2) in discrete velocity fields of numerical groundwater-flow solutions. However, standard random-walk methods for simulating transport and the theory on which they are based (diffusion theory and the theory of stochastic differential equations (SDEs)) only apply when effective transport properties are sufficiently smooth. Limitations of standard theory have precluded development of random-walk methods (diffusion processes) that obey advection dispersion equations in composite porous media. In this paper we (1) generalize SDEs to the case of discontinuous coefficients (i.e., step functions) and (2) develop random-walk methods to numerically integrate these equations. The new random-walk methods obey advection-dispersion equations, even in composite media. The techniques retain many of

* accepted for publication in *Water Resources Research*, 1999.

the computational advantages of standard random-walk methods, including the ability to efficiently simulate solute-mass distributions and arrival times while suppressing errors such as numerical dispersion. Examples relevant to the simulation of subsurface transport demonstrate the new theory and methods. The results apply to problems found in many scientific disciplines and offer a unique contribution to diffusion theory and the theory of SDEs.

4.2 Introduction

Facilitated by geostatistical methods, detailed characterizations of the subsurface can capture the character of intricate heterogeneities that strongly control transport [Coptý and Rubin, 1995; Sheibe and Freyberg, 1995; McKenna and Poeter 1995; Carle et al., 1998]. Adequately resolving subsurface heterogeneity can yield immense computational grids, commonly with greater than 10^6 nodes (e.g., *Tompson* [1993]), that demand specialized numerical techniques to solve governing transport equations. In many cases, random-walk methods are favored over finite-difference, finite-element, and method of characteristic techniques for large problems of this type (e.g., see *Tompson et al.* [1987]; *Tompson and Gelhar* [1990] and Chapter 2, i.e., *LaBolle et al.* [1996]) because of their ability to efficiently simulate solute-mass distributions and arrival times while suppressing errors such as numerical dispersion [*Prickett et al.*, 1981; *Uffink*, 1985; *Ahlstrom et al.*, 1985; *Kinzelbach*, 1988; *Tompson et al.*, 1987].

Spatial averaging [*Plumb and Whitaker*, 1990] of pore-scale equations for transport by advection –and molecular diffusion in porous media gives rise to advection-dispersion equations (ADEs) commonly used to model subsurface transport:

$$\frac{\partial}{\partial t}(\Theta(\mathbf{x}, t)c(\mathbf{x}, t)) = -\sum_i \frac{\partial}{\partial x_i}(v_i(\mathbf{x}, t)\Theta(\mathbf{x}, t)c(\mathbf{x}, t)) + \sum_{i,j} \frac{\partial}{\partial x_i} \left(\Theta(\mathbf{x}, t)D_{ij}(\mathbf{x}, t) \frac{\partial c(\mathbf{x}, t)}{\partial x_j} \right) \quad (4.1)$$

where c [ML^{-3}] is concentration, \mathbf{v} [LT^{-1}] is a velocity, Θ [L^3L^{-3}] is effective porosity, and \mathbf{D} [L^2T^{-1}] is a real symmetric dispersion tensor. Standard random-walk methods (e.g., *Kinzelbach* [1988] and *Tompson et al.* [1987]) approximate solutions to equation (4.1) by simulating sample (particle) paths corresponding diffusion processes described by stochastic differential equations (SDEs). Here, “diffusion processes” refers to Markov processes with continuous sample paths as mathematical models of real subsurface-transport phenomena. Therefore, in the present context, the term “diffusion process” refers to “advection dispersion process.”

Use of equation (4.1) as a model of transport in heterogeneous porous media poses problems in the context of random-walk simulation methods: Standard methods, and the theory on which they are based (i.e., diffusion theory and the theory of SDEs), only apply when coefficients, porosity and dispersion tensor, are sufficiently smooth functions of space (see Chapters 2 and 3, i.e., *LaBolle et al.* [1996] and [1998]). Discontinuities in effective transport properties, however, commonly arise (1) at abrupt contacts between geologic materials (i.e., composite porous media) and (2) in discrete velocity fields of numerical groundwater-flow solutions. As a result, standard random walk methods (and SDEs) cannot simulate transport in heterogeneous porous media with abrupt contacts between geologic materials.

Both interpolation [*LaBolle et al.*, 1996] and “reflection” [*Uffink*, 1985; *Ackerer*, 1985; *Cordes et al.*, 1991; *Semra et al.*, 1993] techniques have been proposed to address the aforementioned limitations of standard random-walk methods. By spatially interpolating coefficients, one can ensure they remain sufficiently smooth throughout the domain such that standard random-walk (or *Itô-Euler* integration) methods can be applied. Accu-

racy of this approach, however, suffers unless one refines the interpolation (i.e., the region over which coefficients are smoothed) and time step, simultaneously [LaBolle *et al.*, 1996], which commonly leads to undesirable increases in computational effort. Furthermore, refining the interpolation ultimately gives rise to the original problem, discontinuous coefficients.

LaBolle et al. [1998] developed necessary conditions for the convergence of diffusion processes to ADEs in composite porous media and applied the new theory to test four one-dimensional “reflection” techniques [Uffink, 1985; Ackerer, 1985; Cordes *et al.*, 1991; Semra *et al.*, 1993]. The term “reflection” is derived from the usual method of reflecting particles to maintain no-flux boundary conditions in a random walk (see *Tompson et al.* [1987]). These techniques rely on either an analytical solution to the specific problem, or the specialized numerical treatment of particle displacements to maintain mass balance at an interface between regions with *constant*, but different, diffusion coefficients. *LaBolle et al.* [1998] showed that two of these reflection techniques fail to solve the specified problem, while the methods of *Uffink* [1985] and *Semra et al.* [1993] succeed. One can show that these methods relate to an analytical solution to the problem of one-dimensional diffusion at an interface. The method of *Semra et al.* [1993] has been recently extended to three dimensions, but remains limited to *constant* coefficients within subdomains (*Semra* [1994], as referenced in *Ackerer* [1999]). General mathematical representations of multi-dimensional diffusion processes obeying ADEs in composite porous media (i.e., porous media characterized by discontinuous coefficients) have remained undeveloped because of limitations of standard diffusion theory [*LaBolle et al.*, 1998].

In this paper, we generalize SDEs to the case of discontinuous coefficients to develop (1) new mathematical representations of diffusion processes that simulate advection and dispersion in composite porous media and (2) random-walk methods for numerical integration of these equations. The new methods retain many of the computational advantages of standard methods (e.g., *Kinzelbach*, 1988; *Tompson et al.*, 1987). Examples demonstrate application of the new theory and methods to problems of transport in porous media. However, our results apply to problems found in numerous scientific disciplines. Further, since the treatment of diffusion processes with discontinuous coefficients is presently not covered in stochastic theory (e.g., as described in *Arnold* [1992]), our results offer a unique contribution to diffusion theory and the theory of SDEs. Before considering the new approximations, we review standard stochastic methods for simulating diffusion processes.

4.3 Standard Methods for Simulating Diffusion Processes

Standard stochastic methods for simulating subsurface transport (e.g., *Kinzelbach*, 1988; *Tompson* [1987]) may be applied when effective transport properties vary smoothly in space. In this case, diffusions corresponding to (4.1) are commonly represented by an *Itô* SDE [*Itô and McKean*, 1961]:

$$\int_{t_0}^t d\mathbf{X}_i(t') = \int_{t_0}^t A_i(\mathbf{X}, t') dt' + (I) \int_{t_0}^t \sum_j B_{ij}(\mathbf{X}, t') dW_j(t') \quad (4.2a)$$

$$A_i(\mathbf{X}, t) = v_i(\mathbf{X}, t) + \Theta^{-1}(\mathbf{X}, t) \sum_j \frac{\partial}{\partial x_j} [\Theta(\mathbf{X}, t) D_{ij}(\mathbf{X}, t)] \quad (4.2b)$$

$$\mathbf{X}(t_0) = \mathbf{X}_0 \quad (4.2b)$$

where the last integral in (4.2a) is referred to as a stochastic integral, (I) denotes the *Itô* interpretation of this integral (defined below), $\mathbf{X}(t)$ [L] is a sample path in space, $\mathbf{B} \bullet \mathbf{B}^T =$

$2\mathbf{D}$, and $\mathbf{W}(t)$ [$T^{1/2}$] is a Brownian motion process such that $\Delta\mathbf{W} = \mathbf{W}(t) - \mathbf{W}(t_0)$ has mean zero and covariance $\Delta t \delta_{ij}$. Note that \mathbf{B} is generally not unique. The coefficients \mathbf{A} [LT^{-1}] and \mathbf{D} are referred to as drift vector and diffusion tensor, respectively, and are defined as

$$\lim_{\Delta t \rightarrow 0} \frac{1}{\Delta t} \langle X_i(t) - X_i(t_0) \rangle = A_i = v_i + \Theta^{-1} \sum_j \frac{\partial}{\partial x_j} (\Theta D_{ij}) \quad (4.3a)$$

$$\lim_{\Delta t \rightarrow 0} \frac{1}{\Delta t} \langle [X_i(t) - X_i(t_0)][X_j(t) - X_j(t_0)] \rangle = \sum_k B_{ik} B_{jk} = 2D_{ij} \quad (4.3b)$$

where $\langle \bullet \rangle$ denotes the expectation. We will refer to a component of the drift that involves gradient terms, such as the second term in the right-hand-side of (4.3a), as a “gradient drift term.”

In general, to arrive at a unique definition for a stochastic integral, it is necessary to specify how it is to be evaluated (see Chapt. 10 of *Arnold* [1992]). The *Itô* stochastic integral specified in (4.2a) is defined as

$$(I) \int_{t_0}^t \sum_j B_{ij}(\mathbf{X}, t') dW_j(t') = ms\text{-}\lim_{n \rightarrow \infty} \sum_{k=1}^n \sum_j B_{ij}[\mathbf{X}(t_{k-1}), t_{k-1}] [W_j(t_k) - W_j(t_{k-1})] \quad (4.4)$$

where *ms-lim* denotes the limit in the mean square [*Gardiner*, 1990]. The *Itô* definition given in (4.4) evaluates \mathbf{B} at location $\mathbf{X}(t_{k-1})$ rendering \mathbf{B} statistically independent of $d\mathbf{W}$ thus ensuring that the integral in (4.4) has mean zero. One well known alternative to the *Itô* interpretation of the stochastic integral is that of *Stratonovich* [1963] in which \mathbf{B} is evaluated at location $[\mathbf{X}(t_{k-1}) + \mathbf{X}(t_k)]/2$, i.e.,

$$\begin{aligned} (S) \int_{t_0}^t \sum_j B_{ij}(\mathbf{X}, t') dW_j(t') \\ = ms\text{-}\lim_{n \rightarrow \infty} \sum_{k=1}^n \sum_j B_{ij} \left[\frac{\mathbf{X}(t_k) + \mathbf{X}(t_{k-1})}{2}, t_{k-1} \right] [W_j(t_k) - W_j(t_{k-1})] \end{aligned} \quad (4.5)$$

where the (S) denotes the *Stratonovich* interpretation. For convenience, herein we will adopt the following notation:

$$(I) \sum_j B_{ij}(\mathbf{X}, t) dW_j(t) = \sum_j B_{ij}(\mathbf{X}, t) dW_j(t) \quad (4.6a)$$

$$(S) \sum_j B_{ij}(\mathbf{X}, t) dW_j(t) = \sum_j B_{ij}(\mathbf{X} + d\mathbf{Y}, t) dW_j(t) \quad (4.6b)$$

$$d\mathbf{Y}(t) = \frac{1}{2} d\mathbf{X}(t) \quad (4.6c)$$

where we have written stochastic integrals as differentials, leaving all integration implied. We will say that \mathbf{B} is evaluated at location \mathbf{X} and $\mathbf{X} + d\mathbf{Y}$ in the *Itô* and *Stratonovich* integrals of (4.6a) and (4.6b), respectively. For $d\mathbf{X} = \mathbf{B}(\mathbf{X} + d\mathbf{Y}, t) \cdot d\mathbf{W}$ and assuming that \mathbf{B} is sufficiently smooth, expanding the *Stratonovich* equation (4.6b) in a Taylor series shows the relationship between *Itô* and *Stratonovich* integrals is given as

$$\begin{aligned} dX_i &= (S) \sum_j B_{ij}(\mathbf{X}, t) dW_j \\ &= \sum_j B_{ij} \left(\mathbf{X} + \frac{1}{2} d\mathbf{X}, t \right) dW_j \\ &= \sum_j B_{ij}(\mathbf{X}, t) dW_j + \frac{1}{2} \sum_{j,l} \frac{\partial B_{ij}(\mathbf{X}, t)}{\partial x_l} dX_l dW_j \\ &= \sum_j B_{ij}(\mathbf{X}, t) dW_j + \frac{1}{2} \sum_{j,l,k} \frac{\partial B_{ij}(\mathbf{X}, t)}{\partial x_l} B_{lk}(\mathbf{X}, t) dW_k dW_j \\ &= \sum_j B_{ij}(\mathbf{X}, t) dW_j + \frac{1}{2} \sum_{j,l} \frac{\partial B_{ij}(\mathbf{X}, t)}{\partial x_l} B_{ij}(\mathbf{X}, t) dt \\ &= (I) \sum_j B_{ij}(\mathbf{X}, t) dW_j + \frac{1}{2} \sum_{j,l} \frac{\partial B_{ij}(\mathbf{X}, t)}{\partial x_l} B_{ij}(\mathbf{X}, t) dt \end{aligned} \quad (4.7)$$

where we have used $dW_k dW_j = dt \delta_{kj}$. Assuming constant Θ , one can show that the following *Stratonovich* SDE obeys equation (4.1) and is equivalent to the *Itô* SDE (4.2a):

$$\begin{aligned}
d\mathbf{X}_i(t) = & \left[v_i(\mathbf{X}, t) + \frac{1}{2} \sum_{j,l} B_{ij} \frac{\partial}{\partial x_l} B_{ij}(\mathbf{X}, t) \right] dt \\
& + \sum_j B_{ij} \left(\mathbf{X} + \frac{1}{2} d\mathbf{X}, t \right) d\tilde{W}_j(t)
\end{aligned} \tag{4.8}$$

where B_{ij} of the stochastic integral is evaluated at time t and location given by the vector $\mathbf{X} + \frac{1}{2} d\mathbf{X}$. Therefore, evaluating \mathbf{B} at various locations, which differ infinitesimally from the current location, and adding or subtracting necessary gradient drift terms allows one to formulate variety of equations that are mathematically equivalent to (4.2a).

Standard random-walk methods for simulating (4.1) are normally based on *Euler* integration of the *Itô* SDE in (4.2a) (e.g., see *Tompson et al.* [1987]). However, equation (4.2a) only applies when coefficients Θ and \mathbf{D} are sufficiently smooth. Therefore, when either \mathbf{D} or Θ are discontinuous, these standard methods fail [*LaBolle*, 1996]. For example, *Euler* approximations to (4.2a) that either evaluate gradient drift terms by finite differences [*Tompson et al.*, 1987] or neglect gradient drift terms all together [*Prickett et al.*, 1981] cannot simulate (4.1) in composite media. Further, results from these methods cannot be improved by refining the time step of the integration scheme. In summary, standard stochastic theory fails to provide a definition for such equations in composite media in which Θ and \mathbf{D} are discontinuous. We address this problem in the following section.

4.4 Diffusion Processes in Composite Media

The methods developed here stem from the premise that SDEs may be generalized to consider discontinuous coefficients, yielding diffusion processes that obey equation (4.1) for both smooth and discontinuous transport properties. By inspection, the principle objection to applying the SDE (4.2a) in composite media is the presence of the gradient drift

term therein, not formally defined when Θ and/or \mathbf{D} are discontinuous, i.e., step functions. We will show that one can formulate equations equivalent in meaning to (4.2a), but free of gradient drift terms. Numerical integration by random walks will demonstrate that these equations correspond to (4.1) in composite media where Θ and \mathbf{D} are discontinuous. These new methods preserve many of the computational advantages of standard random-walk techniques. In Appendix 4A, we consider the new methods in one-dimension and show that they indeed correspond to equation (4.1) in composite media. In Appendix 4B, we show that a similar result may be obtained by applying a stochastic calculus using generalized functions. Next we present these methods and demonstrate their application to subsurface transport problems beginning with the simple case of isotropic dispersion in composite media and then consider the case of anisotropic dispersion.

4.4.1 Isotropic Diffusions

The mathematical representation of isotropic diffusion processes arising from advection and dispersion in composite porous media is relevant to the simulation of transport in heterogeneous porous media. As we will demonstrate in a subsequent paper, the dispersion tensor can often be approximated as isotropic without loss of accuracy where the pore-scale dispersion tensor can be approximated as isotropic with respect to its minor axes (assumed to be orthogonal to the velocity vector), and longitudinal spreading due to explicitly modeled heterogeneities is much greater than longitudinal spreading represented by the pore-scale dispersion tensor. Beginning with the case of constant Θ and isotropic \mathbf{D} , we develop an equation that is equivalent to (4.2a) and yet free of gradient terms. We seek an equation that takes the form of (4.2a) after expanding in Taylor series. By inspection we arrive at the following result:

$$dX_i(t) = v_i(\mathbf{X}, t)dt + \sum_j B_{ij}(\mathbf{X} + d\mathbf{X}, t)dW_j(t) \quad (4.9a)$$

$$B_{ij}(\mathbf{x}, t) = \sqrt{\lambda(\mathbf{x}, t)}\delta_{ij} \quad (4.9b)$$

where λ is the eigenvalue of $2\mathbf{D}$ and B_{ij} is evaluated at time t and location given by the vector $\mathbf{X} + d\mathbf{X}$. For smooth coefficients, equation (4.9a) has been referred to as the “backward *Itô*” stochastic integral [Karatzas and Shreve, 1991]. Expanding (4.9a) in a Taylor series shows that (4.9a) and (4.2a) are indeed equivalent for constant Θ and isotropic \mathbf{D} : For all \mathbf{D} we have

$$\begin{aligned} dX_i &= v_i(\mathbf{X}, t)dt + \sum_j B_{ij}(\mathbf{X} + d\mathbf{X}, t)dW_j \\ &= v_i(\mathbf{X}, t)dt + \sum_j \left(B_{ij}(\mathbf{X}, t) + \sum_{k,l} \frac{\partial B_{ij}(\mathbf{X}, t)}{\partial x_l} B_{lk}(\mathbf{X}, t)dW_k + \dots \right) dW_j \\ &= v_i(\mathbf{X}, t)dt + \sum_{j,l} \frac{\partial B_{ij}(\mathbf{X}, t)}{\partial x_l} B_{lj}(\mathbf{X}, t)dt + \sum_j B_{ij}(\mathbf{X}, t)dW_j \end{aligned} \quad (4.10a)$$

and when \mathbf{D} is diagonal

$$\begin{aligned} dX_i &= v_i(\mathbf{X}, t)dt + \sum_{j,l} \frac{\partial B_{ij}(\mathbf{X}, t)}{\partial x_l} B_{lj}(\mathbf{X}, t)dt + \sum_j B_{ij}(\mathbf{X}, t)dW_j \\ &= v_i(\mathbf{X}, t)dt + \sum_j \frac{\partial D_{ij}(\mathbf{X}, t)}{\partial x_j} dt + \sum_j B_{ij}(\mathbf{X}, t)dW_j \end{aligned} \quad (4.10b)$$

Formally, this Taylor series expansion is not allowed for discontinuous \mathbf{D} ; however, in Appendix 4B we show that one can expand (4.9a) for discontinuous \mathbf{D} using generalized functions. In the following section we introduce a method for numerically integrating (4.9a) and apply this method to clearly demonstrate convergence to equation (4.1) in composite media.

4.4.1.1 Numerical integration

Equation (4.9a) may be integrated over a time step Δt by taking two particle displacements, $\Delta \mathbf{Y}$ and $\Delta \mathbf{X}$, as

$$\Delta X_i = v_i \Delta t + \sum_j B_{ij}(X_l + \Delta Y_l, t) \Delta W_j \quad (4.11a)$$

$$\Delta Y_l = \sum_k B_{lk}(\mathbf{X}, t) \Delta W_k \quad (4.11b)$$

Note that advective transport is not included in equation (4.11b); here velocity only contributes to higher-order terms that can be neglected in the limit, e.g., as in the Taylor series expansion in (4.10a) and (4.10b). To implement (4.11a) and (4.11b), equation (4.11b) is first evaluated to determine the particle displacement $\Delta \mathbf{Y}$. The result is used in (4.11a) to determine $\Delta \mathbf{X}$. This simulation method is illustrated in Figure 4.1. Boundary conditions must be implemented in the application of both (4.11a) and (4.11b). If a particle exits an absorbing or reflecting boundary in the application of (4.11a) or (4.11b), it is either removed from the simulation or reflected in the usual way (see *Tompson et al.* [1987]), respectively.

In Appendix 4A we show that distributions approximated by (4.11a) satisfy (4.1). In Appendix 4B we show that a similar result can be obtained through the use of a stochastic calculus using generalized functions. To our knowledge, this result has not been described elsewhere in the literature. We do not, however, present a formal proof of convergence of these approximations. Such a lengthy proof usually demonstrates convergence only; it does not guarantee a robust approximation. To this end, we will demonstrate convergence and applicability of these approximations through numerical exam-

ples. In all examples, Brownian motions will be simulated by uniformly distributed random variables with mean 0 and variance Δt .

4.4.1.2 Diffusion in one-dimensional composite media.

In this example we consider one-dimensional diffusion in an unbounded domain with governing equation (4.1), constant Θ , $v = 0$ and initial and boundary conditions

$$c_i(x, 0) = \delta(x - x_0) \quad \text{for } x_0 \in \Omega_i \quad (4.12a)$$

$$c_1(-\infty, t) = c_2(+\infty, t) = 0 \quad (4.12b)$$

$$c_1(x, t) = c_2(x, t) \quad \text{on } x = 0 \quad (4.12b)$$

$$\lim_{x \rightarrow 0^-} D_1 \frac{\partial c_1(x, t)}{\partial x} = \lim_{x \rightarrow 0^+} D_2 \frac{\partial c_2(x, t)}{\partial x} \quad (4.12c)$$

$$D(x) = \begin{cases} D_1 & \text{for } x < 0 \\ D_2 & \text{for } x > 0 \end{cases} \quad (4.12d)$$

where $i = 1, 2$ denotes quantities within subdomains Ω_1 and Ω_2 to the left and right, respectively, of the interface located at $x = 0$. First, we apply (4.11a) performing three simulations corresponding to $\Delta t = 100.0$, 10.0 , and 1.0 to demonstrate convergence with decreasing time step of simulated moments to analytical moments of the distribution. In each simulation we use $D_1 = 10.0$, $D_2 = 1.0$ and begin with 1000 particles located at $x_0 = -1.0$. Figures 4.2a and 4.2b plot the mean and standard deviation computed from an analytical solution [see *Carslaw and Jaeger*, 1959] against values computed from particle displacements, given respectively as

$$\bar{X}(t) = \langle X(t) \rangle = \frac{1}{N_p} \sum_{p=1}^{N_p} X_p(t) \quad (4.13a)$$

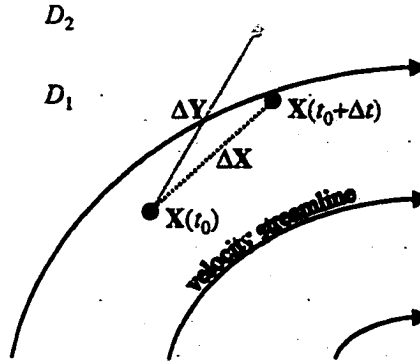


Figure 4.1: The two step process of random-walk simulation of advection and isotropic dispersion in composite porous media for the algorithm given in equations (4.11a) and (4.11b).

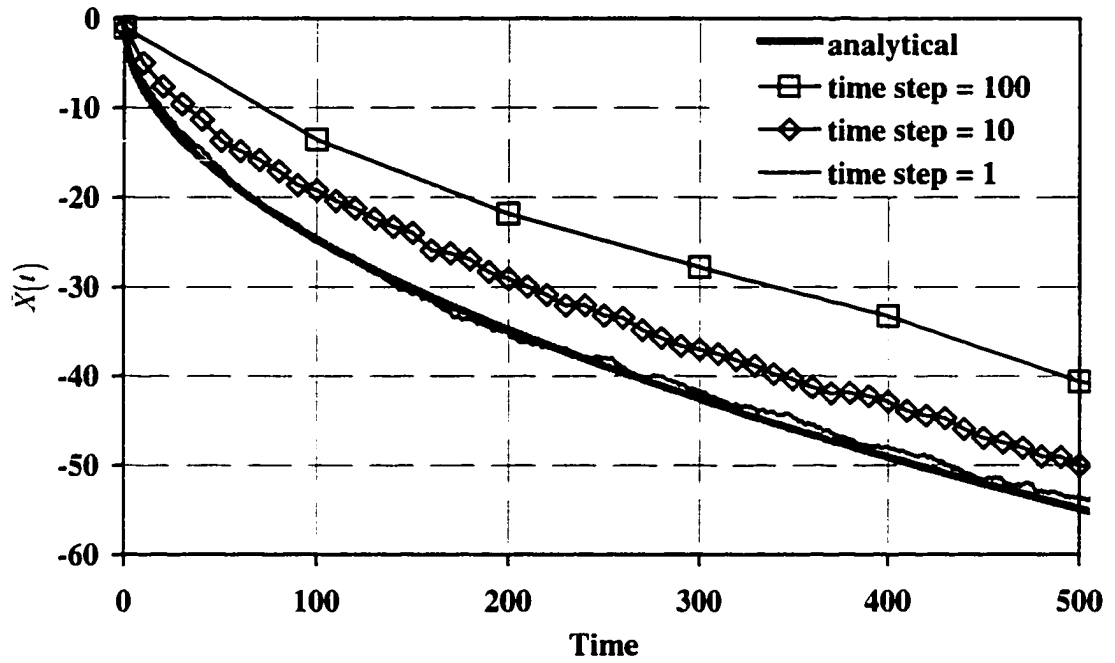
$$\Sigma(t) = \left\langle [X(t) - \bar{X}(t)]^2 \right\rangle^{1/2} = \left\{ \frac{1}{N_p} \sum_{p=1}^{N_p} [X_p(t) - \bar{X}(t)]^2 \right\}^{1/2} \quad (4.13b)$$

where N_p is the total number of particles and $X_p(t)$ is the location of the p th particle at time t .

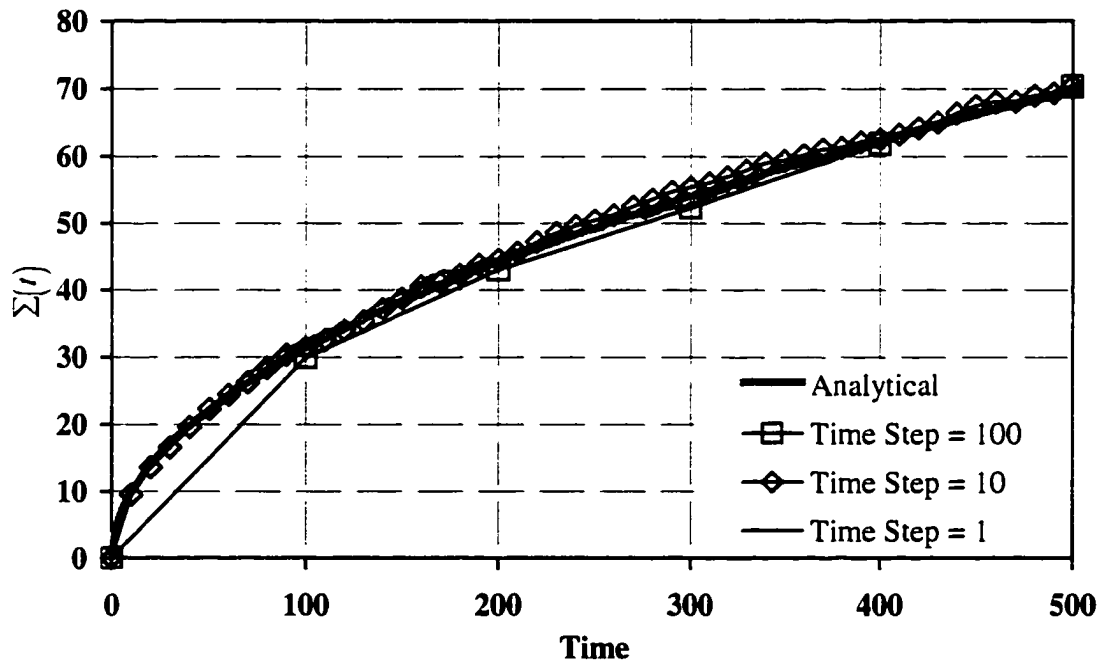
Second, using (4.11a), we perform three simulations corresponding to $D_2 = 2.5, 0.5$ and 0.05 . In each simulation we use $D_1 = 5.0$, $\Delta t = 0.01$, $x_0 = -5.5$ and 10^5 particles. Figure 4.3 compares simulated density at time $t = 6$, computed by summing particle masses within unit lengths along the x -axis, with analytical distributions (see *Carslaw and Jaeger*, 1959) to (4.1) with initial and boundary conditions (4.12a) – (4.12d).

Numerical simulation results presented here compare well with analytical solutions and demonstrate convergence of (4.11a) and (4.9a) to equation (4.1) in one-dimension with discontinuous coefficients. As we will show, extension to (multi-dimensional) isotropic diffusions for hyper-plane interfaces follows directly from this result by noting that diffusion processes in the different coordinate directions are independent in this case.

(4.2a)



(4.2b)



Figures 4.2a and 4.2b: Simulation results for (a) $\bar{X}(t)$ and (b) $\Sigma(t)$ are compared with analytical values for $\Delta t = 10.0, 1.0, 0.1,$ and 0.01 .

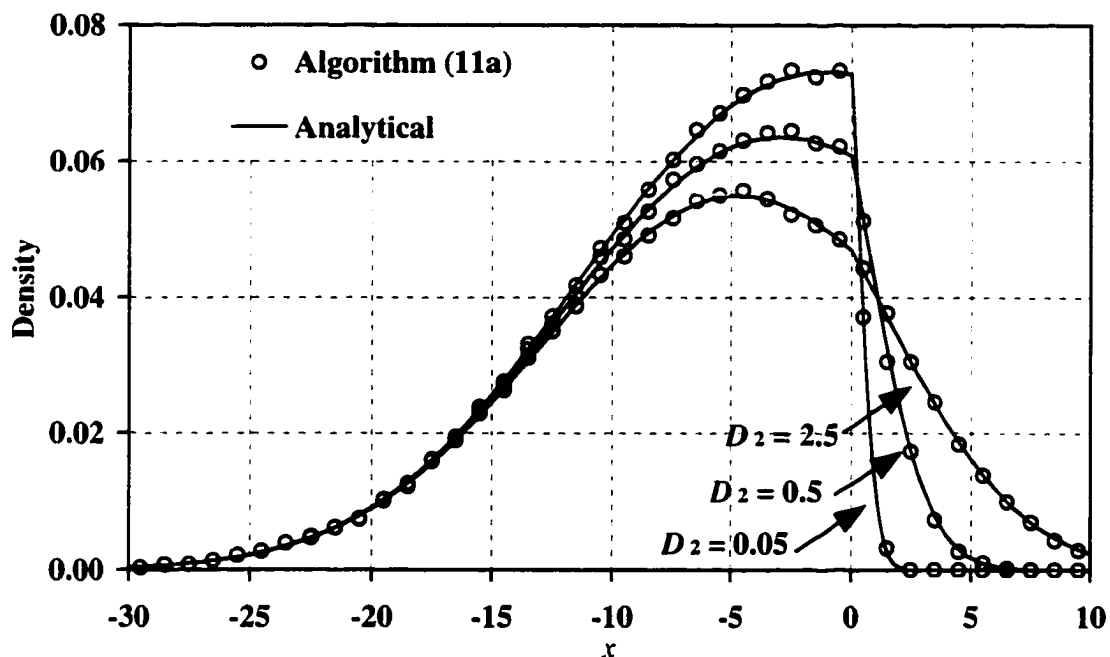


Figure 4.3: Simulation results for concentration are compared with analytical solutions for $D_1 = 5.0$ and $D_2 = 2.5$ (diamonds), 0.5 (squares), and 0.05 (circles).

4.4.1.3 Effective diffusivity of composite media.

In this example, we estimate effective diffusivity of composite media. The specific geometry considered here is that of circular cylinders packed in regular square arrays within a matrix of contrasting material as shown in Figure 4.4. Dispersion tensors of both materials are constant and isotropic. Transport is described by (4.1) with constant Θ and $\nu = 0$. This classic problem has received much attention [Rayleigh, 1892; Runge, 1925; Keller, 1963; Sangani and Acrivos, 1983; Quintard and Whitaker, 1993] and accurate experimental and analytical values of effective diffusivity are available [Perrins et al., 1979].

We estimate the effective diffusivity of a periodic array by specifying reflecting boundaries at lines ABC and DEF and absorbing boundaries at lines AF and CD as

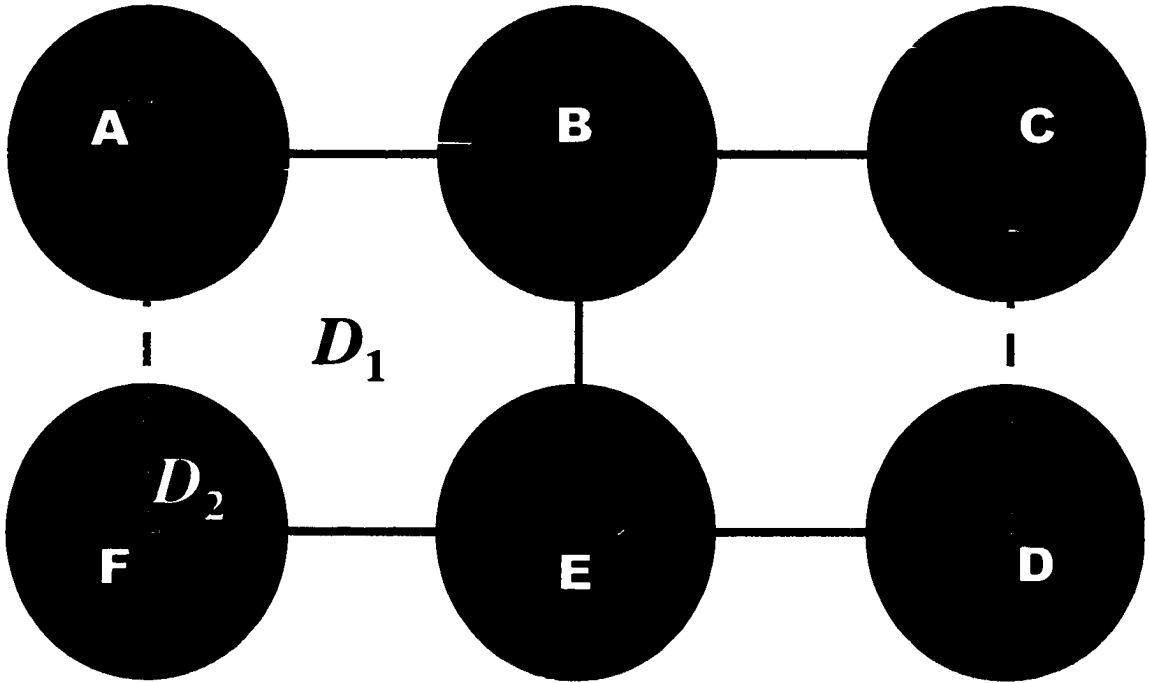


Figure 4.4: Square array of cylinders with known diffusivity, D_2 , embedded in a matrix with contrasting diffusivity, D_1 .

shown in Figure 4.4. Simulation proceeds by releasing particles at time $t=0$ and random locations with uniform distribution along the line BE that bisects the system. Particle paths are simulated using (4.11a) until particles exit the system by crossing absorbing boundaries at lines AF or CD. Effective diffusivity is given by the relationship

$$\bar{D} = L_{AB}^2 \left(\frac{2}{N_p} \sum_{p=1}^{N_p} \tau_p \right)^{-1} \quad (4.14)$$

where τ_p is the elapsed time from release until particle p exits the system and L_{AB} is the length of line AB.

The matrix diffusivity is arbitrarily chosen as 1.0. Simulations are performed for a range of cylinder volume fractions, controlled by varying cylinder diameter, and diffusivities. In each simulation 1,000 particles are released; time step is dynamically controlled to ensure particles cannot bypass subdomains in any single step of the algorithm

given by (4.11a). Figure 4.5 compares simulated effective diffusivities with values reported by *Perrins et al.* [1979] for a range of cylinder volume fractions and diffusivities. Simulation results compare well with reported values as expected due to the previous success of (4.11a) in one dimension.

4.4.1.4 Discussion

Our results show that diffusions described by (4.9a) obey equation (4.1) in composite media with discontinuities in effective transport properties. Furthermore, the numerical integration method (4.11a) “accurately” solves this equation.

Convergence and analysis of errors associated with the numerical simulation of SDEs is a developing field (e.g., see *Kloeden and Platen* [1992]). Verification of convergence and quantification of accuracy may generally be addressed by comparing numerical results with known analytical solutions, as we have done here, or benchmarking against established numerical methods as in the following section. Since we cannot consider all of the many problems to which (4.11a), and the other approximations that follow, may be applied, we suggest verification by a similar procedure to assess accuracy and convergence when the methods are used under circumstances other than those considered herein.

The examples presented above were for isotropic diffusions with constant Θ and $\mathbf{v} = 0$. Next we present a more general multidimensional approximation for anisotropic diffusions. Examples that follow will consider advection and dispersion in composite porous media.

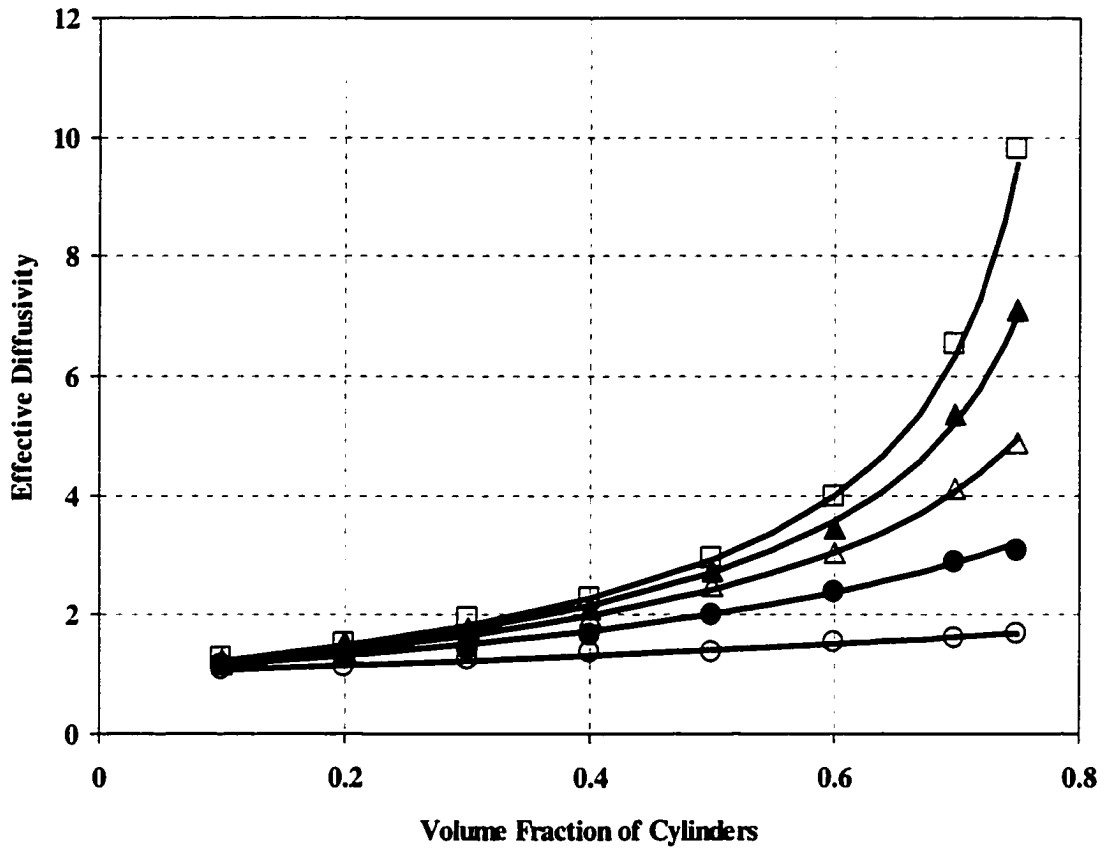


Figure 4.5: Simulated effective diffusivities are compared with values reported by *Perins et al.* [1979] for cylinder volume fractions of 0.1, 0.2, 0.3, 0.4, 0.5, 0.6, 0.7, and 0.75, matrix diffusivity $D_1 = 1$, and cylinder diffusivities, $D_2 = 2$ (solid circles), 5 (triangles), 10 (diamonds), 20 (squares), and 50 (open circles).

4.4.2 Anisotropic Diffusions

As with the isotropic case, we find ourselves faced with the following problem: Eliminate the gradient drift term in (4.2a) in the anisotropic case. Note that this problem is not trivial. Nevertheless, with considerable effort, we arrived at the following inspired result:

$$\begin{aligned}
 d\mathbf{X}_i(t) &= v_i(\mathbf{X}, t) dt \\
 &+ \frac{1}{2} \sum_{j,k} \Theta^{-1/2}(\mathbf{X}, t) \hat{B}_{ijk} \left(X_i + \Theta^{-1/2}(\mathbf{X}, t) \sum_{m,n} \hat{B}_{imn}(\mathbf{X}, t) dW_m, t \right) dW_j, \\
 &+ \frac{1}{2} \sum_{j,k,m,n} Z_{imn}(\mathbf{X}, t) \Theta^{-1/2}(\mathbf{X}, t) \hat{B}_{mjk} \left(X_i + \lambda_n^{1/2}(\mathbf{X}, t) dW_i, t \right) dW_j,
 \end{aligned} \tag{4.15a}$$

$$\hat{B}_{ijk}(\mathbf{x}, t) = \Theta^{1/2}(\mathbf{x}, t) \lambda_k^{1/2}(\mathbf{x}, t) Z_{ijk}(\mathbf{x}, t) \quad (4.15b)$$

$$Z_{ijk}(\mathbf{x}, t) = (e_k(\mathbf{x}, t))_i (e_k(\mathbf{x}, t))_j \quad (4.15c)$$

where e_k is the normalized eigenvector corresponding to the k th eigenvalue λ_k of $2\mathbf{D}$ and, for example, in the first term on the rhs of (4.15a), \hat{B}_{ijk} is evaluated at time t and location given by the vector whose l th component is $X_l + \Theta^{-1/2}(\mathbf{X}, t) \sum_{m,n} \hat{B}_{lmn}(\mathbf{X}, t) dW_m$. For isotropic \mathbf{D} , $\lambda = \lambda_k, \forall k$, and using relationships given in Appendix 4C, equations (4.15a) and (4.15b) simplify considerably:

$$\begin{aligned} dX_i(t) &= v_i(\mathbf{X}, t) dt \\ &+ \Theta^{-1/2}(\mathbf{X}, t) \sum_j B_{ij}(\mathbf{X} + \Theta^{-1/2}(\mathbf{X}, t) d\mathbf{X}, t) dW_j(t) \end{aligned} \quad (4.16a)$$

$$B_{ij}(\mathbf{x}, t) = \sqrt{\Theta(\mathbf{x}, t) \lambda(\mathbf{x}, t)} \delta_{ij} \quad (4.16b)$$

Further, for constant Θ , (4.16a) and (4.16b) reduce to (4.9a) and (4.9b). Therefore, (4.9a) can be viewed as a special case of (4.15a).

Integration of (4.15a) may proceed according to a discrete-time random walk that includes the approximations

$$\begin{aligned} \Delta X_i &= v_i(\mathbf{X}, t) \Delta t \\ &+ \frac{1}{2} \Theta^{-1/2}(\mathbf{X}, t) \sum_{j,k} \hat{B}_{ijk}(X_l + \Delta \hat{Y}_l, t) \Delta W_j \end{aligned} \quad (4.17a)$$

$$+ \frac{1}{2} \Theta^{-1/2}(\mathbf{X}, t) \sum_{j,k,m,n} Z_{imn}(\mathbf{X}, t) \hat{B}_{mjk}(X_l + \Delta U_{nl}, t) \Delta W_j$$

$$\Delta \hat{Y}_l = \Theta^{-1/2}(\mathbf{X}, t) \sum_{m,n} \hat{B}_{lmn}(\mathbf{X}, t) \Delta W_m \quad (4.17b)$$

$$\Delta U_{nl} = \lambda_n^{1/2}(\mathbf{X}, t) \Delta W_l \quad (4.17c)$$

First, equations (4.17b) and (4.17c) are evaluated to determine $\Delta\hat{Y}$ and $\Delta U_n, \forall n$. These results are used in (4.17a) to determine $\Delta\mathbf{X}$. As with the (4.11a) and (4.11b), boundary conditions must be implemented in the application of each step of the algorithm, (4.17a) - (4.17c).

When coefficients are sufficiently smooth, (4.15a) is a SDE. In Appendix 4C, we expand this SDE in Taylor series to show that it is indeed equivalent to (4.2a) in this case. Standard stochastic theory (e.g., see *Arnold* [1992]) shows that diffusions described by (4.2a), and therefore (4.15a), obey equation (4.1) when coefficients are smooth. Next we demonstrate that (4.17a) converges to equation (4.1) in composite media and is applicable to the simulation of subsurface transport.

4.4.2.1 Anisotropic diffusion in composite media

In this example we simulate anisotropic diffusion in composite media. The system illustrated in Figure 4.6 is a composite of two media with contrasting diffusion (dispersion) tensors whose principle axes, designated by λ_1 , are oriented at an angle ϕ with the x -axis; eigenvectors corresponding to λ_1 and λ_2 are given as $\mathbf{e}_1 = (\sin\phi, \cos\phi)$ and $\mathbf{e}_2 = (-\sin\phi, \cos\phi)$, respectively. Two problems are considered. In the first problem we test the ability of approximation (4.17a) to maintain the invariant distribution, i.e., a uniform number density, for the system in Figure 4.6 given periodic boundaries in the x -direction and reflective, no-flux boundaries at $y = 0$ and $y = 2$. In each of the four simulations, a total of 5,000 particles are initially distributed uniformly over the domain and the system is evolved over time using the parameters specified in Table 4.1. Results for first moments in the x - and y -directions plotted in Figures 4.7a – 4.7d indicate that approximation (4.17a) can successfully maintain the invariant distribution for these problems.

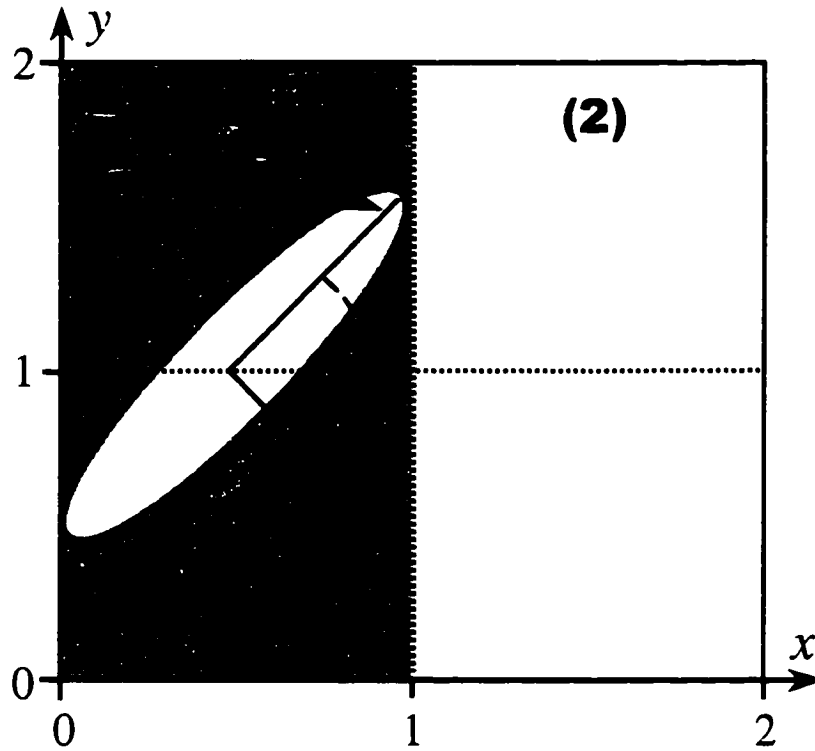
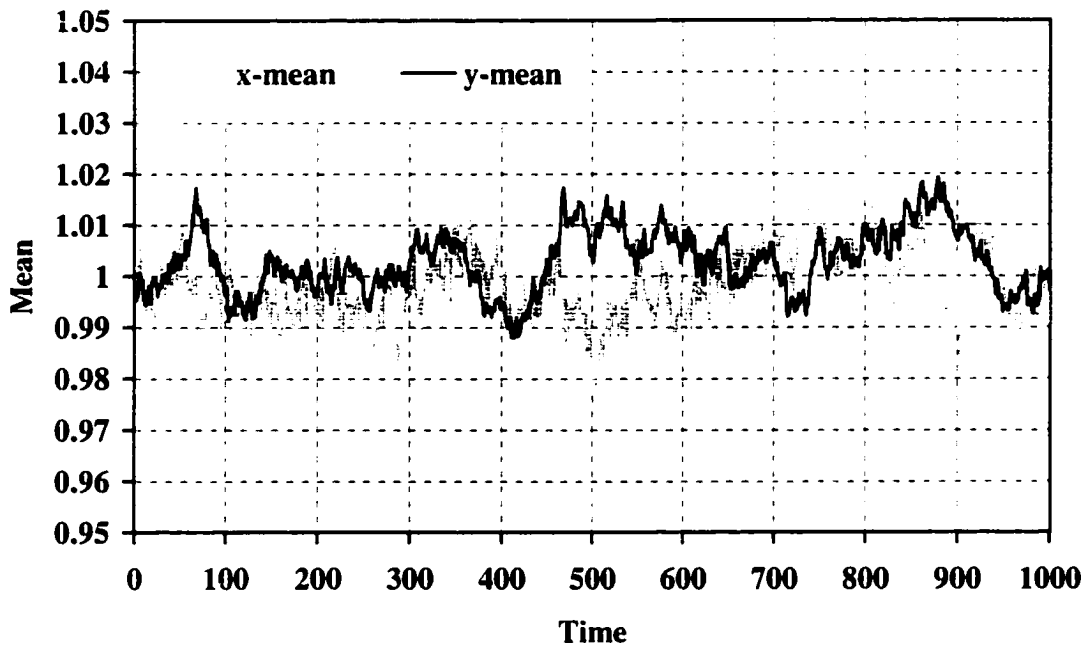


Figure 4.6: Composite media with anisotropic diffusion tensors.

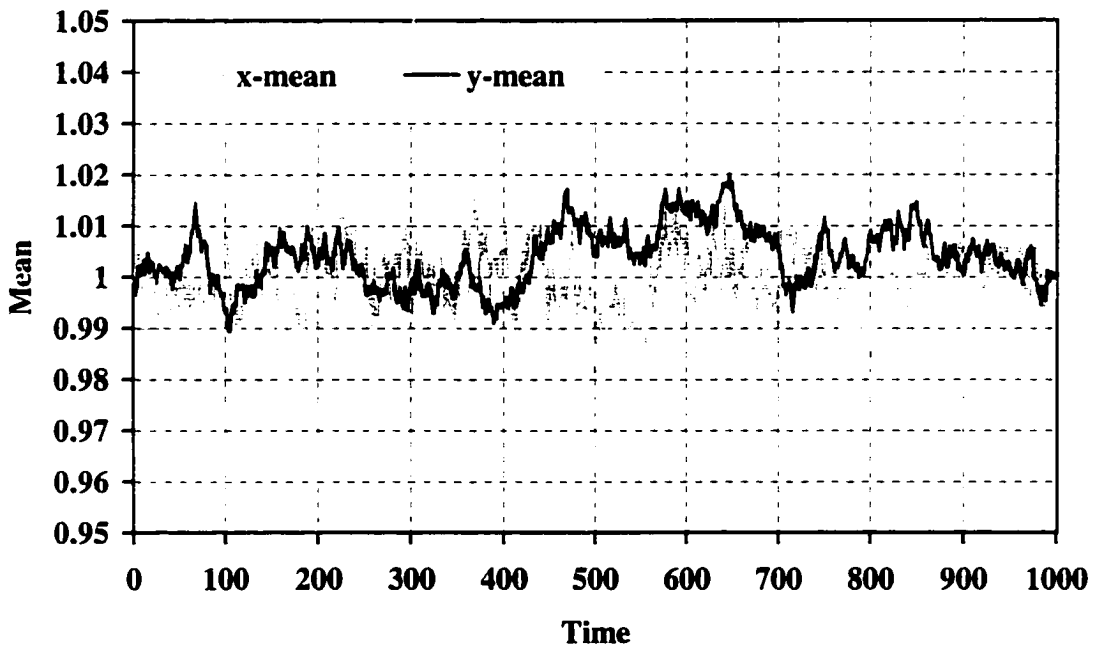
Table 4.1: Parameters corresponding to simulation results presented in Figures 4.7a-4.7d and 4.8a-4.8d.

Figures	Region 1			Region 2		
	λ_1	λ_2	ϕ	λ_1	λ_2	ϕ
7a & 8a	2×10^{-2}	2×10^{-3}	90°	2×10^{-2}	2×10^{-3}	0°
7b & 8b	2×10^{-2}	2×10^{-3}	-45°	2×10^{-2}	2×10^{-3}	45°
7c & 8c	2×10^{-2}	2×10^{-3}	30°	2×10^{-3}	2×10^{-4}	30°
7d & 8d	2×10^{-2}	2×10^{-3}	70°	2×10^{-3}	2×10^{-4}	0°

(4.7a)

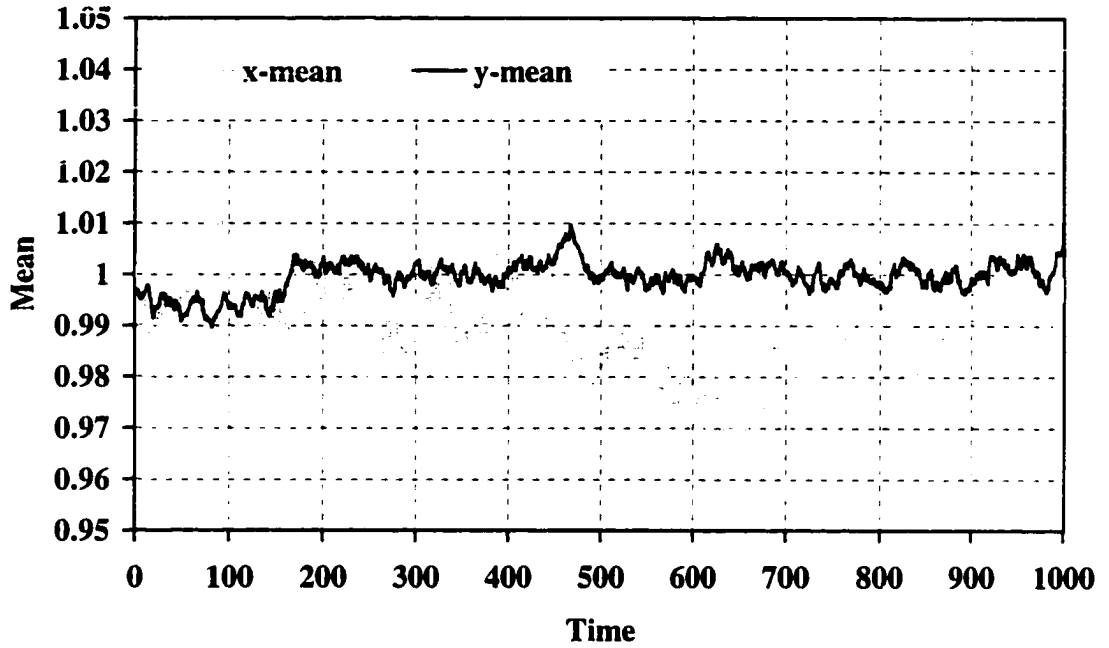


(4.7b)

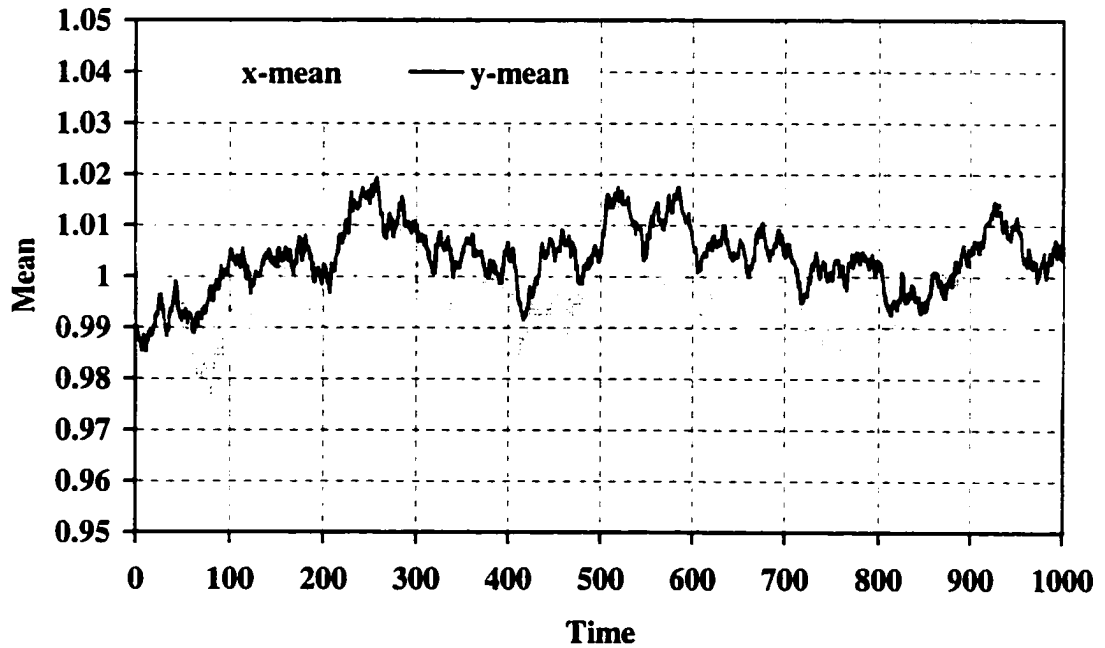


Figures 4.7a – 4.7b: Simulated first moments in the x - and y -directions as a function of time for the system illustrated in Figure 4.6 with periodic boundaries in the x -direction and reflective, no-flux boundaries at $y = 0$ and $y = 2$, initially uniform number density, and parameters given in Table 4.1.

(4.7c)



(4.7d)



Figures 4.7c – 4.7d: Simulated first moments in the x - and y -directions as a function of time for the system illustrated in Figure 4.6 with periodic boundaries in the x -direction and reflective, no-flux boundaries at $y = 0$ and $y = 2$, initially uniform number density, and parameters given in Table 4.1.

In the second problem, we compare predictions for evolution of concentration from approximation (4.19a) with finite difference numerical solutions to (4.1) for the system in Figure 4.6 with absorbing (zero-concentration) boundaries on $x = 0$, $x = 2$, $y = 0$, and $y = 2$ and initial distribution $c(\mathbf{x},0) = c_0$ in the region $0.99 < x < 1.00$ and $0.99 < y < 1.00$ and $c(\mathbf{x},0) = 0$ outside this region. The finite difference algorithm is implemented (a) using an explicit updating scheme. Choosing $\Delta x = \Delta y = 0.005$ and $\Delta t = 0.0005$ satisfies criteria for numerical stability [Peaceman, 1977]. Particle simulations are implemented using 10^6 particles. Coarse particle and finite difference solution contours of $c(\mathbf{x},t)/c_0$ at $t = 5.0$ plotted in Figures 4.8a – 4.8d for parameters given in Table 4.1 compare well. The results herein clearly demonstrate that diffusions described by equation (4.15a) and approximation (4.17a) obey equation (4.1) for the cases considered here.

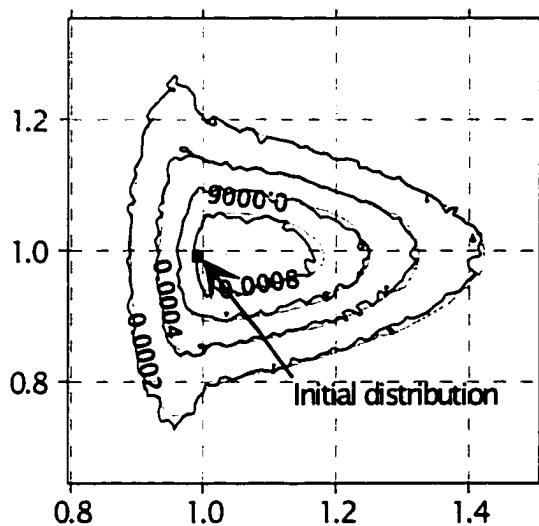
4.4.2.2 Advective-dispersive transport in composite media

In this example we simulate advective-dispersive transport according to (4.1) for the system illustrated in Figure 4.6 with absorbing (zero concentration) boundaries on $x = 0$, $x = 2$, $y = 0$, and $y = 2$. The functional form of the hydrodynamic-dispersion tensor used here is given as

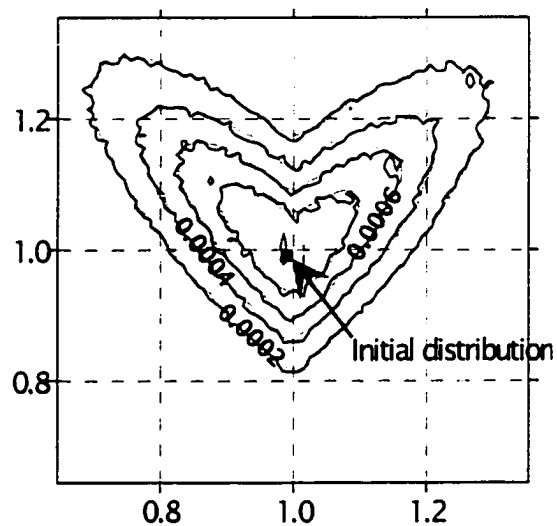
$$D_{ij} = (|\mathbf{v}|\alpha_T + D^*)\delta_{ij} + (\alpha_T - \alpha_L)v_i v_j / |\mathbf{v}| \quad (4.18)$$

where α_T and α_L [L] are transverse and longitudinal dispersivities, respectively, and D^* is effective molecular diffusivity [L^2T^{-1}]. Velocity direction is oriented at an angle ϕ with the x -axis as illustrated in Figure 4.6. We compare predictions from approximation (4.17a) with finite difference numerical solutions to (4.1). Again, the finite difference algorithm uses an explicit updating scheme. Choosing $\Delta x = \Delta y = 0.005$ and $\Delta t = 0.0005$

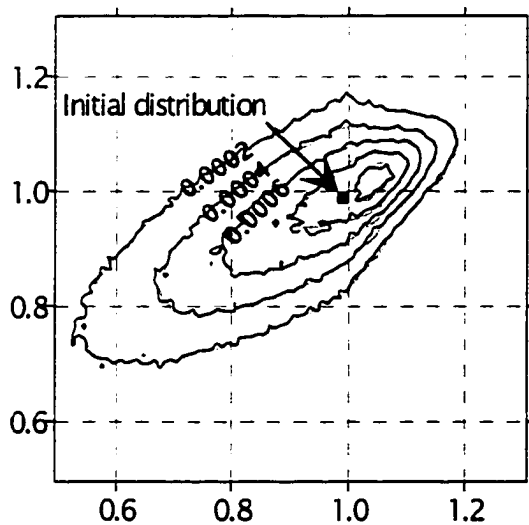
(4.8a)



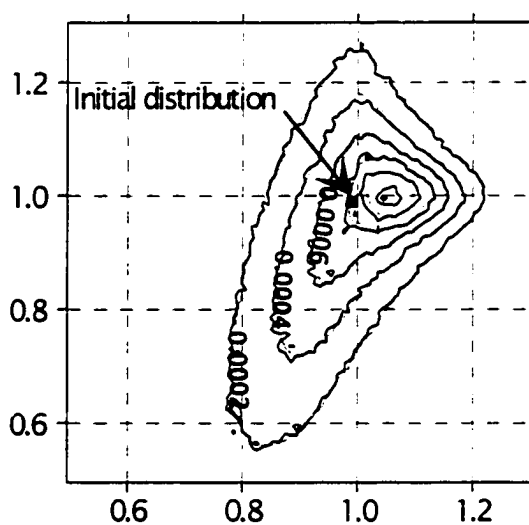
(4.8b)



(4.8c)



(4.8d)



Figures 4.8a-4.8d: Contours of $c(x,t)/c_0$ from simulations of anisotropic diffusion in the composite media shown in Figure 4.6 with absorbing (zero concentration) boundaries on $x = 0$, $x = 2$, $y = 0$, and $y = 2$, initial distribution $c(x,0) = c_0$ in the region $0.99 < x < 1.00$ and $0.99 < y < 1.00$ and $c(x,0) = 0$ outside this region, and parameters given Table 4.1.

satisfies the stability criteria referenced in section 2.3.1 and ensures a grid Peclet number $P_e \approx \Delta x/\alpha_L$ less than one. Particle simulations use 10^6 particles. As in the previous simulations, the initial distribution in each simulation is $c(\mathbf{x},0) = c_0$ specified within a square region of $\Delta x = \Delta y = 0.01$, as shown in Figures 4.9a – 4.9c, and $c(\mathbf{x},0) = 0$ outside of this region.

Coarse particle and finite difference solution contours of $c(\mathbf{x},t)/c_0$ at $t = 2.5, 5.0$, and 5.0 plotted in Figures 4.9a, 4.9b and 4.9c, respectively, for parameters given in Table 4.2 compare well. These and the previous results show that diffusions described by equation (4.15a) correspond with equation (4.1) and that approximation (4.17a) simulates equation (4.1) in composite media with surprising accuracy.

4.5 Discussion and Conclusions

Standard diffusion theory only applies when effective transport properties are sufficiently smooth, yet discontinuities in transport properties arise naturally in porous media at abrupt contacts between geologic materials with contrasting transport properties. Limitations of standard diffusion theory have precluded development of diffusion processes that obey spatially-averaged transport equations in composite media.

Table 4.2: Parameters Corresponding to Simulation Results Presented in Figures 4.9a-4.9c

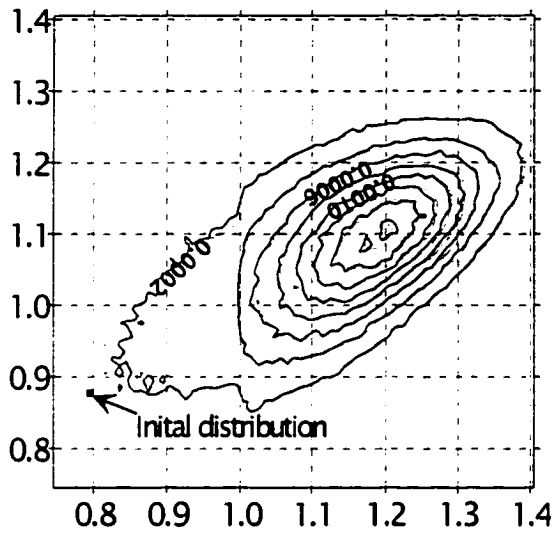
Region 1

Figure	Θ_1	$\Theta_1 \mathbf{v} $	α_L	α_T	ϕ	D^*
4.9a	1/3	$\Theta_1(10^{-1})$	10^{-1}	10^{-2}	-45°	10^{-5}
4.9b	1/3	$\Theta_1(10^{-1})$	10^{-1}	10^{-2}	30°	10^{-5}
4.9c	1/3	$\Theta_1(10^{-1})$	10^{-1}	10^{-2}	60°	10^{-5}

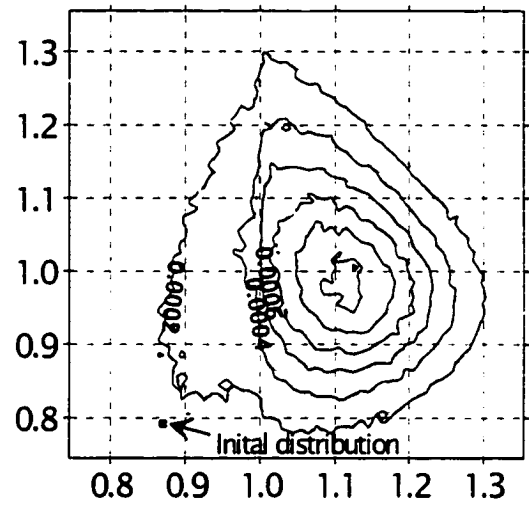
Region 2

Figure	Θ_2	$\Theta_2 \mathbf{v} $	α_L	α_T	ϕ	D^*
4.9a	1/3	$\Theta_1(10^{-1})$	10^{-1}	10^{-2}	45°	10^{-5}
4.9b	1/2	$\Theta_1(10^{-1})$	$\Theta_2(10^{-2})/\Theta_1$	1.5×10^{-3}	30°	10^{-5}
4.9c	1/2	$\Theta_1(5 \times 10^{-2})$	$\Theta_2(2 \times 10^{-2})/\Theta_1$	3.0×10^{-3}	0°	10^{-5}

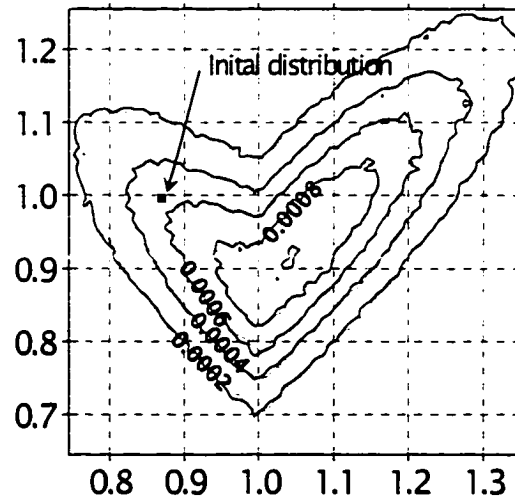
(4.9a)



(4.9b)



(4.9c)



Figures 4.9a-4.9c: Contours of $c(\mathbf{x},t)/c_0$ from simulations of advective-dispersive transport in the composite media shown in Figure 4.6 with absorbing (zero concentration) boundaries on $x = 0$, $x = 2$, $y = 0$, and $y = 2$, initial distribution $c(\mathbf{x},0) = c_0$ as shown and $c(\mathbf{x},0) = 0$ outside this region, and parameters given Table 4.2.

In this paper we have (1) generalized SDEs to the case of discontinuous coefficients and (2) developed random-walk methods for numerically integrating these equations. The new results apply to problems found in many scientific disciplines and offer a unique contribution to diffusion theory and the theory of SDEs. Examples demonstrated convergence of the new methods to ADEs in composite media and applications to subsurface-transport problems including: (1) one-dimensional diffusion in composite porous media with constant coefficients in subdomains, (2) isotropic two-dimensional diffusion in a system of circular cylinders packed in regular square arrays within a matrix of contrasting material, (3) two-dimensional anisotropic diffusion in a composite system with contrasting diffusion tensors and (4) transport by advection and dispersion in composite porous media.

Standard theory shows that diffusions described by the new generalized SDEs obey ADEs when coefficients are sufficiently smooth. Further, we have demonstrated that these diffusions obey ADEs in composite media. Thus, in cases where coefficients are smooth, we conclude that the new methods may often be more robust approximations than standard *Itô-Euler* techniques.

The new simulation techniques possess the computational advantages of standard random-walk methods, including the ability to efficiently simulate solute-mass distributions and arrival times while suppressing errors such as numerical dispersion, common to finite difference methods when Peclet numbers are large. As such, the new methods are appropriate for problems characterized by immense computational grids, such as those now commonly produced through the use of geostatistical simulation techniques for subsurface characterization. Finally, unlike alternatives relying on *Itô-Euler* integration and

spatial interpolation to ensure smooth coefficients, the new methods will converge exactly in the limit, without the need to simultaneously refine the interpolation scheme and time step.

4.6 References

- Ackerer, Ph., Comments on "Diffusion theory for transport in porous media: Transition-probability densities of diffusion processes corresponding to advection-dispersion equations" by E.M. LaBolle, J. Quastel, and G.E. Fogg, *personal communication*, 1999.
- Ackerer, Ph., Propagation d'un fluide en aquifère poreux saturé en eau. Prise en compte et localisation des hétérogénéités par outils théoriques et expérimentaux, Ph.D. thesis, Université Louis Pasteur de Strasbourg, France, 1985.
- Ahlstrom, S.W., H.P. Foote, R.C. Arnett, C.R. Cole and R.J. Serne, Multi-component mass transport model: theory and numerical implementation. Rep. BNWL-2127, Battelle Pacific Northwest Lab., Richland, Washington, 1977.+
- Arnold, L., *Stochastic Differential Equations: Theory and Applications*, Krieger Publishing Company, Florida, 1992.
- Carle, S.F., E.M. LaBolle, G.S. Weissmann, D. VanBrocklin, and G.E. Fogg, Geostatistical simulation of hydrofacies architecture: A transition probability/Markov approach, in *SEPM Concepts in Hydrogeology and Environmental Geology No. 1, Hydrogeologic Models of Sedimentary Aquifers*, G.S. Fraser and J.M. Davis (eds), Tulsa Oklahoma, 1998.
- Carslaw, H.S. and J.C. Jaeger, *Conduction of heat in solids*, Clarendon Press, Oxford, 363-365, 1959.
- Coptly, N. and Y. Rubin, A stochastic approach to the characterization of lithofacies from surface seismic and well data, *Water Resources Research*, 31(7), 1673-1686, 1995.
- Cordes, C., H. Daniels, and G. Rouvé, A new very efficient algorithm for particle tracking in layered aquifers, in *Computer Methods in Water Resources II, Vol. 1: Groundwater Modelling and Pressure Flow*, Sari, D.B., C.A. Brebbia, and D. Ouazar (eds), Springer-Verlag, 41-55, 1991.
- Gardiner, C.W., *Handbook of Stochastic Methods for Physics Chemistry and the Natural Sciences*, Springer-Verlag, Berlin, 1990.
- Itô, K. and H.P. McKean, *Diffusion Processes and their Sample Paths*, Springer-Verlag, New York, 1961.
- Karatzas, I. and S.E. Shreve, *Brownian Motion and Stochastic Calculus*, Springer-Verlag, New York, 470 p, 1991.
- Keller, J.B., Conductivity of a dense medium containing a dense array of perfectly conducting spheres or cylinders, *J. Appl. Physics.*, 34, 991, 1963.
- Kinzelbach, W., The random walk method in pollutant transport simulation, in *Groundwater Flow and Quality Modelling*, ed. Custidio, E., A. Gurgui, and J.P. Lobo

- Ferreria. NATO ASI Series C: Math and Phys. Sci. 224: 227-246. Reidel Publishing Company, 1988.
- Kloeden, P.E. and E. Platen, *Numerical Solution of Stochastic Differential Equations*, eds. A.V. Balakrishnan, I. Karatzas, and M. Yor, Springer-Verlag, Heidelberg, 1992.
- LaBolle, E.M., G.E. Fogg, and A.F.B. Tompson, Random-walk simulation of transport in heterogeneous porous media: Local mass-conservation problem and implementation methods, *Water Resources Research*, 32(3), 583-593, 1996.
- LaBolle, E.M., J. Quastel, and G.E. Fogg, Diffusion theory for transport in porous media: Transition-probability densities of diffusion processes corresponding to advection-dispersion equations, *Water Resources Research*, 34(7), 1685-1693, 1998.
- McKenna S.A. and E.P. Poeter, Field example of data fusion in site characterization, *Water Resources Research*, 31(12), 3229-3240, 1995.
- Peaceman, D.W. *Fundamentals of Numerical Reservoir Simulation*, Elsevier Scientific Publishing Company, 1977.
- Perrins, W.T., D.R. McKenzie, and R.C. McPhedran, Transport properties of regular arrays of cylinders, *Proc. R. Soc. Lond. A*, 369, 207-225, 1979.
- Plumb, O.A. and S. Whitaker, Diffusion, adsorption and dispersion in porous media: Small-scale averaging and local-volume averaging, in *Dynamics of Fluids in Hierarchical Porous Media*, ed. Cushman, J.H., Academic Press, Inc., California, 97-176, 1990.
- Prickett, Th.A., Th.G. Naymik and C.G. Longquist, A random walk solute transport model for selected groundwater quality evaluations, Rep. Illinois State Water Survey, Urbana Illinois, 1981.
- Quintard, M. and S. Whitaker, Transport in ordered and disordered porous media: Volume-averaged equations, closure problems, and comparison with experiment, *Chemical Engineering Science*, Vol. 48, No 14, 2537-2564, 1993.
- Rayleigh, R.S., On the influence of obstacles arranged in rectangular order upon the properties of medium, *Phil. Mag.* 34, 481, 1892.
- Runge, I., On the electrical conductivity of metallic aggregates, *Z. Tech. Phys.*, 6, 61, 1925.
- Sangani, A.S. and A. Acrivos, The effective conductivity of a periodic array of spheres, *Proc. R. Soc. Lond. A*, 386, 263-275, 1983.
- Semra, K., Ph. Ackerer, and R. Mosé, Three-dimensional groundwater quality modelling in heterogeneous media, in *Water Pollution II, Modelling, Measuring and Prediction*, Wrobel, L.C. and C.A. Brebbia (eds), Computational Mechanics Publications, Southampton Boston, 3-11, 1993.
- Semra, K., Moélisation tridimensionnelle du transport d'un traceur en milieu poreux saturé hétérogène: Evaluation des théories stochastiques, Ph.D. Thesis, University Luis Pasteur de Strasbourg, France, 1994.
- Sheibe, T.D. and D.L. Freyberg, Use of sedimentological information for geometric simulation of natural porous media structure, *Water Resources Research*, 31(12), 3259-3270, 1995.
- Stratonovich, R.L., *Topics in the theory of random noise*, Vol. 1, New York, Gordon and Breach, 1963.

- Tompson, A.F.B., E.G. Vomoris, and L.W. Gelhar, Numerical simulation of solute transport in randomly heterogeneous porous media: motivation, model development, and application, Report UCID-21281, Lawrence Livermore National Laboratory, 1987.
- Tompson, A.F.B. and L.W. Gelhar, Numerical simulation of solute transport in three-dimensional randomly heterogeneous porous media, *Water Resources Research*, 26(10), 2541-2562, 1990.
- Tompson, A.F.B., Numerical simulation of chemical migration in physically and chemically heterogeneous porous media, *Water Resources Research*, 29(11), 3709-3726, 1993.
- Uffink, G.J.M., A random walk method for the simulation of macrodispersion in a stratified aquifer, in *Relation of Groundwater Quality and Quantity*, IAHS Pub No. 146, 103-114, 1985.

Appendix 4A: Necessary Conditions for Weak Convergence

LaBolle et al. [1998] use a graphical technique to show that approximations with symmetric transition-probability density satisfy necessary conditions for weak convergence developed therein. Since transition-probability densities specified by (4.11a) and similar approximations are asymmetric, however, the simple graphical techniques used in *LaBolle et al.* [1998] are not applicable here. Instead, here we will show mathematically that (4.11a) approximates the diffusion equation of interest.

Functions $p(x,t)$ satisfying the one-dimensional diffusion equation

$$\int f(x,t) \frac{\partial p(x,t)}{\partial t} dx = \int (D'(x,t)f'(x,t) + D(x,t)f''(x,t))p(x,t) dx \quad (4A.1)$$

for all smooth and bounded test functions f are weak solutions of (4.1) with $\nu = 0$ [*LaBolle et al.*, 1998], where the f' and f'' denote the first and second partial derivatives of f with respect to x . For the problem at hand, it is convenient to consider the case in which $D(x,t)$ has constant values within subdomains and a single jump of size $|D_2 - D_1|$ at x_0 , $D = D_1$ for $x < x_0$, and $\nu = 0$. Here, $D' = 0$ except at x_0 where it is given as

$$D' = (D_2 - D_1)\delta(x - x_0) \quad (4A.2)$$

Substituting this result into (4A.1) yields

$$\begin{aligned} \int f \frac{\partial p}{\partial t} dx &= \int (D'f' + Df'')p dx \\ &= \int [(D_2 - D_1)\delta(x - x_0)f' + Df'']p dx = \int Df''p dx + (D_2 - D_1)f p|_{x_0} \end{aligned} \quad (4A.3)$$

We will show that the density $p_\epsilon(x,t)$ generated by (4.11a) satisfies (4A.3).

To facilitate computations, we will consider the following variation of approximation (11a):

$$\Delta X(t) = \frac{1}{2} [B(X + B(X)Z) + 2B(X) - B(X - B(X)Z)]Z \quad (4A.4)$$

where Z has distribution $\Phi(Z)$ with mean zero and variance $\Delta t = \varepsilon^2$. We could work directly with (4.11a), but use of (4A.4) simplifies the math that follows. The density p_ε generated by the Markov-chain approximation (4A.4) satisfies the equation [LaBolle *et al.*, 1998]

$$\int_0^t \int f(x,s) \frac{\partial p_\varepsilon(x,s)}{\partial t} dx ds = \int_0^t \int L_\varepsilon f(x,s) p_\varepsilon(x,s) dx ds + o(\varepsilon^2) \quad (4A.5a)$$

$$L_\varepsilon f(x,t) = \frac{1}{\varepsilon^2} \int (f(z,t) - f(x,t)) p_\varepsilon(z, t + \varepsilon^2 | x, t) dz \quad (4A.5b)$$

where L_ε is commonly referred to as the generator (or infinitesimal operator) of the Markov chain [Arnold, 1992]. Expanding f in a Taylor series yields

$$\begin{aligned} & \varepsilon^2 \int_0^t \int f(x,s) \frac{\partial p_\varepsilon(x,s)}{\partial t} dx ds \\ &= \int_0^t \int \int (f(z,s) - f(x,s)) p_\varepsilon(z, s + \varepsilon^2 | x, s) p_\varepsilon(x,s) dx dz ds + o(\varepsilon^2) \\ &= \int_0^t \int \int \left[(z-x) f'(x,s) - \frac{1}{2} (z-x)^2 f''(x,s) \right] p_\varepsilon(z, s + \varepsilon^2 | x, s) p_\varepsilon(x,s) dx dz ds \\ &+ o(\varepsilon^2) \end{aligned} \quad (4A.6)$$

Noting that $(z-x)$ is a realization of $\Delta X(t)$, we have, retaining terms to order ε^2 .

$$\begin{aligned} & \int (z-x) p(z, t + \varepsilon^2 | x, t) dz \\ &= \frac{1}{2} \int [B(x + B(x)Z) + 2B(x) - B(x - B(x)Z)] Z \Phi(Z) dZ \\ &= \frac{1}{2} \int [B(x + B(x)Z) - B(x - B(x)Z)] Z \Phi(Z) dZ \end{aligned} \quad (4A.7a)$$

$$\begin{aligned} & \frac{1}{2} \int (z-x)^2 p(z, t + \varepsilon^2 | x, t) dz \\ &= \frac{1}{8} \int [B(x + B(x)Z) + 2B(x) - B(x - B(x)Z)]^2 Z^2 \Phi(Z) dZ \\ &= \varepsilon^2 \bar{D}(x) + o(\varepsilon^2) \end{aligned} \quad (4A.7b)$$

where $\bar{D} = (D_1 + D_2)/2$ at x_0 and $\bar{D} = B^2/2$ elsewhere. Substituting these relationships into (4A.6), we have

$$\begin{aligned} \varepsilon^2 \int_0^t \int f \frac{\partial p_\varepsilon}{\partial s} dx ds &= \int_0^t \int \int \left[(z-x)f' - \frac{1}{2}(z-x)^2 f'' \right] p_\varepsilon(z, s + \varepsilon^2 |x, s) p_\varepsilon dx dz ds \\ &= \frac{1}{2} \int_0^t \int \int [B(x+BZ) - B(x-BZ)] Z f' p_\varepsilon \Phi(Z) dx dZ ds \\ &\quad + \varepsilon^2 \int_0^t \int \bar{D} f'' p_\varepsilon dx ds + o(\varepsilon^2) \end{aligned} \quad (4A.8)$$

where we have dropped explicit reference to (x,t) . On the interval $[x_0 - B_1 Z, x_0 + B_2 Z]$, B on either side of x_0 will take on the value of B from the remaining side. For all such cases, in the limit,

$$\begin{aligned} \lim_{\varepsilon \rightarrow 0} \frac{1}{2\varepsilon^2} \int \int_{x_0 - B_1 Z}^{x_0 + B_2 Z} [B(x+B(x)Z) - B(x-B(x)Z)] Z f' p_\varepsilon \Phi(Z) dx dZ \\ = \lim_{\varepsilon \rightarrow 0} \frac{1}{2\varepsilon^2} \int \int_{x_0 - B_1 Z}^{x_0 + B_2 Z} (B_2 - B_1) Z f' p_\varepsilon \Phi(Z) dx dZ = \frac{1}{2} (B_2 + B_1) (B_2 - B_1) f' p_\varepsilon \Big|_{x_0} \\ = \frac{1}{2} (B_2^2 - B_1^2) f' p_\varepsilon \Big|_{x_0} = (D_2 - D_1) f' p_\varepsilon \Big|_{x_0} \end{aligned} \quad (4A.9)$$

Outside of this interval we have

$$\lim_{\varepsilon \rightarrow 0} \frac{1}{2\varepsilon^2} \int \int_{x \notin [x_0 - B_1 Z, x_0 + B_2 Z]} [B(x+BZ) - B(x-BZ)] Z f' p_\varepsilon \Phi(Z) dx dZ = 0 \quad (4A.10)$$

because D is constant in this case. From (4A.9) and (4A.10) we have, in the limit,

$$\lim_{\varepsilon \rightarrow 0} \frac{1}{2\varepsilon^2} \int \int [B(x+BZ) - B(x-BZ)] Z f' p_\varepsilon \Phi(Z) dZ dx = (D_2 - D_1) f' p_\varepsilon \Big|_{x_0} \quad (4A.11)$$

Substituting this result into equation (4A.8) yields, in the limit,

$$\begin{aligned} \int_0^t \int f \frac{\partial p_\varepsilon}{\partial t} dx ds &= \int_0^t \int \bar{D} f'' p_\varepsilon dx ds + \int_0^t (D_2 - D_1) f' p_\varepsilon \Big|_{x_0} ds \\ &= \int_0^t \int D f'' p_\varepsilon dx ds + \int_0^t (D_2 - D_1) f' p_\varepsilon \Big|_{x_0} ds \end{aligned} \quad (4A.12)$$

where the last equality is justified since singular values of $\bar{D} > 0$ have no effect on the diffusion process. Equation (4A.12) has the same form as (4A.3), therefore the density generated by (4A.4), and version (4.11a) of this approximation, satisfy (4A.3) associated with this equation. Similar results can be developed for the algorithm in (4.19a). In Appendix 4B we show how this result implies a stochastic calculus with generalized functions.

Appendix 4B: Stochastic Calculus with Generalized Functions

The forgoing result suggests that one can apply a stochastic calculus with generalized functions to obtain the desired result. For example, in one dimension expanding (4.9a) yields

$$\begin{aligned}
 dX &= B(X + BdW, t)dW \\
 &= B(X, t)dW + B(X, t)\frac{\partial B(X, t)}{\partial x}dWdW \\
 &= B(X, t)dW + \frac{\partial D(X, t)}{\partial x}dt \\
 &= B(X, t)dW + \frac{\partial D(X, t)}{\partial x}\Big|_{x \neq x_0} dt + [D_2(X, t) - D_1(X, t)]\delta(X - x_0)dt
 \end{aligned} \tag{4B.1}$$

which from standard theory corresponds to the diffusion equation

$$\frac{\partial p}{\partial t} = D \frac{\partial^2 p}{\partial x^2} + \left[\frac{\partial D}{\partial x} \Big|_{x \neq x_0} + (D_2 - D_1)\delta(x - x_0) \right] \frac{\partial p}{\partial x} \tag{4B.2}$$

Equation (4B.2) is equivalent to (4A.3) for the problem considered therein.

Appendix 4C: Taylor Series Expansion of Equation (4.15a)

When coefficients are smooth, (4.15a) is a SDE. Here we expand this equation to show that it is indeed equivalent to the SDE given in (4.2a). Expanding the second term in the right-hand-side of (4.15a) in Taylor series for sufficiently smooth \mathbf{D} and Θ yields:

$$\begin{aligned}
& \Theta^{-1/2}(\mathbf{X}, t) \sum_{j,k} \hat{B}_{ijk} \left(X_t + \Theta^{-1/2}(\mathbf{X}, t) \sum_{m,n} \hat{B}_{imn}(\mathbf{X}, t) dW_{m,t} \right) dW_j \\
&= \Theta^{-1/2}(\mathbf{X}, t) \sum_j \left(\sum_k \hat{B}_{ijk}(\mathbf{X}, t) + \Theta^{-1/2}(\mathbf{X}, t) \sum_{k,l,m,n} \frac{\partial \hat{B}_{ijk}(\mathbf{X}, t)}{\partial x_l} \hat{B}_{imn}(\mathbf{X}, t) dW_m + \dots \right) dW_j \\
&= \Theta^{-1/2} \sum_{j,k} \hat{B}_{ijk} dW_j + \Theta^{-1} \sum_{j,k,l,n} \frac{\partial \hat{B}_{ijk}}{\partial x_l} \hat{B}_{ijn} dt + o(dt) \tag{4C.1} \\
&= \sum_{j,k} \lambda_k^{1/2} Z_{ijk} dW_j + \Theta^{-1/2} \sum_{j,k,l,n} \frac{\partial}{\partial x_l} (\Theta^{-1/2} \lambda_k^{1/2} Z_{ijk}) \lambda_n^{1/2} Z_{ijn} dt + o(dt) \\
&= \sum_{j,k} \lambda_k^{1/2} Z_{ijk} dW_j + \Theta^{-1/2} \sum_{j,k,m,n} \frac{\partial}{\partial x_j} (\Theta^{-1/2} \lambda_n^{1/2} Z_{imn}) \lambda_k^{1/2} Z_{mjk} dt + o(dt)
\end{aligned}$$

where we have omitted explicit reference to evaluation of terms at (\mathbf{X}, t) and used the following relationships

$$Z_{ijk} = Z_{jik} \tag{4C.2a}$$

$$\sum_k Z_{ijk} = \delta_{ij} \tag{4C.2b}$$

$$\sum_m Z_{imn} Z_{mjk} = Z_{ijk} \delta_{nk} \tag{4C.2c}$$

where $\delta_{nk}=1$ for $n=k$ and 0 otherwise. Expanding the third term on the right-hand-side of (4.15a) in Taylor series yields

$$\begin{aligned}
& \Theta^{-1/2}(\mathbf{X}, t) \sum_{j,k,m,n} Z_{imn}(\mathbf{X}, t) \hat{B}_{mjk} \left(X_t + \lambda_n^{1/2}(\mathbf{X}, t) dW_{l,t} \right) dW_j \\
&= \Theta^{-1/2}(\mathbf{X}, t) \sum_{j,k,m,n} Z_{imn}(\mathbf{X}, t) \left(\hat{B}_{mjk}(\mathbf{X}, t) + \frac{\partial \hat{B}_{mjk}(\mathbf{X}, t)}{\partial x_l} \lambda_n^{1/2}(\mathbf{X}, t) dW_l + \dots \right) dW_j \\
&= \Theta^{-1/2} \sum_{j,k,m,n} Z_{imn} \left(\hat{B}_{mjk} dW_j + \frac{\partial \hat{B}_{mjk}}{\partial x_j} \lambda_n^{1/2} dt \right) + o(dt) \tag{4C.3} \\
&= \sum_{j,k} \lambda_k^{1/2} Z_{ijk} dW_j + \Theta^{-1/2} \sum_{j,k,m,n} \frac{\partial}{\partial x_j} (\Theta^{-1/2} \lambda_k^{1/2} Z_{mjk}) \lambda_n^{1/2} Z_{imn} dt + o(dt)
\end{aligned}$$

where again we have used (4C.2a)-(4C.2c) and omitted explicit reference to evaluation of terms at (\mathbf{X}, t) . Expressing (4.15a) in terms of (4C.1) and (4C.3) we have

$$\begin{aligned}
dX_i &= v_i dt + \sum_{j,k} \lambda_k^{1/2} Z_{ijk} dW_j \\
&+ \frac{1}{2} \Theta^{-1/2} \sum_{j,k,m,n} \lambda_k^{1/2} Z_{mjk} \frac{\partial}{\partial x_j} (\Theta^{1/2} \lambda_n^{1/2} Z_{imn}) dt \\
&+ \frac{1}{2} \Theta^{-1/2} \sum_{j,k,m,n} \frac{\partial}{\partial x_j} (\Theta^{1/2} \lambda_k^{1/2} Z_{mjk}) \lambda_n^{1/2} Z_{imn} dt + o(dt)
\end{aligned} \tag{4C.4}$$

which one can show is equivalent to (4.2a) using the following relationships:

$$\sum_k \lambda_k Z_{mjk} = \sum_{k,m,n} \lambda_n^{1/2} Z_{imn} \lambda_k^{1/2} Z_{mjk} = 2D_{ij} \tag{4C.5a}$$

$$\sum_k \lambda_k^{1/2} Z_{ijk} = \sum_{k,m,n} \lambda_k^{1/2} Z_{imn} Z_{mjk} = \left((2\mathbf{D})^{1/2} \right)_{ij} \tag{4C.5b}$$

$$\begin{aligned}
&\frac{1}{2} \Theta^{-1/2} \left[\sum_{j,k,m,n} \frac{\partial}{\partial x_j} (\Theta^{1/2} \lambda_n^{1/2} Z_{imn}) \lambda_k^{1/2} Z_{mjk} + \sum_{j,k,m,n} \lambda_n^{1/2} Z_{imn} \frac{\partial}{\partial x_j} (\Theta^{1/2} \lambda_k^{1/2} Z_{mjk}) \right] \\
&= \Theta^{-1} \frac{\partial}{\partial x_j} (\Theta D_{ij})
\end{aligned} \tag{4C.5c}$$

Chapter 5

On the Role of Molecular Diffusion in Contaminant Migration and Remediation in an Alluvial Aquifer System

5.1 Introduction

In this paper, we explore the role heterogeneity and diffusion in the migration and recovery of a conservative solute in an alluvial aquifer system underlying Lawrence Livermore National Laboratory (LLNL), Livermore, California (Figure 1). Specifically, we are concerned with the sequestration of contaminants in low-permeability materials, the role of diffusion in this process, and its effects on pump-and-treat (PAT) remediation at the site. Other mechanisms known to sequester contaminants, including entrapment of non-aqueous phase liquid (NAPL) contamination or biogeochemical conditions favoring degradation and *significant* reduction of mobility due to sorption, have not been observed in the saturated sediments of the site [Hoffman *et al.*, 1997]. Nevertheless, contaminant concentrations persist near suspected source areas, even after years of active PAT remediation. As the LLNL site is highly heterogeneous with a large volume fraction of low-permeability silts and clays, dispersion, accelerated by diffusion into these materials, arises as a primary mechanism for the natural attenuation of contaminant migration. This study is facilitated by generic numerical simulations of flow and transport in detailed

-

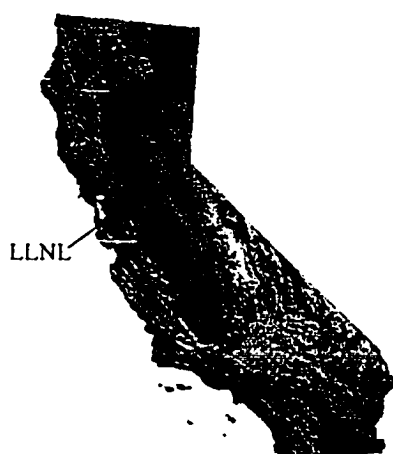


Figure 5.1: Location Lawrence Livermore National Laboratory.

transition-probability based geostatistical simulations of the LLNL site [Carle, 1996; Carle *et al.*, 1998]. Models are resolved to a discretization of 10.0 m, 5.0 m and 0.5 m in the strike, dip and vertical directions of the alluvial fan system. To our knowledge, this work constitutes the first use of geologic characterizations in such detail to explore the role of diffusion in contaminant migration and remediation in highly heterogeneous aquifers.

5.2 Background

Extraction of contaminated groundwater by means of wells (PAT) is the most common remedial technology employed today [NRC, 1994; Berglund, 1995]. The National Research Council (NRC) [1994] recently acknowledged that, at most waste sites, aquifer restoration by PAT is theoretically possible, but time frames to achieve drinking water standards may be unreasonably long, in some cases perhaps centuries. At many contamination sites, reasons for long times to cleanup using PAT technology have been attributed, in part, to the sequestration of contaminants in regions relatively inaccessible to

flow [Mackay and Cherry, 1989; Mercer et al., 1990; Nyer, 1993; NRC, 1994; Berglund, 1994; Berglund and Cvetkovic, 1995].

Alluvial aquifer systems commonly contain substantial volume fractions, as high as 20 to 80 percent, of low conductivity (K) silts and clays. The groundwater in such regions is not necessarily immobile; nevertheless, transport may often be approximated as purely diffusive when time-scales associated with advective transport are very long compared to those of molecular diffusion. Once present in low-permeability materials, contaminants may act as long-term sources with migration rate controlled by molecular diffusion [Mackay and Cherry, 1989; Mercer et al., 1990; NRC, 1994; Cohen et al., 1997]. Mean residence times for contamination in low-permeability materials with length scales on the order of meters, and transport controlled by the rate of diffusion, may be on the order of centuries to millennia.

Matrix diffusion has been recently acknowledged as an effective passive, or natural attenuation, remedial technology [OSWER Directive 9200.4-17, 1997]. In 1997, the EPA endorsed natural attenuation as a means of achieving remediation objectives stating that “natural attenuation processes may reduce contaminant mass or concentration at sufficiently rapid rates to be integrated into a site’s soil or groundwater remedy” [OSWER Directive 9200.4-17, 1997]. The role of dilution in the risk posed by contamination depends on the character of the structure and distribution of subsurface materials, as well as their hydraulic and transport properties. The OSWER Directive 9200.4-17 [1997] concludes that “decisions to employ monitored natural attenuation as a remedy or remedy component should be thoroughly and adequately supported with site specific characterization data and analysis.”

Realistic site-specific predictions of transport must account for the complex geometry of subsurface materials and their associated hydraulic and transport properties, while honoring lithologic data [NRC, 1994]. Due to the practical limitations of most site characterization efforts, however, data are usually gathered from only a fraction of a percent of the subsurface. Because the subsurface is inherently heterogeneous, the usual paucity of data renders deterministic site characterization an impossible task. Indeed, previous studies demonstrating the important role of matrix diffusion in attenuating the contaminant migration (e.g., *Gillham et al.*, 1984; *Feenstra et al.*, 1984; *Wilson, et al.*, 1993) have relied simple models as surrogates for real heterogeneous systems.

Sparse data in the face of complex heterogeneity has motivated development of stochastic subsurface transport theory (e.g., *Gelhar and Axness*, 1983; *Gelhar*, 1986; *Gelhar*, 1993; *Dagan*, 1989). Stochastic theoretical models treat subsurface flow and transport in a probabilistic framework with hydraulic and transport properties as random functions of space. Prevailing models generally rely on simple boundary conditions and characterizations of heterogeneity amenable to analytical solution. Such simplifications can lead to unrealistic results, e.g., that predict effects of pore-scale dispersion and diffusion are negligible for statistically isotropic media (e.g., *Gelhar and Axness*, 1983; *Gelhar*, 1986; *Gelhar*, 1993) or completely ignore these processes [*Dagan*, 1989; *Cvetkovic et al.*, 1991]. *Cvetkovic et al.* [1991] state that “except for stratified formation[s] with flow parallel to stratifications and large travel time (*Matheron and de Marsily*, 1980) pore scale dispersion [including molecular diffusion] has been found to play a minor role compared to heterogeneity ...” This conclusion begs the question: How can pore-scale dispersion “play a minor role” in the migration of contaminants when large volume frac-

tions of low-permeability clays and silts, often as high as 50% or more, are common to most sedimentary systems, including many alluvial-fan and fluvial deposits of the western United States and elsewhere. At present, theoretical models applicable to complex geologic systems and boundary and initial conditions of real flow problems are not available, emphasizing the need for alternative approaches that account for uncertainty and complex heterogeneity in predictions of contaminant migration.

One alternative to dealing with complex heterogeneity is to construct detailed numerical models that describe the character of subsurface heterogeneity and honor lithologic data crucial for prediction. Geologic process-based models [Tezloff and Harbaugh, 1989; Koltermann and Gorelick, 1992] and geostatistical simulation methods [Deutsch and Journel, 1992; Poeter and Mckenna, 1995; Carle et al., 1998] can simulate three-dimensional stratigraphic sequences in detail [Carle, 1996]. It is generally difficult to generate process-based simulations that honor lithologic data [Carle, 1996]. Conditional geostatistical simulation methods can honor lithologic data, but most techniques rely on abundant data (not generally available) to quantify spatial variability. Alternatively, the transition probability-based geostatistical approach of Carle et al. [1998] can be used to build plausible models of spatial variability from interpretive and quantitative analyses of geologic systems; these models are used to simulate detailed three-dimensional stratigraphic sequences that honor lithologic data [Carle, 1996]. Importantly, this approach acknowledges the role of uncertainty in subsurface characterization and has been used successfully to simulate hydrostratigraphic sequences that reproduce field observations from well interference tests [Carle, et al., 1996] and isotopic studies of mean groundwater age [Tompson et al., 1998].

Presently, detailed characterizations of subsurface heterogeneity are not used in the design of remediation systems and the study of processes that affect their performance. To our knowledge, this paper presents the first study using detailed (on the order of meters) site-specific characterizations to explore the role of diffusion in the migration of contaminants and PAT remediation system performance on a decadal time scale. This paper is organized as follows: a brief introduction to the LLNL site is presented followed by a description of the stochastic modeling procedure including geostatistical site characterization and flow and transport simulations; finally, we explore the role of diffusion in contaminant migration and PAT system performance.

5.3 Study Area

Lawrence Livermore National Laboratory (LLNL) is located in the Livermore Valley of the Coast Range of California (Figure 5.1). The aquifer system consists of a network of ancient stream channel, levee and debris flow deposits embedded in fine-grained low-permeability floodplain deposits [Noyes, 1991; Carle *et al.*, 1998]. The saturated unconsolidated materials of the site generally exhibit a low organic carbon content (< 0.1%) and biogeochemical conditions favoring contaminant degradation and significant reduction of mobility due to sorption have not been observed [Hoffman *et al.*, 1997]. Thus dispersion and dilution appear to be the primary mechanisms for the natural attenuation of contaminant migration.

The numerous contaminants, primarily volatile organic compounds, present in the alluvial fan deposits underlying the site extend over a region of several km² and to depths as great as 100 m [Thorpe *et al.*, 1990; Carle *et al.*, 1998]. This study focuses on a portion of the upper aquifer, the detailed study described in Chapter 5 of Carle [1996] (Fig-

ure 5.2). Groundwater contamination, consisting primarily of trichloroethylene (TCE) and perchloroethylene (PCE), is believed to have originated from multiple sources some 50 years ago [Tompson, 1998]. The coarse monitoring network of the site has generally been in operation largely less than 10 years, so detailed observations of contaminant transport are limited. Contamination is believed to exist primarily in the dissolved phase as non-aqueous phase liquids (NAPLs) have not been observed. Nevertheless, high concentrations are generally observed close to suspected or known contaminant source areas. Contamination is slowly moving toward municipal wells of the City of Livermore; PAT is currently being used for remediation and plume containment. During the course of more than 8 years of remediation, distal plumes have shown dramatic reductions in concentration whereas concentrations of source areas have generally persisted [Hoffman, 1997]. One objective of this study is to explore the role of diffusion in the phenomenon through the use of detailed simulations of flow and transport.

5.4 Simulation Procedure

The simulation procedure consists of (1) generating 10 conditional simulations of hydrostratigraphic architecture, (2) specifying hydraulic and transport properties of hydrofacies, (3) simulating steady-state ambient and stressed (in response to pumping) groundwater flow fields, (4) simulating scenarios of ambient contaminant migration followed by migration in response to PAT remediation.

Ideally, to fully describe ensemble transport characteristics, one would hope to implement this procedure with many more than 10 conditional simulations. However, the scope of this work does not include a characterization of transport in a large ensemble of realizations. Computational limitations at the time this work was performed prohibited

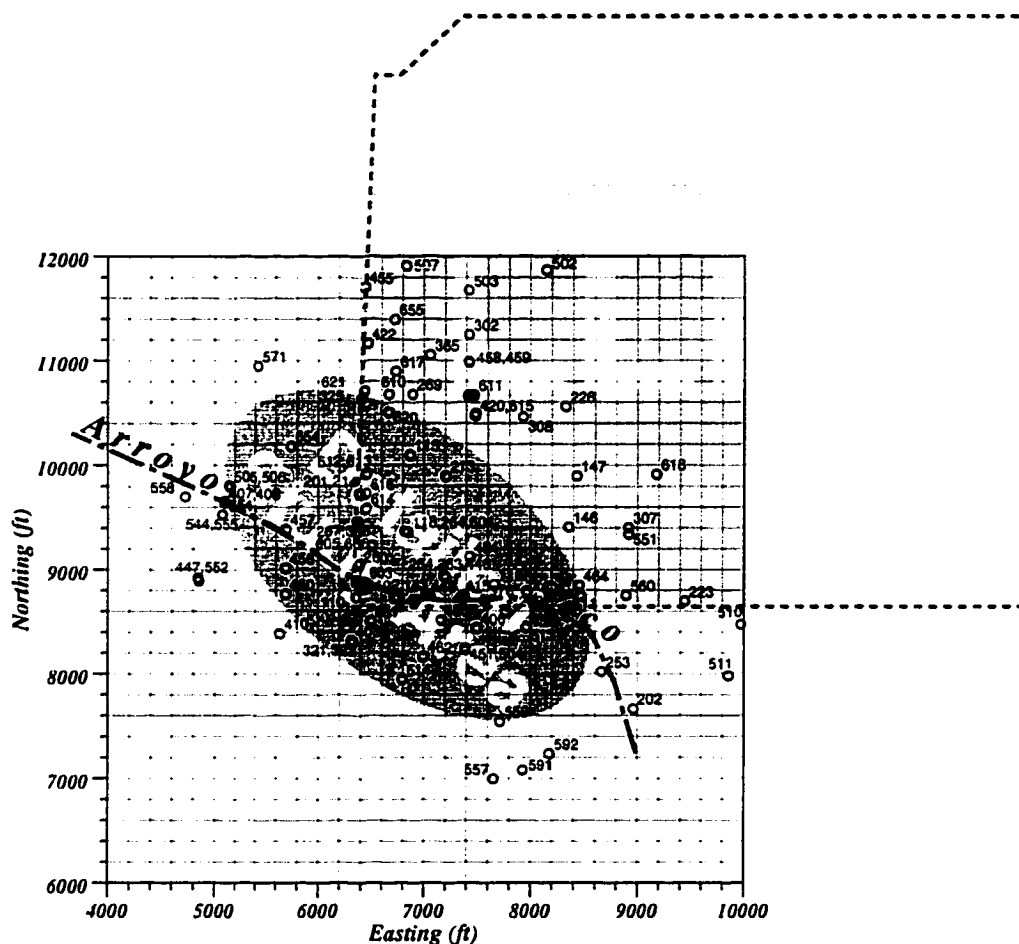


Figure 5.2: Detailed study area (after Carle [1996]).

such a study. Nevertheless, the 10 realizations considered are associated with a wide range of transport behavior likely characteristic of such an ensemble.

5.4.1 Geostatistical Simulations

Details of the transition probability-based indicator geostatistical simulations of the field site are described in Carle [1996] and [Carle *et al.*, 1998]. A brief description of these simulations is given here for completeness.

Four hydrofacies, debris flow (7%), floodplain (56%), levee (19%), and channel (18%), were identified from detailed interpretations [Noyes, 1991; Fogg *et al.*, 1998] of

5,500 m of core and subsequently used in the classification of the remainder of the core through interpretation of geophysical logs and textural descriptions of site geologists. This data encompassed a much larger area than the field site considered herein. Vertical transition probability models were measured directly from the data whereas strike and dip direction models are established through geologic interpretation as described in *Carle and Fogg* (1997) and *Carle et al.* [1998]. Mean lengths of the 4 hydrofacies in the dip, strike and vertical directions are summarized in Table 5.1. Elliptical interpolation of transition rates was used to construct the three-dimensional Markov chain models shown for the strike-vertical (x - z), strike-dip (x - y) and dip-vertical (y - z) planes in Figures 5.3, 5.4 and 5.5, respectively. Finally, the geostatistical techniques described in *Carle* [1996] and *Carle et al.* [1998] were used to conditionally simulate 10 realizations of hydrostratigraphy on a rectilinear computational grid with discretization Δx (strike) = 5.0 m, Δy (dip) = 10.0, and Δz (vertical) = 0.5 m, and dimension 81 cubed, as shown in Figures 5.6 and 5.7 for realizations 4 and 7, respectively. The top of the simulation roughly corresponds to the observed water table. On the average, approximately 80% of the channel hydrofacies form a connected network extending in all directions and connecting all boundaries of the domain. Simulations 1 through 10 of this paper are identical to simulations 2 through 11 of *Carle* [1996].

Table 5.1: Mean lengths (m) of hydrofacies in the strike, dip and vertical directions in Markov-chain model.

Hydrofacies	Direction		
	Strike	Dip	Vertical
Debris flows	8.0	24.0	1.1
Floodplain	26.6	66.9	2.1
Levee	6.0	20.0	0.8
Channel	10.0	50.0	1.3

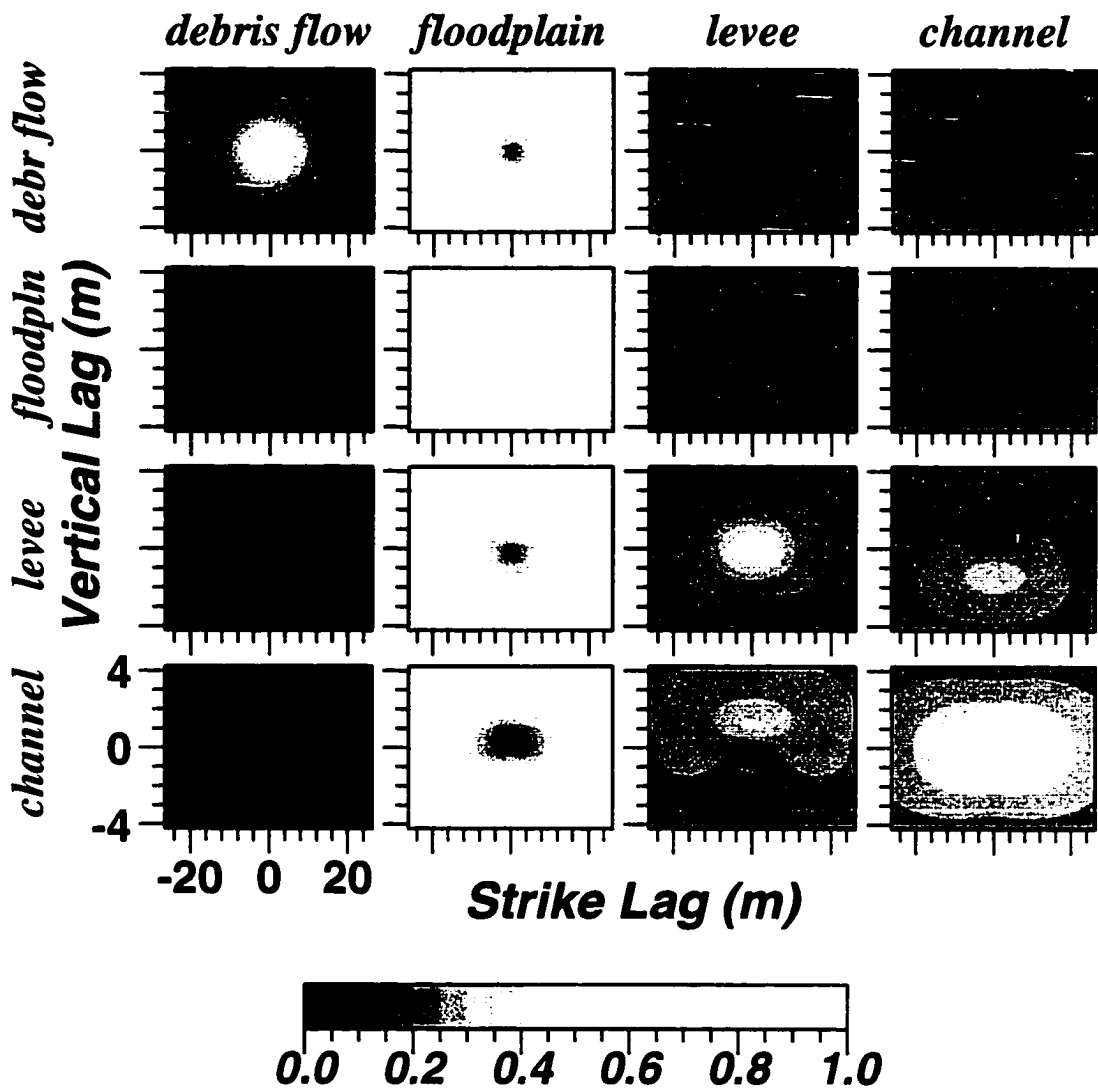


Figure 5.3: Cross section in strike-vertical ($x-z$) plane of interpolated Markov chain model (after Carle [1996]).

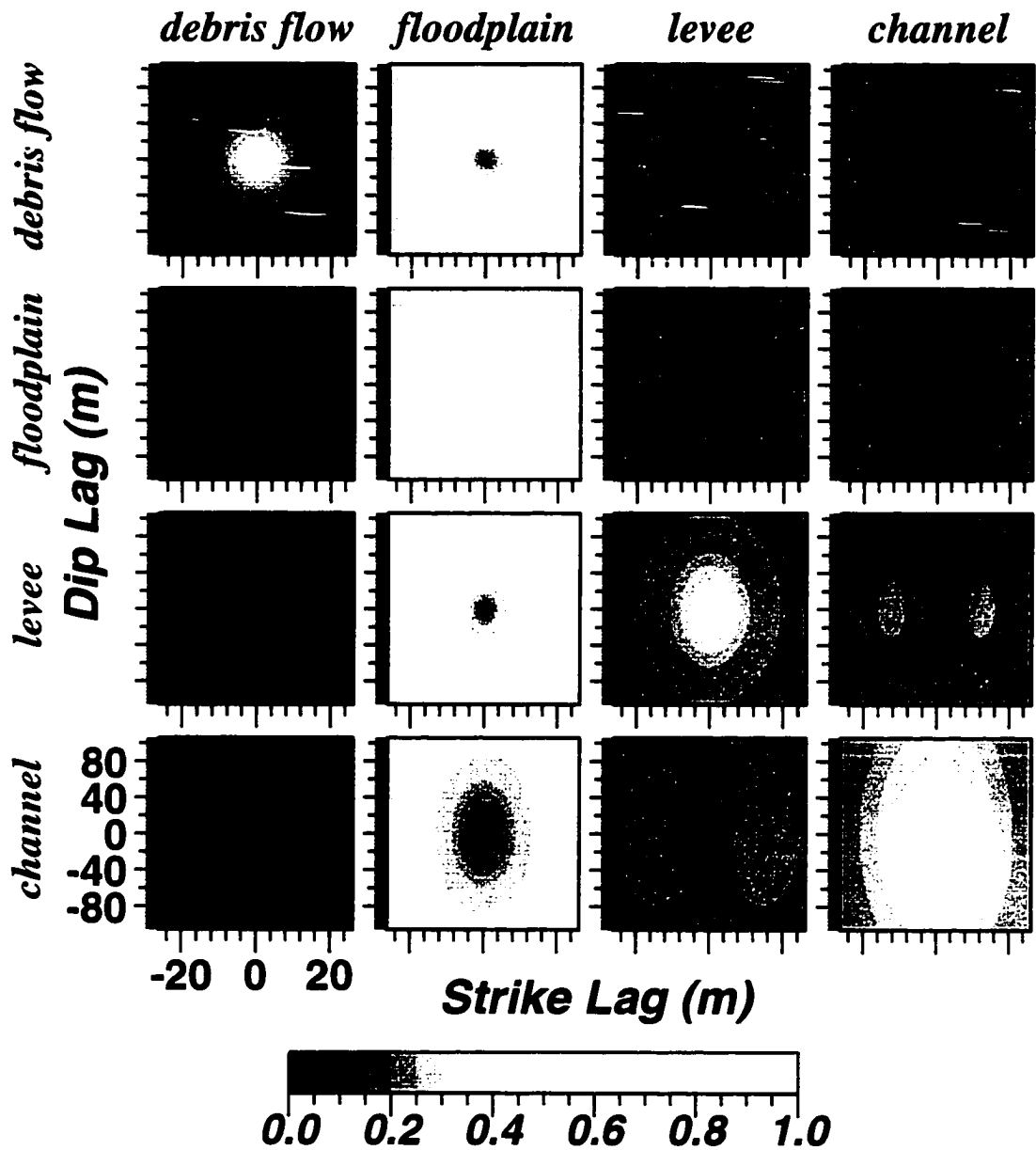


Figure 5.4: Cross section in strike-dip (x - y) plane of interpolated Markov chain model (after Carle [1996]).

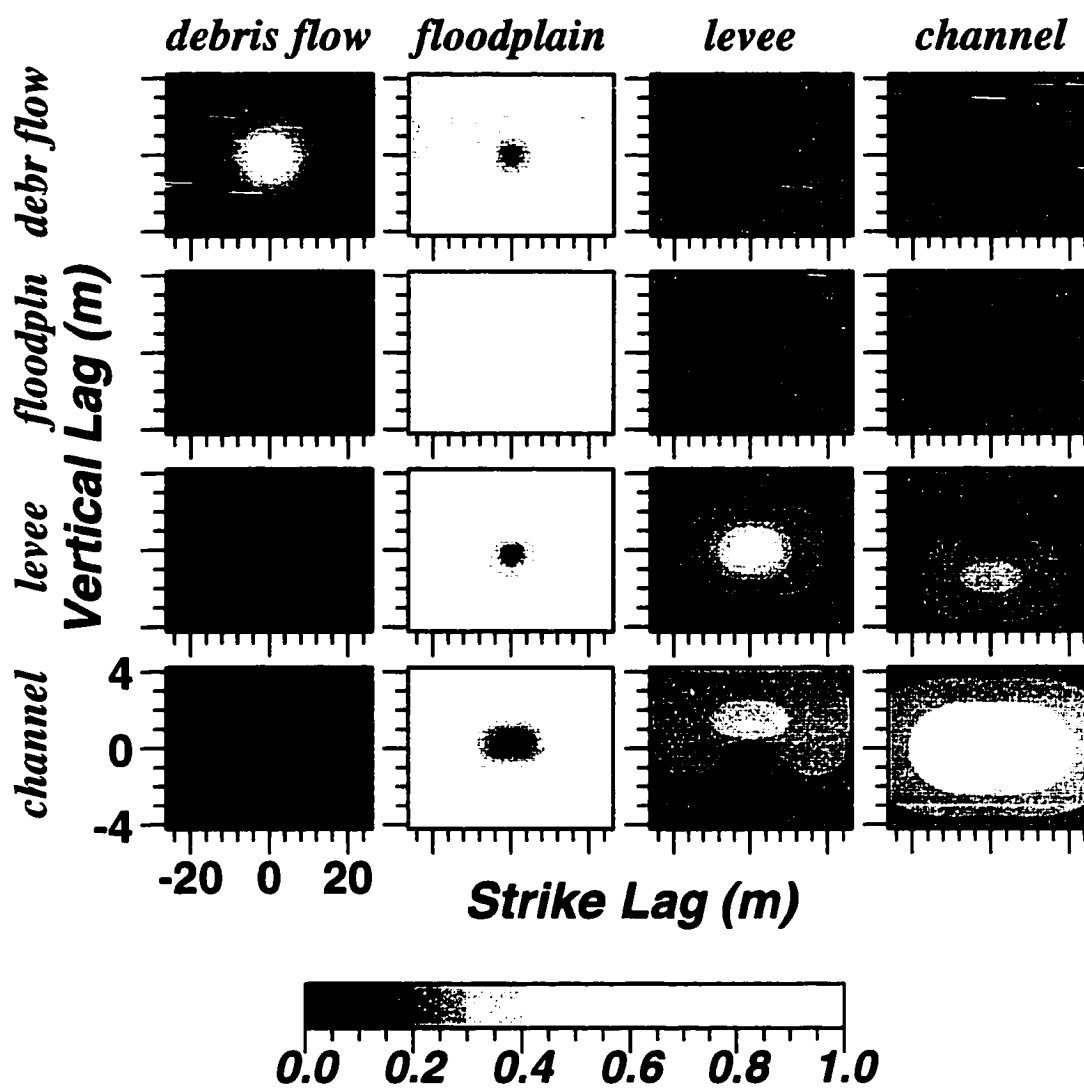


Figure 5.5: Cross section in dip-vertical (y - z) plane of interpolated Markov chain model (after Carle [1996]).

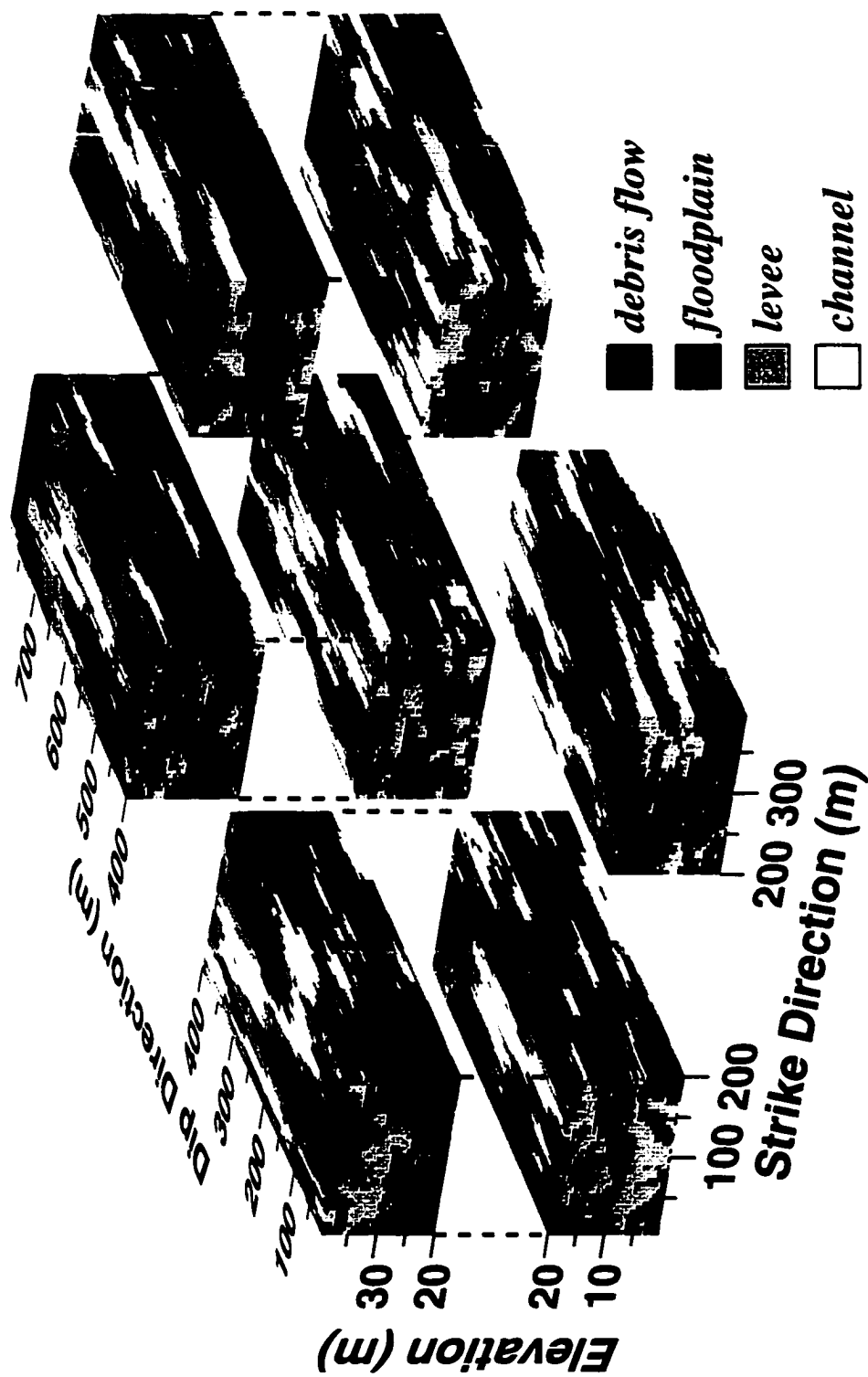


Figure 5.6: Conditional simulation of hydrostratigraphic architecture (realization 4). The pumping well is located in the channel hydrofacies units at the center of the system.

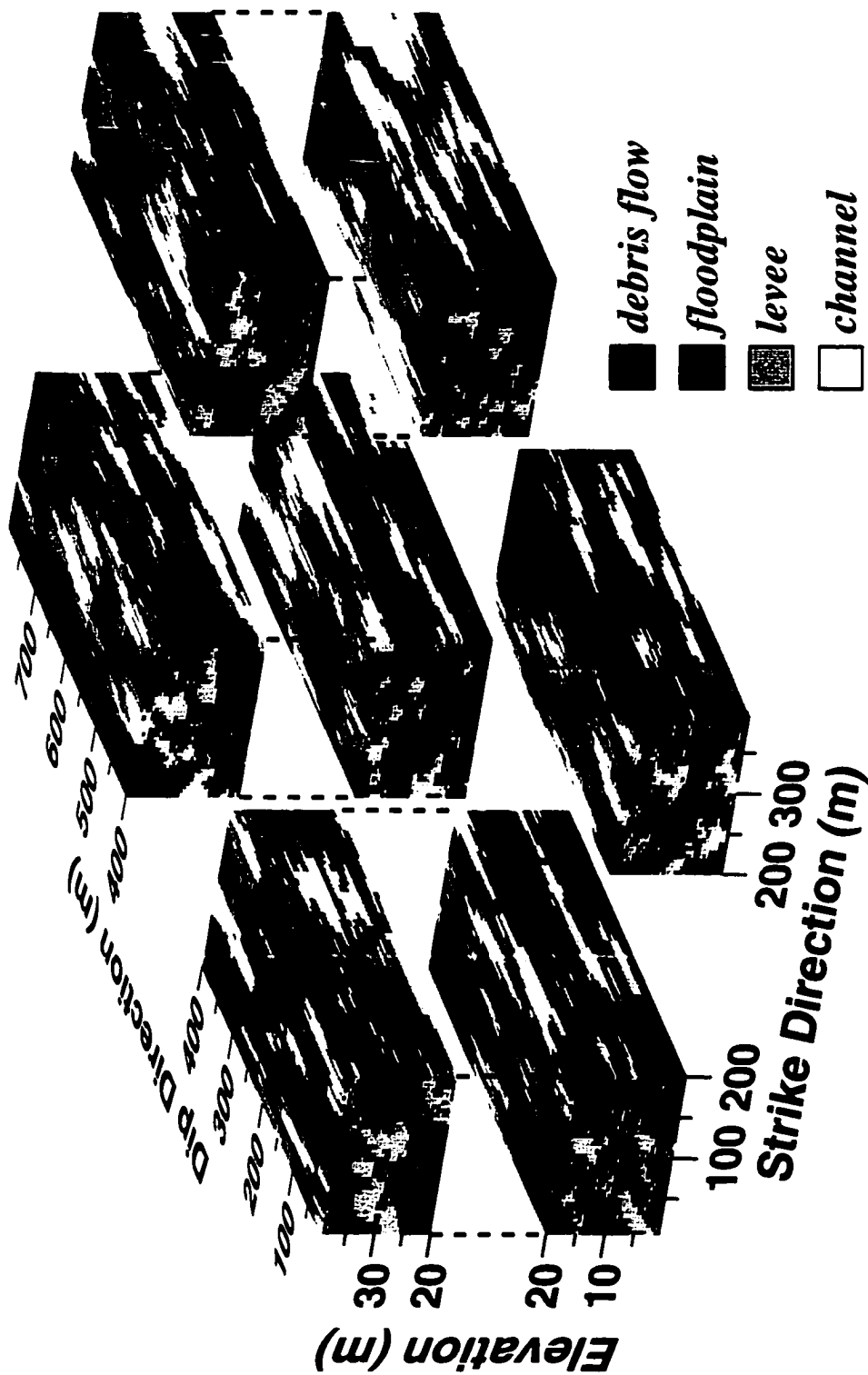


Figure 5.7: Conditional simulation of hydrostratigraphic architecture (realization 7). The pumping well is located in the channel hydrofacies units at the center of the system.

5.4.2 Flow Simulations

Steady-state saturated flow in the system illustrated in Figure 5.8 is described by

$$\frac{\partial}{\partial x_i} \left(K(\mathbf{x}) \frac{\partial h(\mathbf{x})}{\partial x_i} \right) = \sum_w Q_w \delta(\mathbf{x} - \mathbf{x}_w) \quad (5.1)$$

where $h(\mathbf{x})$ is hydraulic head [L], $K(\mathbf{x})$ is hydraulic conductivity [LT^{-1}] (assumed to be isotropic) and Q_w [L^3T^{-1}] is the rate withdrawal due to pumping at location \mathbf{x}_w . Boundary conditions of the flow problems include general head boundaries (GHBs) [McDonald and Harbaugh, 1988] assigned to grid block on vertical and bottom faces and recharge from above assigned to grid blocks on the top face. The saturated flow problems are solved via a block-centered finite difference scheme (see Chapter 2). Due to computational limitations, the model domain includes only a small fraction of the flow system as defined by natural hydrologic boundaries of the aquifer system. The use of GHBs allows for flow to and from the model in response to stresses without the need to extend the computational grid. GHBs are assigned to model nodes on all sides of the domain (Figure 5.8), with the exception of the top (as described in Appendix 5A) to maintain an ambient regional gradient of approximately 0.002 in the dip direction and a small vertical gradient consistent with the recharge boundary at the water table. Recharge is distributed to nodes at the water table as described in Appendix 5A at a rate of 0.034 m/year.

The simulation methodology used here assigns hydraulic properties to the direct outcome of transition probability-based indicator simulations without further grid refinement, i.e., with no variability of properties within hydrofacies. This approach will result, for example, in some instances where grid blocks are isolated in a matrix of contrasting conductivity (see Figure 5B.1). In most cases, a facies body contains multiple nodes vertically

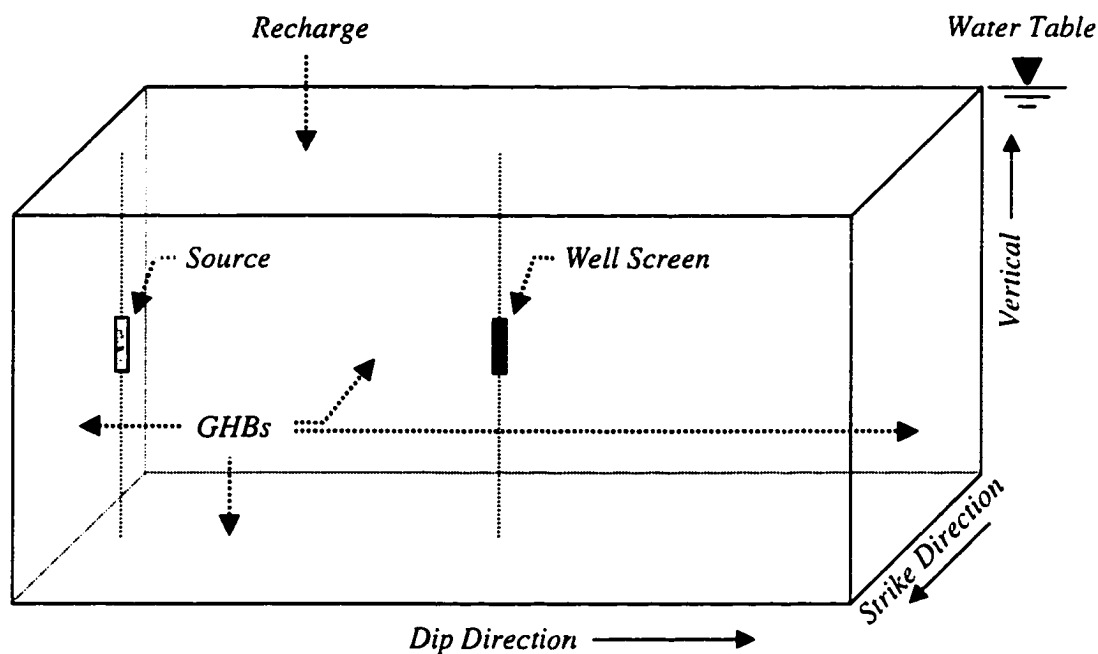


Figure 5.8: Schematic of flow system. The mean direction of flow is in the dip direction.

and horizontally. Nevertheless, as numerical grids are refined (Figure 5B.1), accuracy of flow solutions will improve. Effects of these improvements on flow and transport are considered in grid refinement experiments described in Appendix 5B. Results of these experiments suggest that resolving the numerical grid does not necessarily result in a systematic trend in change in solution. Further, changes with grid refinement are small enough so as to not affect the general nature of the results to be presented herein.

The distributions of field and core measurements of hydraulic conductivity within hydrofacies are shown in Figure 5.9. Hydraulic conductivity values in flow simulations are assigned as constants to hydrostratigraphic units under the assumption that spatial variability within units is small compared to variability between units [Carle, 1996; Fogg *et al.*, 1998]. Carle [1996] successfully calibrated hydraulic conductivity (Table 5.2) of

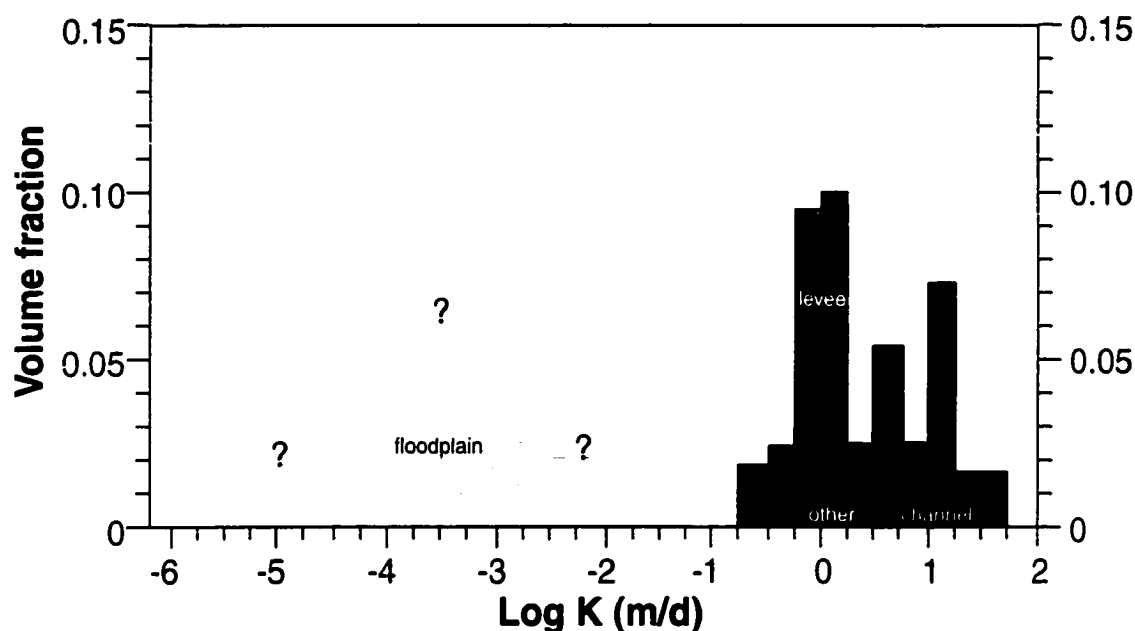
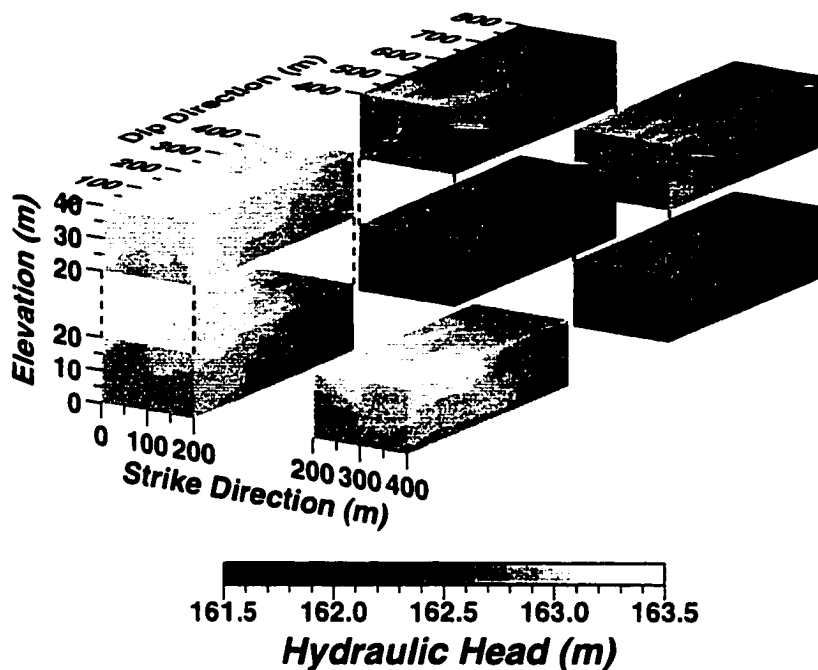


Figure 5.9: Hydraulic conductivity distribution categorized by hydrofacies (from *Fogg et al.*, 1998).

the hydrofacies of the study area to a 24-hour well interference test conducted in April of 1994. *Carle* [1996] observed that system response was particularly sensitive to the specified conductivity of floodplain hydrofacies. Recent measurements of conductivity core from the site (see *Tompson* [1998]) confirm the assumed range, indicated in Figure 5.9 by the question marks, and support use of the calibrated value shown in Table 5.2.

Two steady-state hydraulic scenarios are considered, natural gradient conditions (ambient) and stressed hydraulic conditions corresponding to pumping from well MW-612 (Figure 5.8) at a rate of $50 \text{ m}^3/\text{day}$, comparable to rates applied at the site. Simulated hydraulic heads of realizations 4 and 7 for ambient and stressed hydraulic conditions are shown in Figures 5.10 and 5.11, respectively. Average drawdown of the water table ranged from approximately 0.5 m to 1.0 m, suggesting that the approximation of unconfined conditions as confined has introduced little error in the flow field. Flow simulation results define velocities used in the transport simulation, which are described below.

(a)



(b)

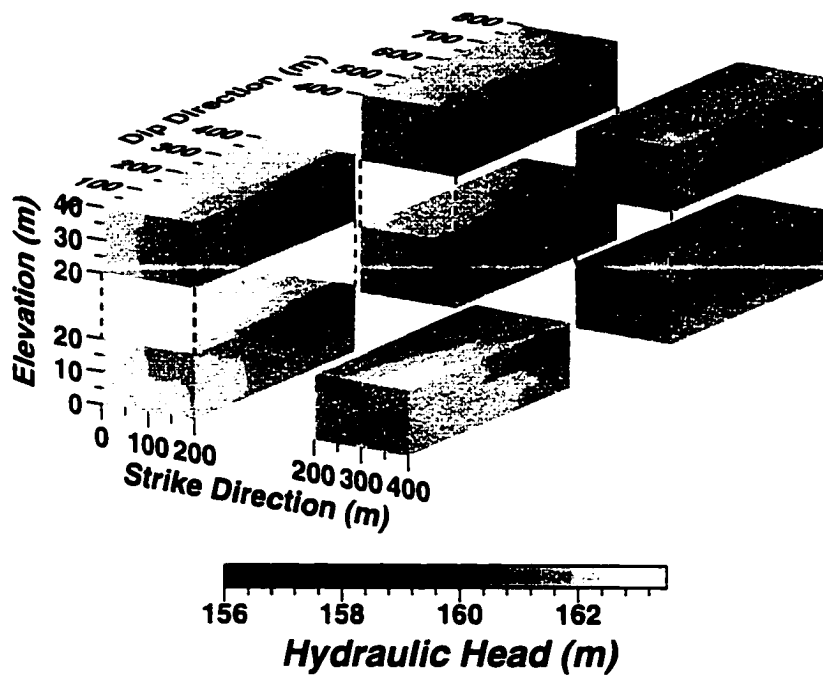
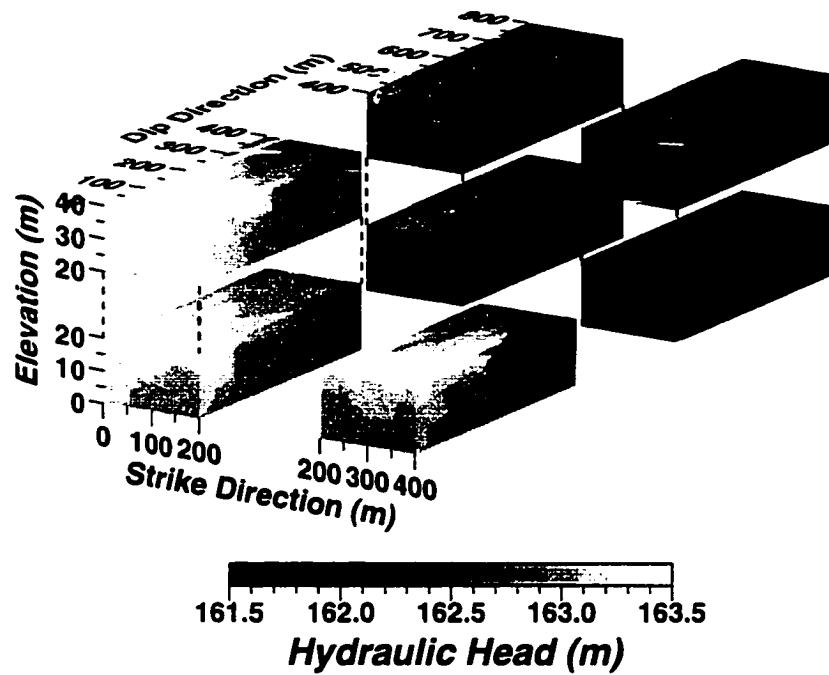


Figure 5.10: Hydraulic head of realization 4 with (a) ambient and (b) stressed hydraulic conditions - pumping well located at the center of the system.

(a)



(b)

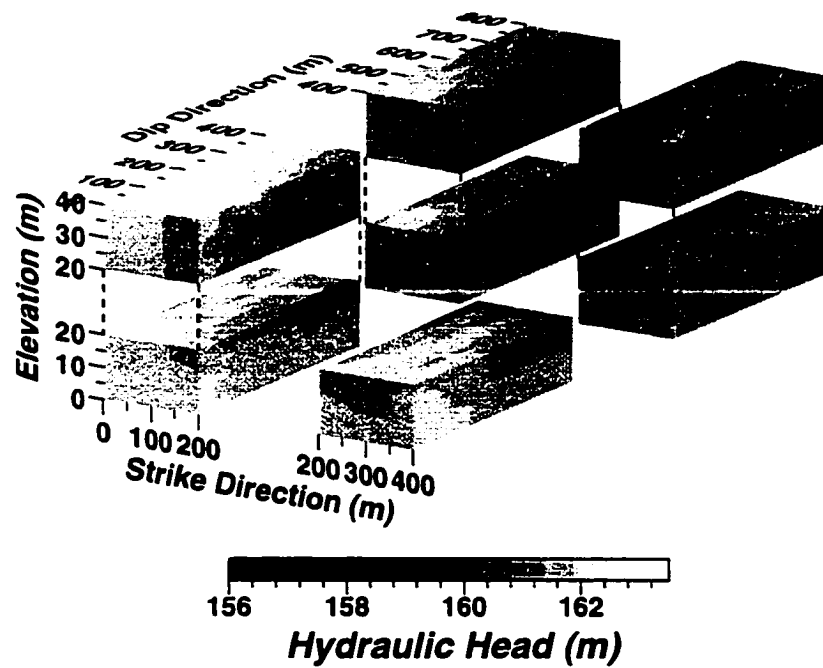


Figure 5.11: Hydraulic head of realization 7 with (a) ambient and (b) stressed hydraulic conditions - pumping well located at the center of the system.

Table 5.2: Hydraulic Properties of Hydrofacies

Hydrofacies	K (m/day)
Debris flows	0.432
Floodplain	4.32×10^{-5}
Levee	0.173
Channel	5.184

5.4.3 Transport Simulations

For the purposes of this study, the solute is assumed to be conservative and nonsorbing. Further, we assume that, due to the highly-resolved numerical grids, variability of hydraulic properties within hydrostratigraphic units is small compared to variability between units and that transport within hydrostratigraphic units is described by a local-scale advection-dispersion equation of the form

$$\frac{\partial c(\mathbf{x}, t)}{\partial t} = - \sum_i \frac{\partial}{\partial x_i} (v_i(\mathbf{x}, t) c(\mathbf{x}, t)) + \sum_{i,j} \frac{\partial}{\partial x_i} \left(D_{ij}(\mathbf{x}, t) \frac{\partial c(\mathbf{x}, t)}{\partial x_j} \right) \quad (5.3)$$

where c is aqueous-phase contaminant concentration, $\mathbf{v} = -K\nabla h/\Theta$ is pore-water velocity, where Θ is an effective porosity (approximated as a constant), and \mathbf{D} is a hydrodynamic dispersion tensor with form

$$D_{ij}(\mathbf{x}, t) = (|\mathbf{v}(\mathbf{x}, t)|\alpha_T + D^*)\delta_{ij} + (\alpha_T - \alpha_L)v_i(\mathbf{x}, t)v_j(\mathbf{x}, t)/|\mathbf{v}(\mathbf{x}, t)| \quad (5.4)$$

where α_T and α_L are transverse and longitudinal dispersivity [L], respectively, D^* is an effective molecular diffusivity [L^2T^{-1}] that accounts for tortuosity, but not a porosity flux correction, as described in the following section.

5.4.3.1 Transport Parameters

Parameters of equation (5.3) include Θ , α_L , α_T and D^* . Dispersivities are approximated as constants. Results presented in Appendix 5C for sensitivity of

contaminant migration to dispersivity show that field scale transport is relatively insensitive to local-scale α_L . Therefore, all simulations will use an isotropic dispersivity, $\alpha_L = \alpha_T$. Based on the assumption of a small degree of local-scale heterogeneity, a local-scale dispersivity of 10^{-2} m is assumed. This value is much closer to reported pore-scale transverse dispersivity values, on the order of 10^{-4} m to 10^{-3} m [Robbins, 1989; Gelhar, 1993], than to asymptotic field-scale values reported for LLNL, on the order of 0.5 m and 5 m in the vertical and strike directions, respectively [Tompson, 1998].

Effective pore-scale aqueous-phase molecular diffusivity in a porous medium is a function of the pore geometry of that medium and the aqueous-phase molecular diffusivity D_{aq} of the constituent. The mean-squared displacement of aqueous-phase solute molecules diffusing in porous media during a time interval Δt is given by the relationship (see equation 3.4b of Chapter 3)

$$\left\langle \sum_i \Delta X_i^2 \right\rangle \propto \tau^{-2} D_{aq} \Delta t = D^* \Delta t \quad (5.3)$$

where the tortuosity $\tau = l_e/l$ accounts for the tortuous paths of length l_e [L] molecules must travel on average to move a distance l in a straight line. Application of D^* in a model of diffusive transport must also account for porosity Θ such that the diffusive flux \mathbf{J}^* takes the form

$$J_i^* = -\Theta(\mathbf{x}) D^*(\mathbf{x}, t) \partial c(\mathbf{x}, t) / \partial x_i \quad (5.4)$$

The molecular diffusivity in water-saturated pores of a porous medium will be independent of pore geometry and equivalent to the aqueous-phase molecular diffusivity D_{aq} provided the mean-free path of a solute molecule is sufficiently smaller than the pore diameter. In cases where the pore diameter is small enough to affect significantly the

molecular diffusivity in the pores, the molecular-diffusion-controlled diffusion process is referred to as Knudsen diffusion. While the latter occurs to some extent in most natural porous media, the mean-free path of most solutes in groundwater under typical field conditions is small relative to the pore geometry of most of the subsurface. Therefore, Knudsen diffusion effects in the current context are assumed to be negligible [Grathwohl, 1998].

Molecular diffusion at the local scale can be an important component of the dispersion process and may be the dominant transport process where time scales associated with advection are much smaller than those of molecular diffusion. These time scales are on the order of $\langle \Delta t_v \rangle = a/|v|$ and $\langle \Delta t_D \rangle = a^2/D^*$ (note that the latter may be deduced from equation 5.3), respectively, where a is a length scale associated with the hydrofacies unit of interest. The ratio $\langle \Delta t_D \rangle / \langle \Delta t_v \rangle$ yields a Peclet number $P_e = |v|a/D^*$ that describes the relative role of advection and diffusion (where we neglect mechanical dispersion). Where $P_e \ll 1$, diffusion may be considered the dominant transport process. Table 5.3 describes the relative influence of diffusion and advection in the 4 hydrofacies units. Calculations, based on regional gradients, calibrated hydraulic conductivity values, and average length scales of hydrofacies units, show that diffusion will tend to control transport in low-permeability floodplain hydrofacies. Due to a moderate dip in the bedding plane and the presence of vertical gradients due to recharge, flow will tend to be horizontal in high- K units and predominately vertical in low- K units. Therefore, these calculations are based on horizontal length scales for channel, levee and debris flow hydrofacies, and vertical length scales for floodplain hydrofacies. Similar results, to those shown in Table 5.3, can be expected under stressed conditions, except in the direct vicinity of the pumping well,

Table 5.3: Controlling Transport Process in Hydrofacies

Hydrofacies	Length Scale a (m)	P_e^a	Dominant Transport Process
Debris flows	24.0	5.9×10^{-3}	Advection
Floodplain	2.1	5.1×10^{-2}	Diffusion
Levee	20.0	2.0×10^{-3}	Advection
Channel	50.0	1.5×10^{-5}	Advection

^a $P_e = Kia/D^* \Theta$, where $\Theta = 0.35$, the regional gradient $i = 0.002$, and $D^* = 10^{-5} \text{ m}^2/\text{day}$.

where gradients could be large enough to induce significant flow through floodplain units. Note that hydraulic conditions may also give rise to low-velocity regions (stagnation zones) in high-permeability hydrofacies.

Effects of diffusion will be most significant in low-permeability clays of the floodplain hydrofacies. *Grathwohl* [1998, p. 92] reported measured values of D^* for TCE in natural clays at 20° C (approximately the average groundwater temperature at LLNL) ranging from approximately 1×10^{-6} to $5.0 \times 10^{-4} \text{ m}^2/\text{day}$. Here, measured values of D^* may include sorption effects; this may account for the large range of reported values. One should expect that the high end of this range must be limited to a theoretical maximum of $D^* = D_{aq} = 9.0 \times 10^{-5} \text{ m}^2/\text{day}$ at 20° C [*Grathwohl*, 1998]. To arrive at a theoretical estimate for a maximum value for D^* , we use the relationship $\tau^{-2} \approx \Theta^{1/2}$ [*Grathwohl*, 1998, p. 34], and assume a maximum $\Theta = 0.45$ for clays of floodplain hydrofacies, to yield a value of $D^* = \Theta^{1/2} D_{aq} = (\sqrt{0.45})(9.0 \times 10^{-5} \text{ m}^2/\text{day}) = 5.2 \times 10^{-5}$, roughly equal to an average of the measured values given in *Grathwohl* [1998, p. 92]. We will assume that the range of uncertainty for D^* is between 10^{-6} and $5.2 \times 10^{-5} \text{ m}^2/\text{day}$; simulations will be performed for a range of D^* from 10^{-7} to $10^{-4} \text{ m}^2/\text{day}$.

The magnitude of D^* will effect the rate of contaminant mass transfer between mobile and immobile regions. In the same time span, the leading edge of contamination may penetrate into a floodplain unit more than 7 times further for $D^* = 5.2 \times 10^{-5} \text{ m}^2/\text{day}$

than for $D^* = 10^{-6} \text{ m}^2/\text{day}$, i.e., over the range of uncertainty in D^* . Similarly, with a decrease in the rate of diffusion, the mean residence time $\langle \Delta t_{D^*} \rangle$ within hydrofacies increases; in the present case, residence times for $D^* = 10^{-6} \text{ m}^2/\text{day}$ are approximately 50 times those for $D^* = 5.2 \times 10^{-5} \text{ m}^2/\text{day}$. Transport parameters used in the experiments that follow are given in Table 5.4. Specific values used in the various experiments are cited where appropriate.

5.4.3.2 Numerical Simulation

Equation (1) is simulated via the random-walk methods described in Chapter 4. Time step is dynamically controlled and analytical advective paths lines (see Chapter 2) are incorporated to ensure greater accuracy in regions dominated by advective transport. Absorbing boundary conditions are prescribed on all model boundaries and in grid blocks corresponding to pumping under stressed hydraulic conditions. A single pumping well is located at the center of the system with screened interval corresponding to grid blocks $i = 41$, $j = 41$, and $39 \leq k \leq 43$. In these grid blocks with active pumping, particles are absorbed within a time step Δt with probability of absorbing a particle in grid block (i,j,k) of $\Delta t Q_w / (\Theta \Delta V_{ijk}) < 1$, where ΔV_{ijk} is the volume [L^3] of grid block (i,j,k) , and i , j , and k index nodal location in the x , y , and z directions, respectively.

The contaminant source is always released in the same 4 grid blocks near the upstream edge of the model as illustrated in Figure 5.8. These grid blocks correspond to observed channel lithologies used to condition geostatistical simulations. The source location is part of the primary channel network (i.e., the largest connected channel network, typically comprised of approximately 80% of the total volume of channel hydrofacies) in all realizations but 2 and 10. In realizations 3 and 9, the source region is somewhat poorly

Table 5.4: Transport Parameters

Parameter	Value
Porosity, Θ	0.35
D^* (m ² /day)	$10^{-7} - 10^{-4}$
$\alpha_L = \alpha_T$ (m) ^a	0.01

^aResults of Appendix 5C show that use of an isotropic local-scale dispersivity yields accurate results.

connected with this network. Experiments, not shown, demonstrate that field-scale transport is not particularly sensitive to the initial lateral distribution of the contaminant source within these 4 grid blocks. Therefore, particles of the source are distributed uniformly along a vertical line at $x = 207.5$ m, $y = 25.0$ m, and $20.75 \text{ m} \leq z \leq 22.25$ m to simulate an instantaneous point source in plan view. In all scenarios, a total of 40,000 particles, 10,000 particles per grid block, define the initial source. For the purposes of evaluating remediation scenarios, source concentrations on a finite difference grid-block basis (as defined in the following section) are assumed to be 5 mg/l (5 ppm), approximately 3 orders of magnitude greater than the maximum contaminant level (MCL) 5 $\mu\text{g/l}$ (5 ppb). Transport simulation results are presented after the following section, describing analyses of particle mass distributions.

5.4.3.4 Analysis of Particle Mass Distributions

Simulation of equation (1) by random walks yields particle mass distributions (see Chapter 2). This section presents various analyses used to describe these distributions including computation of total mass, spatial moments, average plume velocity, macroscopic dispersivity, average concentration, and concentrations at wells.

Consider a distribution of particles with locations $\mathbf{X}_p(t)$ and mass $m_p(t)$, $\mathbf{X}_p(t) \in \Omega$.

Then the total mass $M(t)$ contained in Ω is given by the sum

$$M(t) = \sum_p m_p(t), \forall X_p(t) \in \Omega \quad (5.5)$$

The aqueous-phase concentration $c(\mathbf{x}, t)$ for any \mathbf{x} contained in grid block (i, j, k) will be reported as the average concentration within that block, calculated as

$$\begin{aligned} \Theta c(\mathbf{x}, t) \Big|_{\mathbf{x} \in \Delta V_{ijk}} &= \Theta \langle c(\mathbf{x}, t) \rangle^{\Delta V_{ijk}} = \frac{1}{\Delta V_{ijk}} \int_{\mathbf{x} \in \Delta V_{ijk}} c(\mathbf{x}', t) d\mathbf{x}' \\ &\approx \frac{1}{\Delta V_{ijk}} \sum_p m_p(t), \forall \mathbf{X}_p(t) \in \Delta V_{ijk} \end{aligned} \quad (5.6)$$

For an idealized vertical line source located at \mathbf{x}_s , normalized concentration averaged over the z coordinate can be approximated for constant Θ as

$$\frac{\langle c(\mathbf{x}, t) \rangle^z}{\langle c(\mathbf{x}_s, 0) \rangle^z} \Big|_{\mathbf{x} \in \Delta V_{ij}} = \frac{1}{\langle c(\mathbf{x}_s, 0) \rangle^z L_z} \int_{z \in \Delta V_{ij}} c(\mathbf{x}, t) dz' = \frac{1}{M_0} \sum_p m_p(t), \forall \mathbf{X}_p \in \Delta V_{ij} \quad (5.6)$$

where $\Delta V_{ij} = \sum_k \Delta V_{ijk}$ and $\langle \bullet \rangle^z$ indicates the spatial average over the z -coordinate.

Similarly, concentration averaged over the x and z coordinates can be approximated by

$$\begin{aligned} \frac{\langle c(\mathbf{x}, t) \rangle^{x,z}}{\langle c(\mathbf{x}_s, 0) \rangle^{x,z}} \Big|_{\mathbf{x} \in \Delta V_j} &= \frac{1}{\langle c(\mathbf{x}_s, 0) \rangle^{x,z} L_x L_z} \iint_{\mathbf{x}, z \in \Delta V_j} c(\mathbf{x}, t) dx' dz' \\ &\approx \frac{1}{M_0} \sum_p m_p(t), \forall \mathbf{X}_p \in \Delta V_j \end{aligned} \quad (5.7)$$

Average concentration $\langle c_w(\mathbf{x}_w, t) \rangle^{L_w}$ [ML^{-3}] at the well location \mathbf{x}_w is calculated as an average of the flux-weighted concentrations $c_w(\mathbf{x}_w, t)$ along the length L_w of the well screen as

$$\begin{aligned} \langle c_w(\mathbf{x}_w, t) \rangle^{L_w} \Big|_{t \in \Delta t} &\approx \left\langle \langle c_w(\mathbf{x}_w, t) \rangle^{L_w} \right\rangle^{\Delta t} \\ &= \frac{1}{\Delta t} \int_t^{t+\Delta t} \frac{1}{L_w Q_{\text{TOTAL}}} \int_{L_w} Q_w(\mathbf{x}_w) c_w(\mathbf{x}_w, t) dz dt \approx \frac{1}{\Delta t Q_{\text{TOTAL}}} \sum_{p \in \Pi_{\Delta t}} m_p(t) \end{aligned} \quad (5.8)$$

where $Q_w(\mathbf{x}_w)$ [L^3T^{-1}] is the flow to the well at point \mathbf{x}_w along the well screen, Q_{TOTAL} [L^3T^{-1}] is the total flow to the well, and $\Pi_{\Delta t}$ is the set of particles absorbed in the time span Δt . First and second spatial moments of the mass distribution in Ω are given as

$$\bar{X}_i(t) = \frac{1}{M(t)} \sum_p m_p(t) X_{p,i}(t), \forall \mathbf{X}_p(t) \in \Omega \quad (5.9)$$

$$\Sigma_{ij}(t) = \frac{1}{M(t)} \sum_p m_p(t) [X_{p,i}(t) - \bar{X}_i(t)][X_{p,j}(t) - \bar{X}_j(t)], \forall \mathbf{X}_p(t) \in \Omega \quad (5.10)$$

The spatial moments can be transformed such that coordinates are aligned with the principle axes of Σ . Transformed spatial moments are denoted by $\bar{\mathbf{X}}^*$ and Σ^* with $i=1$ corresponding to the direction of principle axis (assumed to be roughly constant for simplicity). Macroscopic dispersivities as a function of these moments can be approximated as

$$A_i(t) = \frac{1}{2\bar{v}(t)} \frac{d\Sigma_{ii}^*(t)}{dt} = \frac{1}{4\bar{v}(t)\Delta t} [\Sigma_{ii}^*(t + \Delta t) - \Sigma_{ii}^*(t - \Delta t)] \quad (5.11)$$

where \bar{v} is the average velocity of the particle mass distribution in the principle direction given as

$$\bar{v}(t) = \frac{d\bar{X}_1^*(t)}{dt} = \frac{1}{2\Delta t} [\bar{X}_1^*(t + \Delta t) - \bar{X}_1^*(t - \Delta t)] \quad (5.12)$$

Forward and backward difference approximations are substituted where needed. Transport experiments are described in the following section.

5.5 Transport Experiments

The transport experiments considered here explore the role of matrix diffusion in contaminant migration and remediation using the LLNL site as a model. Scenarios 1 - 4 of Table 5.5 simulate ambient contaminant migration for 40-years followed by PAT at a 50 m^3/day rate. Diffusion coefficients D^* of these 4 scenarios range from 10^{-7} to 10^{-4} m^2/day .

Table 5.5: Scenarios 1 – 6

Scenario	D^* (m ² /day)	Equation
1	10^{-4}	ADE
2	5.2×10^{-5}	ADE
3	10^{-6}	ADE
4	10^{-7}	ADE
5	5.2×10^{-5}	Advection diffusion equation
6	0	ADE. No diffusion

Because results will show contaminant migration and remediation is significantly sensitive to the diffusion coefficient within the range of uncertainty, it is important to know if this sensitivity is overwhelmed by uncertainty in other transport parameters, chiefly dispersivity. This issue is addressed by comparing results of scenario 2 with those of scenarios 5 and 6 (Table 5.5) that simulate ambient transport according to an advection diffusion equation ($\alpha_L = \alpha_T = 0$), and advection dispersion equation (ADE) with no diffusion ($D^* = 0$), respectively.

5.5.1 Results and Discussion

Results for transport under ambient hydraulic conditions in scenarios 1 – 4, stressed hydraulic conditions in scenarios 1 - 4, and scenarios 5 and 6 are addressed separately in the sections that follow.

5.5.1.1 Ambient Hydraulic Conditions, Scenarios 1 – 4

Scenarios 1 – 4 simulate transport under ambient hydraulic conditions for 40 years followed by PAT. Scenarios correspond to a range of effective molecular-diffusion coefficient D^* . Results presented here explore the role of diffusion in the ambient migration phase of these scenarios.

5.5.1.1.1 Concentration and mass distributions. Figures 5.12 and 5.13 plot log normalized 40-year x - z average concentrations for scenarios 1 – 4, realizations 1 – 10. A plume generated for a homogeneous system with $\alpha_L = \alpha_T = 0.01$ m and $K = 5.184$ m/day, corresponding to the K of the channel hydrofacies, is shown for reference. Results generally show an increase in holdback of mass, particularly close to the source location at 25 meters, and a corresponding decrease in contaminant mass near the leading edge of the plume, with increase in D^* . For example, all realizations, but 2, 3 and 10, show greater than a half order of magnitude (i.e., *more than a three-fold*) increase in mass holdback near the source with increase in D^* from 10^{-6} to 5.2×10^{-5} m²/day, i.e., over the range of uncertainty in D^* . This result is illustrated more clearly with normalized z -average concentrations at year 40 for scenarios 2 and 3 of realizations 4 and 7 as shown in Figures 4.14 and 4.15, respectively. Note that results for greater values of D^* are consistent with observations of persistent high concentrations near source locations at the LLNL site [Hoffman, 1997].

Realizations 2, 3 and 10 show relatively little downstream migration of mass. Results confirm independent observations that channel hydrofacies of source locations in realizations 2 and 10 do not percolate (i.e., they are not part of a connected channel network that spans the domain in the dip direction), whereas in realization 3, they are poorly connected with the main channel network. Thus, transport behavior depends strongly on the details of the channel network and the distribution of results presented appears to be bimodal. One mode corresponds to realizations in which channel hydrofacies of the source location are a part of the primary network of channels that percolates (connects) completely through the domain. The other mode corresponds to realizations in which

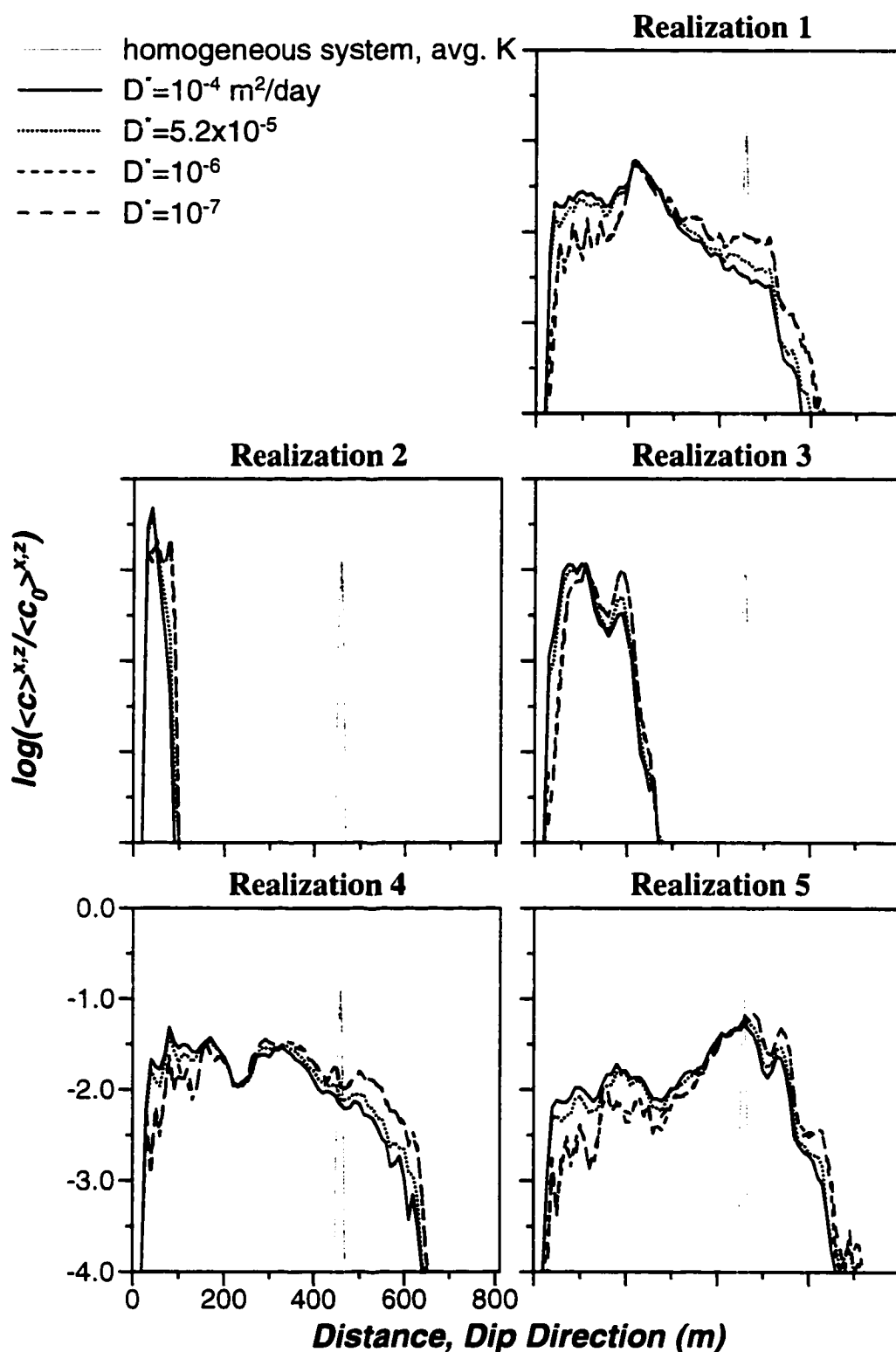


Figure 5.12. Normalized x - z average concentration at year 40 for scenarios 1 – 4, realizations 1 – 5. A plume generated for a homogeneous system with $\alpha_L = \alpha_T = 0.01 \text{ m}$ and $K = 5.184 \text{ m/day}$ is shown for reference.

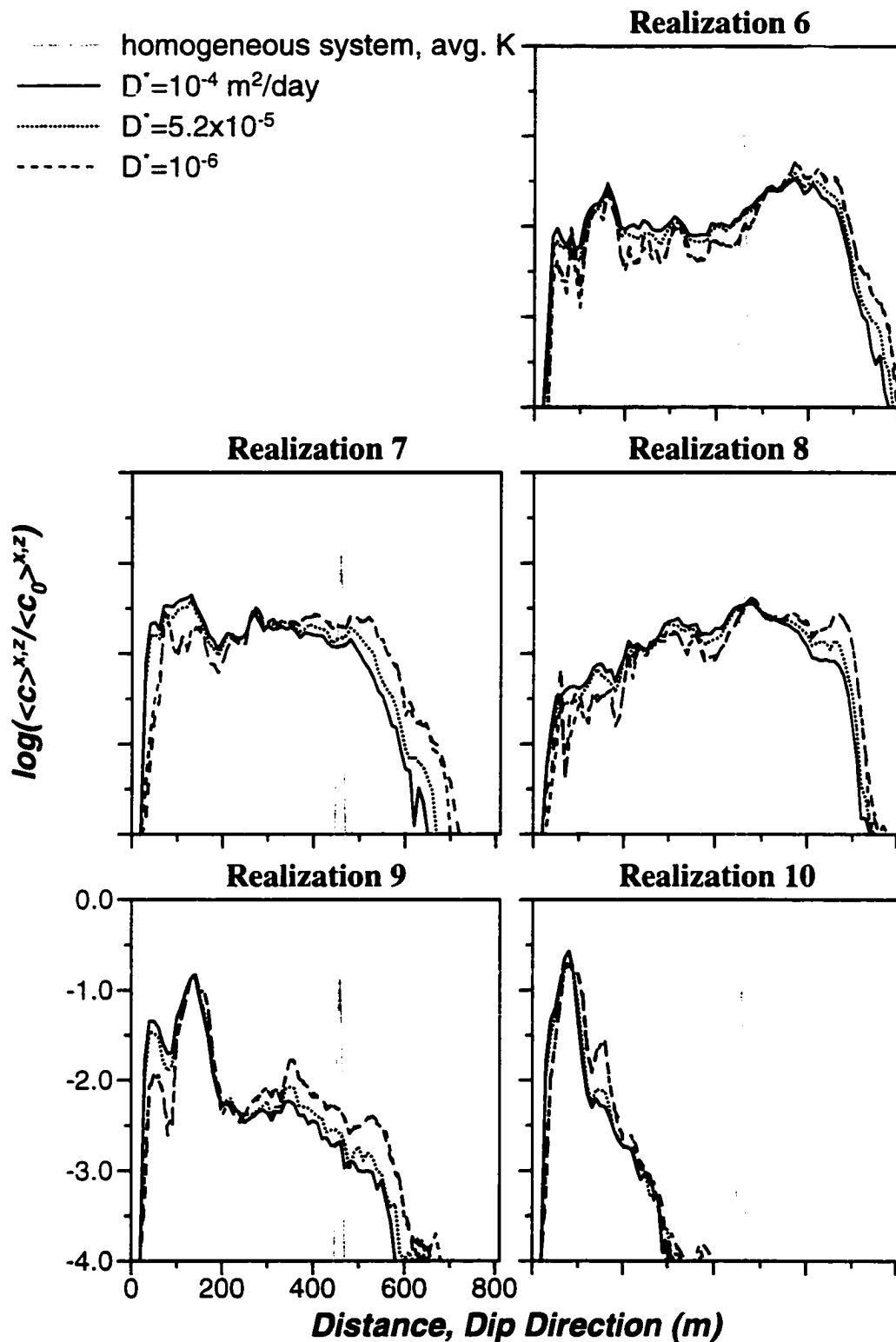


Figure 5.13. Normalized x-z average concentration at year 40 for scenarios 1 – 4, realizations 6 – 10. A plume generated in a homogeneous system with $\alpha_L = \alpha_T = 0.01 \text{ m}$ and $K = 5.184 \text{ m/day}$ is shown for reference.

channel hydrofacies of the source location are either not part of, or are poorly connected with, the primary network of channels. Three dimensional particle distributions are presented in Appendix 5D for scenarios 2 and 3, year 40. These plots clearly illustrate the flow paths of the high- K channels connected with source locations. Increasing D^* results in a noticeable increase in traverse spreading (dispersion) by accelerating diffusion in the low- K matrix surrounding these channels.

5.5.1.1.2 Macrodispersive behavior. Longitudinal first and second spatial moments as a function of time for scenarios 1 – 4, realizations 1 – 10, are shown in Figures 5.16 - 5.19. First moments show a dramatic increase in sequestration of mass with increase in D^* . Surprisingly, results are particularly sensitive in the range of uncertainty, between $D^* = 10^{-6}$ and 5.2×10^{-5} m²/day. In realizations 4 and 7, for example, there is more than a 25% decrease in the extent of downstream migration of the center of mass at year 40 with increase in D^* from 10^{-6} to 5.2×10^{-5} m²/day. Because source locations are in high-permeability channel hydrofacies, an increase in D^* generally results in an initial increase in the net flux of mass from high- to low-permeability hydrofacies, resulting in greater sequestration of contaminants.

With the exception of realization 5, second moments generally show little sensitivity to D^* . An increase in D^* results in a general reduction of mass in the distal plume and a corresponding increase in mass near source locations. Apparently, this shift of mass generally has little affect on second moments. Realization 5, however, shows a significant mass peak near 550 m. Here, increasing D^* flattens the mass distribution enough to significantly increase in the second moment.

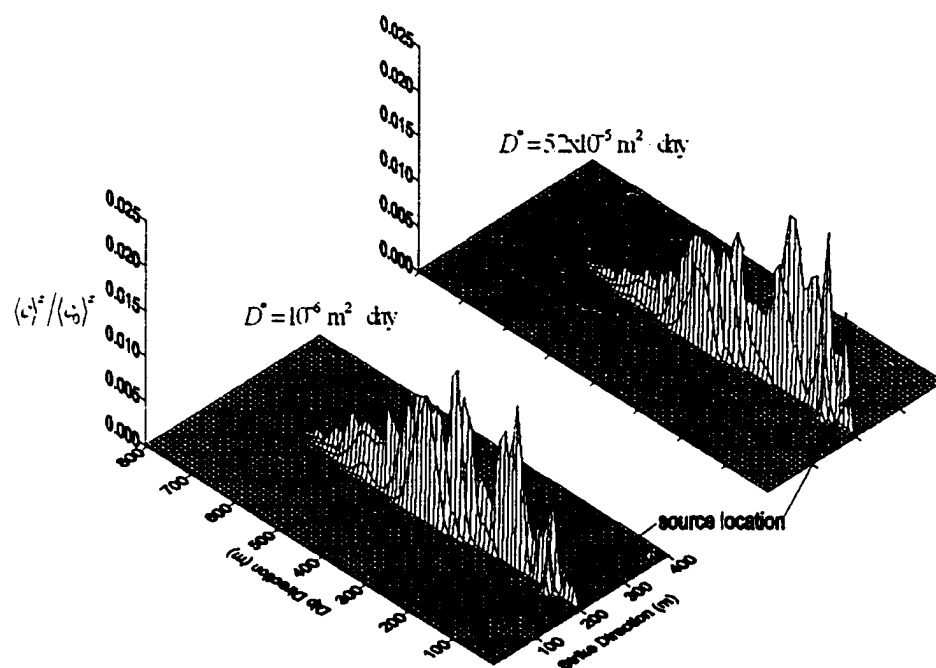


Figure 5.14: Normalized z -average concentrations at year 40 for scenarios 2 ($D^* = 5.2 \times 10^{-5} \text{ m}^2/\text{day}$) and 3 ($D^* = 10^{-6} \text{ m}^2/\text{day}$), realization 4.

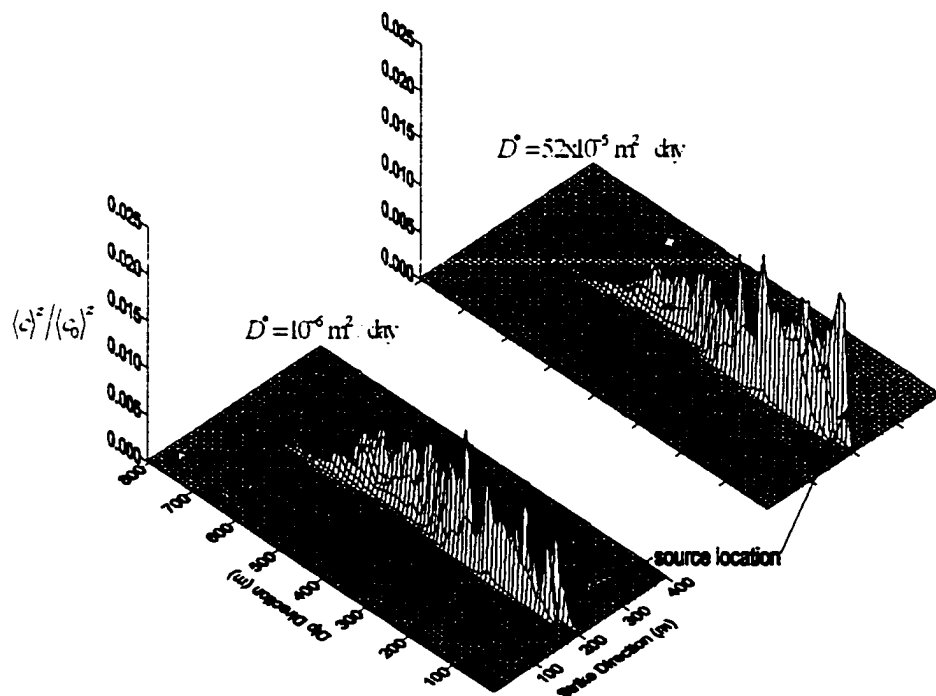


Figure 5.15: Normalized z -average concentrations at year 40 for scenarios 2 ($D^* = 5.2 \times 10^{-5} \text{ m}^2/\text{day}$) and 3 ($D^* = 10^{-6} \text{ m}^2/\text{day}$), realization 7.

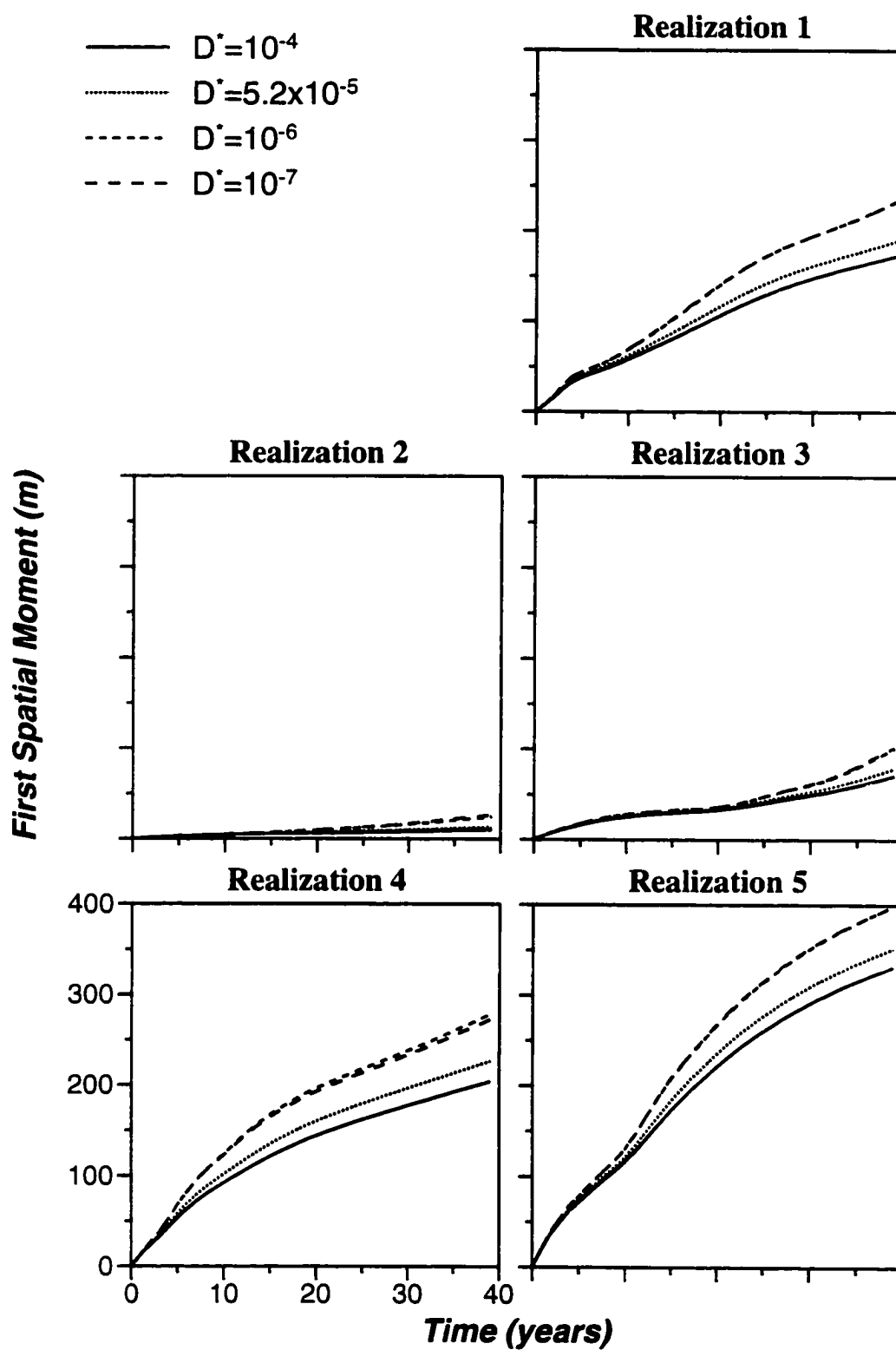


Figure 5.16. First spatial moments for scenarios 1 – 4, realizations 1 – 5.

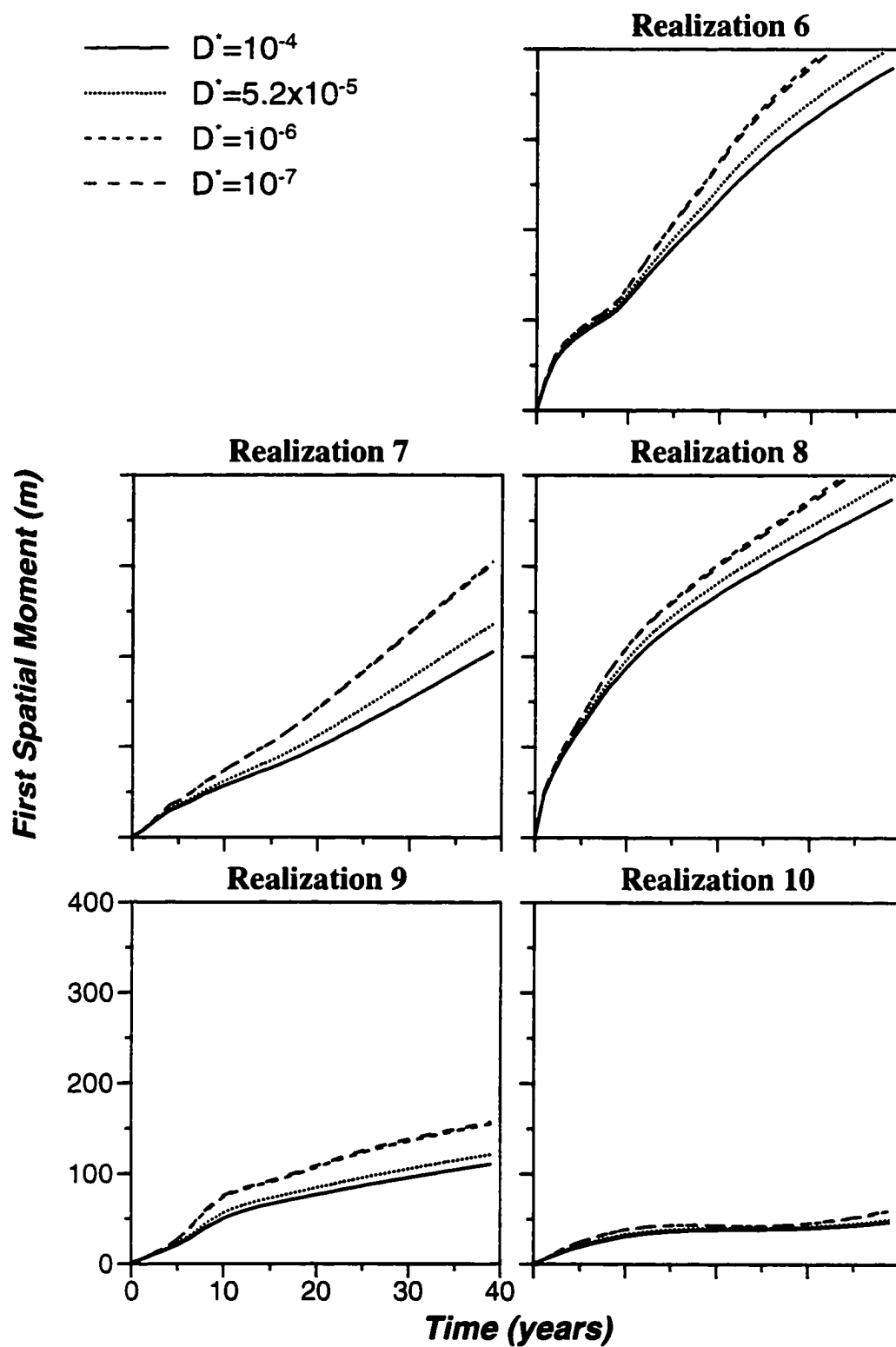


Figure 5.17. First spatial moments for scenarios 1 – 4, realizations 6 – 10.

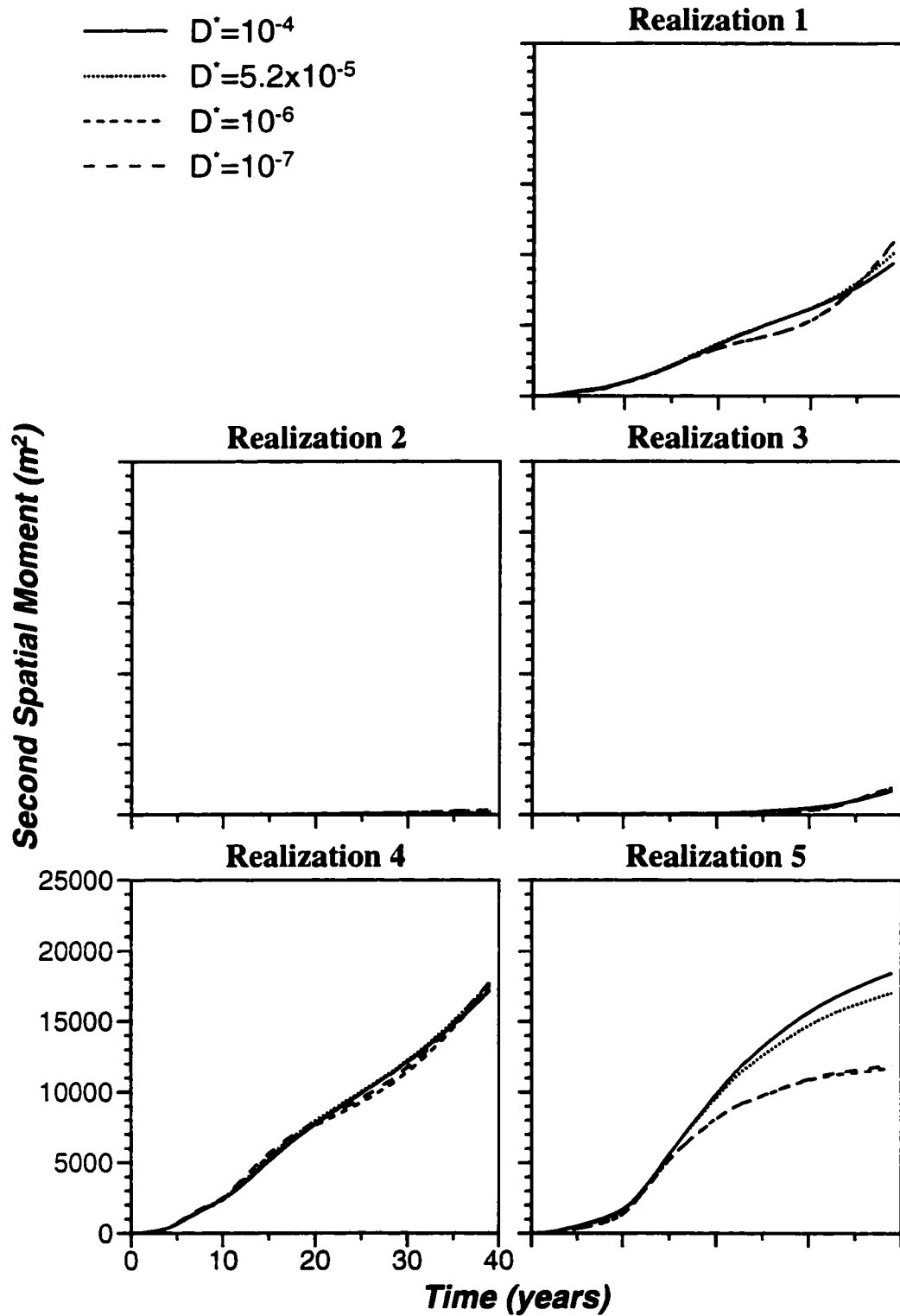


Figure 5.18. Second spatial moments for scenarios 1 – 4, realizations 1 – 5.

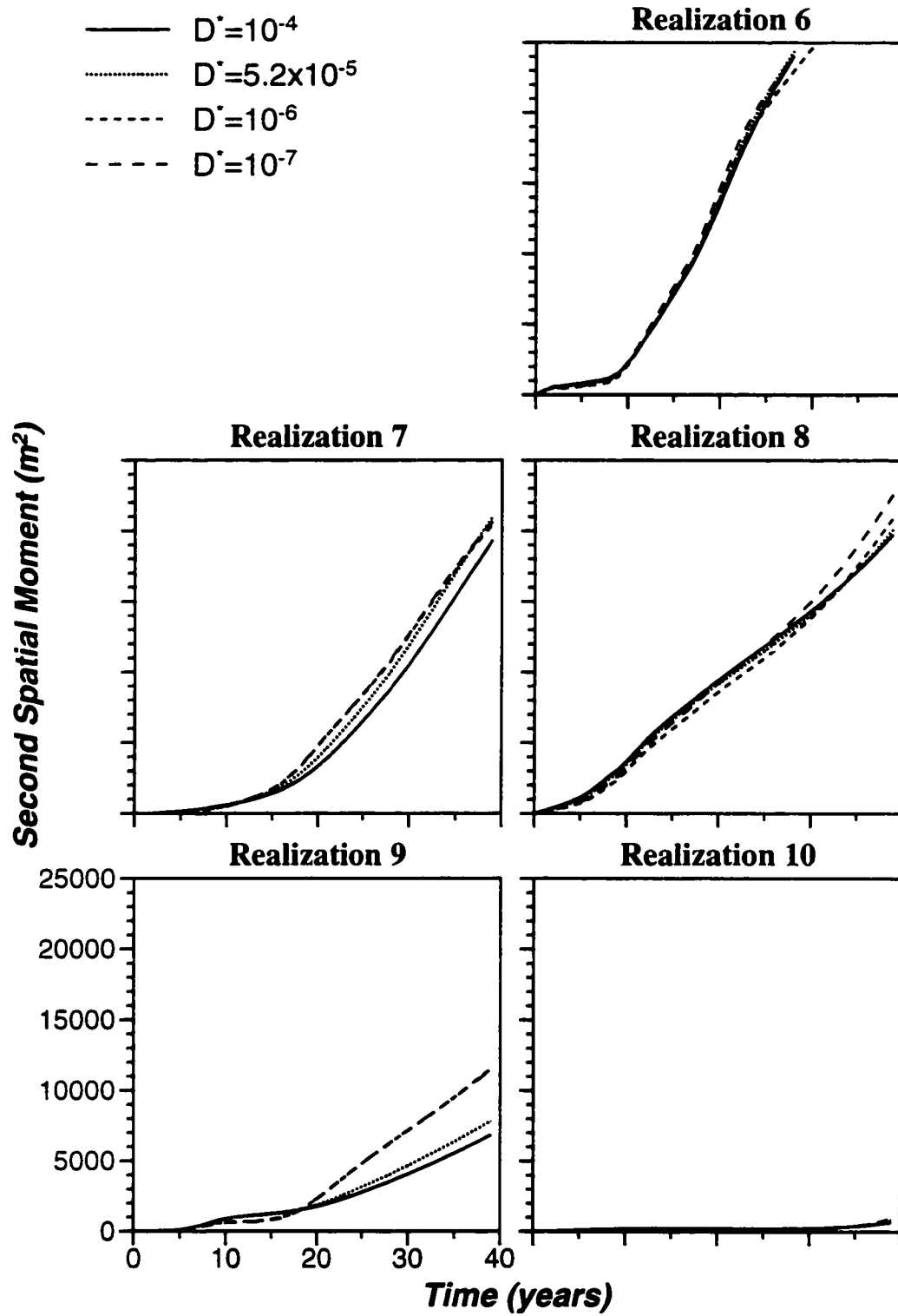


Figure 5.19. Second spatial moments for scenarios 1 – 4, realizations 6 – 10.

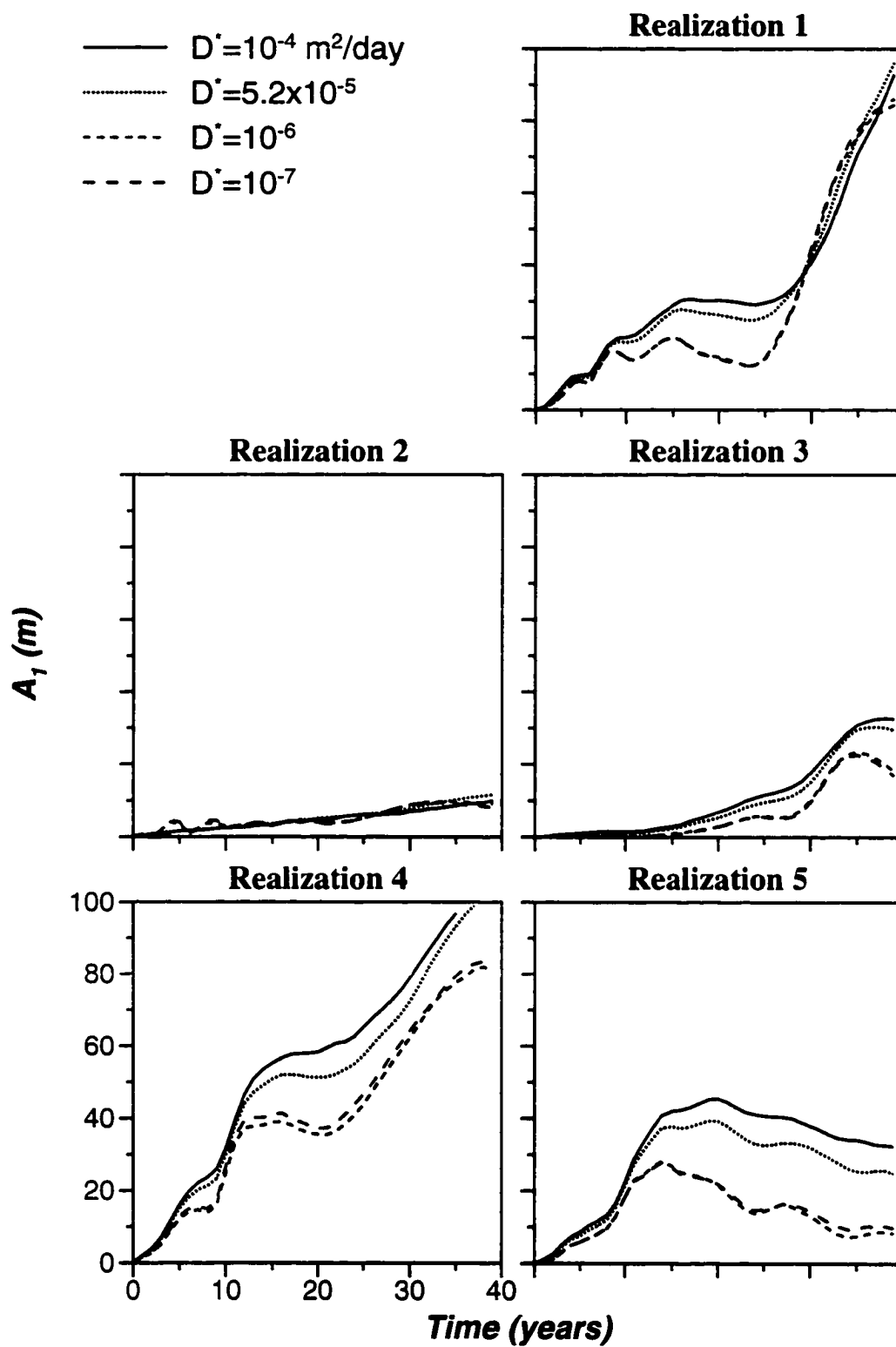


Figure 5.20. Macrodispersion coefficient A_1 a function of time for scenarios 1 – 4, realizations 1 – 5.

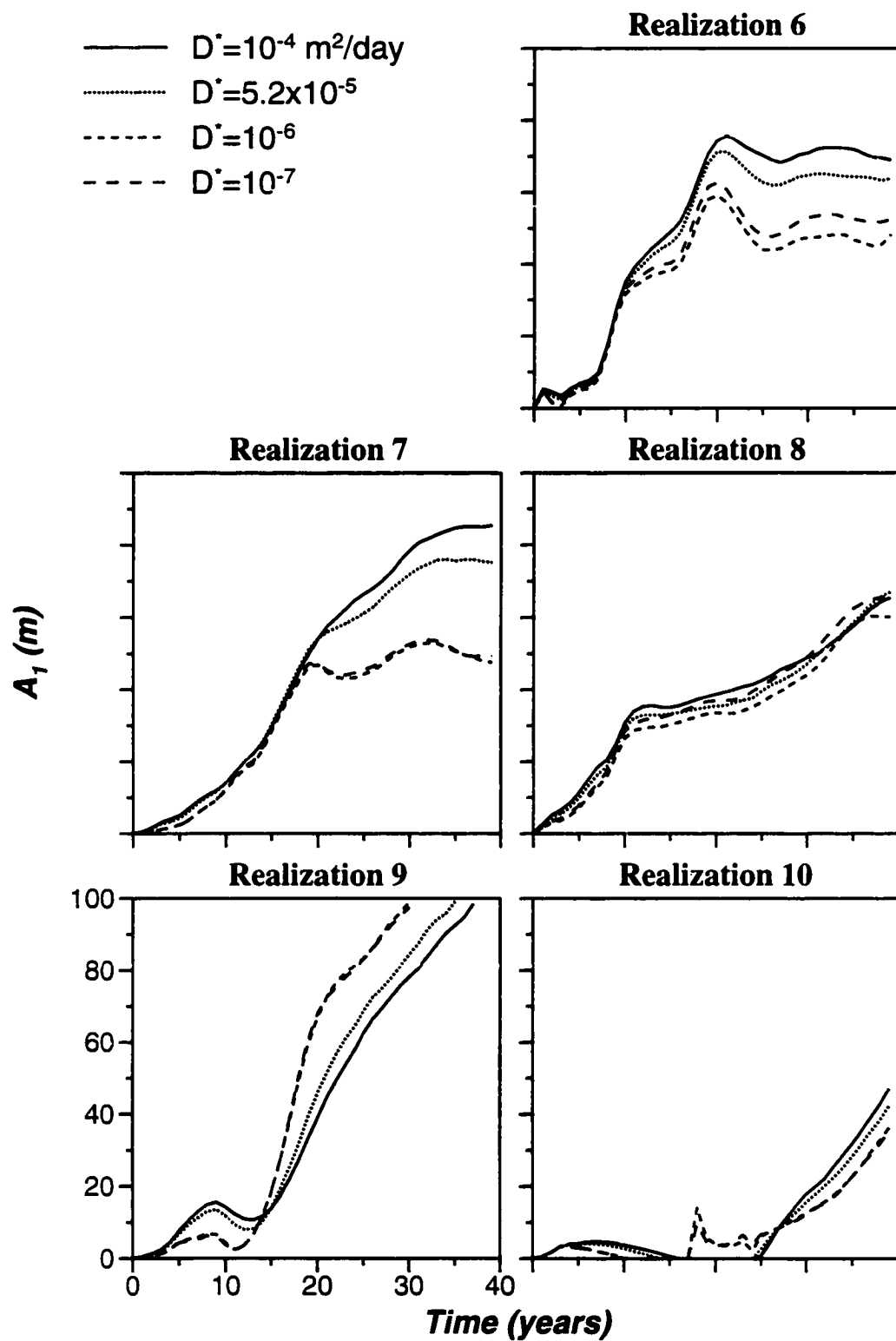


Figure 5.21. Macrodispersion coefficient A_1 a function of time for scenarios 1 – 4, realizations 6 – 10.

The effect of diffusion on longitudinal macrodispersivity A_1 for scenarios 1 - 4 is illustrated in Figures 5.20 and 5.21. At long times results are particularly sensitive over the range of uncertainty in D^* . In several realizations dispersivities appear to reach asymptotic values. However, results presented in the following section show that the partitioning of mass among hydrofacies has not reached an “asymptotic” state, suggesting that asymptotic behavior is not achieved within the 40-year time span. Further, at long times one should expect Taylor-dispersive behavior [Gelhar, 1993], i.e., an inverse relationship between D^* and A_1 , whereas the opposite is generally observed here. Indeed, these results are consistent with estimates for diffusion-rate limited residence times in floodplain hydrofacies on the order of centuries to millenia. Clearly, stochastic theory neglecting diffusion [Dagan, 1989] or that predicts negligible effects due to diffusion [Gelhar, 1993] cannot describe the macrodispersive behavior observed here.

5.5.1.1.3 Partitioning of mass among hydrofacies. Figures 5.22 and 5.23 illustrate how contaminant mass partitions among hydrofacies with time in realizations 1 - 4. In all realizations, increasing D^* results in a significant increase in mass within floodplain hydrofacies and a corresponding decrease in mass within channel and levee hydrofacies. Note that this effect is most pronounced over the range of uncertainty in this parameter, from $D^* = 10^{-6}$ to 5.2×10^{-5} m²/day. For example, in both realizations 4 and 7, increasing D^* from 10^{-6} to 5.2×10^{-5} m²/day results in approximately three times as much mass in floodplain hydrofacies.

Figures 5.24 and 5.25 illustrate the partitioning of mass among hydrofacies at year 40 as a function of distance in the dip direction for scenario 2. Realizations in which channel hydrofacies percolate and are well connected tend to show 2 distinct plumes, one

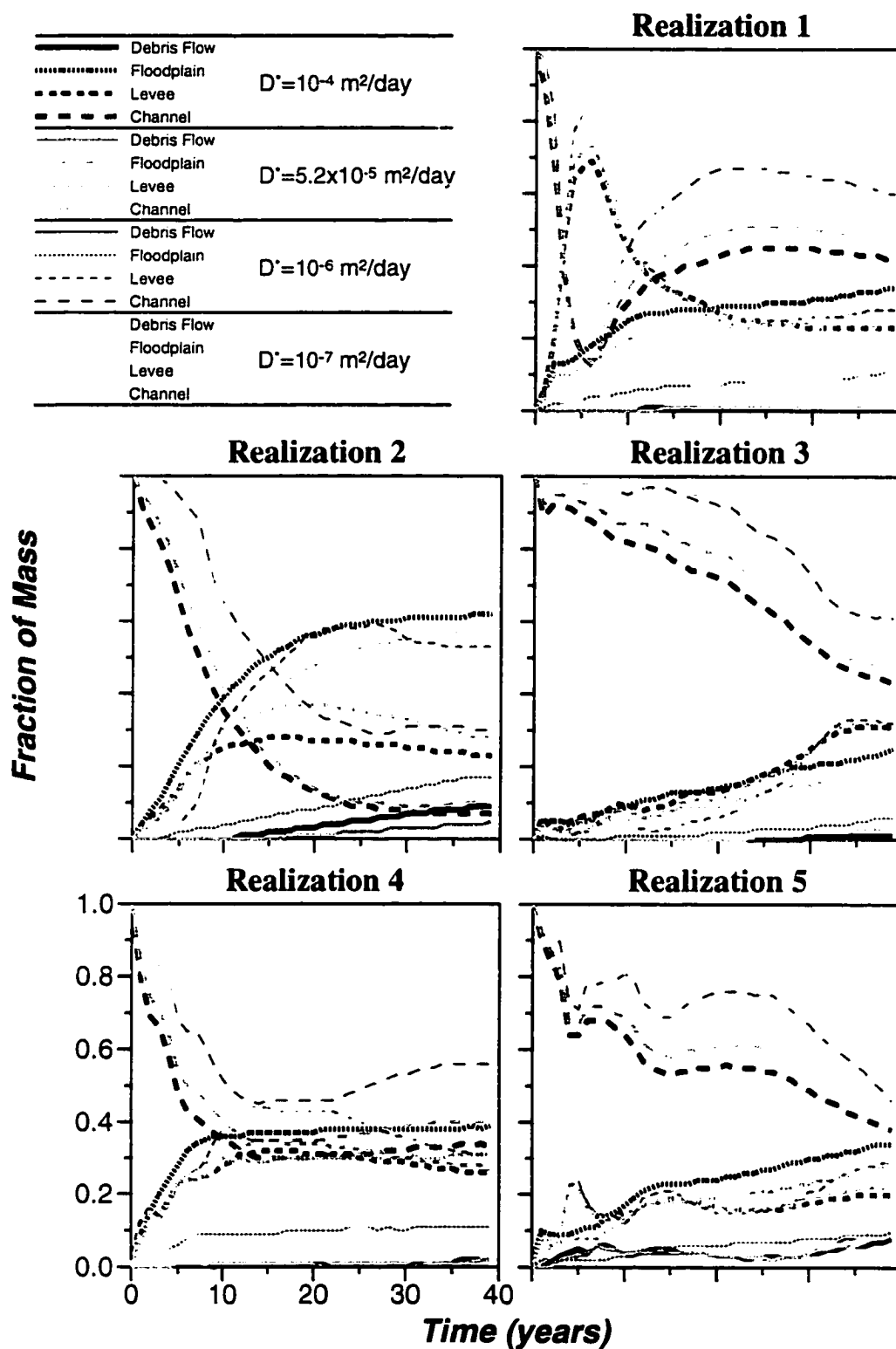


Figure 5.22. Fraction of total mass contained in each of the 4 hydrofacies as a function of time for scenarios 1 – 4, realizations 1 – 5.

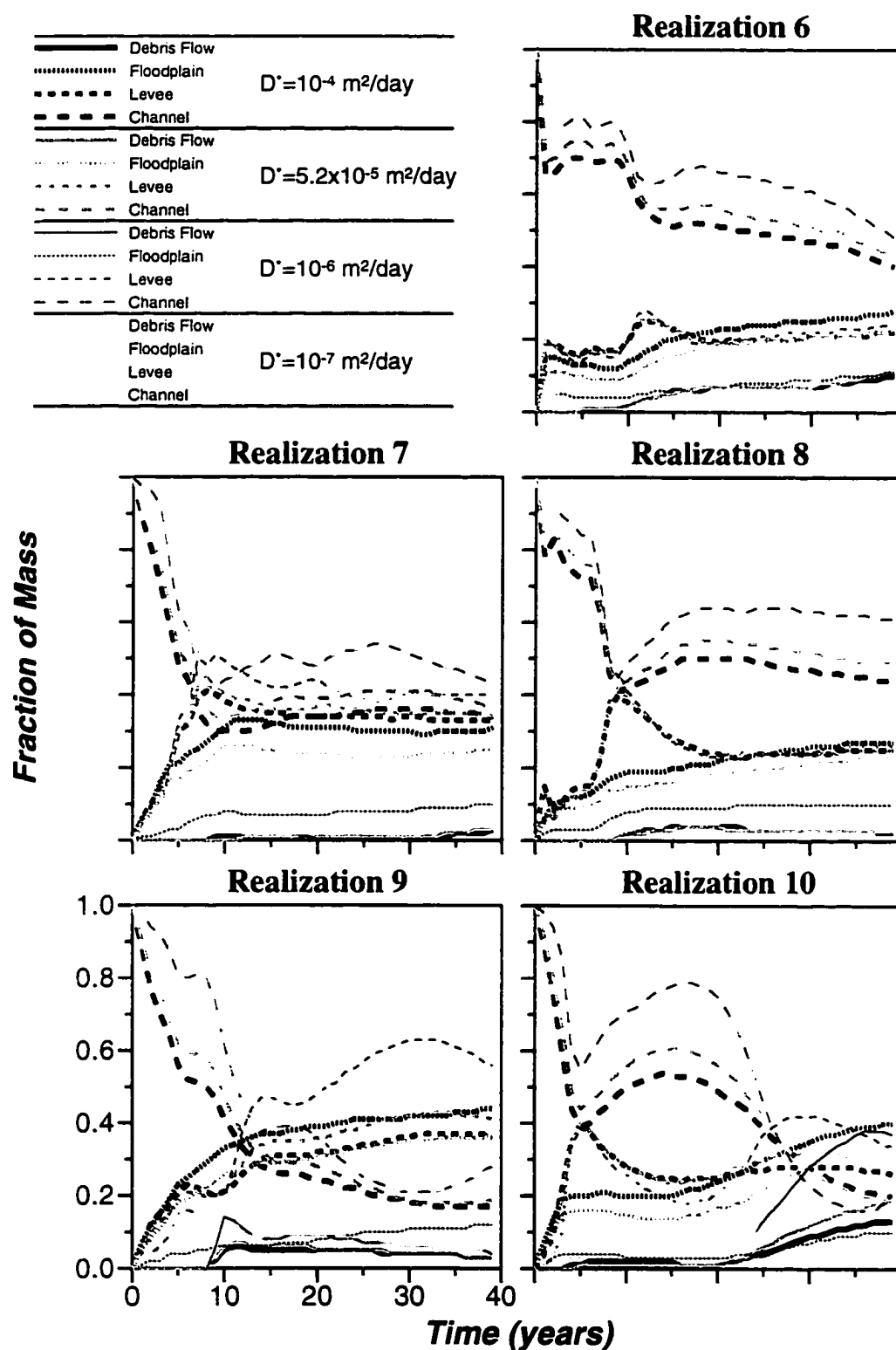


Figure 5.23. Fraction of total mass contained in each of the 4 hydrofacies as a function of time for scenarios 1 – 4, realizations 6 – 10.

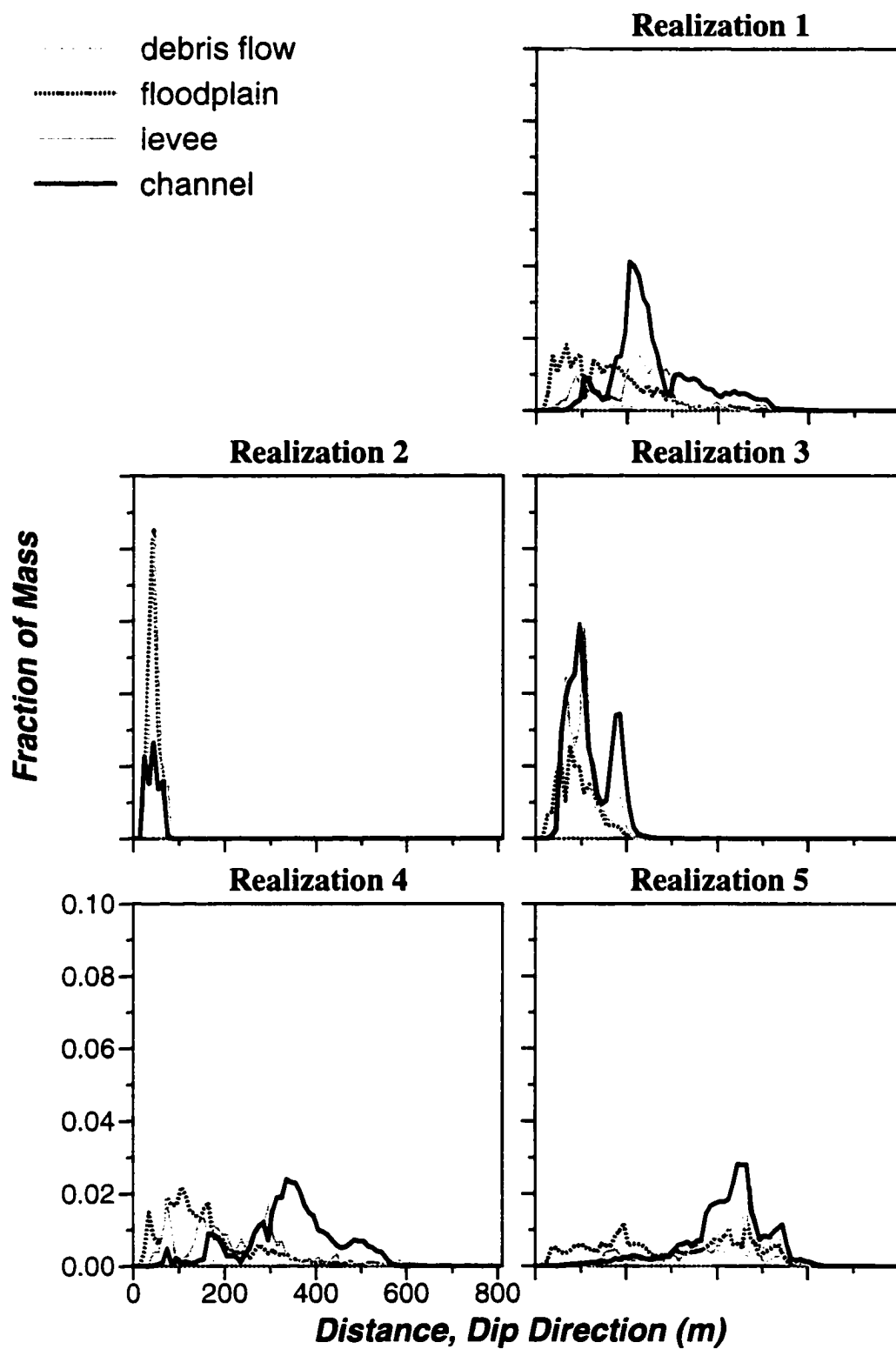


Figure 5.24: Fraction of total mass contained in each of the 4 hydrofacies as a function of distance in the dip direction for scenarios 1 – 4, realizations 1 – 5.

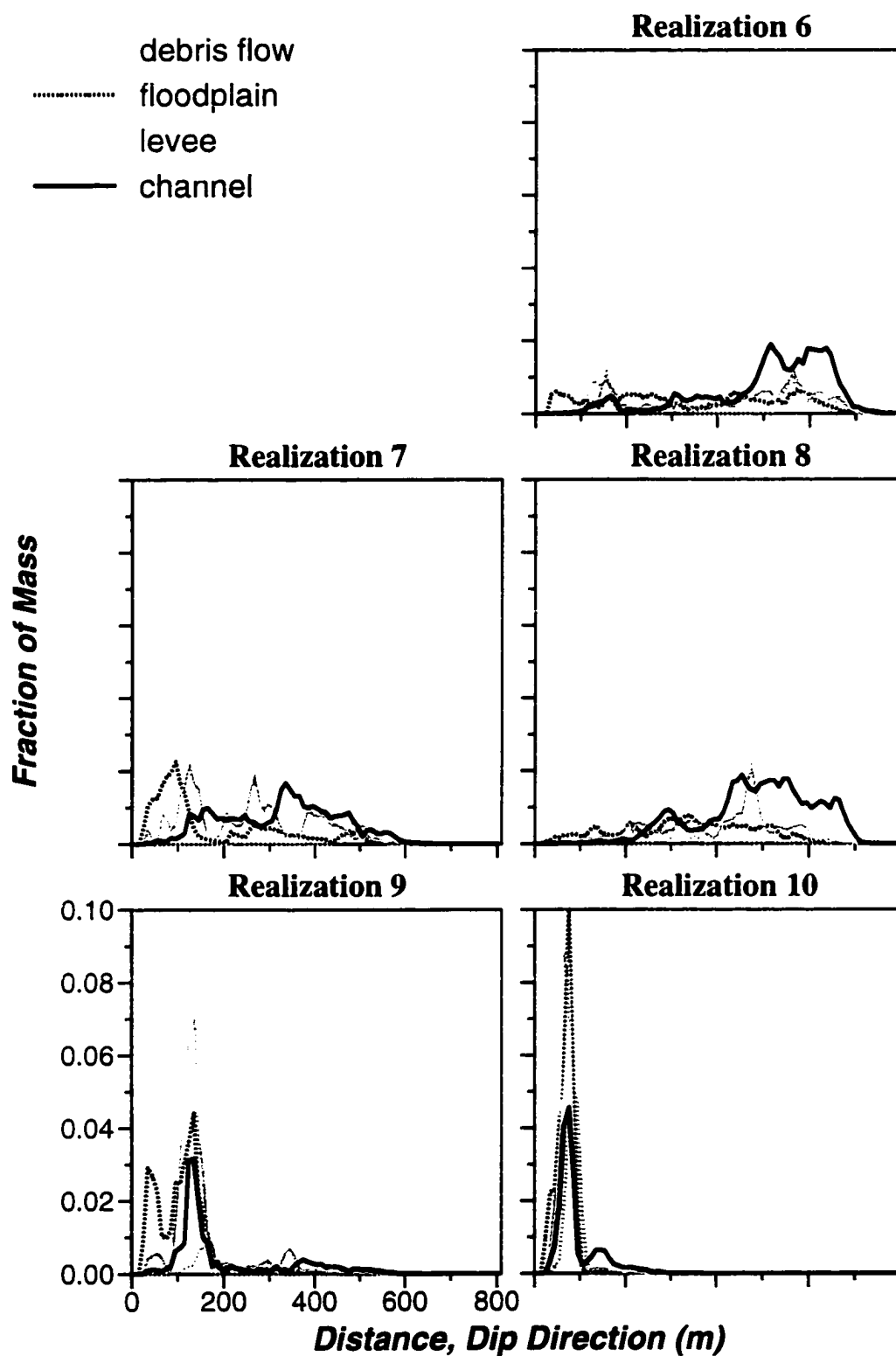


Figure 5.25: Fraction of total mass contained in each of the 4 hydrofacies as a function of distance in the dip direction for scenarios 1 – 4, realizations 6 – 10.

associated with floodplain hydrofacies and the other associated with channel hydrofacies. In all cases, mass in floodplain hydrofacies significantly lags behind mass in channel hydrofacies. This separation between plumes is most pronounced in realizations 4 and 7. Note that mass in channel hydrofacies shows several distinct peaks. These peaks likely correspond to the time spent in the lower- K hydrofacies, e.g., the peak toward the leading edge corresponds to mass that has spent little or no time in non-channel hydrofacies. The following section presents results for the PAT remediation phase of scenarios 1 – 4.

5.5.1.2 Pump and Treat, Scenarios 1 – 4

This section presents results and discussion for the PAT phase of scenarios 1 – 4.

5.5.1.2.1 Mass recovery. Figures 5.26 and 5.27 show the normalized mass remaining $M(t)/M_0$ as a function of time from the start of the remediation process at year 40 for all 10 realizations of heterogeneity. Results show a systematic trend, a decrease in mass remaining in the system with decrease in D^* . Results are most sensitive in the range of uncertainty for D^* , between 10^{-6} and 5.2×10^{-5} m²/day. In those realizations where channel hydrofacies of the source location in do not percolate (realizations 2 and 10), or are poorly connected (realizations 3 and 9), plumes at the start of pumping in year 40 are more isolated near the source than for the other realizations. In this case, PAT with well located at the center of the system results in less recovery of contaminant mass.

Note, that an increase in D^* decreases residence time $\langle \Delta t_D \rangle$ of diffusion processes in floodplain hydrofacies which could, in some instances, result in more rapid remediation. To clearly illustrate the effect of residence time on mass recovery, one would ideally specify the same initial conditions at the start of PAT in all scenarios.

5.5.1.2.2 Partitioning of mass among hydrofacies. Figures 5.28 and 5.29 show the partitioning of mass among hydrofacies as a function of time during the PAT process. These results show a trend of decrease in mass remaining with decrease in D^* that is consistent with the distribution of mass between hydrofacies at the start of pumping (year 40). During ambient migration, an increase in D^* results in corresponding increase of mass in floodplain hydrofacies. Some of this mass in floodplain hydrofacies at the start of pumping is sequestered during the remediation process, as shown.

5.5.1.2.3 Contaminated volume. The effects of D^* on remediation performance as measured by the volume of porous media with concentrations above MCL ($c/c_0 > 10^{-3}$) is illustrated in Figures 5.30 and 5.31 for scenarios 1 – 4, realizations 1 - 10. All simulations show significant tails, indicating long times to site remediation. Results are remarkably sensitive to D^* , particularly within the range of uncertainty, between $D^*=10^{-6}$ and 5.2×10^{-5} m²/day. Trends with change in D^* are mixed due to competing effects of diffusion. With an increase in D^* there is an increase in holdback of mass in floodplain hydrofacies, but also an increase in the rate at which concentrations in floodplains become more diffuse. In those realizations where channel hydrofacies of the source location do not percolate (realizations 2 and 10), or are poorly connected (realizations 3 and 9), plumes at the start of pumping in year 40 are more isolated near the source than for the other realizations. In this case, PAT with the well located at the center of the system may result in increased spreading of plumes. Results stress the need for detailed hydrogeologic characterization, particularly with respect to assessing connectivity of high-permeability hydrofacies.

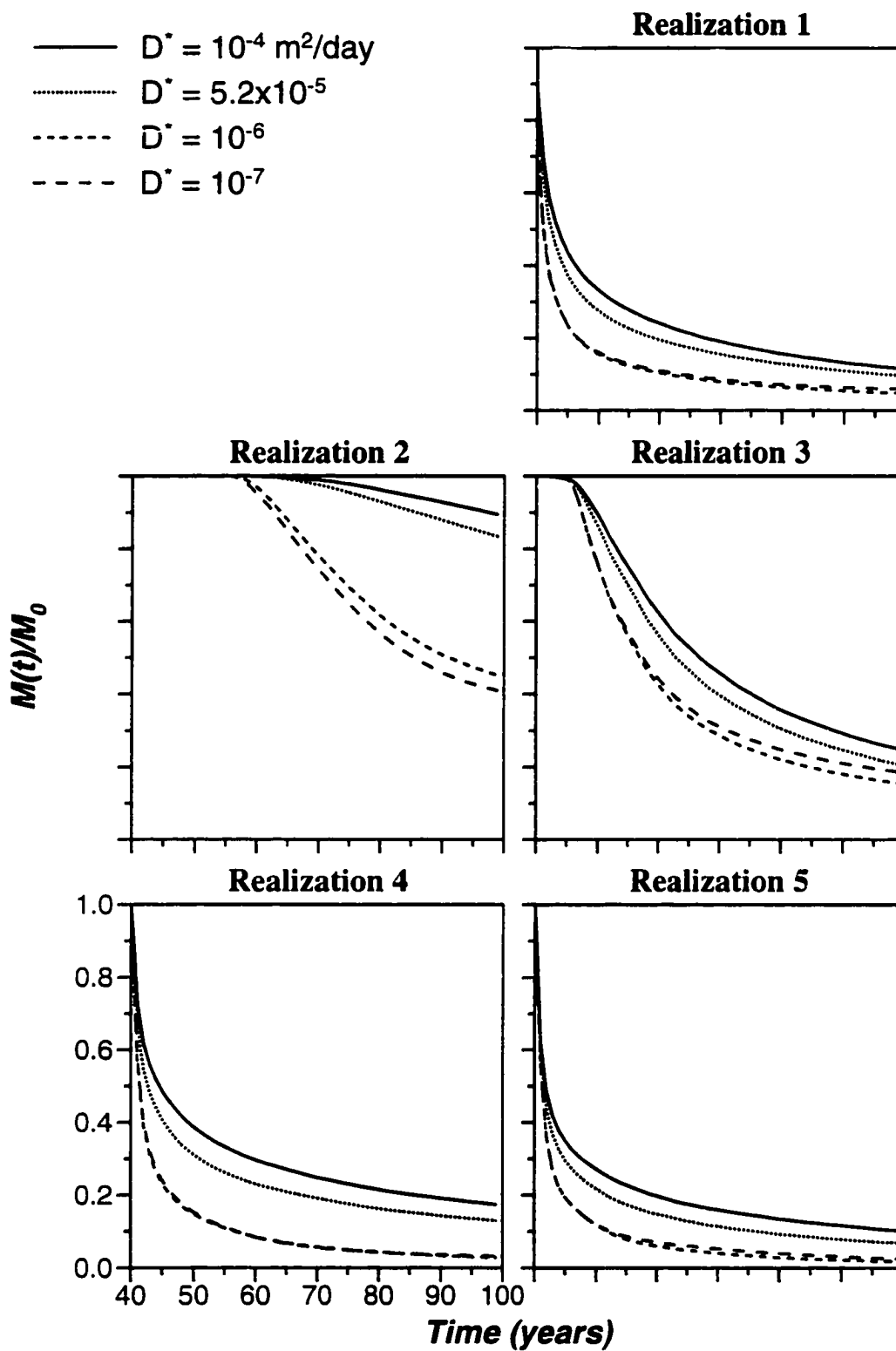


Figure 5.26. Mass remaining $M(t)/M_0$ as a function of time from year 40, the start of pump-and-treat, for scenarios 1 – 4, realizations 1 – 5.

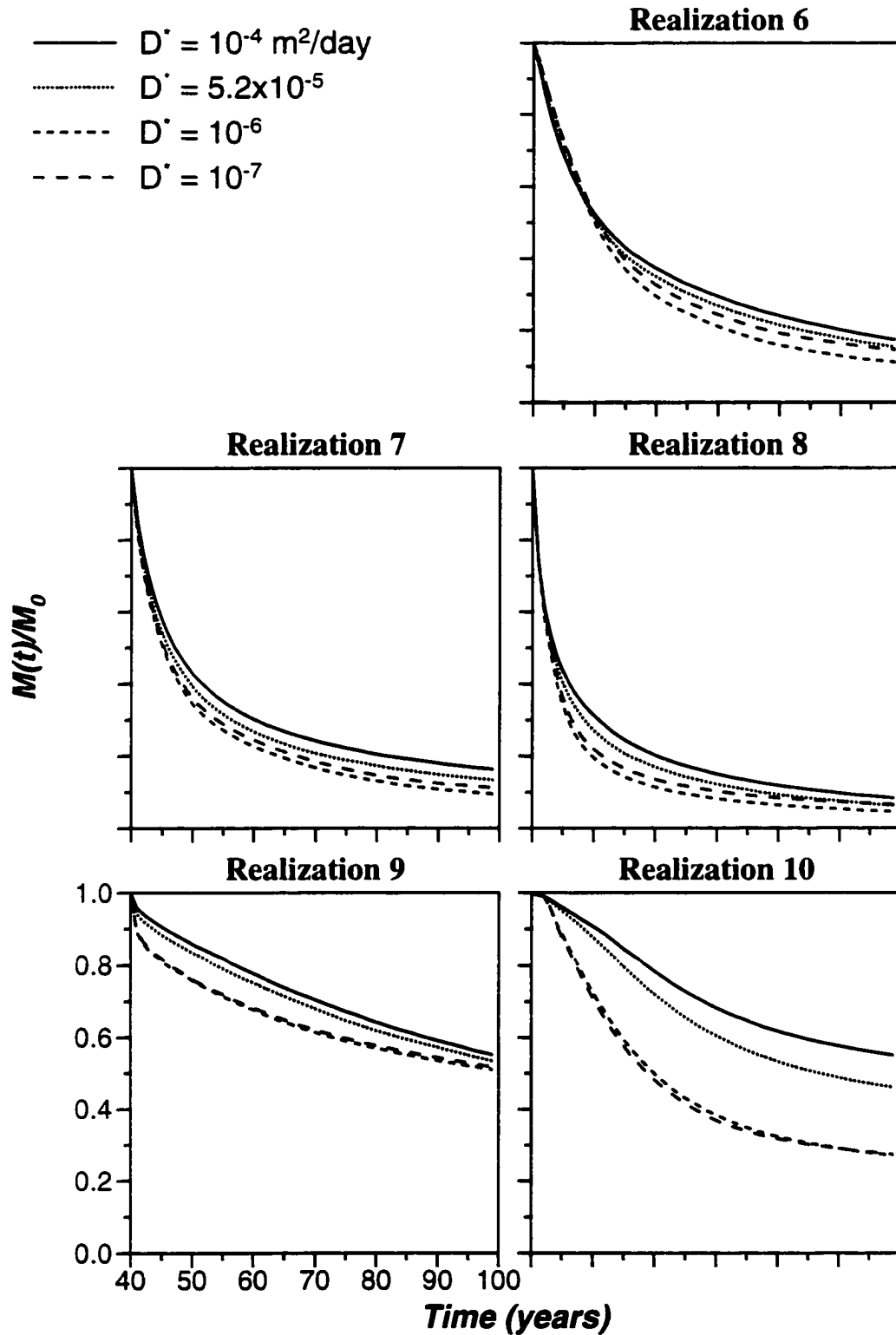


Figure 5.27. Mass remaining $M(t)/M_0$ as a function of time from year 40, the start of PAT, for scenarios 1 – 4, realizations 6 – 10.

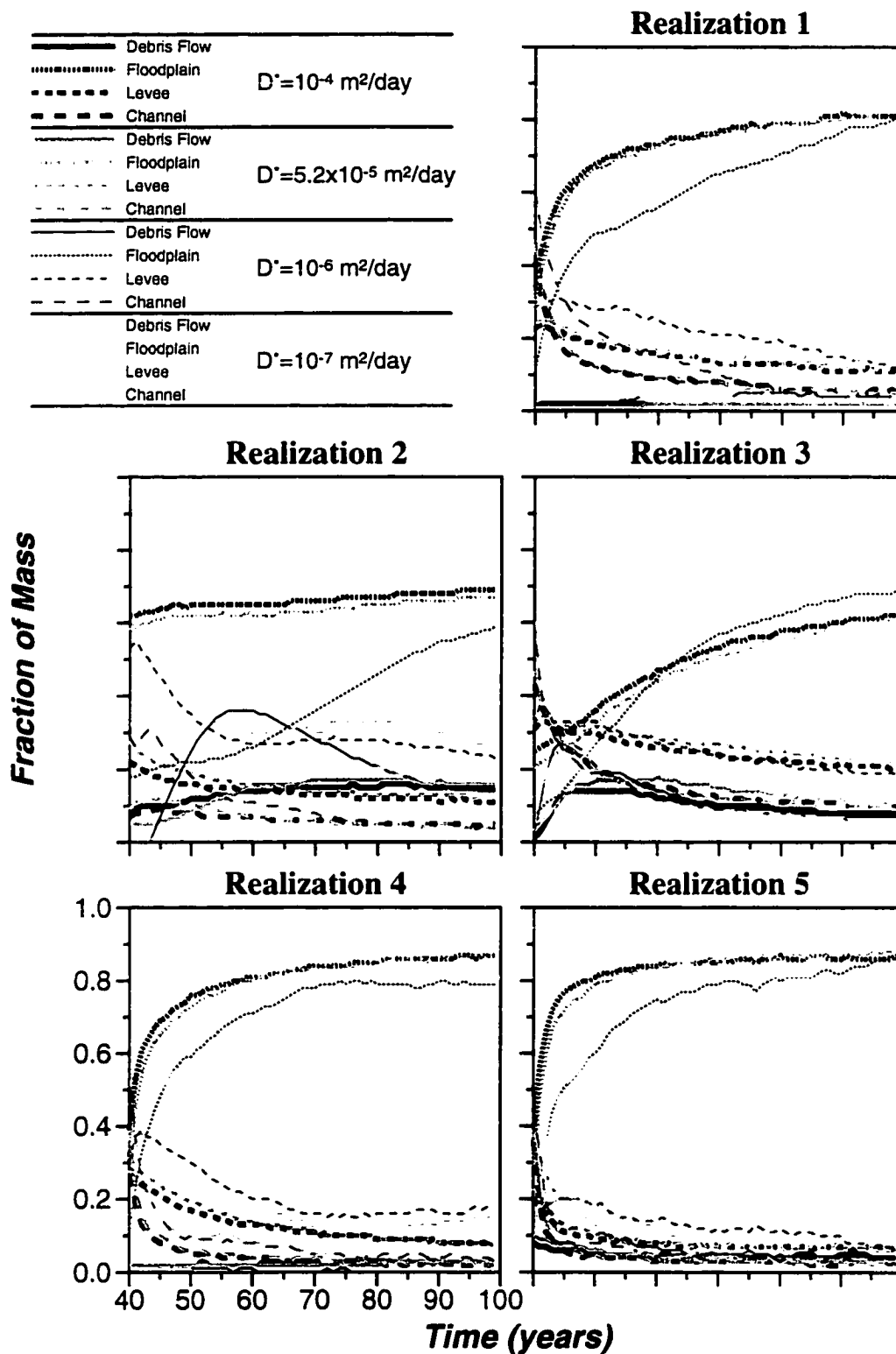


Figure 5.28. Fraction of total mass contained in each of the 4 hydrofacies as a function of time for scenarios 1 – 4, realizations 1 – 5.

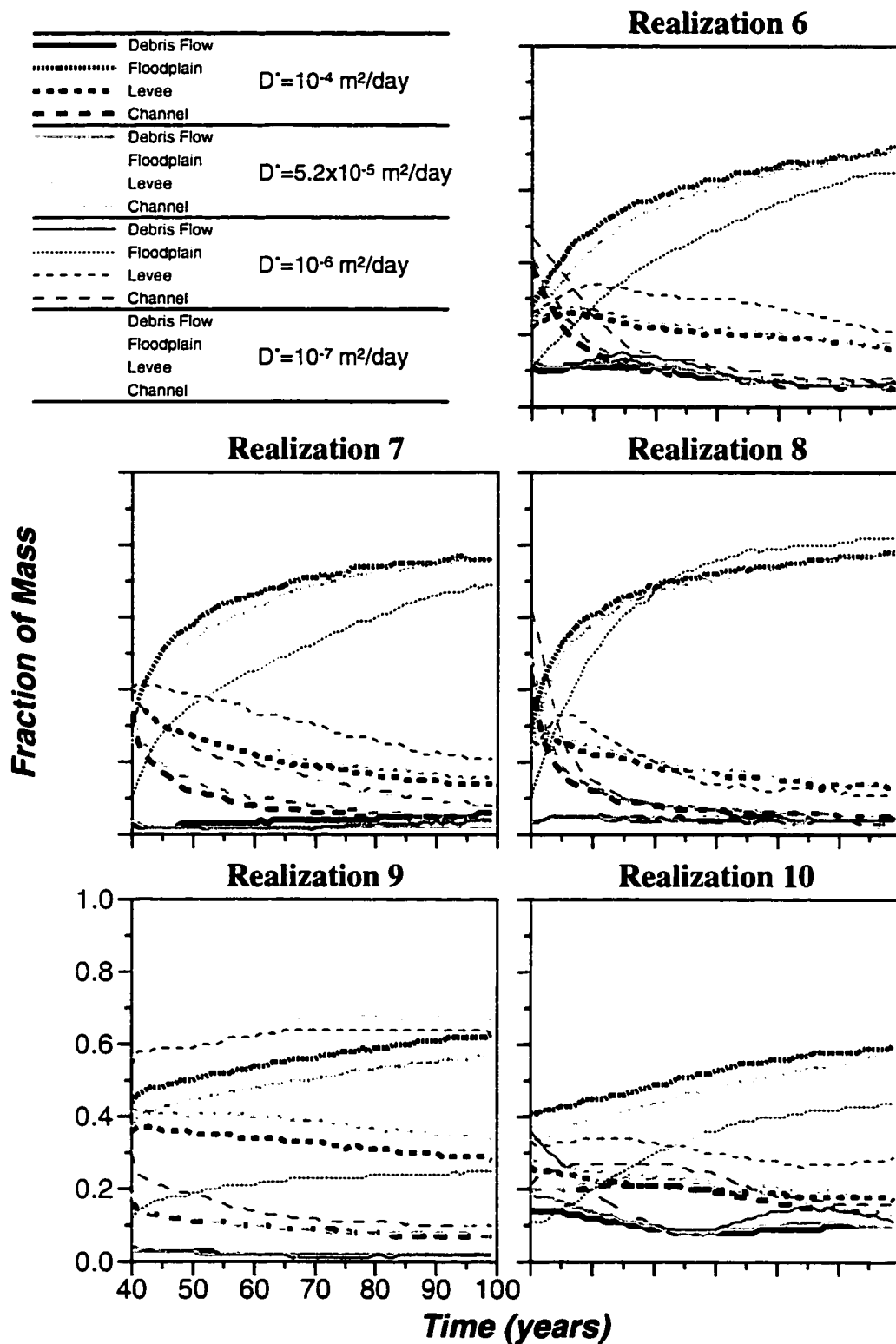


Figure 5.29. Fraction of total mass contained in each of the 4 hydrofacies as a function of time for scenarios 1 – 4, realizations 6 – 10.

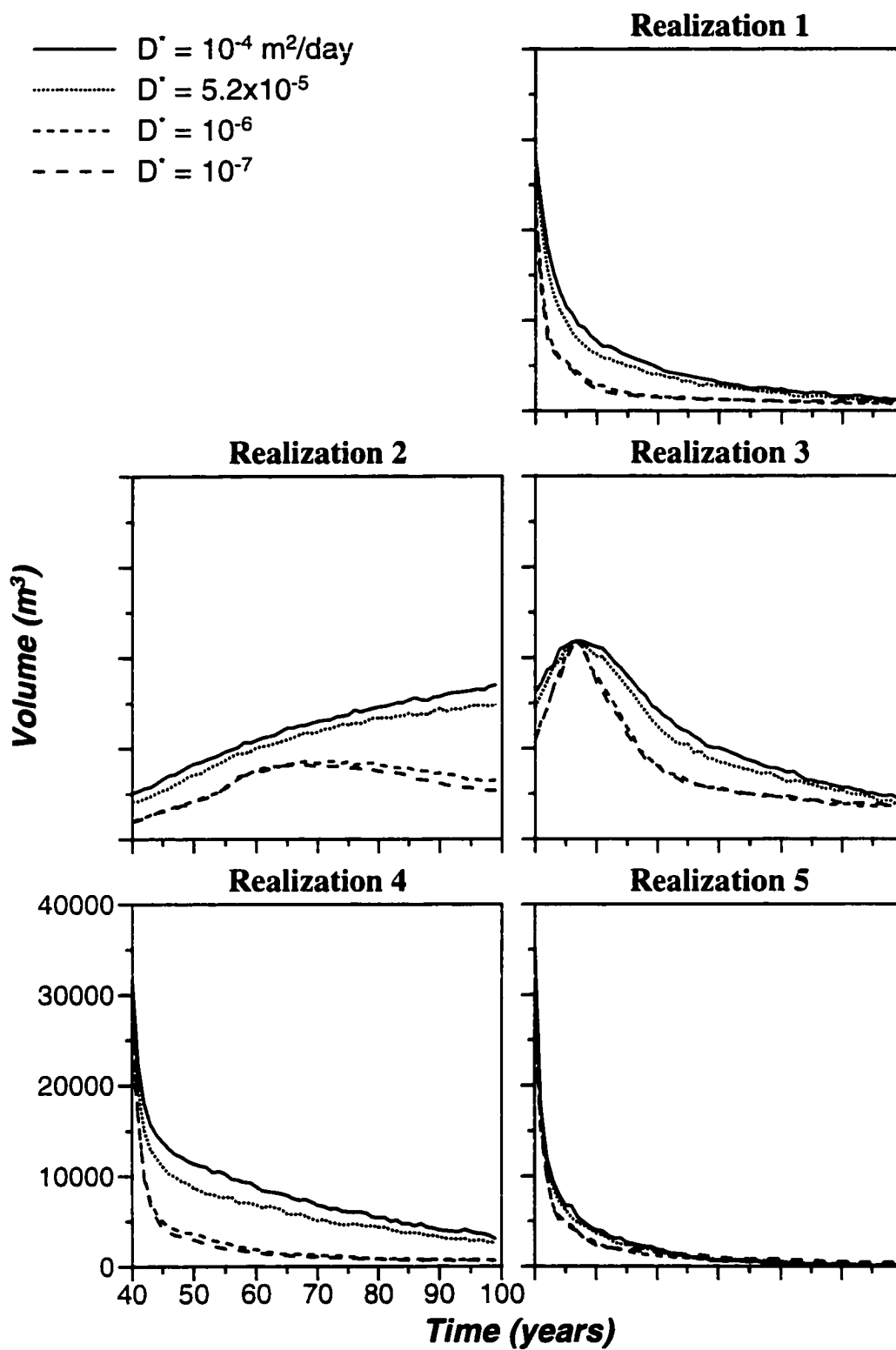


Figure 5.30. Volume of porous media in which concentration is greater than MCL ($c/c_0 > 10^{-3}$) as a function of time from the start of PAT for scenarios 1 – 4, realizations 1 – 5.

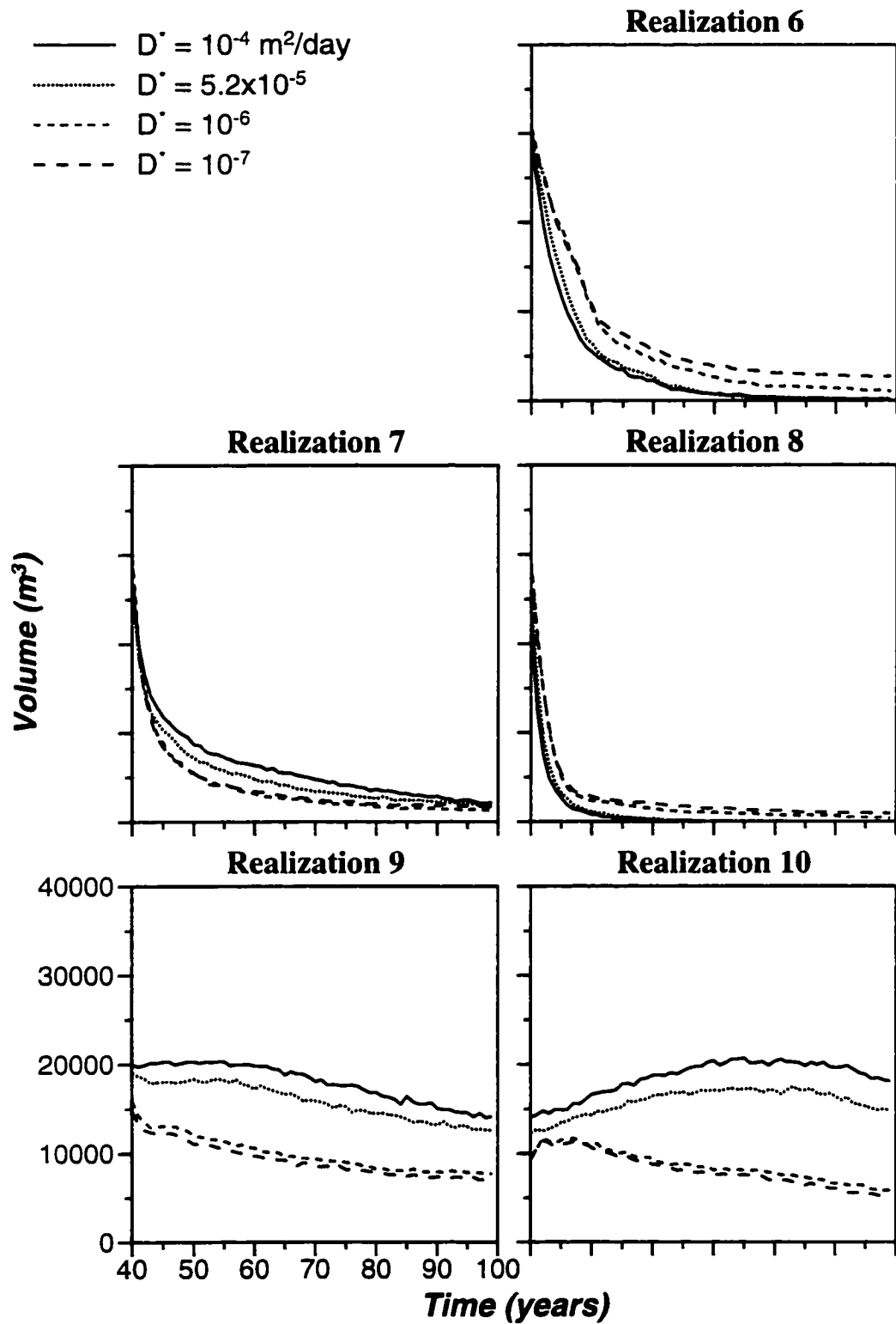


Figure 5.31. Volume of porous media in which concentration is greater than MCL ($c/c_0 > 10^{-3}$) as a function of time from the start of PAT for scenarios 1 – 4, realizations 6 – 10.

5.5.1.2.4 Concentration and mass distributions. Figures 5.32 and 5.33 plot normalized x - z average concentrations at the start of pumping and after 30 years of PAT for scenarios 1 – 4, realizations 1 - 10. In realizations where channel hydrofacies percolate and are well connected with the source, plume sizes and concentrations diminish considerably as a result of PAT. Again, results are most sensitive to D^* in the range of uncertainty, i.e., between 10^{-6} and 5.2×10^{-5} m²/day, with an increase in D^* resulting in a corresponding increase in sequestration of contaminants during remediation. After 30 years of PAT, realizations 1, 3, 4 and 5 for $D^* = 5.2 \times 10^{-5}$ m²/day show as much as an order of magnitude greater x - z average concentration than results for $D^* = 10^{-6}$ m²/day.

Plumes at the start of pumping in year 40 are more isolated near the source for realizations in which channel hydrofacies of the source location fail to percolate (2 and 10), or are poorly connected with the main channel network (3 and 9). These realizations show increased spreading of the plume and/or less reduction in concentration near the source in response to PAT. In realizations where channel hydrofacies percolate and are well connected with the source, Figures 5.32 and 5.33 show the largest decreases in concentration in the distal plume, downstream from the well located at 405 m. Therefore, the distal plume is more easily remediated than the plume near the source, even though the source is located upstream from the well whereas portions of the distal plume are not. This effect is primarily due to the greater extent of contaminant migration into floodplain hydrofacies near source locations and the difficulty in accessing this contamination by advection, and less dependence on location of the pumping well in the distal plume. The effect of diffusion on sequestration of mass near the source is clearly illustrated in Figures 5.34 (realization 4) and 5.35 (realization 7) showing normalized z -average

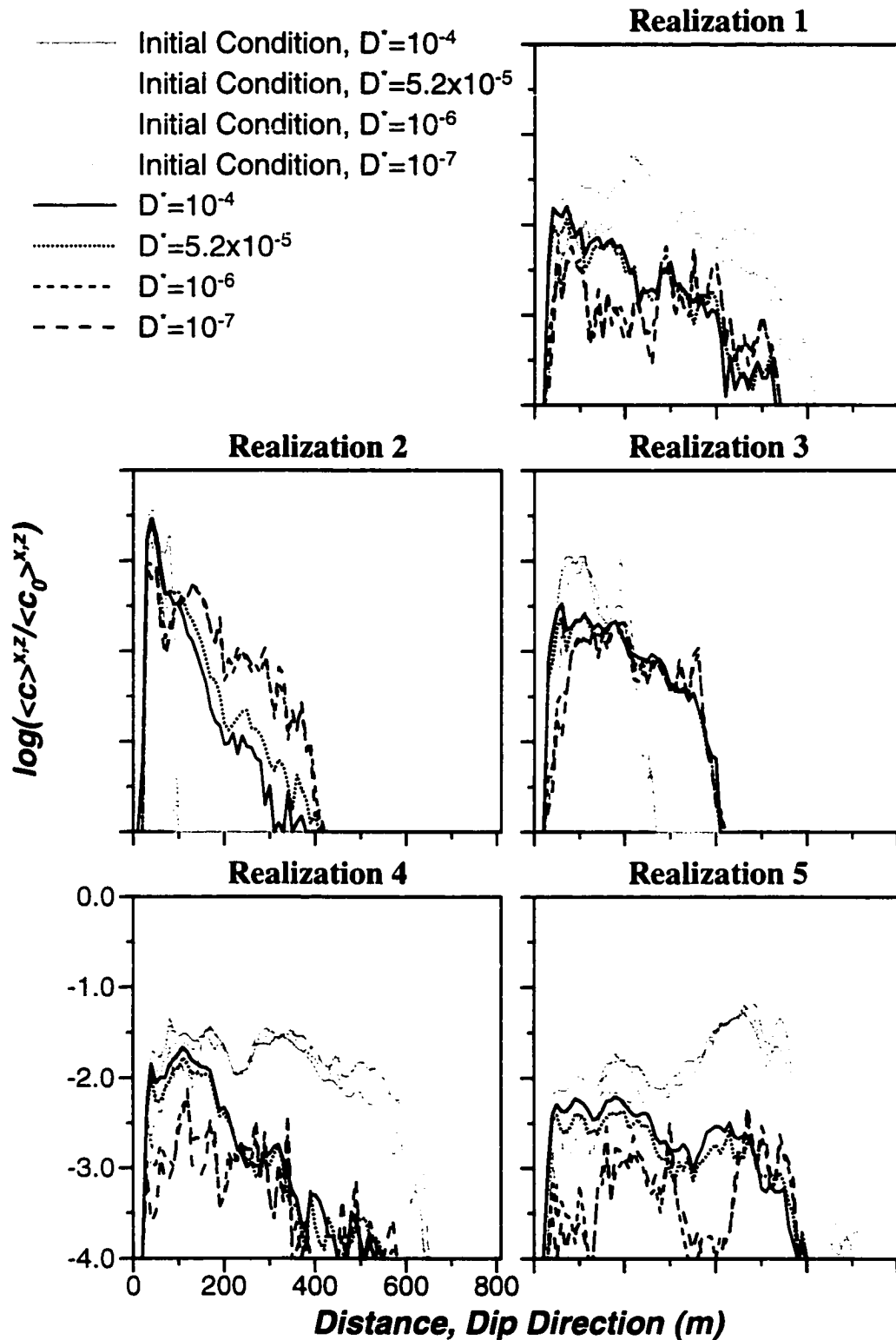


Figure 5.32. Normalized x-z average concentrations at the start of pumping and after 30 years of PAT for scenarios 1 - 4, realizations 1 - 5.

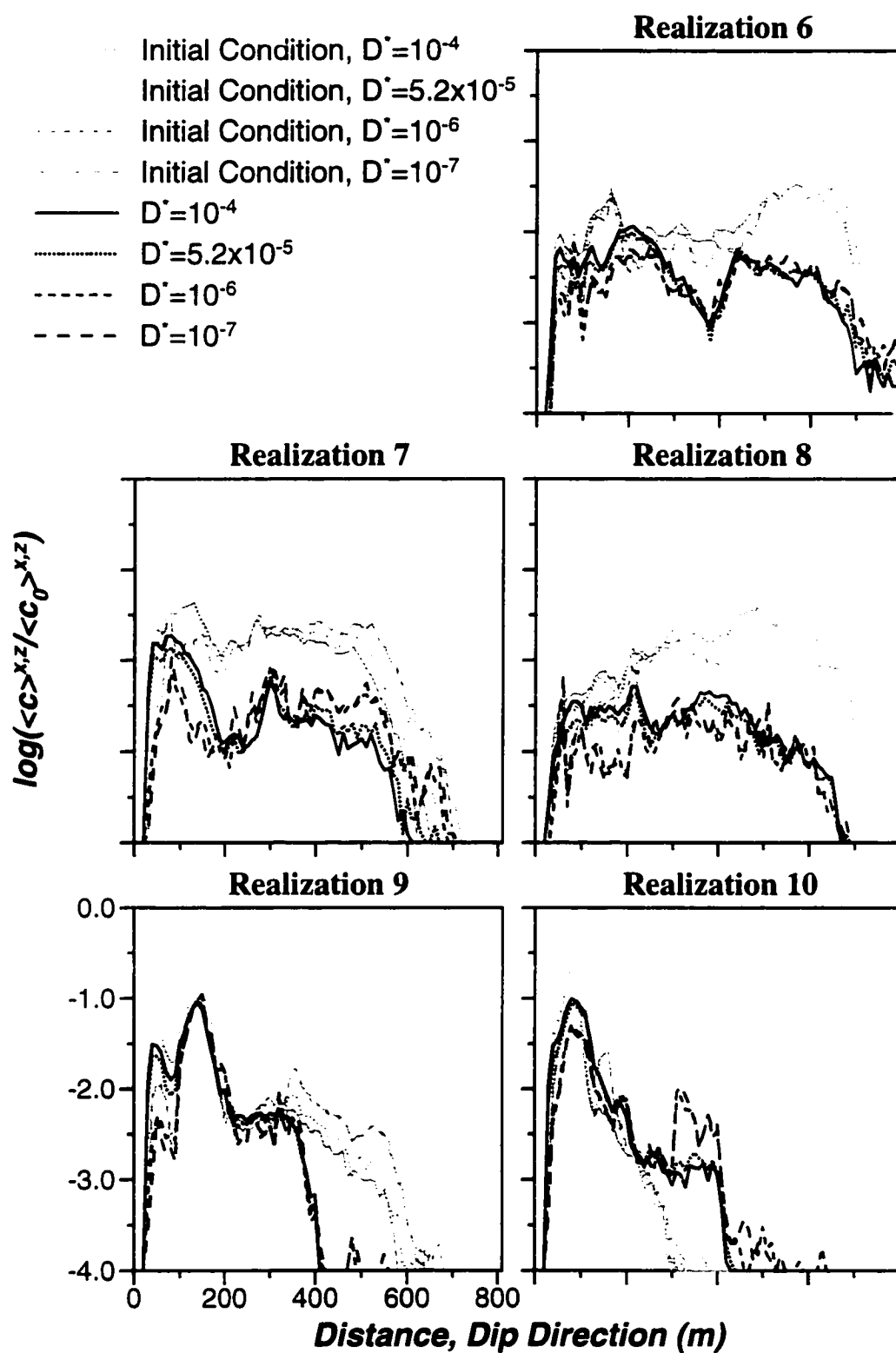


Figure 5.33. Normalized x - z average concentrations at the start of pumping and after 30 years of PAT for scenarios 1 - 4, realizations 6 - 10.

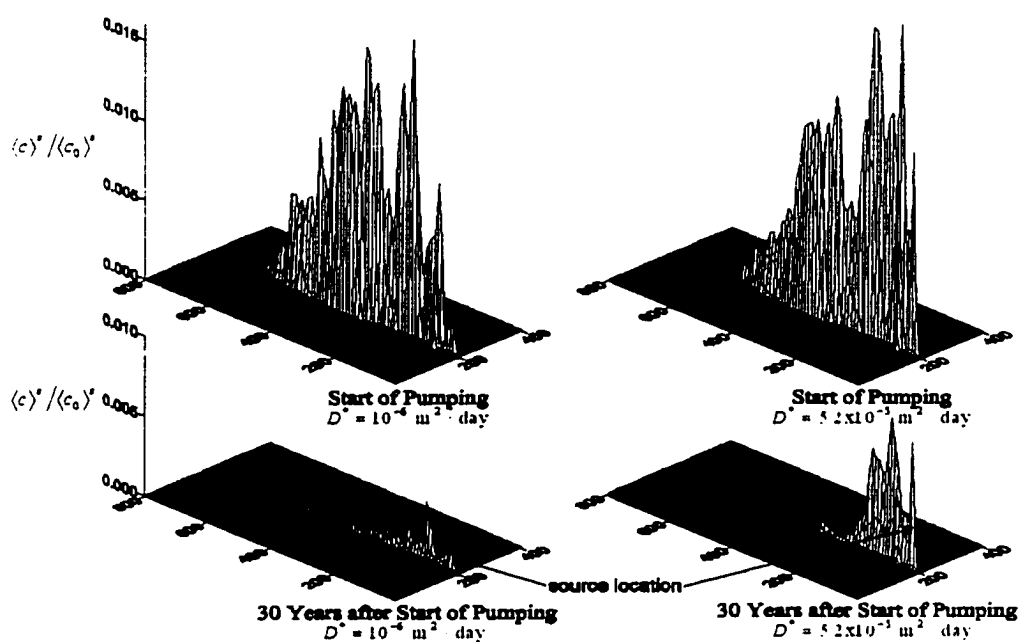


Figure 5.34: Normalized z-average concentrations at year 40 and year 70, 30 years after the start of PAT, for scenarios 2 and 3, realization 4.

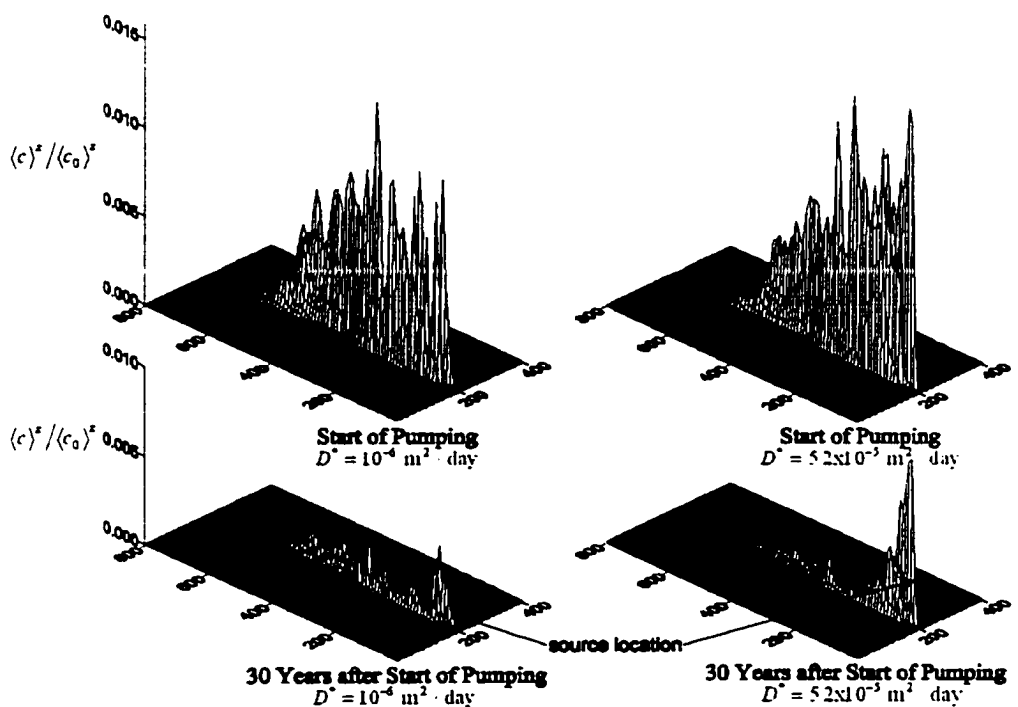


Figure 5.35: Normalized z-average concentrations at year 40 and year 70, 30 years after the start of PAT, for scenarios 2 and 3, realization 4 and 7.

concentrations at the start of, and after 30 years of, PAT for scenarios 2 ($D^* = 10^{-6}$ m²/day) and 3 ($D^* = 5.2 \times 10^{-5}$ m²/day). The degree of increase in sequestration of contaminants with increase in D^* , within the range of uncertainty, is remarkable. These results show that NAPLs need not be present for significant sequestration of mass near source locations.

5.5.1.2.4 Technical impracticability. Consider the results in Figure 5.36 plotting the maximum concentration in the system and concentration at the well for realizations 4. These results, consistent with the character of PAT remediation projects at LLNL [Hoffman, 1997], demonstrate the persistence of high concentrations within the system despite apparent remediation based on concentration at the pumping well. These results show that total remediation of the site within a reasonable time frame is *technically impracticable*. Concentrations near source locations persist for decades, possibly centuries, due to matrix diffusion, emphasizing the need to account for detailed heterogeneity and diffusion at local and intermediate scales in predictions of contaminant migration and remediation.

5.5.1.3 Ambient Transport, Scenarios 5 and 6

Results presented show contaminant migration and remediation are significantly sensitive to diffusion coefficient within the range of uncertainty. Therefore, it is important to know if this sensitivity is overwhelmed by the uncertainty in local-scale dispersivities. Scenarios 9 and 10 (Table 5.6) simulate ambient transport according to an advection diffusion equation ($\alpha_L = \alpha_T = 0$), and ADE with $D^* = 0$, respectively. Figure 5.37 shows normalized x - z average concentrations at the start of pumping and after 30 years of PAT for scenarios 2 (ADE), 5 (advection-diffusion equation) and 6 (ADE, no diffusion), realizations

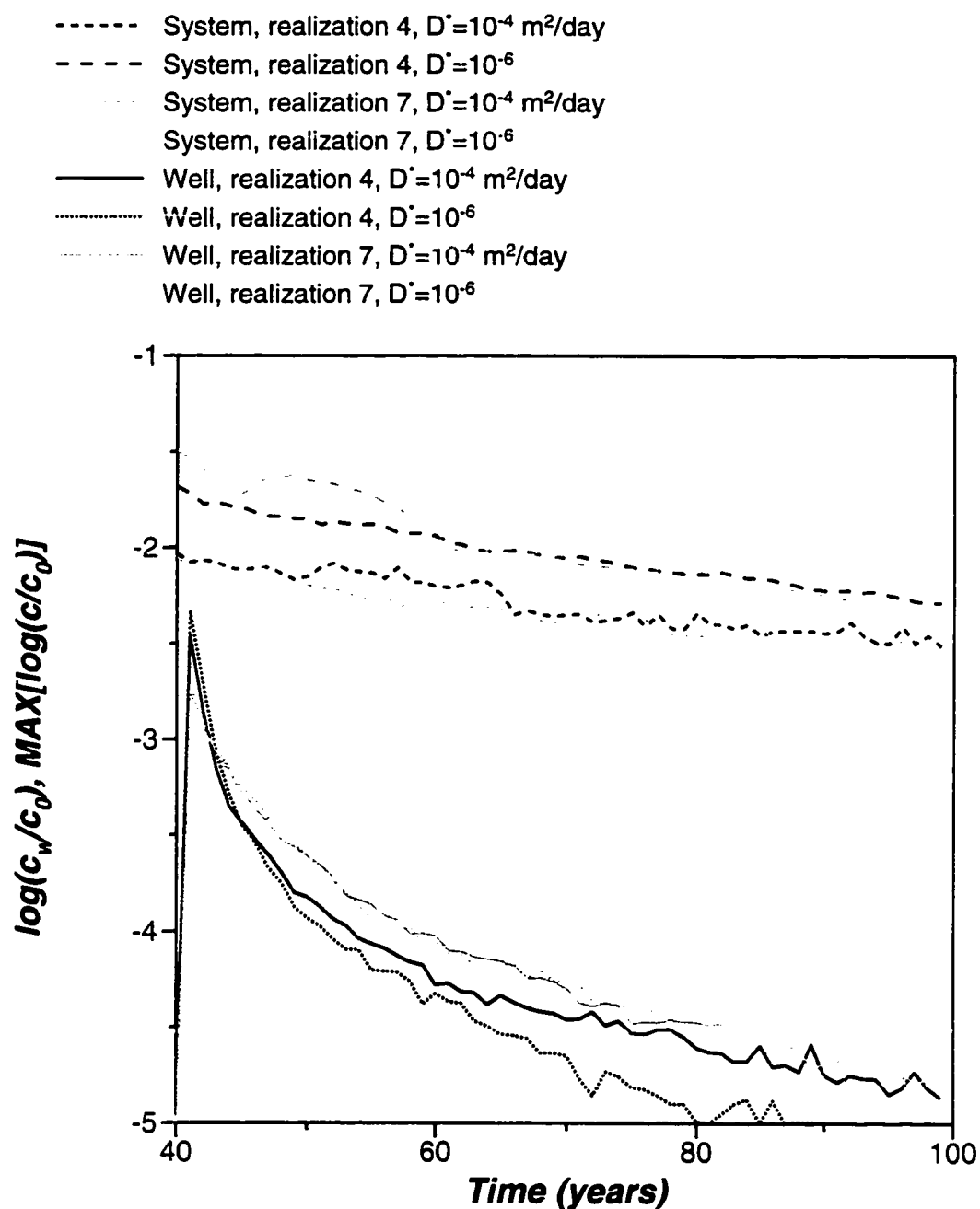


Figure 5.36. Maximum concentration in the system compared with concentration at the pumping well during PAT for scenarios 1 - 4, realizations 4 and 7.

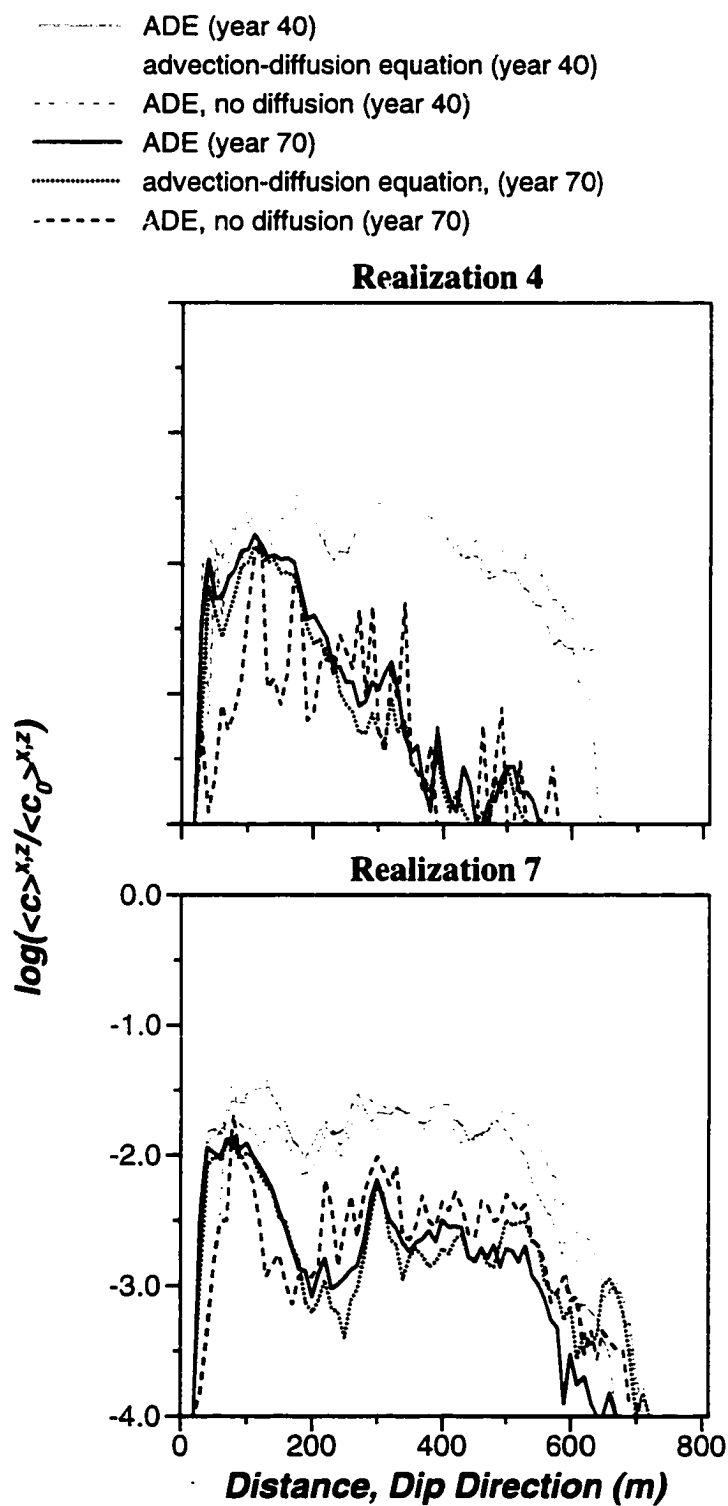


Figure 5.37: Normalized x-z-average concentrations at year 40 and at year 70, 30 years after the start of pump and treat, for scenarios 2 (ADE), 5 (advection diffusion equation) and 6 (ADE, no diffusion), realization 4 and 7.

4 and 7. Advection diffusion equation results are closer in character than results from an ADE with no diffusion to ADE results which include both mechanical dispersion and diffusion. In other words, here the pore-scale diffusion process appears more important than local-scale mechanical dispersion in predicting overall transport behavior.

5.6 Summary and Conclusions

In this paper we have reported on detailed simulations that explore the role of diffusion in contaminant migration and PAT remediation in an alluvial-fan aquifer underlying Lawrence Livermore National Laboratories (LLNL). These experiments have led to insights regarding

- the observed sequestration of contaminants near source locations at LLNL and elsewhere;
- the important role of matrix diffusion in contaminant migration and remediation in alluvial aquifers;
- the need for detailed geologic characterization honoring data;
- the technical impracticability of PAT remediation at LLNL and elsewhere; and
- the feasibility of natural attenuation as a remediation technology.

5.6.1 Sequestration of Contamination near Source Locations

Diffusion of contaminants into low-permeability floodplain hydrofacies (matrix diffusion) can explain the observed sequestration of contamination at LLNL, and elsewhere, characterized by persistent concentrations near suspected source locations. This result, together with the lack of observed NAPL contamination and data suggesting that sorption plays a relatively minor role in the transport of contaminants in saturated sediments of the site [*Hoffman, 1997*], suggests that effective molecular diffusivity is a key factor governing time to cleanup in the active PAT remediation project at the site.

5.6.2 On the Role of Diffusion in Contaminant Migration and Remediation

Ambient contaminant migration and PAT remediation performance were found to be acutely sensitive to the magnitude of the diffusion coefficient, particularly in the range of uncertainty from 10^{-6} to 10^{-5} m²/day. Results for the partitioning of mass, as a function of time, between hydrofacies show that this acute sensitivity is due to the influence of “immobile” water associated with low-permeability floodplain hydrofacies, and their geometry and distribution in the subsurface.

Migration of contaminants into the relatively immobile water of floodplain hydrofacies significantly sequesters contaminants. In ambient transport experiments, increasing diffusion coefficient from 10^{-6} to 5.2×10^{-5} m²/day resulted in as much as a 300% increase in the total mass of contaminants residing within floodplain hydrofacies. This effect corresponded to as much as a 25% decrease in the extent of downstream ambient migration in the center of mass by year 40, as exhibited in results for longitudinal first spatial moments. In the same way, longitudinal macrodispersivity was also sensitive to diffusion. However, results were inconsistent with Taylor dispersion theory suggesting that, even by year 40 and several correlation lengths of migration, ambient transport was still preasymptotic with regards to macrodispersive behavior [Gelhar, 1993; Dagan, 1989]. Indeed, this result is consistent with estimates for diffusion rate limited residence times in floodplain hydrofacies on the order of centuries to millenia.

Once present in the immobile water of low-permeability floodplain hydrofacies, sequestered contaminants behave like long-term sources with rate controlled by the magnitude of diffusion. This effect was clearly illustrated in simulations of PAT wherein re-

sults were particularly sensitive to diffusion coefficient. The PAT phase of scenarios 1 – 4 showed an increase in the mass remaining in the system, with increase in diffusion coefficient, due to a corresponding increase in the extent of migration of contaminants into floodplain hydrofacies during ambient transport, preceding PAT. Remediation of distal contamination was more rapid than contamination near source locations, not only because the pumping well was located in the distal plume, but also due to the greater extent of contaminant migration into floodplain hydrofacies near source locations and the difficulty in accessing this contamination by advection. Predicted sequestration of contaminants near source locations is consistent with results from active remediation projects at LLNL.

5.6.3 Geologic Characterization

Trends in geologic characterization are evolving toward greater consideration for the geologic processes that formed the subsurface. Theoretical models for the spatial correlation of hydraulic properties, amenable to the stochastic analysis of flow and transport, are not necessarily appropriate or accurate descriptions of complex geologic systems. On the other hand, models of facies architecture, for example, are based on characterizations of the geometry and distribution of lithologies related to distinct depositional processes, as opposed to hydraulic properties alone. Thus, there is a scientific basis for modeling the spatial correlation of facies as the processes that deposited them are necessarily spatially correlated.

The character of hydrofacies architecture may be inferred from depositional models and the quantitative analysis of geophysical, core, water quality and hydraulic data. Our results and those of *Carle* [1996] suggest that geologic characterization facilitated by geostatistical methods can be used to simulate the character of alluvial-fan deposits of

LLNL in detail. Carle [1996] showed that the calibrated hydraulic models can approximate observations from well interference tests. Simulations of contaminant migration and remediation presented herein capture the character of observations from the field, namely persistent concentrations, particularly near source locations, even with active PAT remediation.

Results emphasize the important role that details of hydrofacies architecture play in contaminant migration and remediation performance. In this regard, the connectivity of channel hydrofacies arises as an important factor controlling migration and remediation. On the average, approximately 80% of channel hydrofacies (18% by volume) at the LLNL site form a connected network extending in all directions. Transport behavior depends on the details of this network and the distribution of results presented appears to be bimodal. One mode corresponds to realizations in which channel hydrofacies of the source location are a part of the primary network of channels. The other mode corresponds to realizations in which channel hydrofacies of the source location are either not part of, or are poorly connected with, the primary network of channels. Importantly, knowledge of connectivity extrapolated from well-interference tests and/or water-chemistry data may be sufficient to constrain predicted connectivity of geologic characterizations, thereby restricting the range of predicted transport behavior to one mode of the distribution.

5.6.4 Technical Impracticability and Natural Attenuation as a Remediation Technology

The experimental results presented herein suggest that total remediation of the site within reasonable time frame is *technically impracticable*. The U.S. Environmental Protection

Agency bases technical impracticability (TI) determinations on inability to achieve required cleanup levels within a reasonable time frame using available remedial technologies. A TI determination is used to rationalize a change in remediation objectives. Results presented here show that concentrations near source locations will persist for decades, possibly centuries, due to matrix diffusion.

A TI determination does not necessarily imply adoption of monitored natural attenuation as a remedial option. Indeed, such determinations are made independent of one another. However, in the case of LLNL, those processes that render active remediation impracticable, i.e., the sequestration of contaminants in low-permeability materials, significantly dilute contaminant concentrations and limit the extent of migration. In a future paper, we will show how a combination of limited PAT remediation, followed by ambient migration of contaminants, may be an effective remediation alternative for the protection of water quality down gradient from the site, despite the continued persistence of high concentrations near source locations.

5.7 References

- Berglund, S. and V. Cvetkovic, Pump-and-treat remediation of heterogeneous aquifers: Effects of rate-limited mass transfer, *Ground Water*, 33(4), 675-685, 1995.
- Berglund, S., The effect of langmuir sorption on pump-and-treat remediation in a stratified aquifer, *Journal of Contaminant Hydrology*, 18(3), 199-220, 1994.
- Carle, S.F., A transition probability-based approach to geostatistical characterization of hydrostratigraphic architecture, Ph.D. Dissertation, University of California, Davis, 1996.
- Carle, S. F., and G. E. Fogg, Modeling spatial variability with one- and multidimensional Markov chains, *Mathematical Geology*, 28, 453-476, 1997.
- Carle, S.F., E.M. LaBolle, G.S. Weissmann, D. VanBrocklin, and G.E. Fogg, Geostatistical simulation of hydrofacies architecture: A transition probability/Markov approach, in *SEPM Concepts in Hydrogeology and Environmental Geology No. 1, Hydrogeologic Models of Sedimentary Aquifers*, G.S. Fraser and J.M. Davis (eds), SEPM (Society for Sedimentary Geology), Tulsa Oklahoma, 1998.
- Cohen, R.M., J.W. Mercer, R.M. Greenwald, and M.S. Beljin, Design Guidelines for Conventional Pump-and-Treat Systems, EPA/540/S-97/504, p. 38, 1997.

- Cvetkovic, V.D., G.Dagan, and A.M. Shapiro, An exact solution of solute transport by one-dimensional random velocity fields, *Stochastic Hydrology and Hydraulics*, 5, 45-54, 1991.
- Dagan, G, *Flow and Transport in Porous Formations*, Springer-Verlag, Berlin, Heidelberg, 465 pages, 1989.
- Deutsch, C.V. and A.G. Journel, *Geostatistical Software Library and User's Guide*, Oxford University Press, New York, 340 p., 1992.
- Feenstra, S., J.A. Cherry, E.A. Sudicky, and Z. Haq, Matrix diffusion effects on contaminant migration from an injection well in fractured sandstone, *Ground Water*, 22(3), 307-316, 1984.
- Fogg, G.E., C.D. Noyes and S.F. Carle, in press, Geologically-based model of heterogeneous hydraulic conductivity in an alluvial setting, *Hydrogeology Journal*, 6, 131-143, 1998.
- Gelhar, L.W. and C.L. Axness, Three-dimensional stochastic analysis of macrodispersion in aquifers, *Water Resources Research*, 19(1), 161-180, 1983.
- Gelhar, L.W., Stochastic subsurface hydrology from theory to applications, *Water Resources Research*, 22(9), 135S-145S, 1986.
- Gelhar, L.W., *Stochastic Subsurface Hydrology*, Prentice Hall, New Jersey, 1993.
- Gillham, R.W., E.A. Sudicky, J.A. Cherry and E.O. Frind, An advection diffusion concept for solute transport in heterogeneous unconsolidated geologic deposits, *Water Resources Research*, 20(3), 369-378, 1984.
- Grathwohl, P., *Diffusion in Natural Porous Media: Contaminant Transport, Sorption/Desorption and Dissolution Kinetics*, Kluwer Academic Publishers, Norwell, Massachusetts, 1998.
- Hoffman, F., R.G. Blake, Z. Demir, R.J. Gelinas, P.F. McKereghan, and C.D. Noyes, A conceptual model and remediation strategy for VOCs in Low Organic Carbon Unconsolidated Sediments, Lawrence Livermore National Laboratory, UCRL-JC-125199 Rev. 1, 1997.
- Koltermann, C.E. and S.M. Gorelick, Paleoclimatic signature in terrestrial flood deposits, *Science*, 256, 1175-1782, 1992.
- Matheron, G. and G. de Marsily, Is transport in porous media always diffusive? A counterexample, *Water Resources Research*, 16, 901-917, 1980.
- Mackay, D.M. and Cherry, J.A., Groundwater contamination: Pump-and-treat remediation, *Environmental Science and Technology*, 23, 630-636, 1989.
- McDonald, M.G. and Harbaugh, A.W, A modular three-dimensional finite-difference ground-water flow model. U.S. Geological Survey Techniques of Water-Resources Investigations Book 6, Chapter A1, 586 p., 1988.
- Mercer, J.W., D.C. Skipp, and D. Giffin, Basics of Pump-and-Treat Ground-Water Remediation Technology, EPA/600/8-90/003, Ada, Okla., EPA, R.S. Kerr Environmental Research Laboratory, p. 31, 1990.
- National Research Council (NRC), *Alternative for Ground Water Cleanup*, National Academy Press, Washington, D.C., 1994.
- Noyes, C.N., Hydrostratigraphic analysis of the Pilot Remediation Test Area, LLNL, Livermore, California, M.S. Thesis, University of California, Davis, 165 p., 1991.

- Nyer, E.K., Aquifer restoration: Pump and treat and the alternatives, *Groundwater Monitoring and Review*, Winter, 89-92, 1993.
- OSWER Directive 9200.4-17, Use of Monitored Natural Attenuation at Superfund, RCRA Corrective Action, and Underground Storage Tank Sites, U.S. EPA Office of Solid Waste and Emergency Response Directive 9200.4-17, 29 pp, November, 1997.
- Poeter, E.P. and S.A. Mckenna, Reducing uncertainty associated with ground-water flow and transport predictions, *Ground Water*, 33(6), 899-904, 1995.
- Robbins, G.A., Methods for determining transverse dispersion coefficients of porous media in laboratory column experiments, *Water Resources Research*, 25(6), 1249-1258, 1989.
- Gillham, R.W., E.A. Sudicky, J.A. Cherry and E.O. Frind, An advection diffusion concept for solute transport in heterogeneous unconsolidated geologic deposits, *Water Resources Research*, 20(3), 369-378, 1984.
- Tezloff, D.M., and Hargaugh, J.W., *Simulating Clastic Sedimentation*, Van Nostrand Reinhold, New York, 202p., 1989.
- Thorpe, R.K., W.F. Isherwood, M.D. Dresen and C. Webster-Scholten, CERCLA remedial investigation report for the LLNL Livermore site: Lawrence Livermore National Laboratory Report UCAR-10299, 1990.
- Tompson, A.F.B., R.D. Falgout, S.G. Smith, W. J. Bosl, and S.F. Ashby, Analysis of subsurface contaminant migration and remediation using high performance computing, *Advances in Water Resources*, 22(3), pp 203-221, 1998.
- Wilson, D.J., R.D. Mutch, and J.I. Scott, Matrix diffusion in the cleanup of heterogeneous aquifers, *Environmental Monitoring and Assessment*, 26, 49-64, 1993.

Appendix 5A: Boundary Conditions of the Groundwater-Flow Simulations

This appendix describes the boundary conditions of the groundwater-flow simulations. The flow simulations include general head boundaries GHBs [McDonald and Harbaugh, 1988] assigned to grid blocks on vertical and bottom faces, recharge from above assigned to grid blocks on the top face, and pumping at nodes in the center of the domain. Due to computational limitations, the model domain includes only a small fraction of the flow system as defined by natural hydrologic boundaries. The use of GHBs allows for flow to and from the model in response to model stresses.

A GHB specifies a head h^*_{ijk} at some location outside of the model domain and conductance C^*_{ijk} that hydraulically connects this location to a model node with head h_{ijk} , where i, j , and k index nodal locations in the x , y , and z directions. Flow Q_{ijk} to model node (i, j, k) from outside of the model is computed as $Q_{ijk} = C^*_{ijk}(h^*_{ijk} - h_{ijk})$. Conductances associated with GHBs are computed based on the overall conductance, or capacity for flow, of model boundary nodes. Capacity for flow of a boundary node is a function not only of K of that node, but also K of adjacent regions. Capacity for flow may be computed independently from flow simulations as described below.

5A.1: GHB Conductances

Specified GHB conductances are designed to minimize adverse boundary effects (e.g., unrealistic convergence of flow into low- K hydrofacies near boundaries). The total conductance for all grid blocks on a face of the model is computed as $\bar{K}A/L$ where A is the area [L^2] of that face, \bar{K} is the effective hydraulic conductivity [LT^{-1}] in the direction perpendicular to that face (determined from the steady-state flow simulations described

below), and L (= 1600, 400 and 100 m in the x -, y -, and z -coordinate directions) is the specified distance between nodal locations of grid blocks on that face and locations where h^* is supposed to apply. This total conductance is distributed among GHBs of its corresponding face by the relative flow, to each model node of that face, computed independently from a steady-state flow simulation. Boundary conditions of this steady-state flow simulation include constant heads, for grid blocks on faces perpendicular to the coordinate direction of interest, and no-flow for grid blocks on the remaining faces. Conductance for node (i,j,k) is computed as $C_{ijk} = (Q_{ijk} \bar{K} A) / (L Q_{TOTAL})$, where Q_{TOTAL} is the total flow normal to that face. Three steady-state flow simulations, one for each of the coordinate directions, are required to assign conductances to GHB nodes of the model. Heads h^*_{ijk} are specified to maintain, under ambient flow conditions, a dip-direction gradient of 2×10^{-3} , net-zero-flux boundary conditions in the strike direction, and a vertical gradient of 5×10^{-4} .

5A.2: Recharge

Uniformly distributing recharge within the model will result in significant groundwater mounding above grid blocks with a low capacity for flow. To minimize mounding, the total recharge is distributed among boundary nodes of the top face of the model by the relative flow to each node computed independently from a steady-state confined flow simulation. Boundary conditions of this steady-state simulation include constant heads for grid blocks on faces on the top and bottom of the model and no-flow for grid blocks on the remaining faces.

Appendix 5B: Grid Refinement Experiments

Here the effect of grid resolution on flow and contaminant transport is considered. The simulation methodology of Chapter 5 assigns conductivities to the direct outcome of transition probability based indicator simulations without further grid refinement. The approach will result, for example, in grid blocks isolated in a matrix of contrasting conductivity (Figure 5B.1, (1x)). As numerical grids are refined (Figure 5B.1), accuracy of flow solutions will improve. Effects of these improvements on transport may be significant. For experiments in Chapter 5, computational limitations at the time precluded refining the numerical grid. Nevertheless, results of the experiments described below suggest that resolving the numerical grid does not necessarily result in a systematic trend in the solutions. Further, changes with grid refinement are small enough so as to not affect the conclusions of Chapter 5.

5B.1 Simulation Procedure

Flow and transport simulations are performed at the three different grid resolutions, 1x, 3x and 5x, as illustrated in 2-D in Figure 5B.1. Note that grids are resolved while maintaining simulated geometry at 1x resolution. Ten conditional simulations of dimension 105.0, 210.0, and 10.5 m in x -, y - and z -directions, respectively, $\Delta x = 5.0$, $\Delta y = 10.0$, and $\Delta z = 0.5$ m at 1x resolution, are generated from the Livermore data set and conductivities are assigned as described in Chapter 5.

Boundary conditions for the steady-state flow simulations are $h = 0.2$ m at $y = 5.0$ m and $h = 0.0$ m at $y = 205$ m, for all x and z ; no flow at $x = 0$ and $x = 105$ m, for all y and z , and no flow at $z = 0$ and $z = 10.5$, for all x and y . Boundary conditions for transport simulations are specified as absorbing on all sides of the domain, i.e., when particles

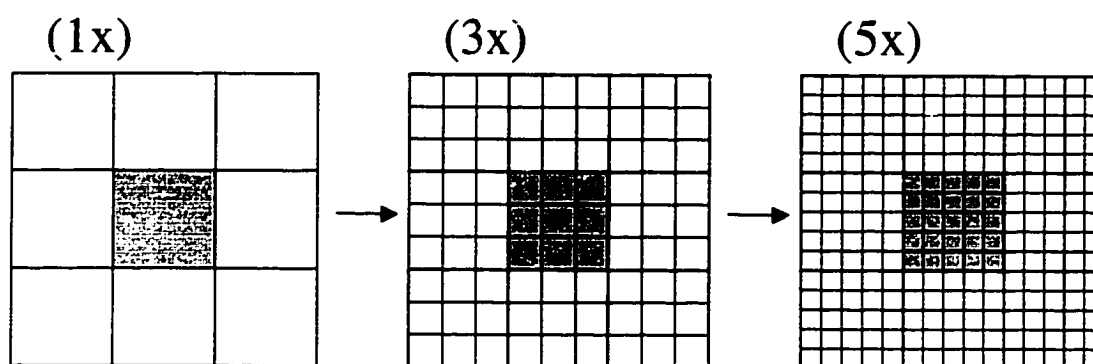


Figure 5B.1: Two-dimensional Illustration of the 3 grid resolutions used. Contrast in shades represents different hydrostratigraphic units. Typically one hydrostratigraphic unit contacts at least several grid blocks in any given direction.

leave the domain through one of the sides, they are eliminated from the simulation. Parameters include $\Theta = 0.35$, $\alpha_L = \alpha_T = 0.01$ m, and $D^* = 10^{-5}$ m²/day. An instantaneous source of 9000 particles at time $t = 0$ is distributed uniformly within the region $55 < x < 60$, $20 < y < 30$, $4.5 < z < 6.5$. This region is conditioned on data that designate channel facies such that facies type of the source location is the same for all ten realizations.

5B.2 Results and Discussion

Simulated hydraulic heads for realization 1 are compared for the three resolutions in Figure 5B.2. These results show an increase in variability of hydraulic head, and therefore velocity, as the grid is refined. Computed 10 year and 20 year x - z -average plumes at the three resolutions and for all ten realizations are compared Figures 5B.3 and 5B.4. Averaging of mass is performed on a grid corresponding to the 1x resolution. Note that mass has exited the end of the domain at 20 years in all simulations, with the exception of realization 2, where channel facies connected with the source location do not percolate (i.e., do not connect in the dip direction). Perhaps the most notable differences between

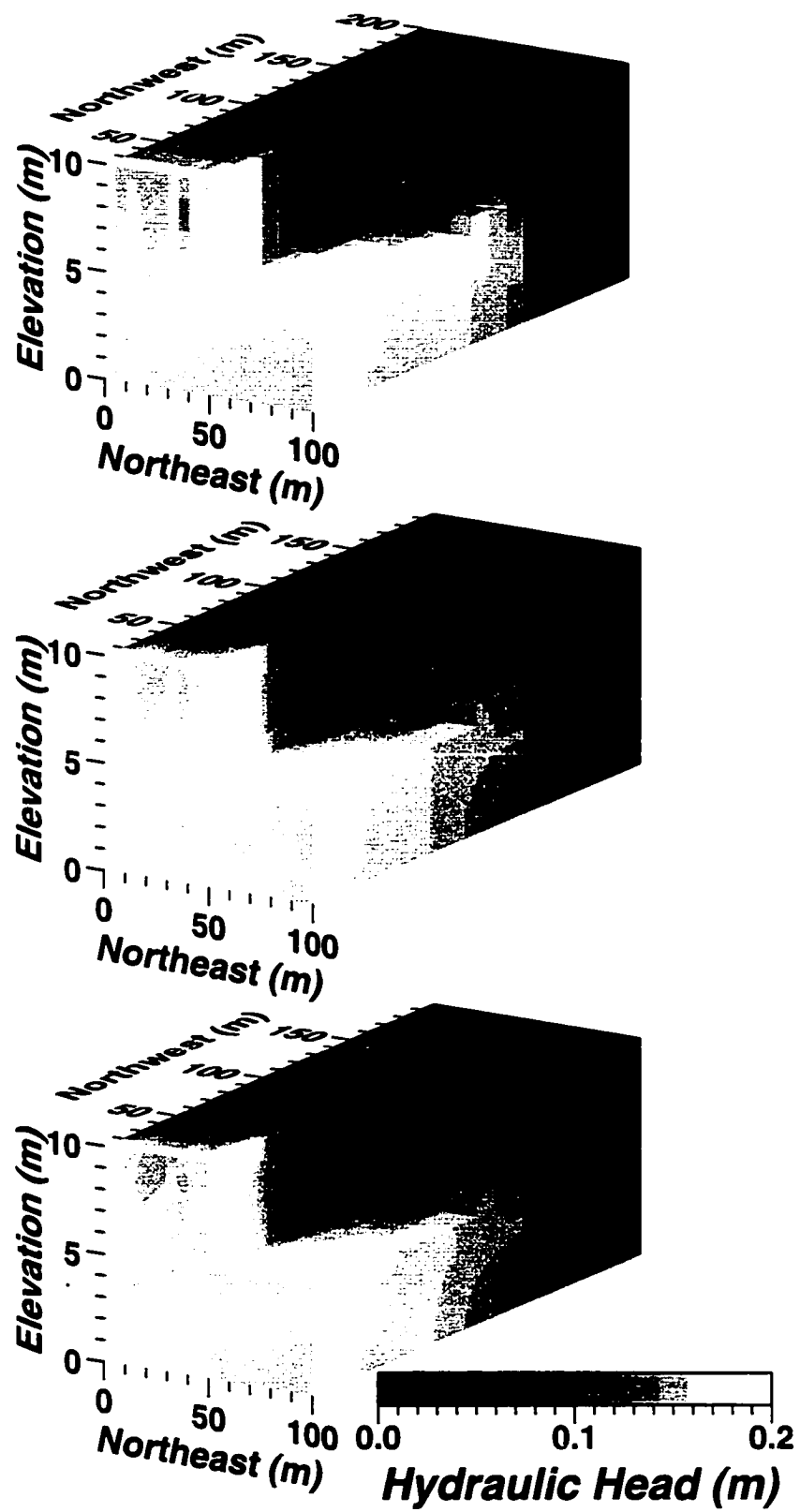


Figure 5B.2: Simulated hydraulic head for realization 2 at 1x (top), 3x (middle) and 5x (bottom) resolutions.

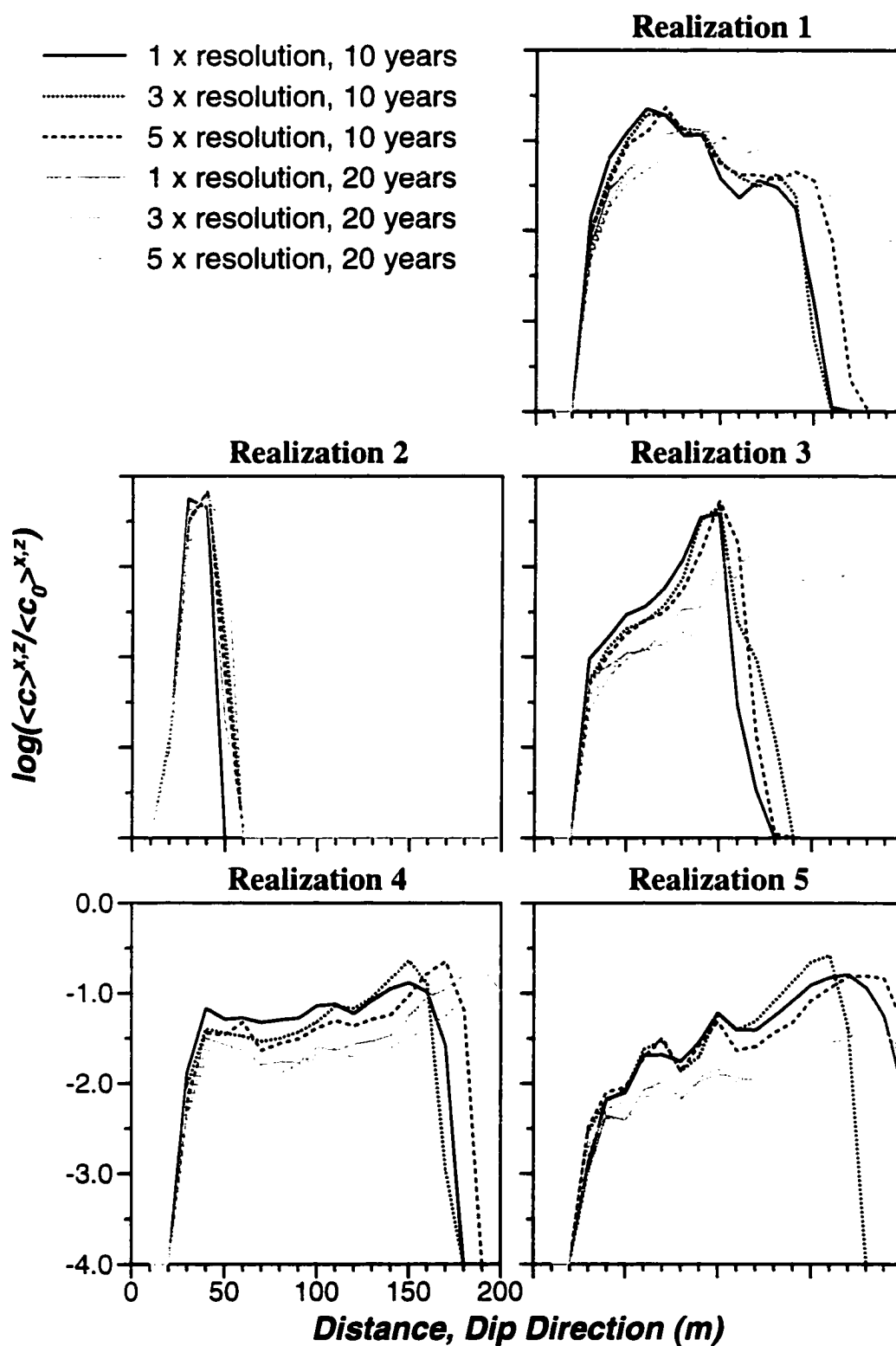


Figure 5B.3: Normalized x - z -average plumes, realizations 1 – 5, at years 10 and 20 are compared for 1x, 3x and 5x resolutions.

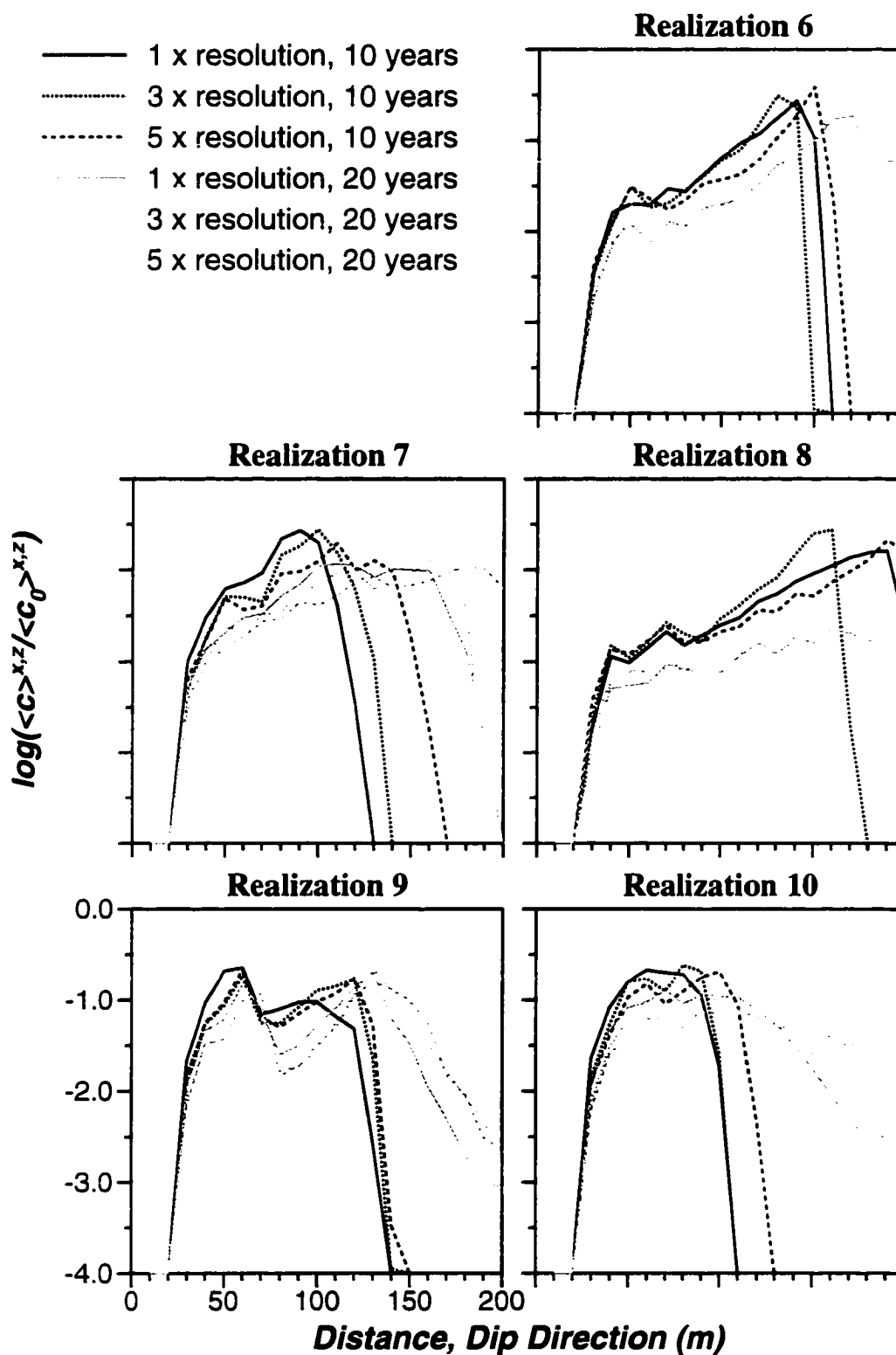


Figure 5B.4: Normalized x - z -average plumes, realizations 6 – 10, at years 10 and 20 are compared for 1x, 3x and 5x resolutions.

simulations at the three resolutions occur at leading edges of the plumes. In all cases, resolving the grid to 5x results in further migration of the leading edge of the plume. However, with the exception of realizations 5 and 7, this increase in downstream migration of the leading edge at 10 years is only between 10 and 20 m, i.e., 1 to 2 grid blocks. Further, changes in extent of migration of the leading edge of the plume with increase in grid resolution do not follow a systematic trend, e.g., in some cases, increasing from 1x to 3x resolution results in a decrease in the extent of migration. In all cases, the upstream edge of the plumes remain essentially unchanged, even though the source was instantaneous.

Transport simulation results for longitudinal first spatial moment at the three grid resolutions and for all ten realizations are compared in Figures 5B.5 and 5B.6. In considering these results, one should bear in mind that the leading edge of most plumes have exited the downstream end of the domain at later times (see Figures 5B.3 and 5B.4). The first moment at 5x resolution is generally greater than at 1x resolution; the exceptions being realizations 5 and 8 that may be discounted due to significant breakthrough of mass at the downstream end of the domain at later times. However, the trend of increase in first moment with increase in grid resolution is not systematic; increasing grid resolution from 1x to 3x does not necessarily result in an increase in the first spatial moment.

Transport simulation results for longitudinal second spatial moment at the three resolutions and for all ten realizations are compared Figures 5B.7 and 5B.8. The second moment at 5x resolution is generally greater than at 1x resolution. However, again, the trend is not systematic; increasing grid resolution from 1x to 3x does not necessarily result in an increase in the second spatial moment.

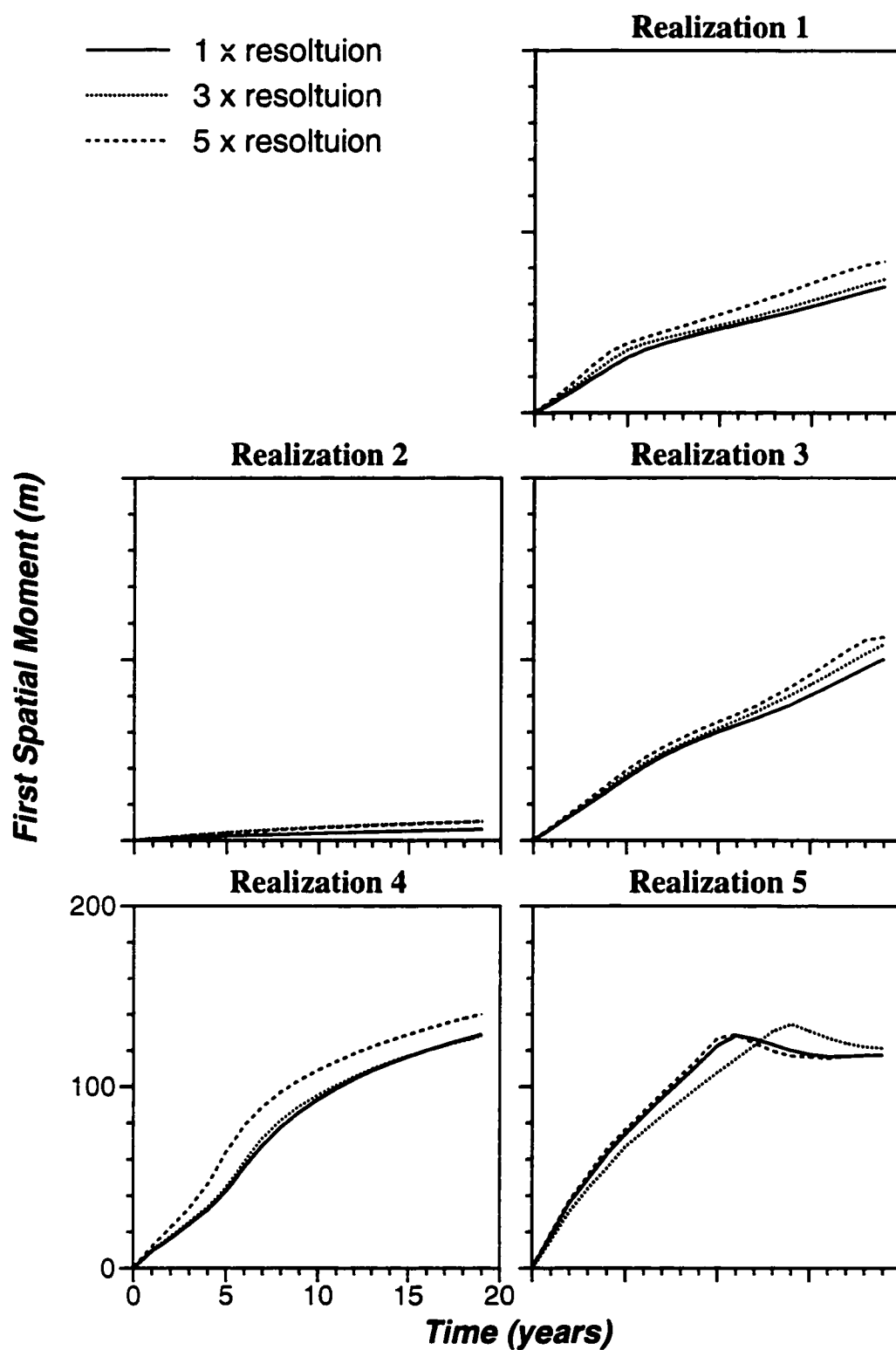


Figure 5B.5: Longitudinal first spatial moments for realizations 1 – 5 are compared for 1x, 3x and 5x resolutions.

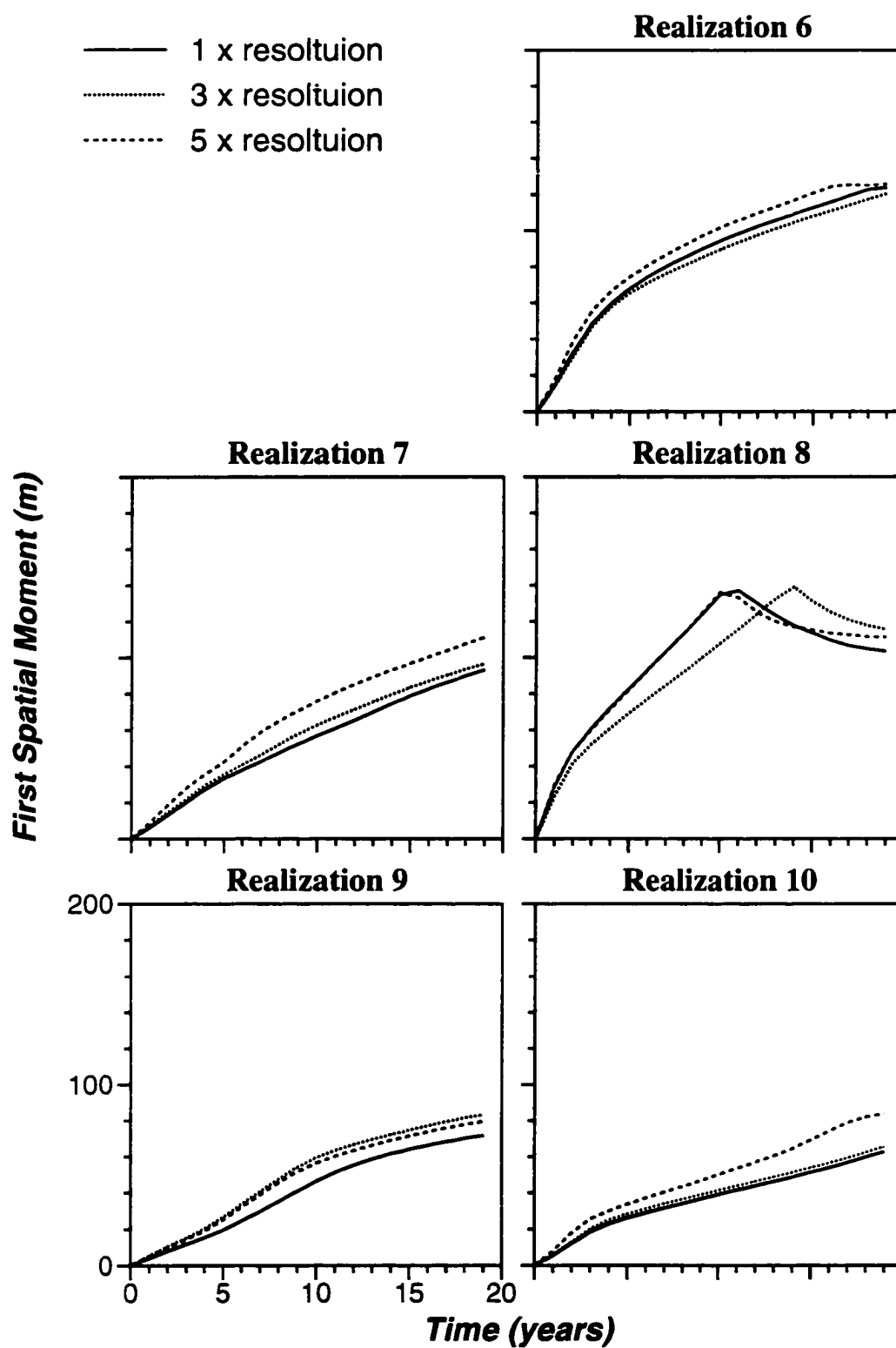


Figure 5B.6: Longitudinal first spatial moments for realizations 6 – 10 are compared for 1x, 3x and 5x resolutions.

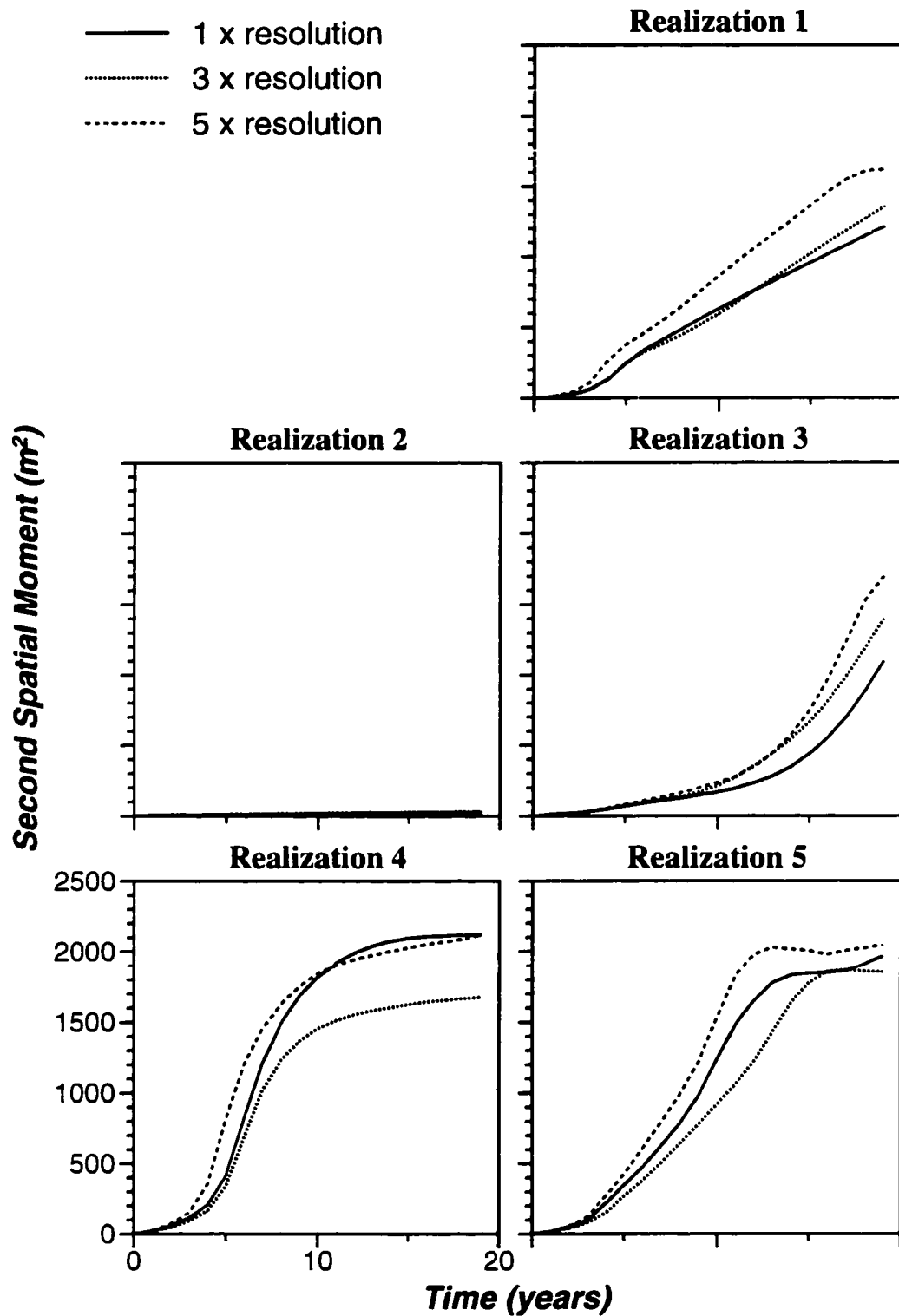


Figure 5B.7: Longitudinal second moments for realizations 1 – 5 are compared for 1x, 3x and 5x resolutions.

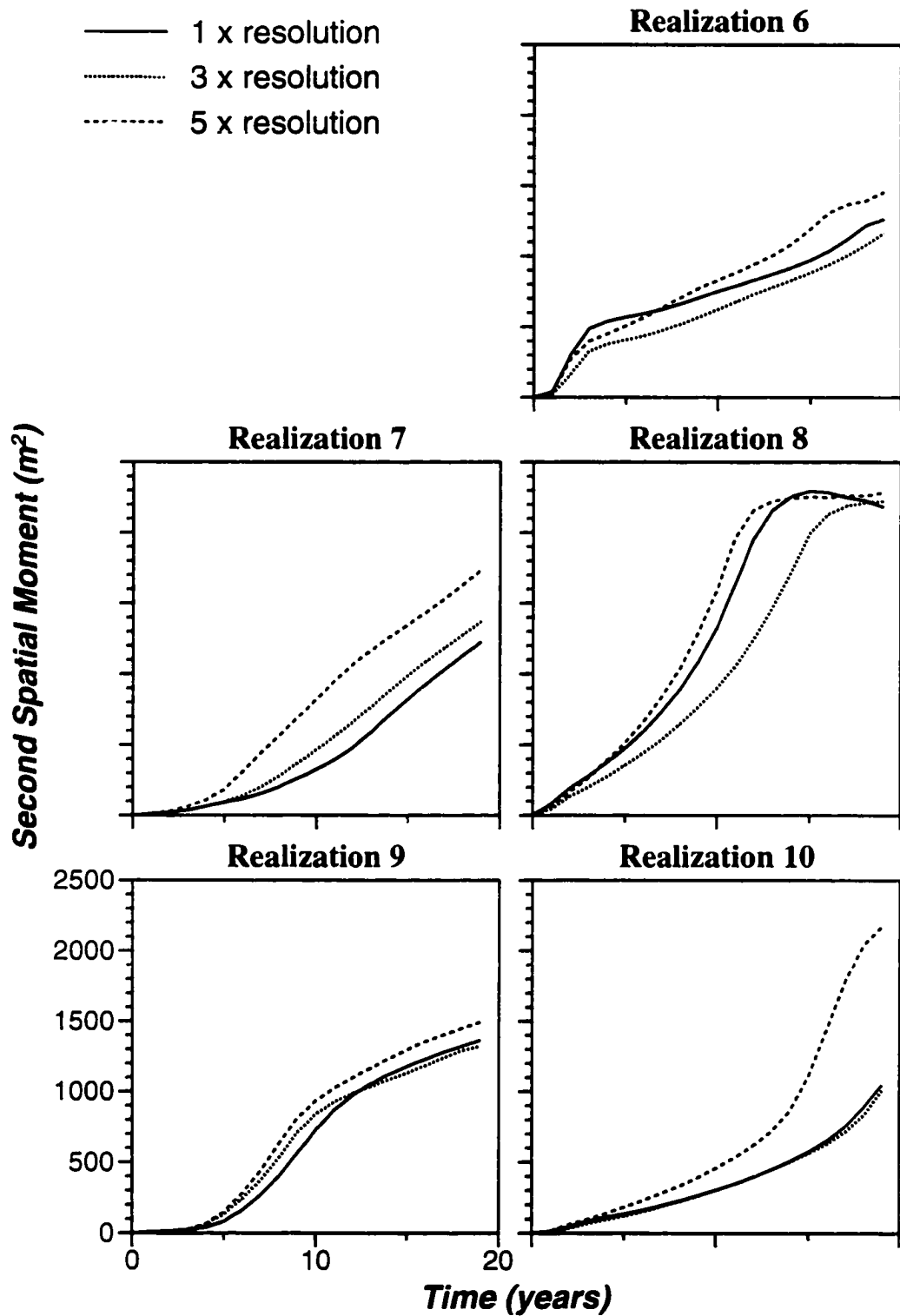


Figure 5B.8: Longitudinal second spatial moments for realizations 6 – 10 are compared for 1x, 3x and 5x resolutions.

Appendix 5C: Sensitivity of Contaminant Migration to Local-Scale Dispersivities

Appropriate values for local-scale longitudinal and transverse dispersivity, α_L and α_T , within hydrofacies are uncertain. Here we consider the effects of local-scale longitudinal and transverse dispersivities on solutions of the advection dispersion equation (1).

5C.1 Simulation Procedure

Five scenarios with values of α_L and α_T that range over two orders of magnitude (Table 5C) are considered. These scenarios test the relative influence α_L and α_T in contaminant migration. A value of $D^* = 10^{-5} \text{ m}^2/\text{day}$ is used in all simulations. Transport simulations are performed for all 10 realizations of heterogeneity with ambient flow conditions through year 40 followed by stressed conditions at the $25 \text{ m}^3/\text{day}$ pumping rate. Initial conditions are specified as an instantaneous line source.

5C.2 Results and Discussion

Normalized x - z average concentrations at year 20 are shown in Figures 5C.1 and 5C.2. Results for scenarios 5C.1 – 5C.3, in which $\alpha_T = 0.01 \text{ m}$, are nearly identical, with the exception of a detectable increase in longitudinal dispersion for $\alpha_L = 0.1 \text{ m}$, even though α_L varies over two orders of magnitude among them. Results show an increase in

Table 5C: Longitudinal and Transverse Dispersivities of Scenarios 5C.1 - 5C.5

Scenario	α_L (m)	α_T (m)	Description
5C.1	1.0	0.01	Anisotropic
5C.2	0.1	0.01	Anisotropic
5C.3	0.01	0.01	Isotropic
5C.4	0.1	0.1	Isotropic
5C.5	0.001	0.001	Isotropic

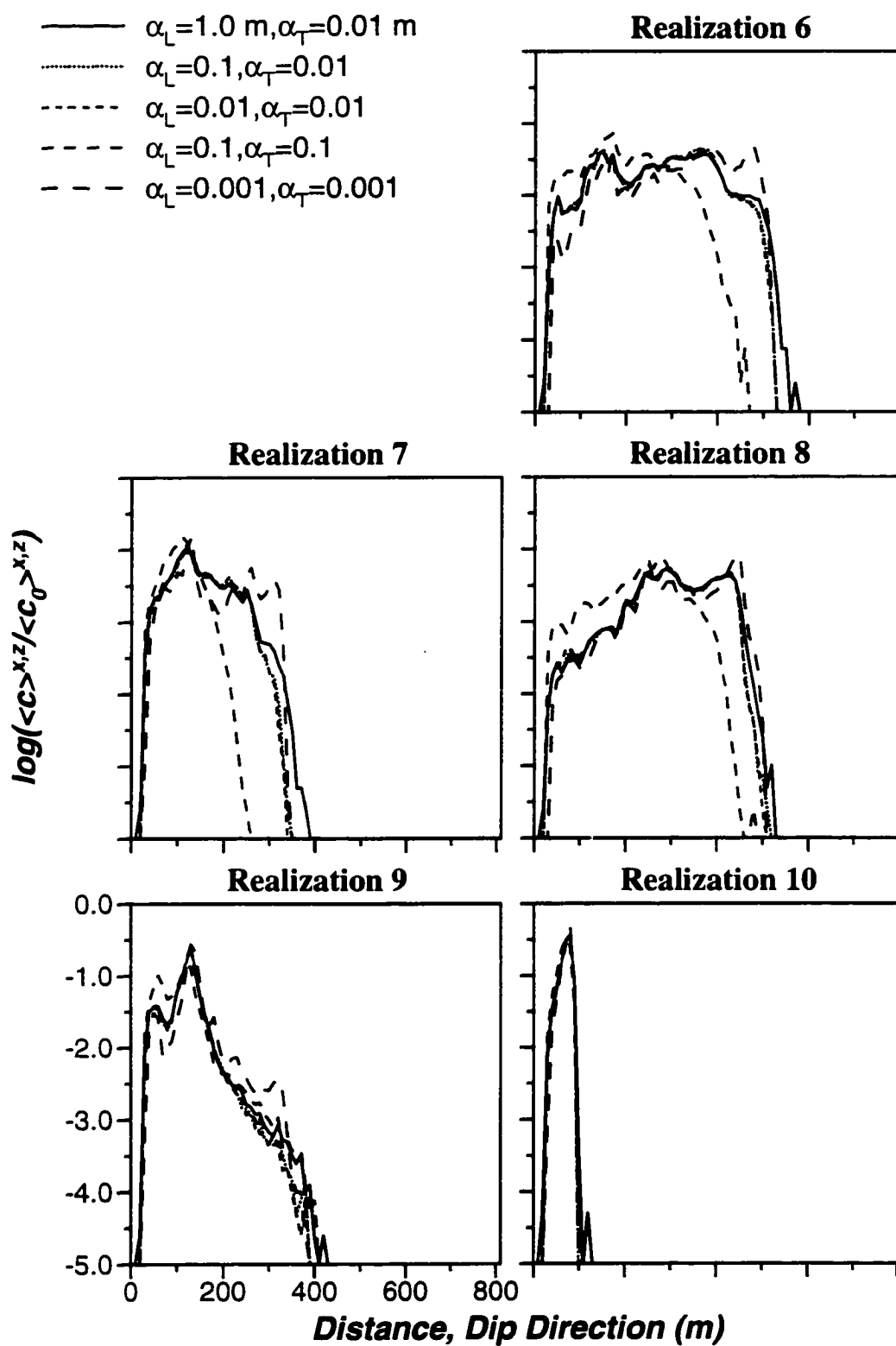


Figure 5C.1: Normalized x - z -average plumes, realizations 1 – 5, at year 20 are compared for scenarios 5C.1 – 5C.5.

dispersion and attenuation of mass with increasing α_T , scenarios 5C.3 – 5C.5. Simulated longitudinal first and second spatial moments are shown in Figures 5C.3 - 5C.6. Again, results for scenarios 5C.1 – 5C.3 are nearly identical, even though α_L varies over two orders of magnitude among them, whereas results for scenarios 5C.3 – 5C.5 show a significant increase in sequestration of mass with increase in α_T . Response of PAT to changes in dispersivities is represented by log concentrations in the pumping well as shown in Figures 5C.7 and 5C.8. Again, results are relatively insensitive to α_L , and sensitive to α_T .

Results demonstrate that solutions are not particularly sensitive to α_L within the ranges considered here. This result was expected as longitudinal dispersion tends to spread mass along velocity streamlines, the effect of which is masked by the much larger macrodispersivity. Results for scenarios 5C.3 – 5C.5 demonstrate significant sensitivity of solutions to α_T , which varies over two orders of magnitude. As transverse dispersion at the local scale increases with α_T , mass more rapidly moves between streamlines. As a result, the plume experiences greater variations in velocity. If initial conditions were unconditional, i.e., distributed uniformly between hydrofacies, increasing α_T could be expected to reduce macrodispersion and attenuation [Gelhar, 1993]. Results demonstrate that use of an isotropic *local-scale* dispersivity equal to the transverse dispersivity yields an accurate approximation for predicting field-scale transport. This result shows that one can use the more efficient isotropic versions of algorithms presented Chapters 1 and 3 without sacrificing accuracy. Further, although changes in solution with α_T are significant and could affect conclusions with regard to specific remediation scenarios to be presented, none appear great enough to affect the more general conclusions regarding the role of diffusion in contaminant migration and remediation at LLNL.

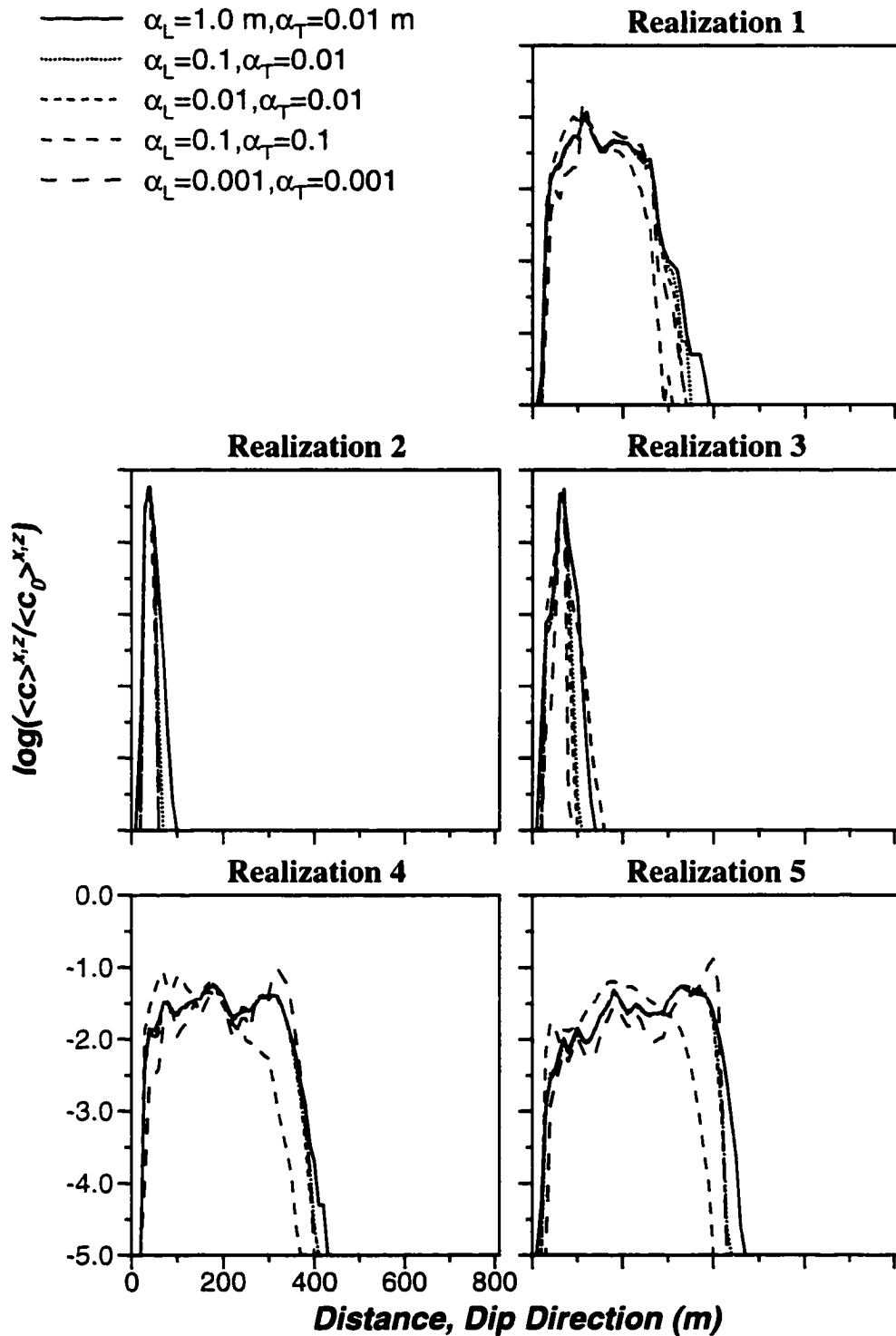


Figure 5C.2: Normalized x - z -average plumes, realizations 6 – 10, at year 20 are compared for scenarios 5C.1 – 5C.5.

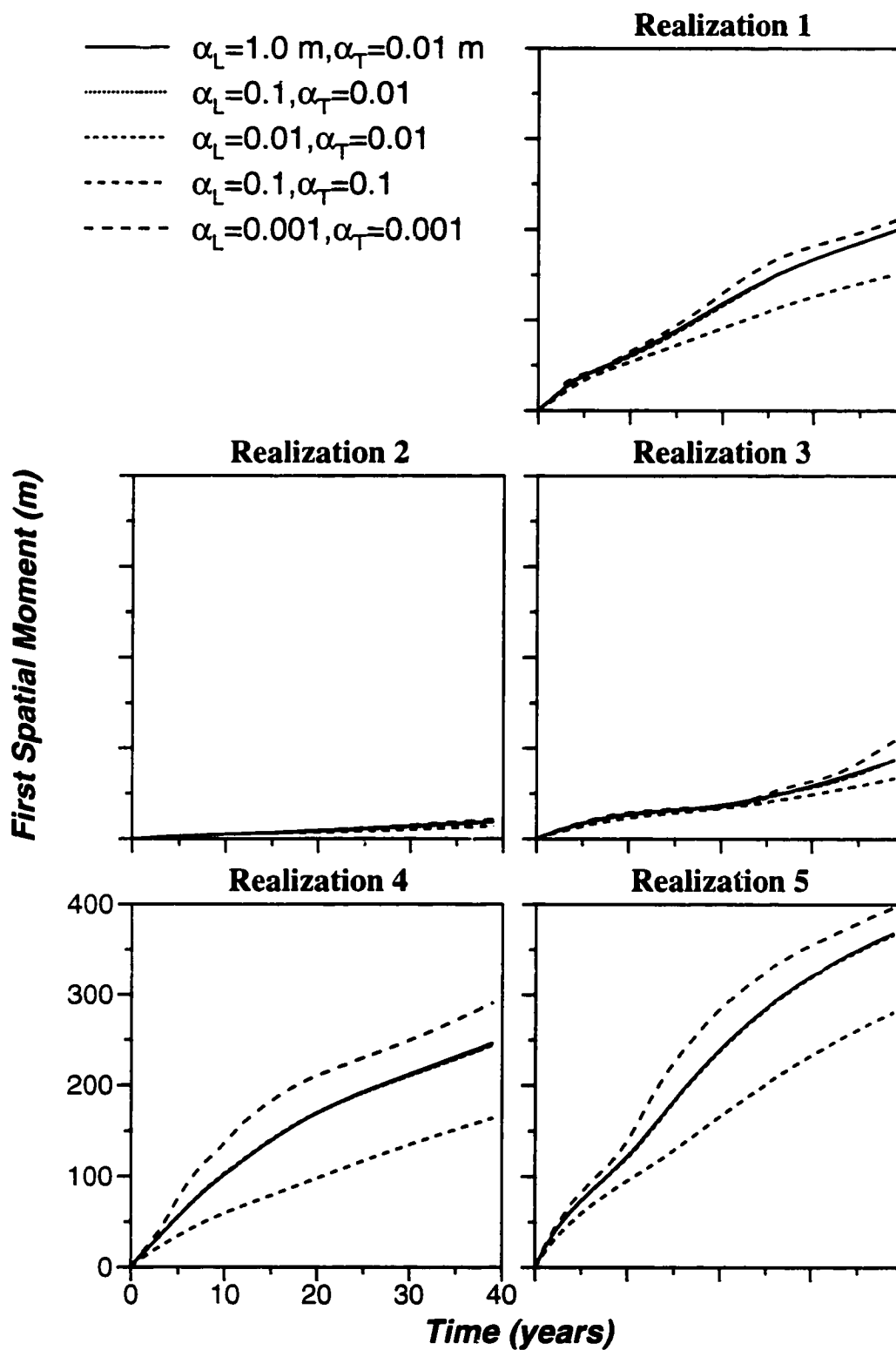


Figure 5C.3: First spatial moments for realizations 1 – 5 are compared for scenarios 5C.1 – 5C.5.

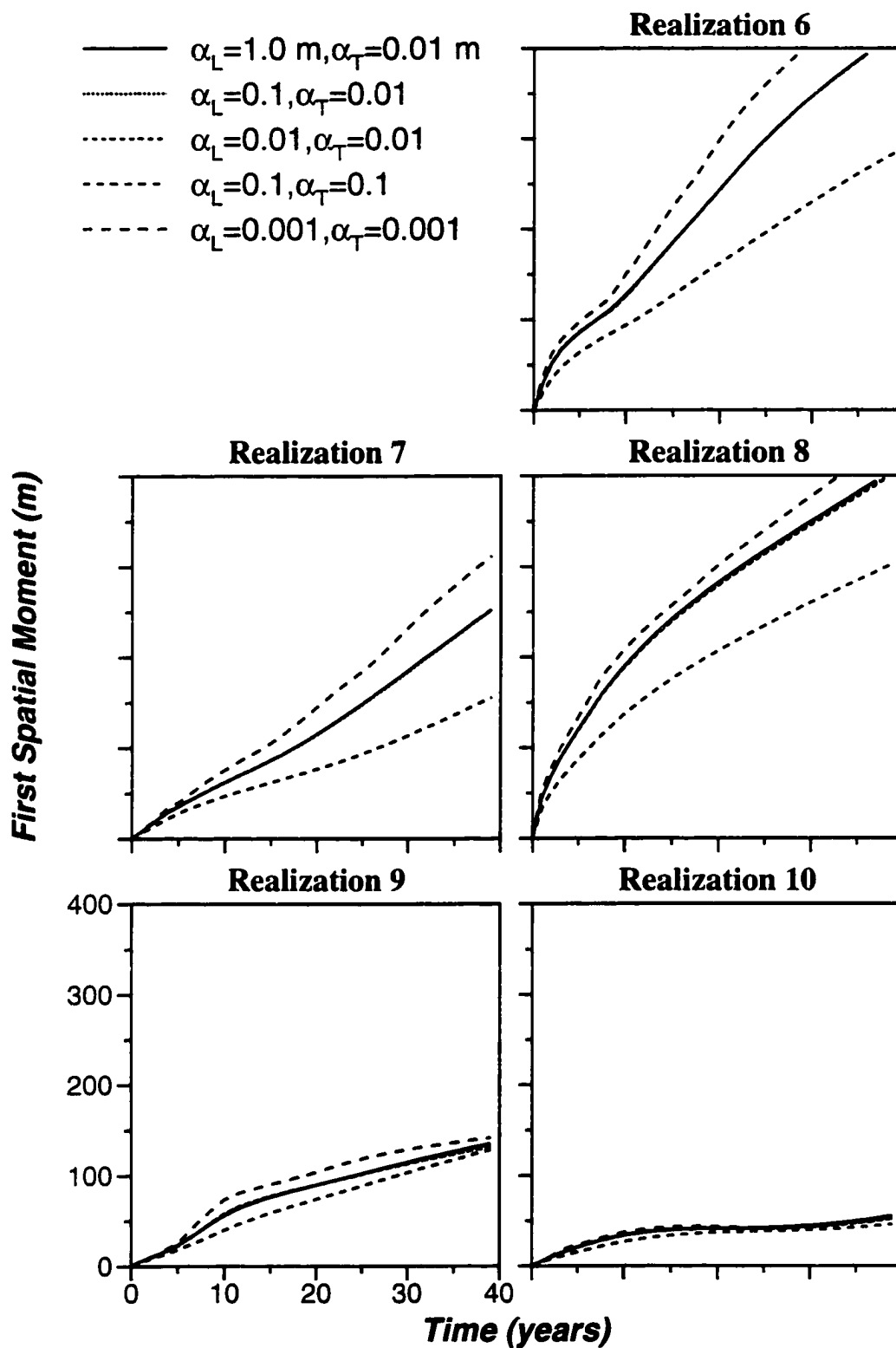


Figure 5C.4: First spatial moments for realizations 6 – 10 are compared for scenarios 5C.1 – 5C.5.

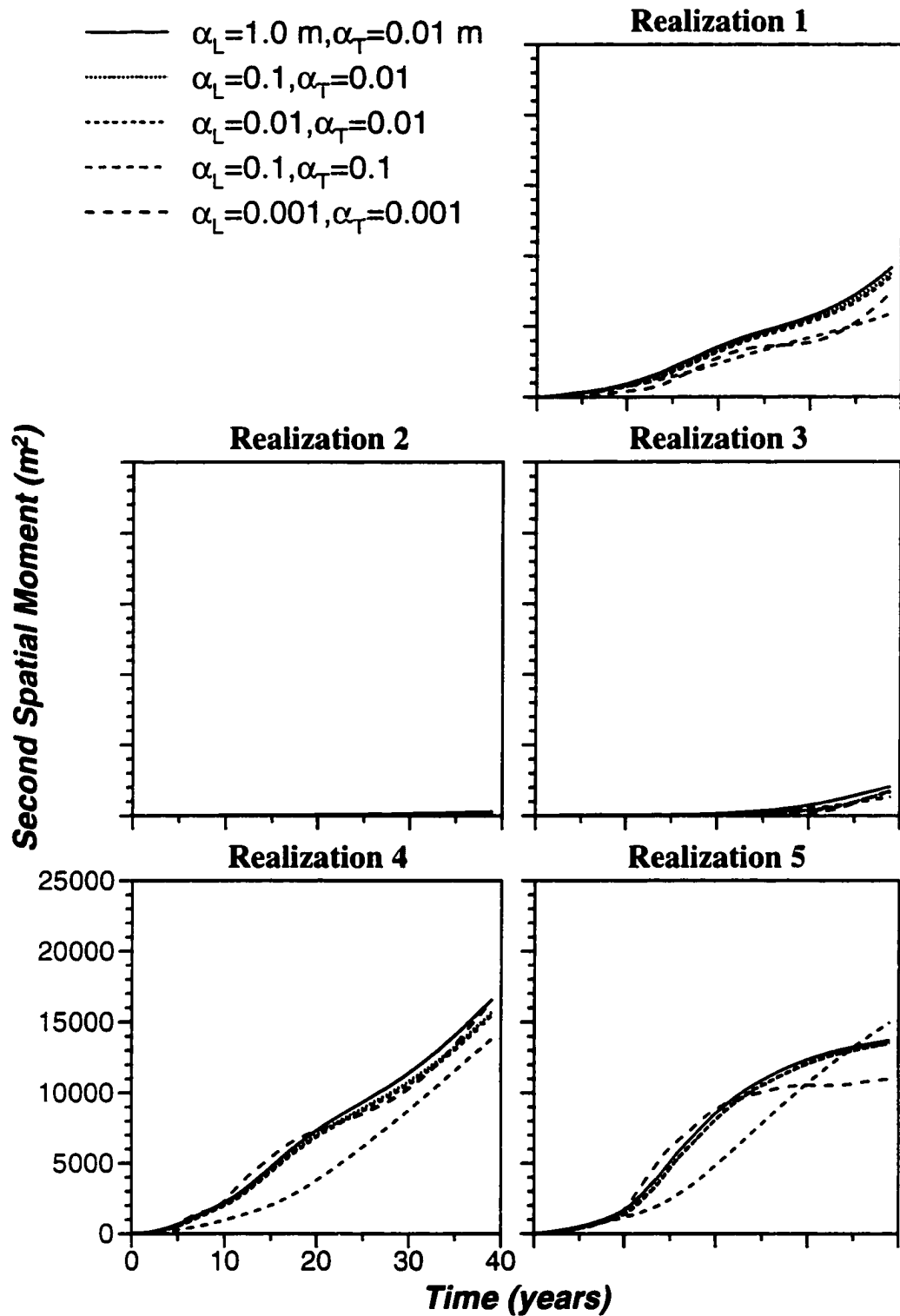


Figure 5C.5: Longitudinal second spatial moments for realizations 1 – 5 are compared for scenarios 5C.1 – 5C.5.

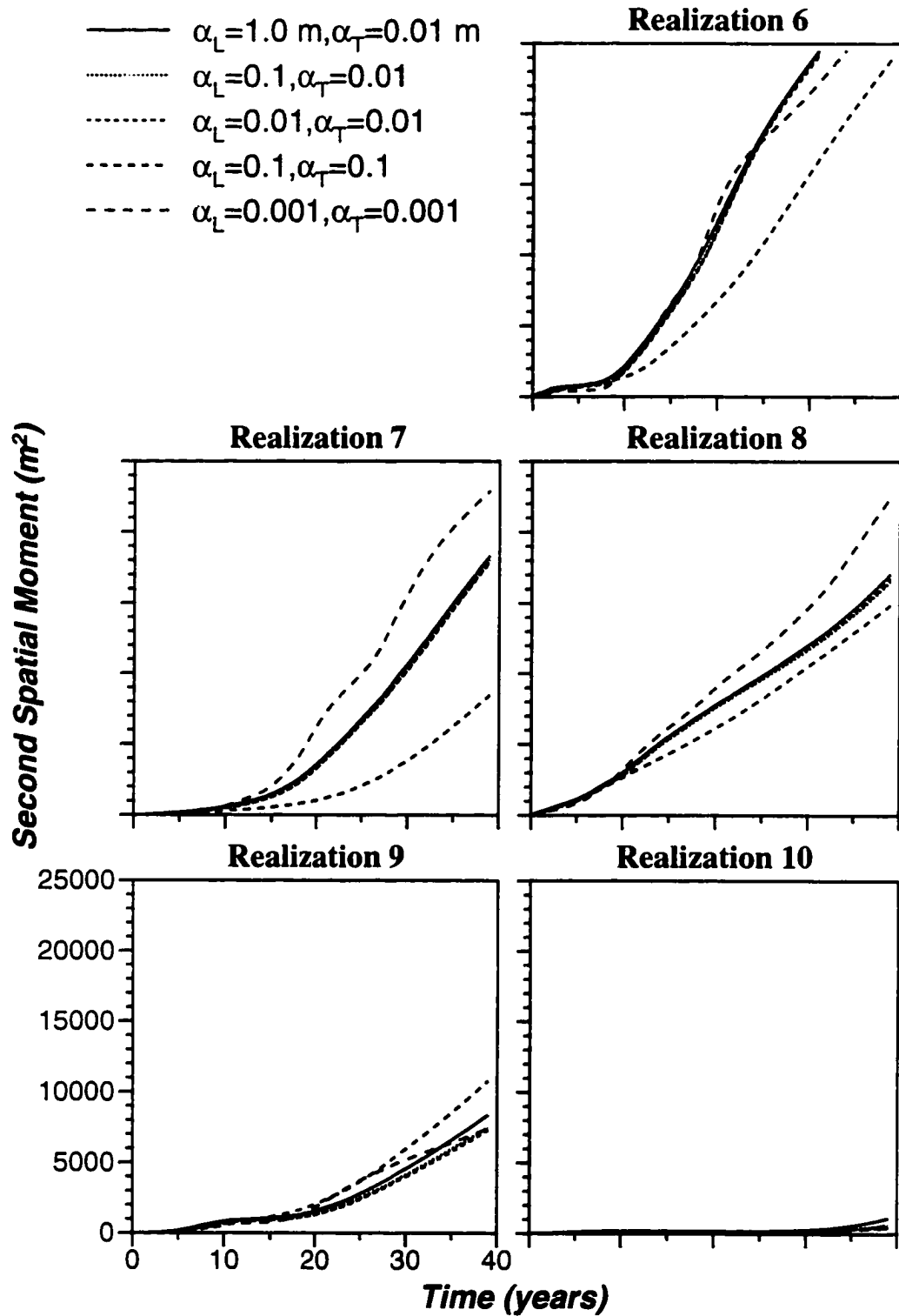


Figure 5C.6: Longitudinal second spatial moments for realizations 6 – 10 are compared for scenarios 5C.1 – 5C.5.

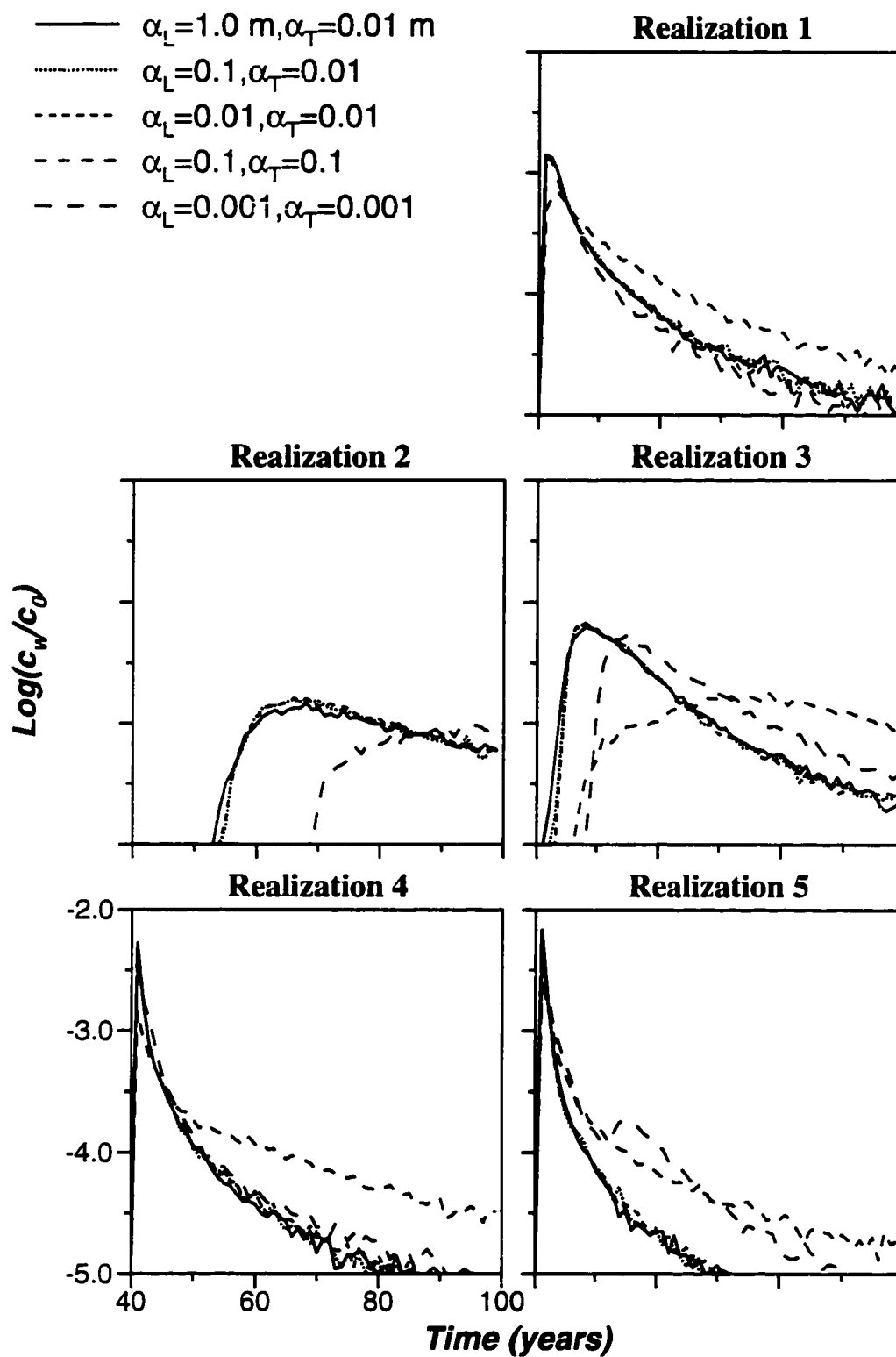


Figure 5C.7: Concentration at the pumping well for realizations 1 – 5 are compared for scenarios 5C.1 – 5C.5.

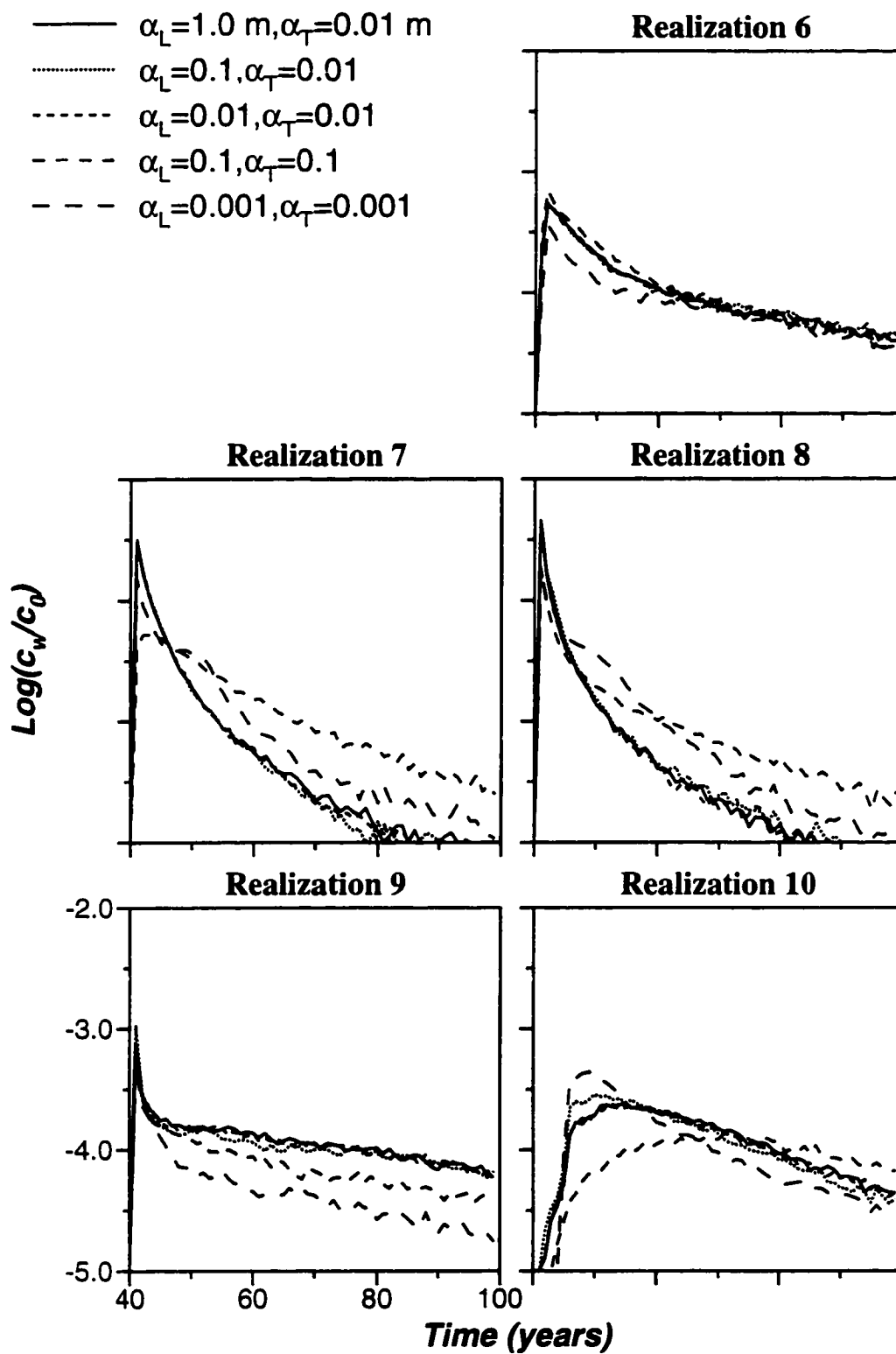


Figure 5C.8: Concentration at the pumping well for realizations 6 – 10 are compared for scenarios 5C.1 – 5C.5.

Appendix 5D: Three Dimensional Particle Distributions

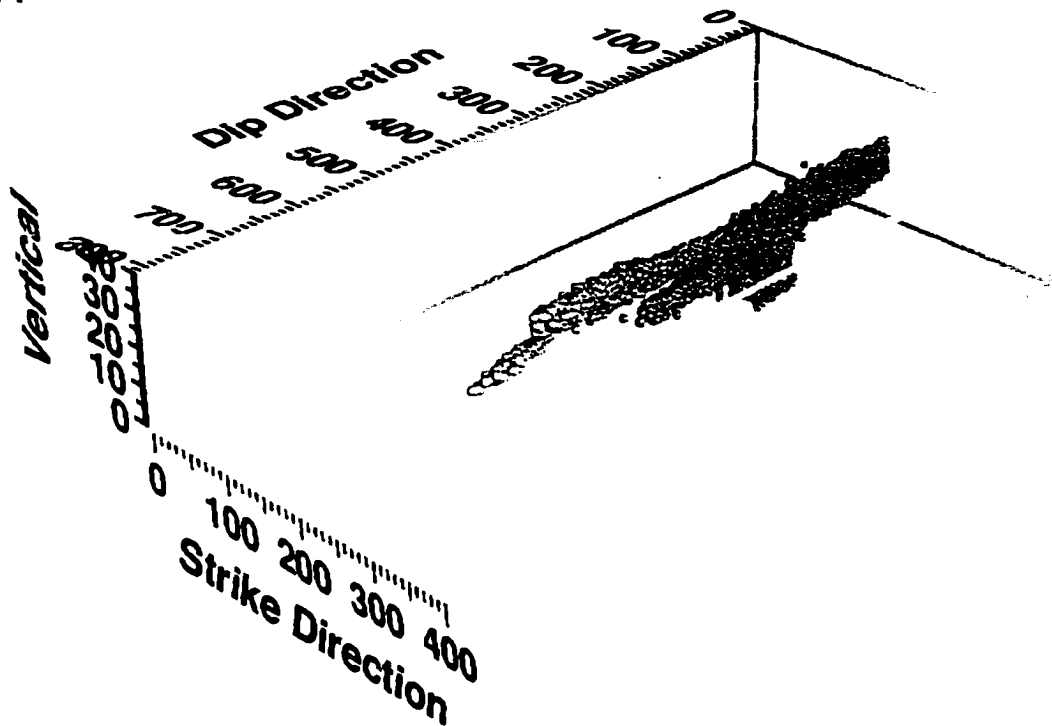


Figure 5D.1a: Three dimensional particle distribution for scenario 2 ($D^* = 5.2 \times 10^{-5}$ m²/day), realization 1, year 40.

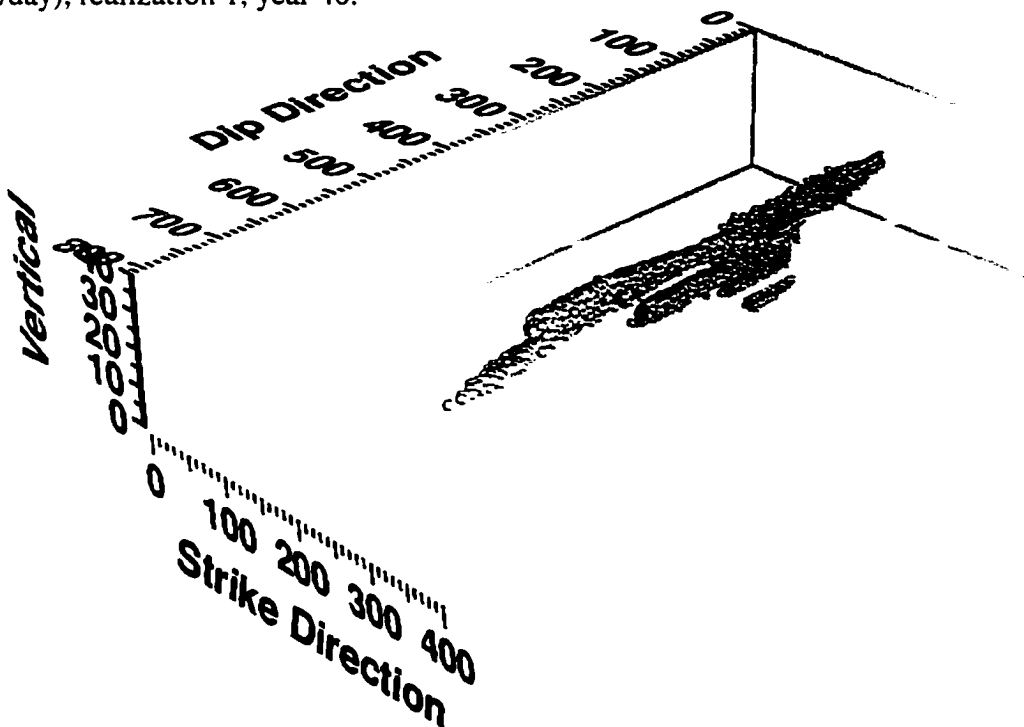


Figure 5D.1b: Three dimensional particle distribution for scenario 3 ($D^* = 10^{-6}$ m²/day), realization 1, year 40.

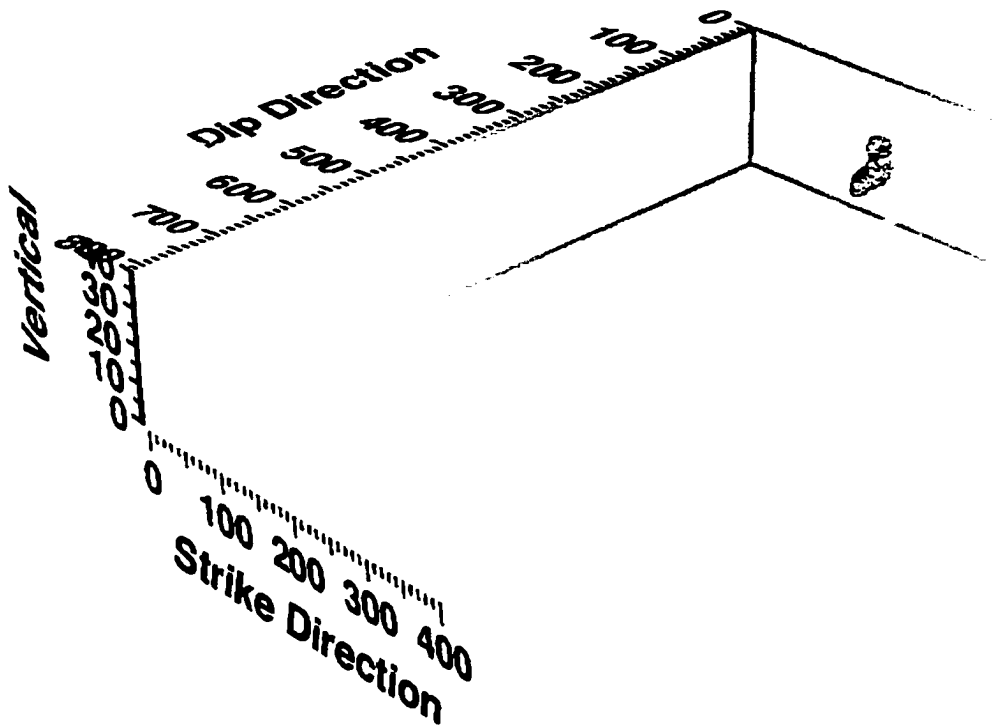


Figure 5D.2a: Three dimensional particle distribution for scenario 2 ($D^* = 5.2 \times 10^{-5}$ m²/day), realization 2, year 40.

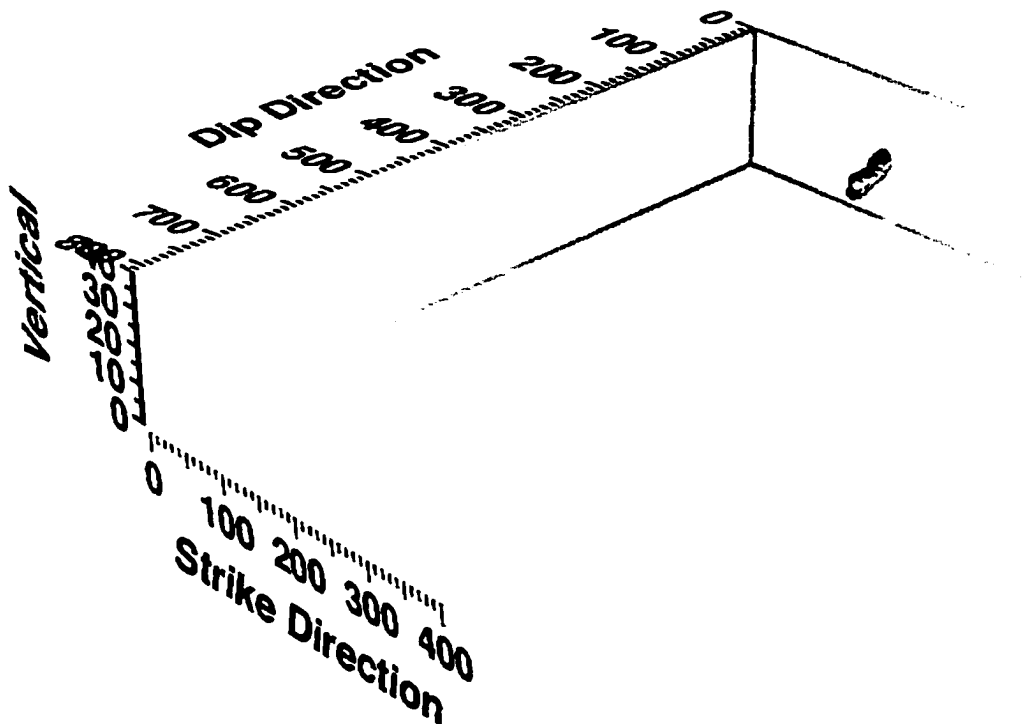


Figure 5D.2b: Three dimensional particle distribution for scenario 3 ($D^* = 10^{-6}$ m²/day), realization 2, year 40.

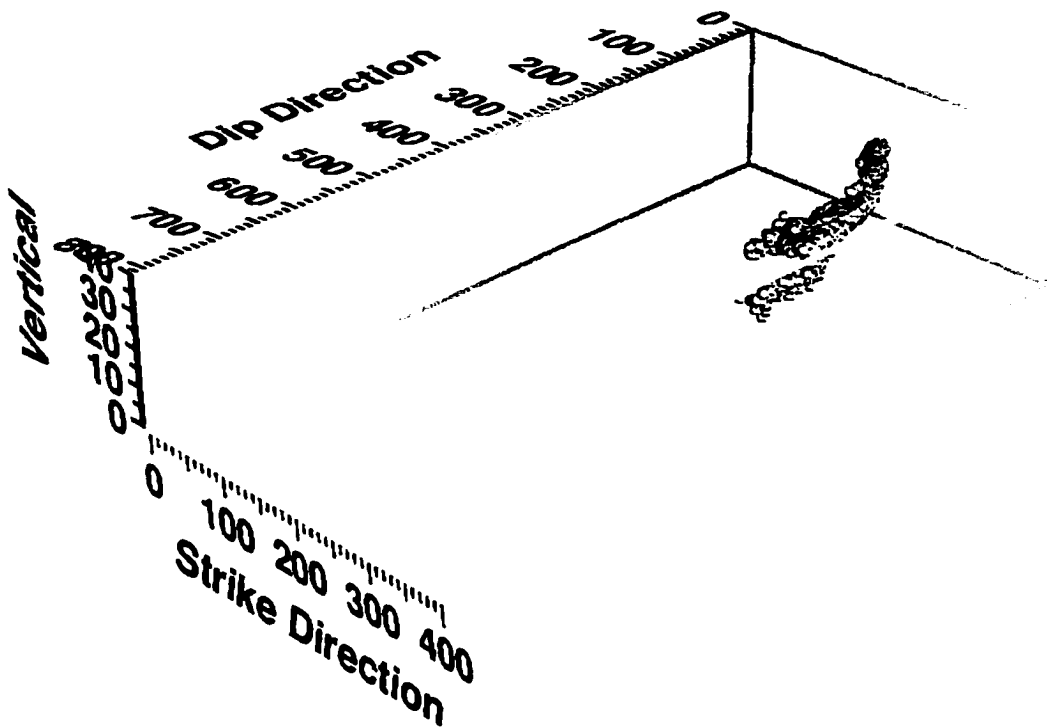


Figure 5D.3a: Three dimensional particle distribution for scenario 2 ($D^* = 5.2 \times 10^{-5}$ m²/day), realization 3, year 40.

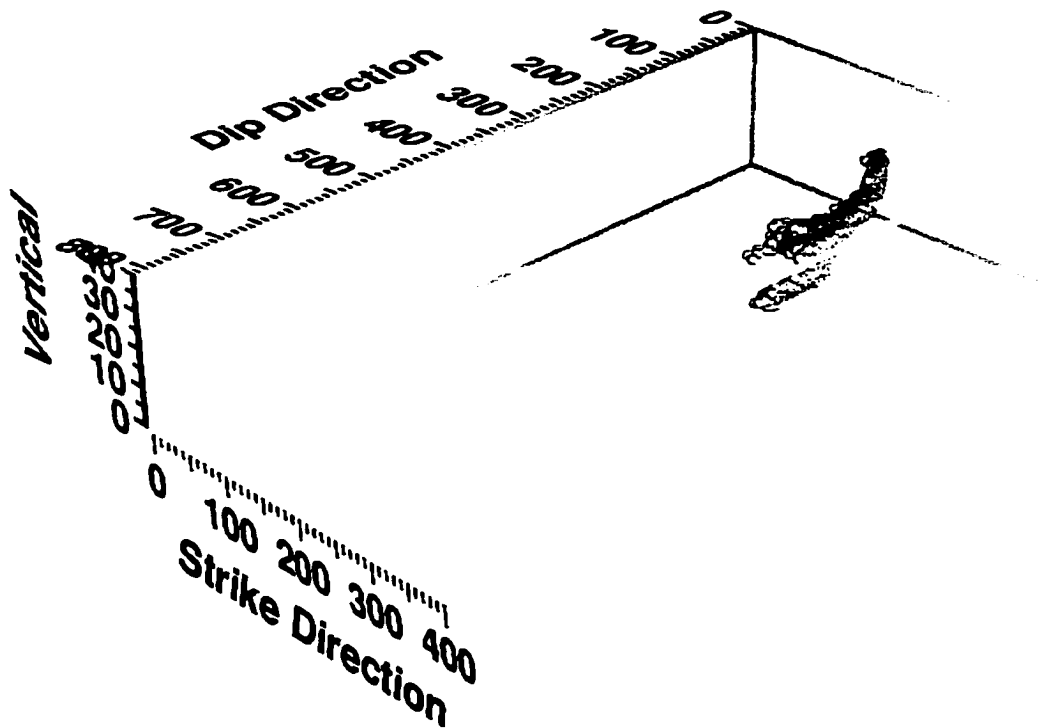


Figure 5D.3b: Three dimensional particle distribution for scenario 3 ($D^* = 10^{-6}$ m²/day), realization 3, year 40.

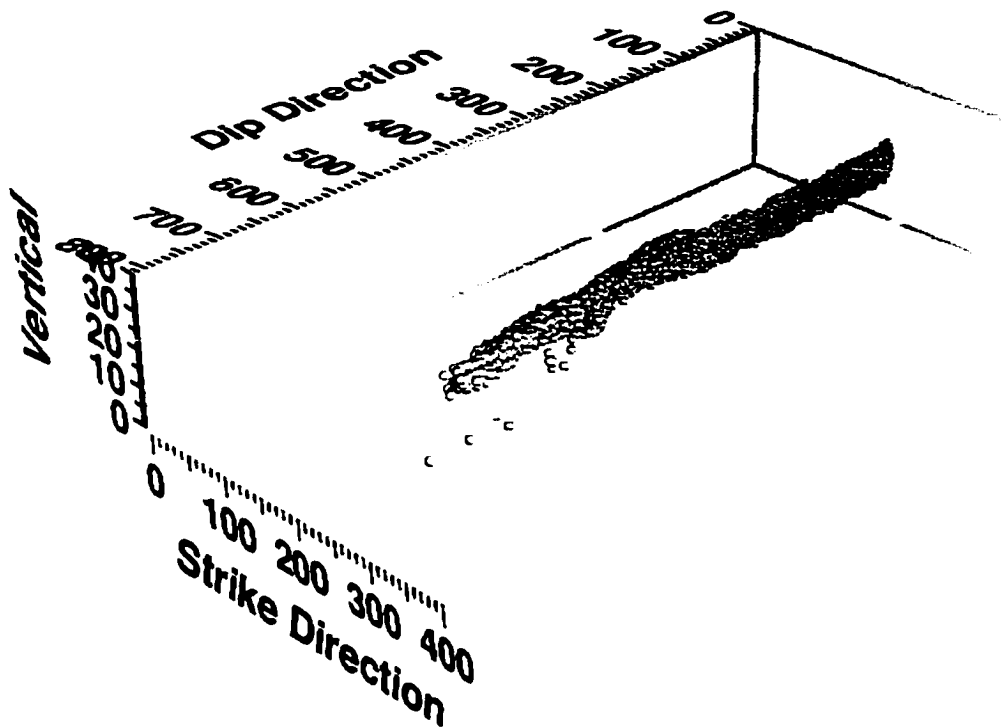


Figure 5D.4a: Three dimensional particle distribution for scenario 2 ($D^* = 5.2 \times 10^{-5}$ m²/day), realization 4, year 40.

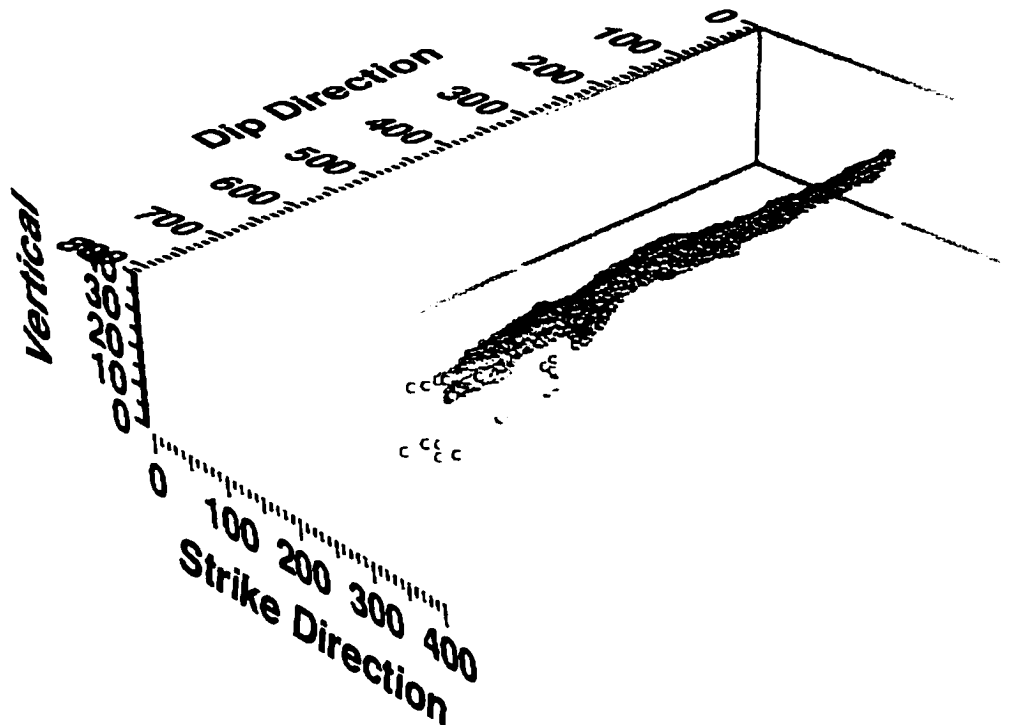


Figure 5D.4b: Three dimensional particle distribution for scenario 3 ($D^* = 10^{-6}$ m²/day), realization 4, year 40.

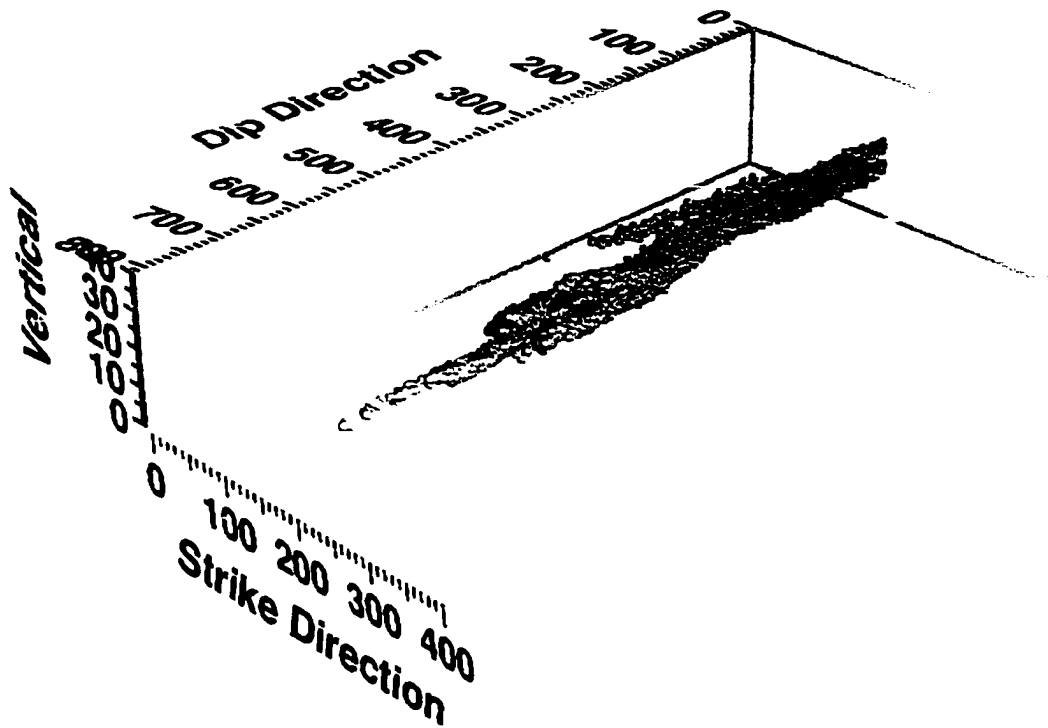


Figure 5D.5a: Three dimensional particle distribution for scenario 2 ($D^* = 5.2 \times 10^{-5}$ m²/day), realization 5, year 40.

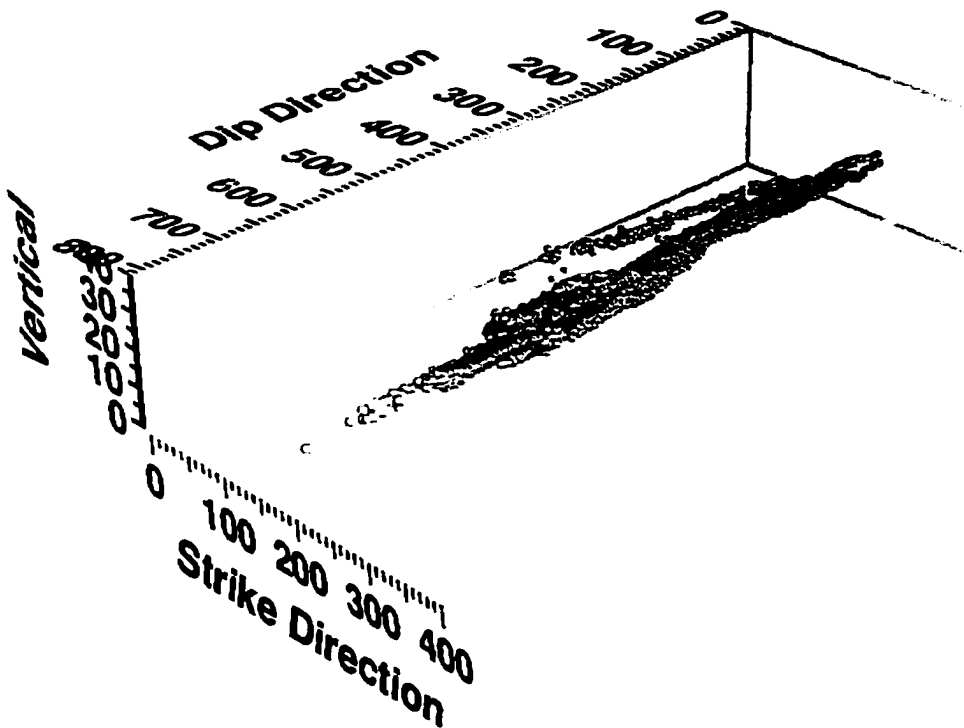


Figure 5D.5b: Three dimensional particle distribution for scenario 3 ($D^* = 10^{-6}$ m²/day), realization 5, year 40.

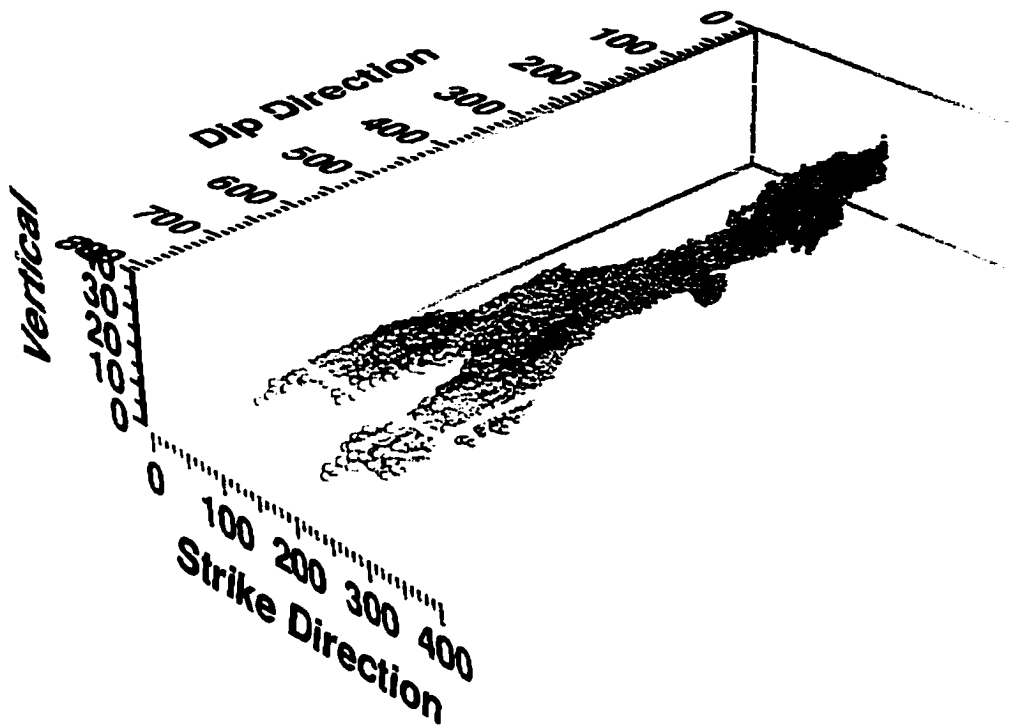


Figure 5D.6a: Three dimensional particle distribution for scenario 2 ($D^* = 5.2 \times 10^{-5}$ m²/day), realization 6, year 40.

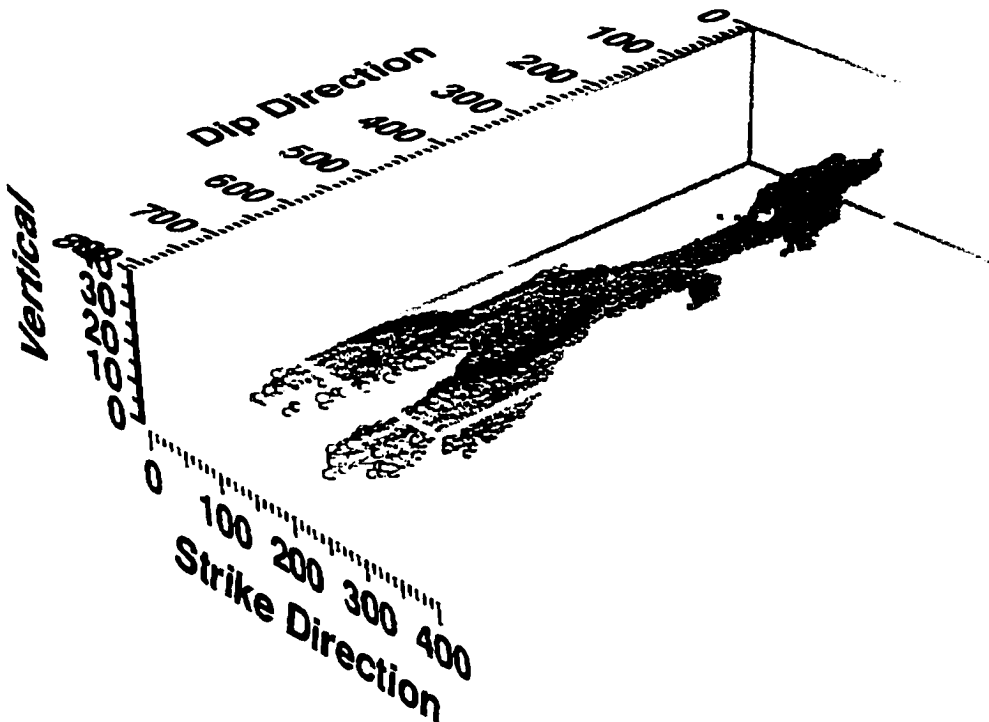


Figure 5D.6b: Three dimensional particle distribution for scenario 3 ($D^* = 10^{-6}$ m²/day), realization 6, year 40.

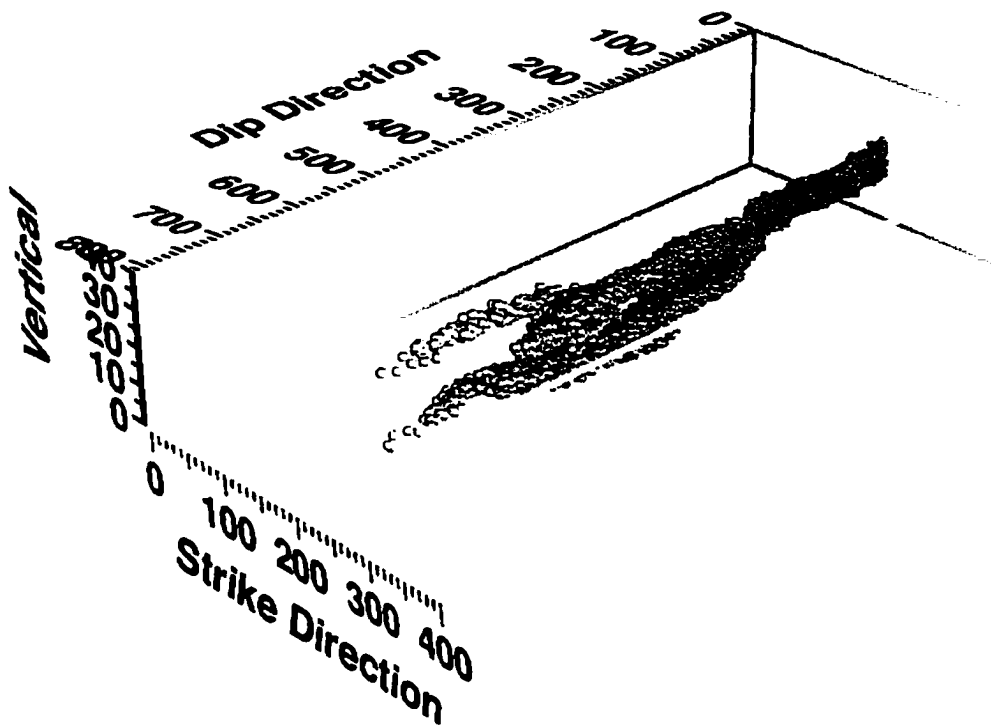


Figure 5D.7a: Three dimensional particle distribution for scenario 2 ($D^* = 5.2 \times 10^{-5}$ m²/day), realization 7, year 40.

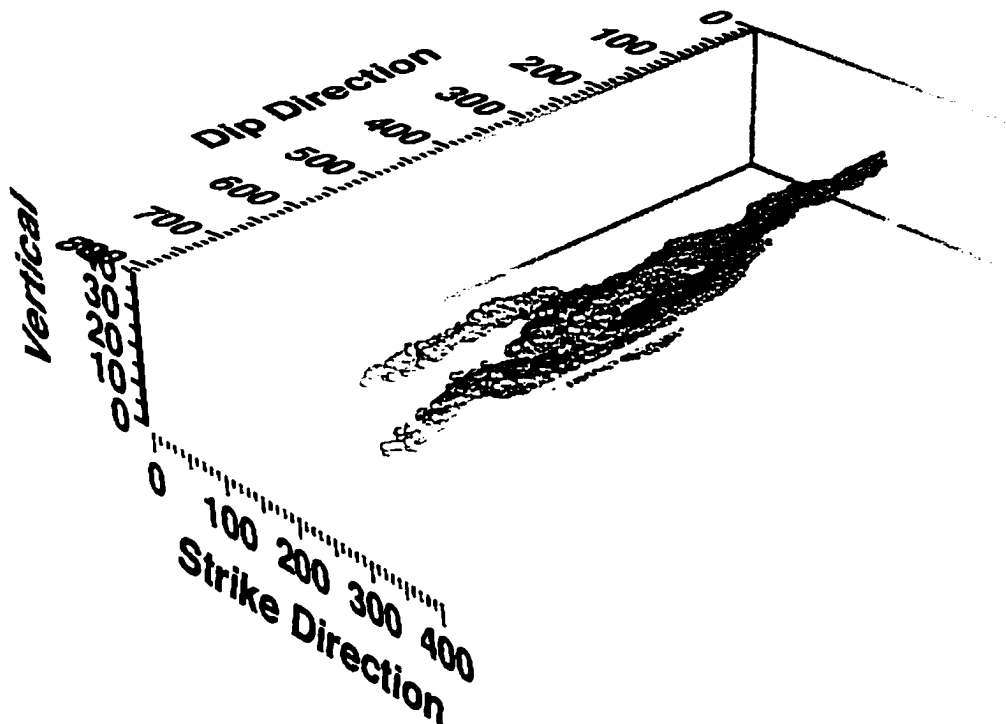


Figure 5D.7b: Three dimensional particle distribution for scenario 3 ($D^* = 10^{-6}$ m²/day), realization 7, year 40.

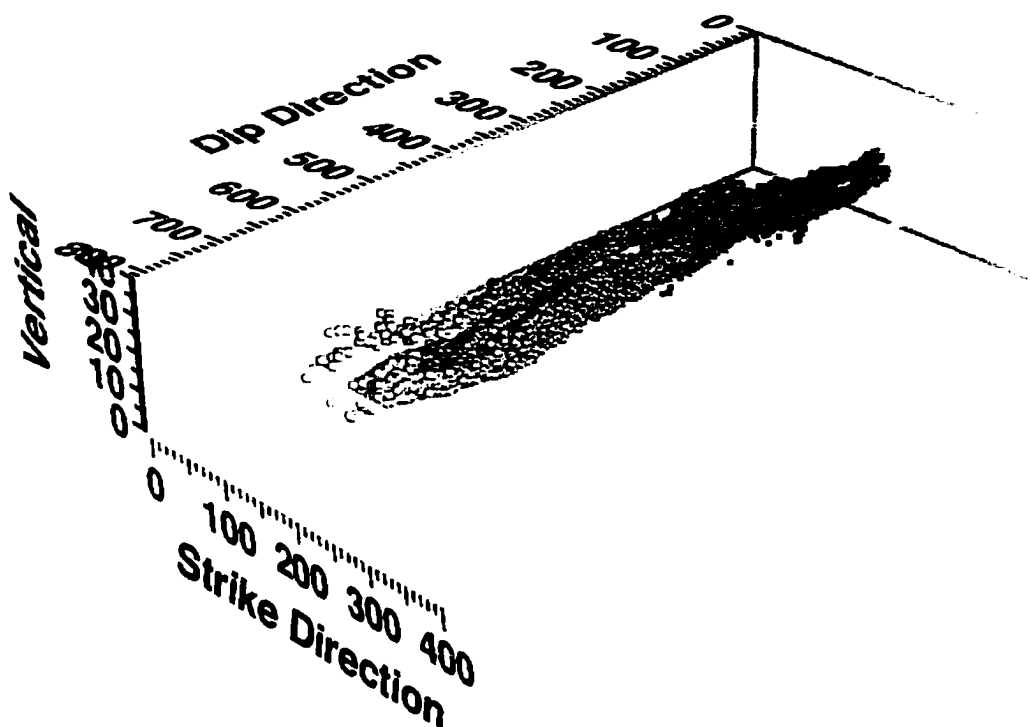


Figure 5D.8a: Three dimensional particle distribution for scenario 2 ($D^* = 5.2 \times 10^{-5}$ m²/day), realization 8, year 40.

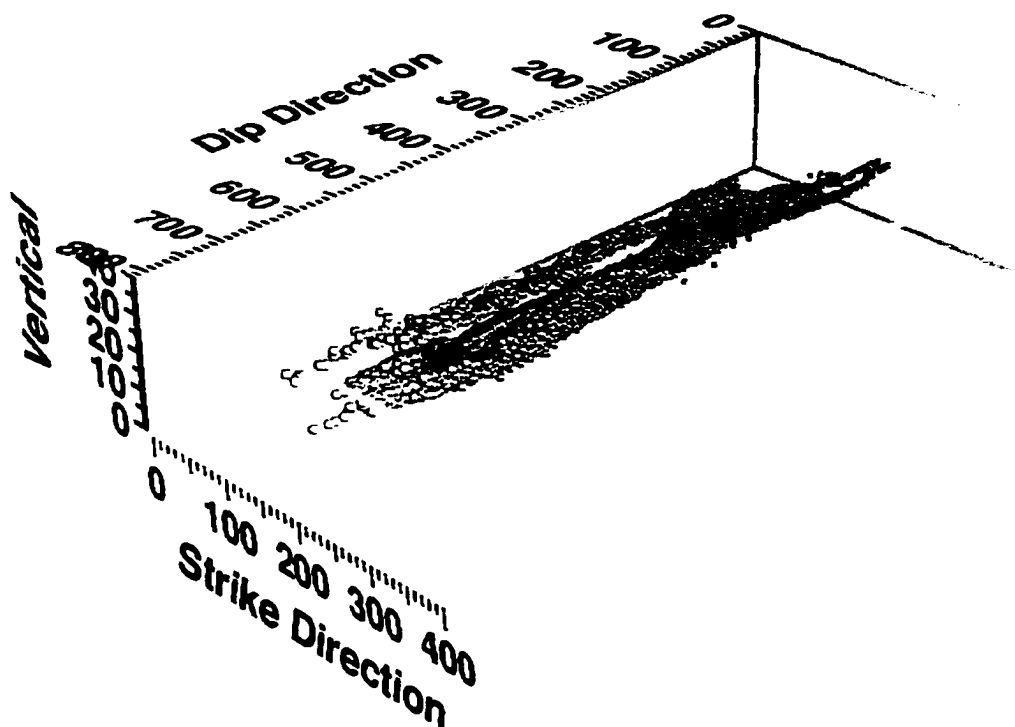


Figure 5D.8b: Three dimensional particle distribution for scenario 3 ($D^* = 10^{-6}$ m²/day), realization 8, year 40.

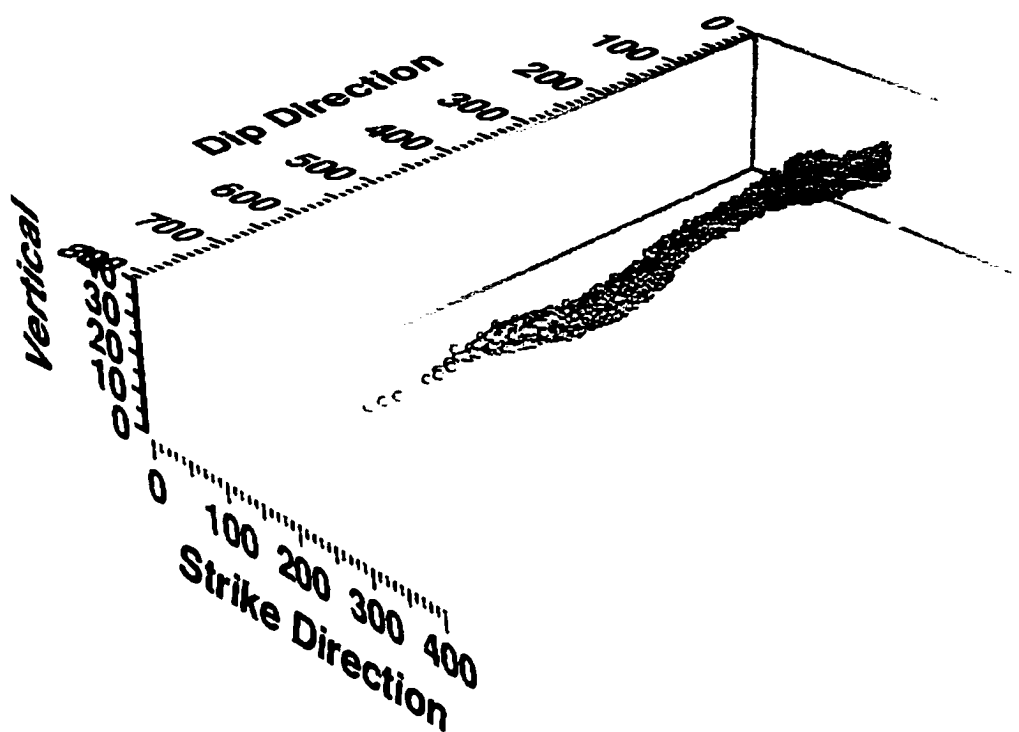


Figure 5D.9a: Three dimensional particle distribution for scenario 2 ($D^* = 5.2 \times 10^{-5}$ m²/day), realization 9, year 40.

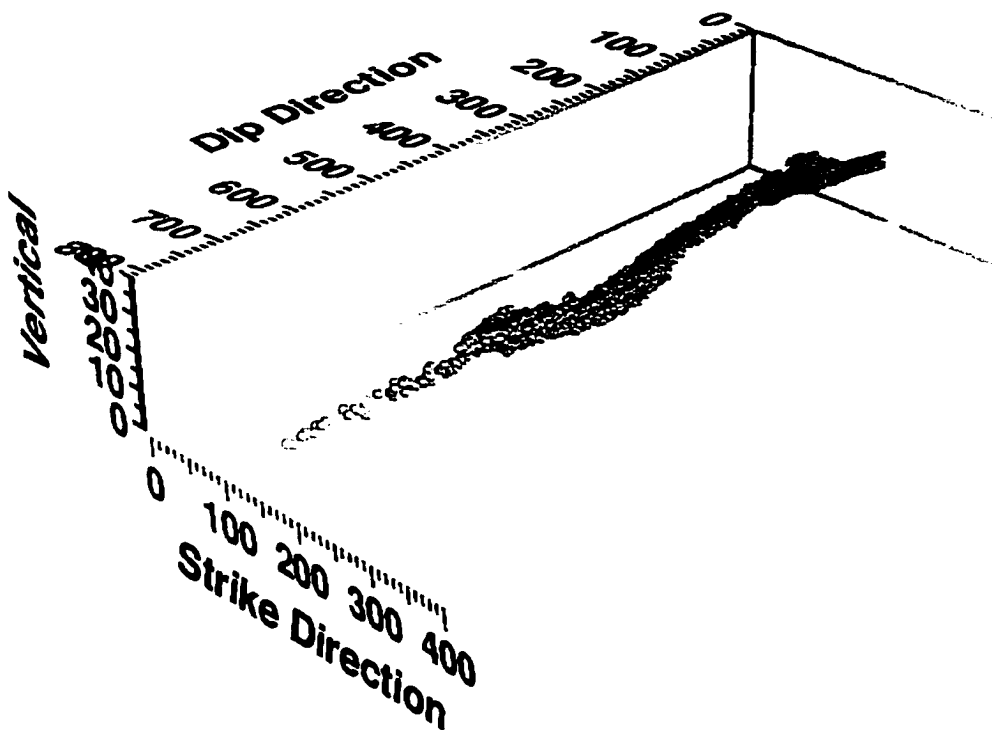


Figure 5D.9b: Three dimensional particle distribution for scenario 3 ($D^* = 10^{-6}$ m²/day), realization 9, year 40.

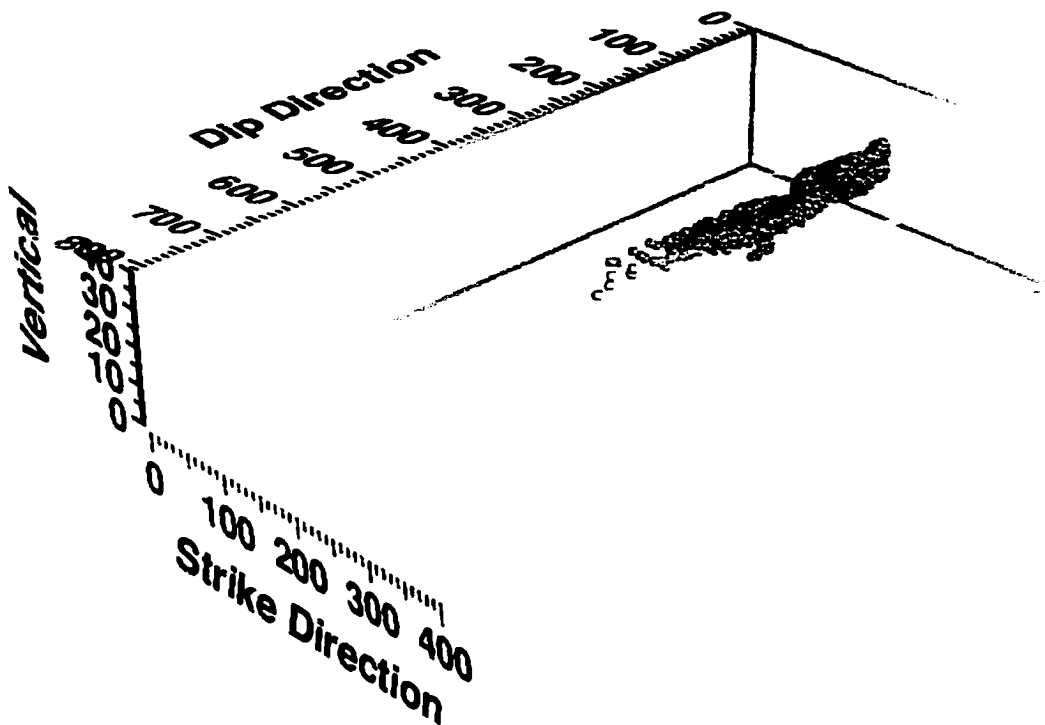


Figure 5D.10a: Three dimensional particle distribution for scenario 2 ($D^* = 5.2 \times 10^{-5}$ m²/day), realization 10, year 40.

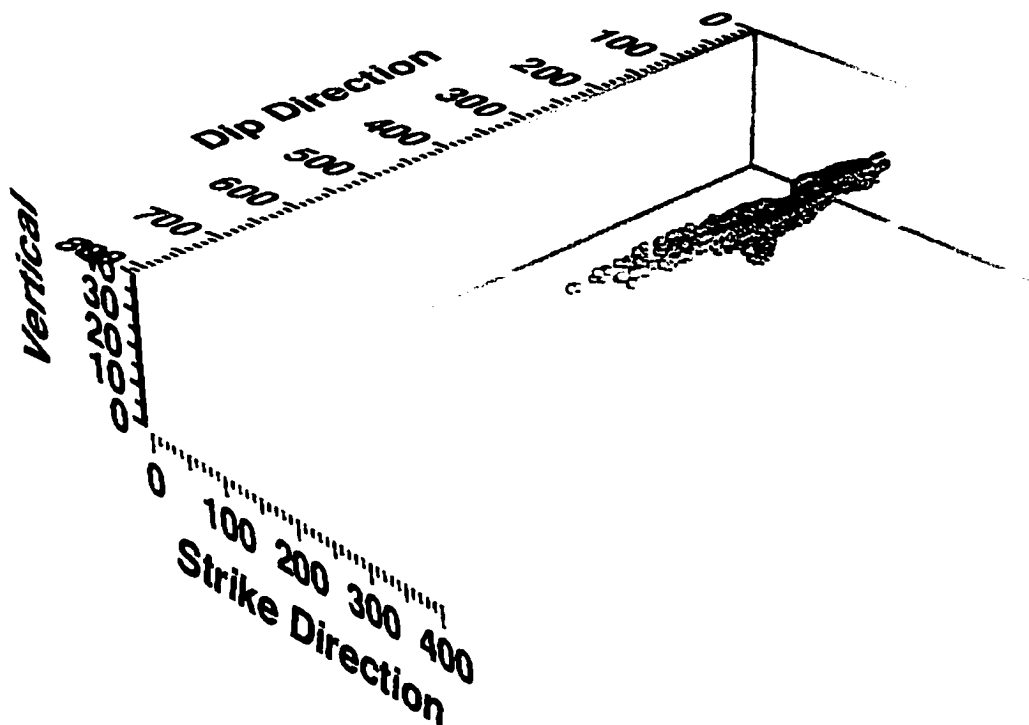


Figure 5D.10b: Three dimensional particle distribution for scenario 3 ($D^* = 10^{-6}$ m²/day), realization 10, year 40.